FCC CDR Volume 4 - Lepton Collider (Concise, short)

Volume Editors

tbd

Chapter Editors

tbd

Cover Design

Firstname. Lastname

Acknowledgements

We wish to acknowledge the extraordinary effort from the FCC Collaboration in production this Conceptual Design Report. We wish to thank the International Advisory Committee members (list of names) for their support in the preparation, review and consolidation of this work. For their constructive comments and guidance, we would like to thank our reviewers: list of names. Finally, we wish to thank the CERN management for their strong support and encouragement.

Trademark notice: All trademarks appearing in this report are acknowledged as such.

Also available at: `http://cds.cern.ch/tbd`

DRAFT FOR ADVISORY COMMITTEE - DO NOT DISTRIBUTE

FCC Collaboration

To be done.

Executive Summary

This is the executive summary of the report.

Contents

DRAFT FOR ADVISORY COMMITTEE - DO NOT DISTRIBUTE

DRAFT FOR ADVISORY COMMITTEE - DO NOT DISTRIBUTE

DRAFT FOR ADVISORY COMMITTEE - DO NOT DISTRIBUTE

DRAFT FOR ADVISORY COMMITTEE - DO NOT DISTRIBUTE

DRAFT FOR ADVISORY COMMITTEE - DO NOT DISTRIBUTE

DRAFT FOR ADVISORY COMMITTEE - DO NOT DISTRIBUTE

DRAFT FOR ADVISORY COMMITTEE - DO NOT DISTRIBUTE

Chapter 1

Physics Discovery Potential

Patrick Janot: Patrick Janot, 20 pages

1.1 Overview

There is a strong scientific case for an electron-positron collider, complementary to the LHC, that can study the properties of the Higgs boson and other particles with unprecedented precision and whose energy can be upgraded. [1]

This strategic guideline from the 2013 update of the European Strategy for Particle Physics (ESPP 2013) defines unambiguously the high standards to be met by the future e^+e^- collider, quite possibly the next high-energy collider to be built. Since its inception, the FCC-ee study has aimed at delivering the e^+e^- collider conceptual design that complies best with this guideline, and consequently offers, in a cost-effective fashion, the broadest physics discovery potential and the most ambitious perspectives for future developments.

As a result of the renewed worldwide interest for e^+e^- physics and the pertaining discovery potential since the observation of the Higgs boson at the LHC, the FCC is not alone in this quest. In the absence of convincing hints for a physics beyond the standard model (BSM) in the LHC data so far, the situation has significantly evolved since 2013, so that not fewer than five e^+e^- collider designs are contemplated today to study the properties of the Higgs boson and other standard model (SM) particles with an unprecedented precision:

- the historical International Linear Collider (ILC [2]) project, for which the above guideline was originally tailored, now focusses on studying the Higgs boson with a centre-of-mass energy $\sqrt{s}$ of 250 GeV [3];
- the Compact Linear Collider (CLIC [4]) reduced their lowest centre-of-mass energy point from 500 to 380 GeV [5], in order to best study the Higgs boson and the top quark;
- a circular collider in the LEP/LHC tunnel (LEP3 [6, 7]), able to study the Z, the W, and the Higgs bosons, with centre-of-mass energies from 80 to 240 GeV;
- the Chinese Circular Electron Positron Collider (CEPC [8, 9]), in a 100 km tunnel and with aims similar to those of LEP3; and
- the Future e^+e^- Circular Collider in a new $\sim$ 100 km tunnel at CERN (FCC-ee, formerly called TLEP [7, 10]), which can study the whole Electroweak sector (Z and W bosons, Higgs boson, top quark) with centre-of-mass energies between 80 and 380 GeV.

The baseline luminosities expected to be delivered at the ILC, CLIC, LEP3, CEPC, and FCC-ee centre-of-mass energies are illustrated in Fig. 1.1. The FCC-ee delivers the highest rates in a very clean, well-

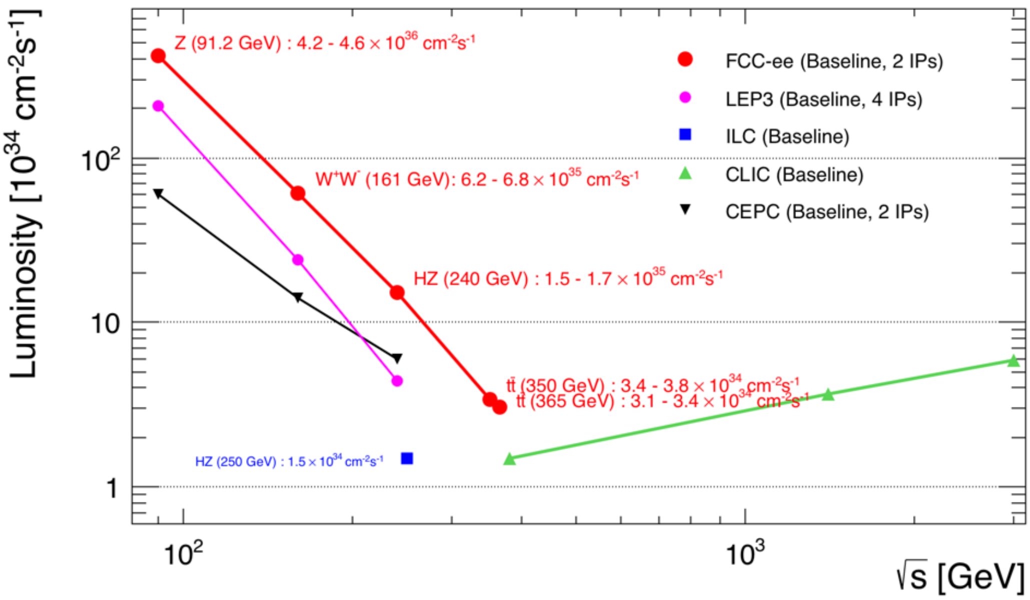

Figure 1.1: Baseline luminosities expected to be delivered (summed over all interaction points) as a function of the centre-of-mass energy, at each of the five worldwide e^+e^- collider projects: ILC (blue square), CLIC (green upward triangles), CEPC (black downward triangles), LEP3 (pink dots), and FCC-ee (red dots). The FCC-ee performance are taken from Section 2 and include a 10% safety margin, the LEP3 numbers result from adapting the FCC-ee optics to the shorter LEP/LHC tunnel, the latest incarnation of the CEPC parameters is inferred from Ref. [11], and the linear colliders luminosities are taken from Refs [3, 5].

defined, and precisely predictable environment, at the Z pole (91 GeV), at the WW threshold (161 GeV), as a Higgs factory (240 GeV), and around the $t\bar{t}$ threshold (350 to 365 GeV), to several interaction points. It also provides high precision center-of-mass energy calibration at the 100 keV level at the Z and W energies. This collider is therefore genuinely best suited to offer extreme statistical precision and experimental accuracy for the measurements of all standard model particle properties; to opens windows to detect new rare processes; and to give opportunities to observe tiny violations of established symmetries.

Historically, such precise measurements or subtle observations have always been precursors for the discovery of new phenomena and new particles, and towards a better theoretical description of fundamental physics. These historical precedents have also shown the important role played by lower-energy precision measurements when establishing road-maps for the observation of new particles with higher-energy machines. In the second half of the 1970's, precision measurements of neutral currents led to infer the existence of the W and Z bosons, as well as the values of their masses, from which the dimensions of the LEP tunnel were determined. The W and Z were then observed in the early 1980's at the CERN Sp$\bar{\text{p}}$S collider with masses in the predicted range. Subsequently, as described in more details in Section 1.2, the CERN LEP e^+e^- collider measured the properties of the Z and W bosons with high precision in the 1990's [12, 13]. These precise measurements could determine in a definitive way the number of light, active neutrinos, as well as infer the mass of the so far unseen top quark, which was soon discovered at the FNAL Tevatron within the predicted mass range. Having fixed m_{top}, the ensemble of precision measurements at LEP/SLC, the Tevatron and low energy inputs, led in turn to a $\pm 30\%$ accurate prediction for the mass of the Higgs boson, which was observed in 2012 at the LHC within the predicted mass range. it is important to note that these predictions were based on the standard model with no additional particle content than the one we know today.

With the Higgs boson discovery, the standard model seems complete, and its predictions have

DRAFT FOR ADVISORY COMMITTEE - DO NOT DISTRIBUTE

no more flexibility beyond the uncertainties on the theoretical calculations and on the input parameters. After this great success, should we stop our investigations? Of course not. Several experimental facts are telling us without any doubt that new phenomena must exist: the gravitational and cosmological evidence for non-baryonic dark matter; the cosmological baryon-antibaryon asymmetry; the finite albeit extremely small neutrino masses, etc., are all evidence for physics beyond the standard model. There is no unique theoretical guidance today able to tell unambiguously either the energy scale where new physics is to be looked for, nor its couplings to the standard model particles.The null result of experiments at colliders so far is an indication that either the scale is too high, or the couplings are too small. Any new lead would be a major discovery whether it is the discovery of a new particle, of a new so far unobserved phenomenon, or a non-trivial deviation from the standard model predictions.

The next accelerator project must allow the broadest possible field of research. This is definitely the case for the FCC. The FCC-ee, to begin with, would measure the Z, W, Higgs, and top properties ine^+e^- collisions, either for the first time or with a huge jump in statistics and precision, thereby giving access to either much higher scales or much smaller couplings. FCC-ee is the most powerful of the proposed e^+e^- colliders — all things being equal, in particular the price tag[1]. The FCC-ee is proposing a broad, multifaceted exploration to:

1. further constrain, at once (i.e., with a single machine and the same detectors), a large number of precise observables and parameters the standard model;
2. unveil small but significant deviations with respect to its predictions;
3. observe rare but unambiguously new processes or particles, beyond the standard model expectations;
4. and therefore, maximizes the chances to make a major discovery.

The FCC-ee also meets in the most ambitious manner the last criterion of the ESPP 2013 guideline (*[...] and whose energy can be upgraded*), as the FCC-ee tunnel is designed to ultimately host the FCC-hh, a hadron collider with a centre-of-mass energy of 100 TeV. The FCC-hh physics reach at the energy and precision frontiers exceeds that of any proposed linear collider energy upgrade. It also greatly benefits from the measurements provided by the FCC-ee. The multiple synergies between the FCC-ee and the FCC-hh are discussed in the Volume 1 of this Conceptual Design Report.

The FCC-ee design study primary goal was to demonstrate the feasibility of the accelerator. This as been done beautifully, confirming and even exceeding the original luminosity expectations. A compelling run plan was elaborated. Great confidence can be given for the integration of the detectors at the collision points, and in the ability to reach the beam energy calibration targets. The exploration of the physics capabilities is still at a preliminary stage: it is not easy to imagine all systematic errors, all rare phenomena and all new physics scenarios accessible when extending the LEP statistics from 10^7 Z decays at LEP to 510^{12} at FCC-ee! Nevertheless the most straightforward studies presented in the next sections will give a flavour of the extraordinary physics potential of FCC-ee.

1.2 Precision Electroweak Measurements

Since the early work by Veltman [14], it has been known that the electroweak radiative corrections are sensitive to particles that couple to the electroweak interactions and that could be at much higher masses than accessible with the centre-of-mass energies available. The case of the top quark and Higgs boson masses were particularly interesting since their effect would not decouple at high mass, because they break the SU(2) symmetry. Further studies in the late 80's led to the realisation that these radiative corrections could be separated in blocks with different sensitivities and which modify the relationships

[1] The LEP3 facility can be built at much smaller cost than the other e^+e^- colliders, as it reuses existing infrastructure, at the expense of not being able to measure the top-quark properties, and therefore of reducing the sensitivity to new phenomena with respect to the FCC-ee.

DRAFT FOR ADVISORY COMMITTEE - DO NOT DISTRIBUTE

between observables. This allows precision measurements to explore the possible presence of further particles coupled to the Standard Model interactions in a broad way. The FCC-ee will provide precision measurements at the Z, the W the Higgs and the top, and will also perform measurements of 'noise parameters' such as the top quark mass and $\alpha_{\mathrm{QED}}(m_{\mathrm{Z}}^2)$. A sensitivity for new particles with masses of up to 10-70 TeV (if they decouple) and possibly much beyond (if they don't).

1.2.1 Current Situation

As briefly mentioned above, the Z lineshape parameters (the Z mass m_{Z}, the Z width Γ_{Z}, and the peak cross section σ^0) fitted to the LEP per-mil precision measurements of fermion pair production cross sections at and around the Z pole [12], were sensitive to the yet unobserved top quark and to a lesser extent to the putative Higgs boson, as illustrated in the Feymann diagrams of Fig. 1.2. Similarly, the

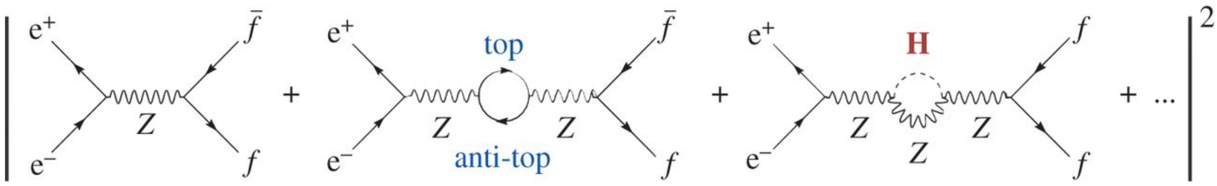

Figure 1.2: Schematic representation of the perturbative expansion for calculating the cross section for e$^+$e annihilation into a pair of leptons or quarks (denoted f, for fermions); the representative higher order diagrams involving quantum loops with top quarks and a Higgs boson are indicated.

measurements of fermion pair asymmetries allow the determination of the effective weak mixing angle $\sin^2\theta_{\mathrm{W}}^{\mathrm{eff}}$, which can be predicted in the SM:

$$\sin^2\theta_{\mathrm{W}}^{\mathrm{eff}}\cos^2\theta_{\mathrm{W}}^{\mathrm{eff}} = \frac{\pi\alpha_{\mathrm{QED}}(m_{\mathrm{Z}}^2)}{\sqrt{2}G_{\mathrm{F}}m_{\mathrm{Z}}^2} \times (1+\Delta\kappa), \tag{1.1}$$

where $\alpha_{\mathrm{QED}}(m_{\mathrm{Z}}^2)$ is the electromagnetic coupling constant evaluated at the Z pole, G_{F} is the Fermi constant, m_{Z} is the Z boson mass, and $\Delta\kappa$ is a small correction factor that depends on the top quark and the Higgs boson masses via the graphs displayed in Fig. 1.2. The magnitude of the second graph of Fig. 1.2 is proportional to the square of the top quark mass and is therefore expected to be much larger than that of the third one, proportional to $\log(m_{\mathrm{H}}/m_{\mathrm{Z}})$, and amounts to about ten times the measurement accuracy. As a consequence, LEP was able to predict the mass of the top quark within the SM (assuming that no other particle than the Higgs boson would impact the radiative corrections):

$$m_{\mathrm{top}}^{\mathrm{SM}} = 173^{+13}_{-10}\ \mathrm{GeV}. \tag{1.2}$$

The W boson mass may in turn be predicted within the SM:

$$m_{\mathrm{W}}^{\mathrm{SM}} = \left[\frac{\pi\alpha_{\mathrm{QED}}(m_{\mathrm{Z}}^2)}{\sqrt{2}G_{\mathrm{F}}\sin^2\theta_{\mathrm{W}}^{\mathrm{eff}}} \times \frac{1}{1-\Delta r}\right]^{\frac{1}{2}}, \tag{1.3}$$

where Δr is yet another small correction factor that depends on the top quark and the Higgs boson masses. Numerically, the W mass was predicted with a remarkable precision (which includes the above uncertainty on the top quark mass and the absence of knowledge of the Higgs boson at the time):

$$m_{\mathrm{W}}^{\mathrm{SM}} = 80.362^{+0.032}_{-0.031}\ \mathrm{GeV}. \tag{1.4}$$

DRAFT FOR ADVISORY COMMITTEE - DO NOT DISTRIBUTE

By increasing its centre-of-mass energy to above the W^+W^- production threshold, LEP was then able to measure the W mass directly with a similar precision [13]. The Tevatron later improved this precision by about a factor two [REF], and observed for the first time the top quark [REFERENCE], at the mass predicted by LEP in the context of the standard model *and nothing else*:

$$
\begin{aligned}
m_{\rm W}^{\rm direct} &= 80.385 \pm 0.015 \text{ GeV}, & (1.5)\\
m_{\rm top}^{\rm direct} &= 173.34 \pm 0.76(\text{exp}) \pm 0.50(\text{th}) \text{ GeV}. & (1.6)
\end{aligned}
$$

These direct measurements of $m_{\rm W}$ and $m_{\rm top}$ were then used to determine the magnitude of the second graph of Fig. 1.2 (and of a similar term in Δr), and made the third graph become the dominant term of the perturbative expansion. As a consequence, the LEP and Tevatron measurements were able to infer the existence of a Higgs boson and to predict its mass within the SM:

$$
m_{\rm H}^{\rm SM} = 98^{+25}_{-21} \text{ GeV}. \quad (1.7)
$$

The LHC observed the production of the Higgs boson in 2012 for the first time, at a mass well compatible with the LEP prediction in the context of the standard model *and nothing else*. The current overall situation of the standard model fit to the precision measurements available to date is summarized in Fig. 1.3 [15]. The fit prediction for the W mass and the weak mixing angle within the SM:

$$
\begin{aligned}
m_{\rm W} = &\; 80.3584 \;\; \pm 0.0055_{m_{\rm top}} \pm 0.0025_{m_{\rm Z}} \pm 0.0018_{\alpha_{\rm QED}} \\
&\qquad\qquad \pm 0.0020_{\alpha_{\rm S}} \pm 0.0001_{m_{\rm H}} \pm 0.0040_{\rm theory} \text{ GeV} \\
= &\; 80.358 \;\; \pm 0.008_{\rm total} \text{ GeV}, \\
\sin^2\theta_{\rm W}^{\rm eff} = &\; 0.231488 \;\; \pm 0.000029_{m_{\rm top}} \pm 0.000015_{m_{\rm Z}} \pm 0.000035_{\alpha_{\rm QED}} \\
&\qquad\qquad \pm 0.000010_{\alpha_{\rm S}} \pm 0.000001_{m_{\rm H}} \pm 0.000047_{\rm theory} \\
= &\; 0.23149 \;\; \pm 0.00007_{\rm total}, \qquad (1.8)
\end{aligned}
$$

are also very compatible with the world average of their direct measurements within current uncertainties:

$$
\begin{aligned}
m_{\rm W} &= 80.385 \pm 0.015 \text{ GeV} \\
\sin^2\theta_{\rm W}^{\rm eff} &= 0.23153 \pm 0.00016. \qquad (1.9)
\end{aligned}
$$

1.2.2 Opportunities at the FCC-ee: The Z Pole

Electroweakly-coupled new physics would appear either as additional/different contributions to the perturbative expansion of the electroweak observable predictions, similar to those shown in Fig. 1.2, or as modifications of the tree-level couplings to leptons and quarks. From the agreement between the predictions and the direct measurements, it follows that the effect of new physics, if any, must be smaller than the current uncertainties. The next significant step in this quest is therefore to drastically reduce these uncertainties, typically by one order of magnitude or more. In this section, it is assumed that theoretical uncertainties can be brought, by the calculation of missing QED, EW and QCD higher orders, to a level similar to, or smaller than, that of the experimental uncertainties. This issue is addressed in more details in Section 1.5.

Numerically, the FCC-ee is able to deliver about 10^5 times the luminosity that was produced by the Large Electron-Positron collider (LEP) at the Z pole, i.e., typically $10^{11}\text{Z} \to \mu^+\mu^-$ or $\tau^+\tau^-$ decays and 2×10^{12} hadronic decays. Measurements with a statistical precision up to 300 times smaller than at LEP (from a few per mil to 10^{-5}) are therefore at hand.

Forward-backward and polarisation asymmetries at the Z pole are a powerful experimental tool

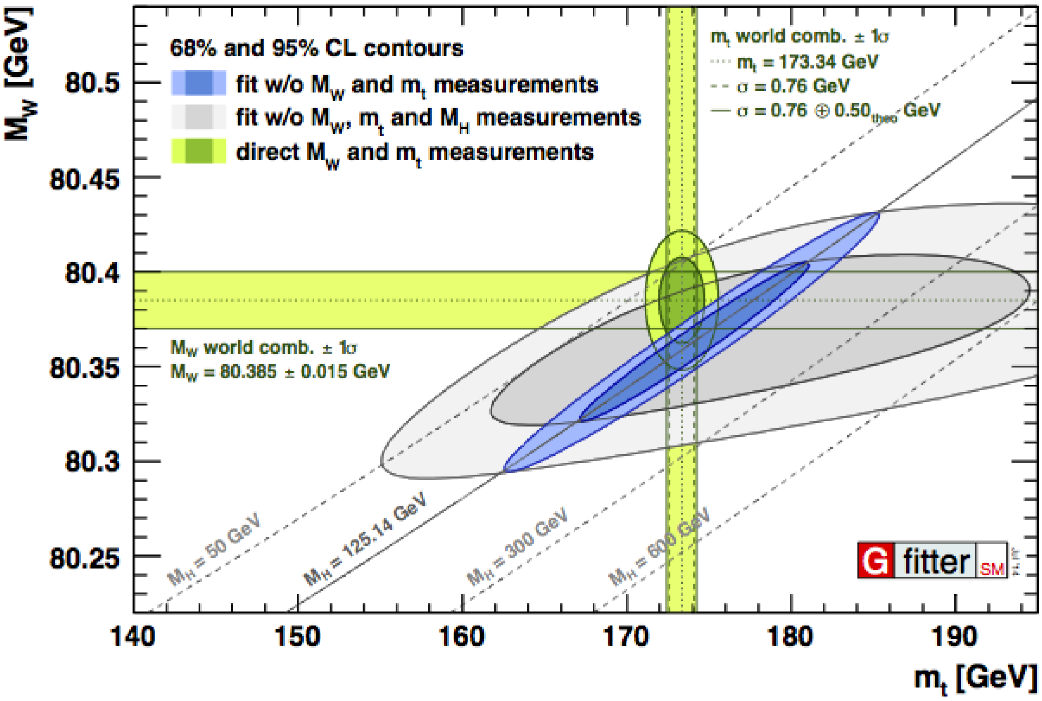

Figure 1.3: Contours of 68% and 95% confidence level obtained from fits of the standard model to the precision measurements available to date, in the $(m_{\rm top}, m_{\rm W})$ plane. The grey area is the result of the fit without the direct measurements of the W, top, and Higgs masses, while the narrower blue area includes the Higgs boson mass measurement at the LHC. The horizontal and vertical green bands and the combined green area indicate the 1σ regions of the $m_{\rm W}$ and $m_{\rm top}$ measurements (world averages).

to measure $\sin^2\theta_{\rm W}^{\rm eff}$, which regulates the difference between the right-handed and left-handed fermion couplings to the Z. With unpolarised incoming beam, the amount of Z polarisation at production is

$$\mathcal{A}_e = \frac{2v_{\rm e}/a_{\rm e}}{1+(v_{\rm e}/a_{\rm e})^2} \quad \text{and} \quad v_{\rm e}/a_{\rm e} = 1 - 4\sin^2\theta_{\rm W}^{\rm eff}, \tag{1.10}$$

and the resulting forward-backward asymmetry amounts to $A_{\rm FB}^{\rm ff} = \frac{3}{4}\mathcal{A}_{\rm e}\mathcal{A}_{\rm f}$. From the experimental point of view, the $\rm e^+e^- \to Z \to \mu^+\mu^-$ process is a golden channel for an accurate measurement of $A_{\rm FB}$. The dominant source of experimental uncertainty is identified as the knowledge of the centre-of-mass energy. Indeed, in the vicinity of the Z pole, $A_{\rm FB}^{\mu\mu}$ exhibits a strong quasi-linear $\sqrt{s}$ dependence

$$A_{\rm FB}^{\mu\mu}(s) \simeq \frac{3}{4}\mathcal{A}_{\rm e}\mathcal{A}_{\mu} \times \left[1 + \frac{8\pi\sqrt{2}\alpha_{\rm QED}(s)}{m_{\rm Z}^2 G_{\rm F}\left(1-4\sin^2\theta_{\rm W}^{\rm eff}\right)^2}\frac{s-m_{\rm Z}^2}{2s}\right], \tag{1.11}$$

caused by the off-peak interference between the Z and the photon exchange in the process $\rm e^+e^- \to \mu^+\mu^-$. If the centre-of-mass energy can be determined with a precision of 0.1 MeV, as advocated in Section 2.7, the resulting uncertainty on $A_{\rm FB}^{\mu\mu}$ amounts to 9×10^{-6} (a factor three larger than the statistical uncertainty), which propagates to an uncertainty on $\sin^2\theta_{\rm W}^{\rm eff}$ of 6×10^{-6}. Among the other asymmetries to be measured at the FCC-ee, the τ polarisation asymmetry in the $\tau\to\pi\nu_\tau$ decay mode provides a similarly accurate determination of $\sin^2\theta_{\rm W}^{\rm eff}$, with a considerably smaller $\sqrt{s}$ dependence.

An experimental precision better than 5×10^{-6} is therefore a robust target for the measurement

DRAFT FOR ADVISORY COMMITTEE - DO NOT DISTRIBUTE

of $\sin^2\theta_{\rm W}^{\rm eff}$ at the FCC-ee, corresponding to more than a thirty-fold improvement with respect to the current precision of 1.6×10^{-4} (Eq. 1.9).

For this accuracy to become useful in constraining new physics, the experimental accuracy of the $\sin^2\theta_{\rm W}^{\rm eff}$ SM prediction (Eq. 1.8) needs to be brought to a similar level. The largest parametric uncertainty on the prediction, 3.5×10^{-5}, arises from the limited knowledge of the electromagnetic coupling constant evaluated at the Z mass scale. It is hoped that this figure can be reduced by a factor of two with a better determination of the hadronic vacuum polarisation, in part with future low-energy $\rm e^+e^-$ data and in part with the use of perturbative QCD [16]. The large luminosity offered by the FCC-ee allows a direct determination of $\alpha_{\rm QED}(m_{\rm Z}^2)$ to be contemplated [17], from the slope of the muon forward-backward asymmetry as a function of the centre-of-mass energy in the vicinity of the Z pole (Eq. 1.11). As displayed in Fig. 1.4, the statistical accuracy of this measurement is minimal just below ($\sqrt{s}=87.9$ GeV) and just above ($\sqrt{s}=94.3$ GeV). It is shown in Ref. [17] that the statistical precision on $\alpha_{\rm QED}$ is smaller than the current uncertainty by a factor of four with an integrated luminosity of $40\ {\rm ab}^{-1}$ at each of these two points. Because most systematic uncertainties are common to both points and almost perfectly cancel in the slope determination, the experimental uncertainty is statistics dominated as long as the centre-of-mass energy spread can be determined to a relative accuracy better than 1%, which is deemed achievable at the FCC-ee. More studies are needed to understand if the $\alpha_{\rm QED}(m_{\rm Z}^2)$ determination can profit from the centre-of-mass energy dependence of other asymmetries.

An experimental relative accuracy of 3×10^{-5} on $\alpha_{\rm QED}(m_{\rm Z}^2)$ can be achieved at the FCC-ee, from the measurement of the muon forward-backward asymmetry with $40\ {\rm ab}^{-1}$ of centre-of-mass energies $\sim$3 GeV below and $\sim$3 GeV above the Z pole. The corresponding parametric uncertainties on the $\sin^2\theta_{\rm W}^{\rm eff}$ and $m_{\rm W}$ SM predictions are accordingly reduced from 3.5×10^{-5} and 1.8 MeV to 9×10^{-6} and 0.5 MeV, respectively.

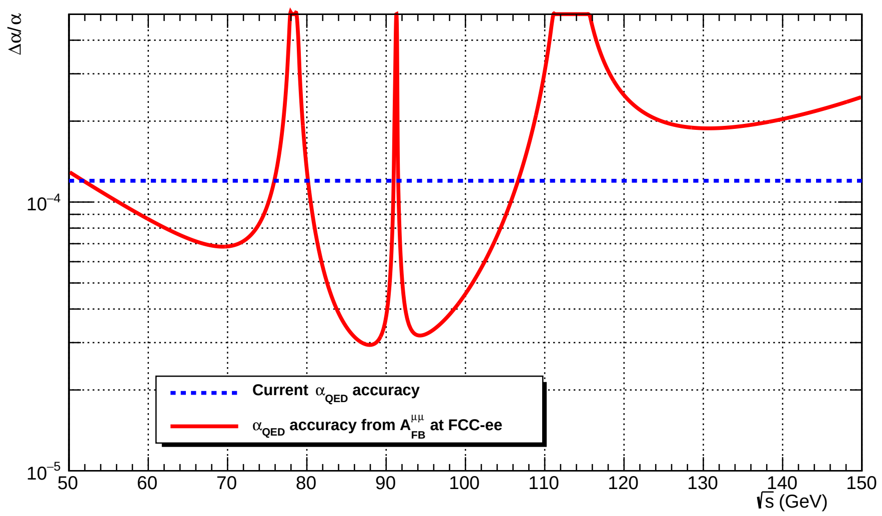

Figure 1.4: Relative statistical accuracy of the $\alpha_{\rm QED}$ determination from the muon forward-backward asymmetry at the FCC-ee, as a function of the centre-of-mass energy. The integrated luminosity is assumed to be $80\ {\rm ab}^{-1}$ around the Z pole, and to follow the profile of Fig. 1.1 for other centre-of-mass energies. The dashed blue line shows the current uncertainty.

The next parametric uncertainty to address at the Z pole is obviously that arising from the Z mass. The Z mass and width were determined at LEP from the line shape scan to be $m_{\rm Z}=91187.5\pm2.1$ MeV and $\Gamma_{\rm Z}=2495.2\pm2.3$ MeV, with data taken mostly at $\sqrt{s}=89.4$, 91.2, and 93 GeV. The statistical errors of 1.2 MeV and 2 MeV would be reduced below 4 keV and 7 keV at the FCC-ee, with data taken

DRAFT FOR ADVISORY COMMITTEE - DO NOT DISTRIBUTE

at 87.9, 91.2, 93.9 GeV (also optimal for the measurement of $\sin^2\theta_{\rm W}^{\rm eff}$ and $\alpha_{\rm QED}(m_{\rm Z}^2)$). In both cases, the systematic uncertainty was dominated at LEP by the error pertaining to the beam energy calibration (1.7 MeV, and 1.2 MeV). As suggested in Section 2.7, a continuous measurement with resonant depolarisation of single bunches should allow a reduction of this uncertainty to below 0.1 MeV. With these levels of precision, however, other experimental uncertainties start playing an important role, especially for the Z width. For example, the FCC-ee beam energy spread (~ 60 MeV) needs to be known to better than 0.2% (0.1 MeV), and the integrated luminosity needs to be measured with a point-to-point relative accuracy of the order of 5×10^{-5}. Studies have shown that both figures are achievable at the FCC-ee. REFERENCE?

Overall experimental uncertainties of 0.1 MeV or better are achievable for the Z mass and width measurements at the FCC-ee. The corresponding parametric uncertainties on the $\sin^2\theta_{\rm W}^{\rm eff}$ and $m_{\rm W}$ SM predictions are accordingly reduced to 6×10^{-7} and 0.12 MeV, respectively.

The ratio R_ℓ of the Z hadronic width to the Z leptonic width, $R_\ell = 20.767\pm0.025$, has been used at LEP for the determination of the strong coupling constant at LEP, and yielded

$$\alpha_{\rm s}(m_{\rm Z}^2) = 0.1196\pm0.0028\,({\rm exp.})\pm0.0009\,({\rm th.})$$

The experimental uncertainty was dominated by the statistics of the Z leptonic decays and therefore a combination of the three lepton species — with the assumption of lepton universality — was required. At the FCC-ee, the statistical uncertainty is negligible and the measurement of R_μ, yielding an experimental precision of 0.001 from the knowledge of the detector acceptance, suffices. The experimental uncertainty on $\alpha_{\rm s}(m_{\rm Z}^2)$ shrinks accordingly to 0.00015. A similar figure can be obtained from the measurements of the hadronic and leptonic decay branching ratio of the W boson, copiously produced with the FCC-ee running at larger centre-of-mass energies.

An absolute (relative) uncertainty of 0.001 (5×10^{-5}) on the ratio of the Z hadronic-to-leptonic partial widths (R_ℓ) is well within the reach of the FCC-ee. The same relative uncertainty is expected for the ratios of the Z leptonic widths, which allows a stringent test of lepton universality. The overall uncertainty on $\alpha_{\rm s}(m_{\rm Z}^2)$ obtained from R_ℓ drops by more than an order of magnitude. The corresponding parametric uncertainties on the $\sin^2\theta_{\rm W}^{\rm eff}$ and $m_{\rm W}$ SM predictions are accordingly reduced to 10^{-6} and 0.2 MeV, respectively.

1.2.3 Opportunities at the FCC-ee: The $\rm W^+W^-$ and $\rm t\bar{t}$ Threshold

The safest and most sensitive way to determine the W boson and top quark masses and widths is to measure the sharp increase of the $\rm e^+e^-\to W^+W^-$ and $\rm e^+e^-\to t\bar{t}$ cross sections at the production thresholds, at centre-of-mass energies around twice the W and top masses. In both cases, the mass can be best determined at a quasi-fixed point where the cross section dependence on the width vanishes: $\sqrt{s}\simeq$ 162.5 GeV for $m_{\rm W}$ and 342.5 GeV for $m_{\rm top}$. The cross section sensitivity to the width is maximum at $\sqrt{s}\simeq$ 157.5 GeV for $\Gamma_{\rm W}$, and 344 GeV for $\Gamma_{\rm top}$. In principle, data at no other centre-of-mass energies are needed to unambiguously determine the masses and widths of the W and the top. The top situation, however, is different, because the top mass will not be known to better than ±1 GeV from hadron collider measurements, so that a 4 GeV window must be explored at the FCC-ee for the mass determination. In addition, the $\rm t\bar{t}$ cross section depends on the large top Yukawa coupling to the Higgs boson, arising from the Higgs boson exchange at the $\rm t\bar{t}$ vertex. This dependence needs to be fitted away with supplementary data at even higher centre-of-mass energies. However, the otherwise large dependence of the cross section on the strong coupling constant is of no concern at the FCC-ee because of its accurate measurement from the Z and W leptonic-to-hadronic width ratios. The non-$\rm t\bar{t}$ background, on the other hand, needs to be evaluated from data at lower centre-of mass energies.

With a luminosity of 25 $\rm fb^{-1}$ recorded at eight different centre-of-mass energies (340, 341, 341.5, 342, 343, 343.5, 344, and 345 GeV), the top-quark mass, width, and Yukawa coupling can be determined with a statistical precision of ±17 MeV, ±40 MeV, and $\pm9\%$, respectively. The centre-of-mass energies can be measured from the final state reconstruction of $\rm e^+e^-\to W^+W^-$ events and from the knowledge

DRAFT FOR ADVISORY COMMITTEE - DO NOT DISTRIBUTE

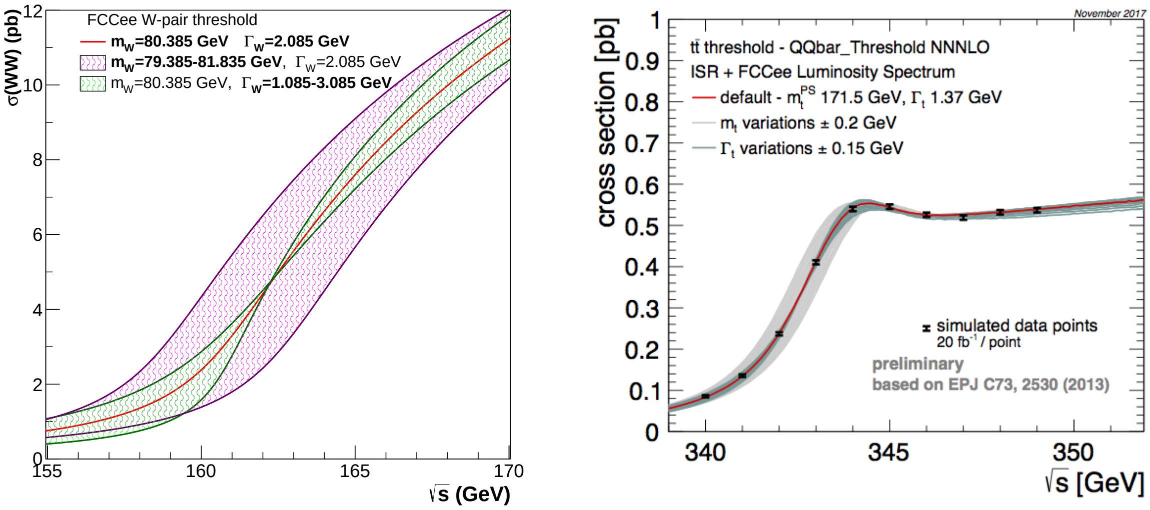

Figure 1.5: Production cross section of W-boson (left) and top-quark (right) pairs on the vicinity of the production thresholds, with different values of the masses and widths.

of the W mass with a precision of ~ 10 MeV, which causes a 3 MeV uncertainty on the top-quark mass. Today's theory uncertainty due to missing higher orders in QCD is at a the 40 MeV level for the mass and the width.

An uncertainty of 20 (40) MeV is achievable for the top-quark mass (width) measurement at the FCC-ee. The corresponding parametric uncertainties on the $\sin^2\theta_W^{eff}$ and m_W SM predictions are accordingly reduced to 6×10^{-7} and 0.11 MeV, respectively.

With all the above measurements, the total parametric uncertainty on the W mass is dominated by the FCC-ee determination of $\alpha_{QED}(m_Z^2)$ and amounts to ~ 0.6 MeV. To reach a similar statistical accuracy from the measurement of the $e^+e^- \rightarrow W^+W^-$ cross section at production threshold and a simultaneous fit of m_W and Γ_W, a luminosity of ~ 4 ab^{-1} needs to be accumulated at $\sqrt{s} = 157.5$ and 162.5 GeV. The corresponding precision on the W width is about 1.5 MeV. For the measurements not to be limited by systematic uncertainties, the centre-of-mass energy must be measured with a precision of 0.5 MeV or better, the detector acceptance, the luminosity, and the WW cross section prediction must be controlled to a few 10^{-4} and the background must be known to a few per mil. While challenging, these conditions are not more stringent that the requirements at the Z pole and are deemed achievable at the FCC-ee.

An experimental precision of 0.5 (1.5) MeV for the W mass (width) is within reach at the FCC-ee, with 10 ab^{-1} accumulated at the W pair production threshold.

The measurement of the Z decay width into invisible states is of great interest as it constitutes a direct test of the unitarity of the PMNS matrix – or of the existence of right-handed quasi-sterile neutrinos, as pointed out in Ref. [18]. At LEP, it was mostly measured at the Z pole from the peak hadronic cross section to be, when expressed in terms of active neutrinos, $N_\nu = 2.984 \pm 0.008$. At the FCC-ee, the measurement of the peak hadronic cross-section at the Z pole is likely to be dominated by systematic uncertainties, related on one hand to the theoretical prediction of the low-angle Bhabha-scattering cross section (used for the integrated luminosity determination), and to the absolute integrated luminosity experimental determination, on the other.

At the FCC-ee, the use of radiative return to the Z [19], $e^+e^- Z\gamma$, at larger centre-of-mass energies, is likely to offer a more accurate measurement of the number of neutrinos. Indeed, this process provides a very clean photon-tagged sample of on-shell Z bosons, with which the Z properties can be measured.

DRAFT FOR ADVISORY COMMITTEE - DO NOT DISTRIBUTE

From the WW threshold scan alone, the cross section of about 5 pb [20–23] ensures that 10 million $Z\gamma$ events will be produced with a $Z \to \nu\bar{\nu}$ decay and a high-energy photon in the detector acceptance. The three million $Z\gamma$ events with leptonic Z decays will in turn provide a direct measurement of the ratio $\Gamma_Z^{inv}/\Gamma_Z^{lept}$, in which uncertainties associated with absolute luminosity and photon detection efficiency cancel. The 40 million $Z\gamma$ events with either hadronic or leptonic Z decays will also provide a cross check of the systematic uncertainties and backgrounds related to the QED predictions for the energy and angular distributions of the high-energy photon. The invisible Z width will thus be measured with a dominant statistical error corresponding to 0.001 neutrino family. Data at higher energies contribute to further reduce this uncertainty by about 20%. A somewhat lower centre-of-mass energy, for example $\sqrt{s} = 125$ GeV – with both a larger luminosity and a larger $Z\gamma$ cross section and potentially useful for Higgs boson studies – would be even more appropriate for this important measurement.

The FCC-ee has the potential to deliver an overall, statistics-dominated, uncertainty smaller than 0.0008 of a SM neutrino for the Z invisible width.

A complete set of electroweak precision measurements requires the precise determination of the electroweak couplings of the top quark, which may carry enhanced sensitivity to new physics. It is shown in Ref. [24] that the polarisation of the top quark arising from its parity-violating couplings to the Z in the process $e^+e^- \to t\bar{t}$ allows a simultaneous measurement of these couplings without incoming beam polarisation, and with an optimal centre-of-mass energy of 365 GeV. With one million $t\bar{t}$ events (corresponding to an integrated luminosity of $1.5\ ab^{-1}$ at $\sqrt{s} = 365$ GeV), the vector and axial top-quark couplings to the Z can be measured with a precision of 0.5% and 1.5%, respectively, from an analysis of the angular and energy distributions of the leptons (e, μ) from the top-quark semi-leptonic decays. The production cross section needs to be predicted with a couple of per-cent precision in order not to dominate the coupling uncertainties.

1.2.4 Global Electroweak Fit with the FCC-ee Measurements

Once the W boson and the top-quark masses are measured with precisions of a few tenths and a few tens of MeV, respectively and with the measurement of the Higgs boson mass at the LHC (to be further improved at the FCC-ee), the SM prediction of a number of observables sensitive to electroweak radiative corrections become absolute with no remaining additional parameters. Any deviation will be a demonstration of the existence of new, weakly interacting particle(s). As just discussed, the FCC-ee offers the opportunity of measurements of such quantities with precisions between one and two orders of magnitude better than the present status of these measurements. The theoretical prediction of these quantities with a matching precision is an incredible challenge, but the genuine ability of these tests of the completeness of the Standard Model to discover new weakly-interacting particles beyond those already known is a fundamental motivation to take it up and bring it to a satisfactory conclusion.

As an illustration, the result of the fit of the SM to all the electroweak precision observables measured at the FCC-ee but the m_W and m_{top} direct measurements, as obtained with the GFitter program [15] under the assumptions that all relevant theory uncertainties can be reduced to match the experimental uncertainties, is displayed in Fig. 1.6 as 68% C.L. contours in the (m_{top}, m_W) plane. This fit is compared to the direct m_W and m_{top} measurements at the W^+W^- and the $t\bar{t}$ thresholds. A comparison with the precisions obtained with the current data at lepton and hadron colliders, as well as with LHC projections, is also shown.

1.3 The Higgs Boson

Owing to its recent discovery at the LHC, the Higgs boson is the least understood of all particles in the standard model. Precise, model-independent, measurements of its properties are therefore in order to unravel the mystery surrounding this particle. The LHC and its high-luminosity upgrade will provide insights on the Higgs boson couplings to the heaviest SM particles (Z, W, t, b, τ, μ), and achieve a

DRAFT FOR ADVISORY COMMITTEE - DO NOT DISTRIBUTE

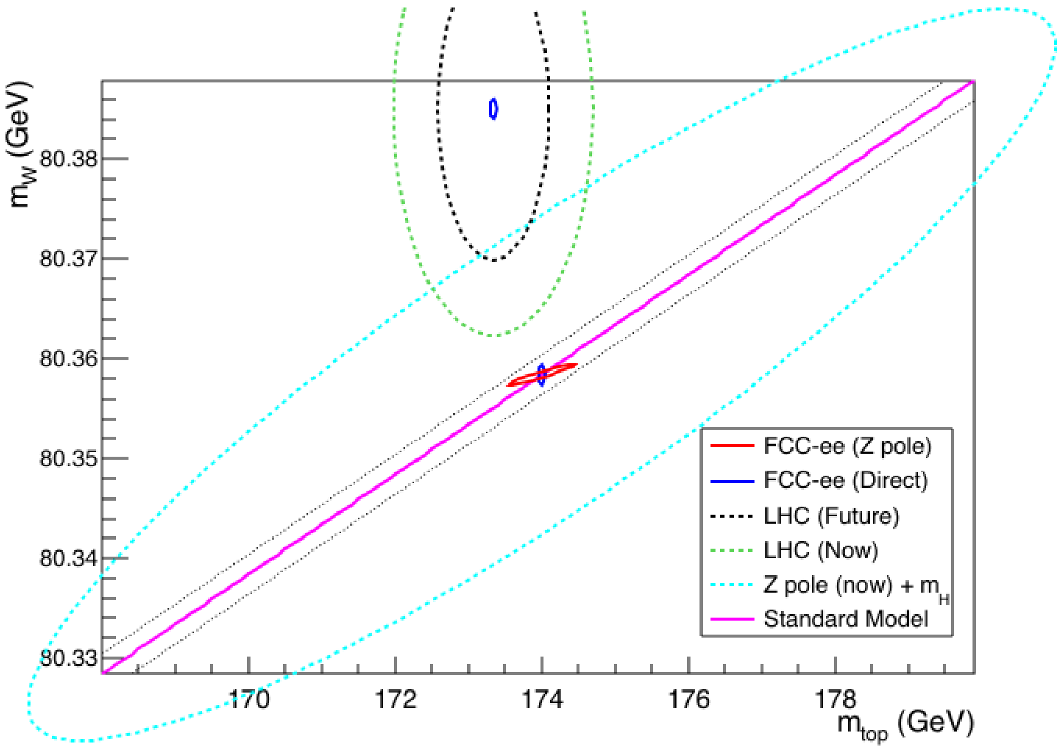

Figure 1.6: Contours of 68% confidence level obtained as in Fig. 1.3 from fits of the standard model to the electroweak precision measurements offered by the FCC-ee, in the $(m_{\rm top}, m_{\rm W})$ plane: the red ellipse is obtained from the FCC-ee measurements at the Z pole, while the blue ellipses arise from the FCC-ee direct measurements of the W and top masses. One of the two blue ellipses is centred around the central values measured today, the other is central around the values predicted by the standard model (pink line) for $m_{\rm H} = 125.14$ GeV. The two dotted line around the standard model prediction illustrate the uncertainty from the Z mass measurement if it were not improved at the FCC-ee. The green ellipse corresponds to the current W and top mass uncertainties from the Tevatron and the LHC, as in Fig. 1.3. The potential future improvements from the LHC are illustrated by the black dashed ellipse. The cyan ellipse corresponds to the dark blue 68% CL contour of Fig. 1.3 that includes all current Z pole measurements and the current Higgs boson mass measurement at the LHC.

precision that is qualitatively up to the 5% level, under a number of model-dependent assumptions. New interactions between the Higgs boson and other new particles at higher energy scales Λ will typically modify the Higgs boson couplings to SM particles (denoted $g_{\rm HXX}$ for the coupling of the Higgs boson to particle X), either at tree level or via quantum corrections. Coupling deviations $\delta g_{\rm HXX}$ with respect to their SM predictions are typically smaller than 5% for an energy scale Λ of 1 TeV, with a dependence that is inversely proportional to Λ^2, where Λ is related to the mass of the new particle by an additional factor of a coupling strength.

1.3.1 Model-independent Coupling Determination from the Higgs Boson Decay Branching Fractions

From the previous argument we see that a sub-percent accuracy on a given coupling measurement is needed to access the 10 TeV energy scale, or even to exceed it by an analysis of the deviation pattern among all couplings. Similarly, in the SM quantum corrections to Higgs couplings are at the level of $\sim$ few %, thus to truly probe the quantum nature of the Higgs boson we must push below this level of precision.

DRAFT FOR ADVISORY COMMITTEE - DO NOT DISTRIBUTE

An experimental sample of at least one million Higgs bosons has to be produced and analysed to potentially reach this statistical precision. Production at $\mathrm{e^+e^-}$ colliders is mainly via the Higgsstrahlung process $\mathrm{e^+e^-} \rightarrow \mathrm{HZ}$ and WW fusion $\mathrm{e^+e^-} \rightarrow (\mathrm{WW} \rightarrow \mathrm{H})\nu\bar{\nu}$. The cross sections are displayed in Fig. 1.7 as a function of the centre-of-mass energy. The total cross section presents a maximum at $\sqrt{s} = 260$ GeV, but the number of Higgs events produced per unit of time is largest at $\sqrt{s} = 240$ GeV, as a consequence of the specific circular-collider luminosity profile (Fig. 1.1). As the cross section amounts to 200 fb at this energy, the production of one million events requires an integrated luminosity of at least $5\ \mathrm{ab}^{-1}$ at $\sqrt{s} = 240$ GeV in order to reach sub-percent precisions on the Higgs boson couplings. This sample, dominated by the Higgsstrahlung process, is usefully complemented with the $1.5\ \mathrm{ab}^{-1}$ at $\sqrt{s} = 365$ GeV (needed for the measurement of the top electroweak couplings) by about 180,000 HZ events and 45,000 WW-fusion events.

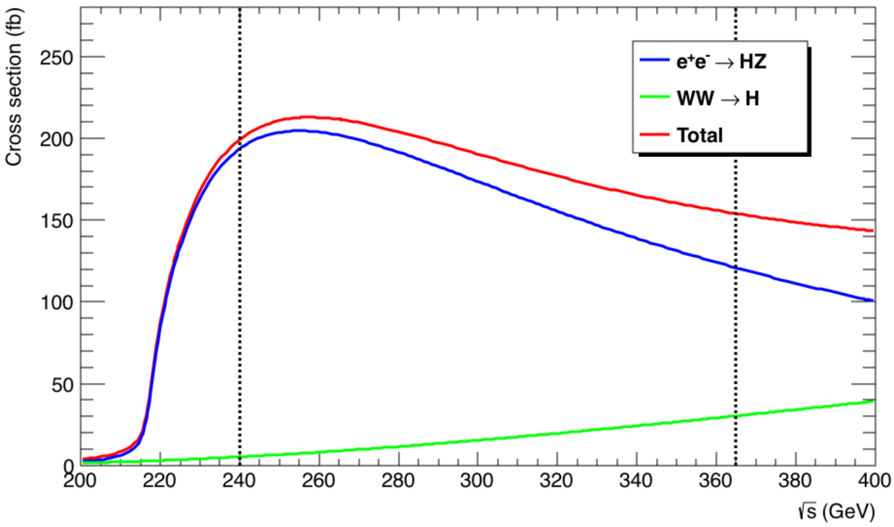

Figure 1.7: The Higgs boson production cross section as a function of the centre-of-mass energy in unpolarized $\mathrm{e^+e^-}$ collisions. The blue and green curves stand for the Higgsstrahlung and WW fusion processes, respectively, and the red curve displays the total production cross section. The vertical dashed lines indicate the centre-of-mass energies of choice at the FCC-ee for the measurement of the Higgs boson properties.

At $\sqrt{s} = 240$ GeV, the model-independent determination of Higgs boson couplings follows the strategy described in Refs. [10, 25], with an improved analysis that exploits the superior performance of the CLD detector design (Section). There are a number of steps in this determination.

The total Higgs production cross section is determined from counting $\mathrm{e^+e^-} \rightarrow \mathrm{HZ}$ events tagged with a leptonic Z decay, $\mathrm{Z} \rightarrow \ell^+\ell^-$, independently of the Higgs boson decay. An example of such an event is displayed in Fig. 1.8 (left). The mass of the system recoiling against the lepton pair is calculated with precision from the lepton momenta and the total energy-momentum conservation: $m_R^2 = s + m_\mathrm{Z}^2 - 2\sqrt{s}(E_{\ell^+} + E_{\ell^-})$, so that HZ events have m_R equal to the Higgs boson mass m_H and can be easily counted from the accumulation around m_H. Their number allows the HZ cross section, σ_HZ to be precisely determined in an model-independent fashion. This precision cross section measurement alone is a powerful probe of the quantum nature of the Higgs boson. Under the assumption that the coupling structure is identical in form to the SM, this cross section is proportional to the square of the Higgs boson coupling to the Z, g_HZZ.

Building upon this powerful model-independent measurement, the Higgs boson width can then be inferred by counting the number of HZ events in which the Higgs boson decays into a pair of Z bosons.

DRAFT FOR ADVISORY COMMITTEE - DO NOT DISTRIBUTE

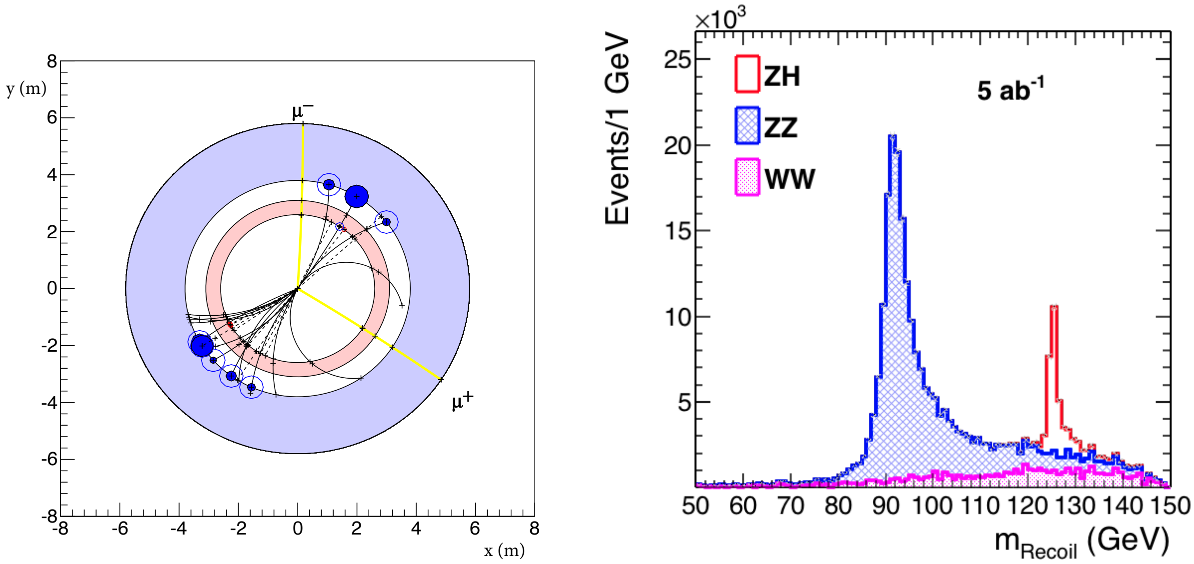

Figure 1.8: (Left) A schematic view, transverse to the detector axis, of an $\mathrm{e^+e^-} \rightarrow \mathrm{HZ}$ event with $\mathrm{Z} \rightarrow \mu^+\mu^-$ and with the Higgs boson decaying hadronically. The two muons from the Z decay are indicated. (Right) Distribution of the mass recoiling against the muon pair, determined from the total energy-momentum conservation, with an integrated luminosity of $5\ \mathrm{ab}^{-1}$ and the CLD detector design. The peak around 125 GeV (in red) consists of HZ events. The rest of the distribution (in blue and pink) originate from ZZ and WW production.

Table 1.1: Relative statistical uncertainty on the Higgs boson couplings and total decay width, as expected from the FCC-ee data. The accuracies expected with $5\ \mathrm{ab}^{-1}$ at 240 GeV are given in the first row. The second row of the Table includes the additional $0.2 + 1.5\ \mathrm{ab}^{-1}$ at $\sqrt{s} = 350$ and 365 GeV. The last row assumes in addition that the Higgs boson state is CP even and that the Higgs sector is CP conserving, as in Ref. [26], for a more straightforward comparison with the LHC capabilities. The last column is the constraint on the Higgs boson branching fraction to exotic particles (invisible or not).

g_{HZZ}	g_{HWW}	g_{Hbb}	g_{Hcc}	g_{Hgg}	$g_{\mathrm{H}\tau\tau}$	$g_{\mathrm{H}\mu\mu}$	$g_{\mathrm{H}\gamma\gamma}$	Γ_{H}	$\mathrm{BR}_{\mathrm{exo}}$
0.19%	1.0%	1.1%	1.2%	1.3%	1.1%	7.7%	2.0%	2.3%	0.58%
0.18%	0.23%	0.52%	0.87%	0.98%	0.66%	7.6%	1.8%	1.2%	0.55%
0.06%	0.11%	0.23%	0.84%	0.97%	0.60%	7.6%	1.7%	1.2%	0.20%

Under the same coupling assumption, this number is proportional to the ratio $\sigma_{\mathrm{HZ}} \times \Gamma(\mathrm{H} \rightarrow \mathrm{ZZ})/\Gamma_{\mathrm{H}}$, the numerator of which is proportional to g^4_{HZZ} and thus is known from the measurement of g_{HZZ} described above, hence Γ_{H} can then be extracted.

Finally, employing this width extraction, the exclusive decays of the Higgs boson $\mathrm{H} \rightarrow \mathrm{b\bar{b}}$, $\mathrm{c\bar{c}}$, gg, $\tau^+\tau^-$, $\mu^+\mu^-$, $\mathrm{W^+W^-}$, $\gamma\gamma$, and invisible Higgs boson decays (tagged with the presence of just one Z boson and missing energy in the event), are selected, which measures $\sigma_{\mathrm{HZ}} \times \Gamma(\mathrm{H} \rightarrow \mathrm{XX})/\Gamma_{\mathrm{H}}$. With σ_{HZ} and Γ_{H} known, the corresponding numbers of events are proportional to the square of the g_{HXX} coupling involved. A significantly improved measurement of Γ_{H} and of g_{HWW} can be achieved from the WW-fusion process at $\sqrt{s} = 350$ and 365 GeV.

In practice, the couplings, the width and the branching fractions, are determined with a global fit of the numbers of observed events, signal selection efficiencies and numbers of events expected from background, which closely follows the logic of Ref. [26]. The results of this fit are summarized in Table 1.1.

DRAFT FOR ADVISORY COMMITTEE - DO NOT DISTRIBUTE

To be written in this section:

1. Finish the above section (invisible BR, exotic BR, etc.)
2. The ttH coupling
3. the HHH coupling
4. the eeH coupling
5. The invisible branching ratio
6. CP studies
7. ...

1.4 New physics discovery potential

1.4.1 Generic Constraints on Effective Interactions from Precision Measurements

Effective field theories (EFT) provide a general framework for stringent tests of BSM physics, if the mass of the new particles is significantly above the energy scale of the processes of interest. In this so-called SMEFT, the effective interactions are built from the SM particles under the assumption that the Higgs boson belongs to an $SU(2)_L$ doublet and respects the Lorentz and SM gauge invariances. An infinite set of operators satisfy these conditions. They can be ordered according to their canonical mass dimensions in an effective Lagrangian:

$$\mathcal{L}_{\rm Eff} = \sum_{d=4}^{\infty} \frac{1}{\Lambda^{d-4}} \mathcal{L}_d = \mathcal{L}_{\rm SM} + \frac{1}{\Lambda}\mathcal{L}_5 + \frac{1}{\Lambda^2}\mathcal{L}_6 + \ldots, \qquad \mathcal{L}_d = \sum_i C_i \mathcal{O}_i. \tag{1.12}$$

In (1.12) the cut off of the EFT is denoted by Λ, each $\mathcal{L}_d$ contains operators $\mathcal{O}_i$ of mass dimension d, and $\mathcal{L}_4 \equiv \mathcal{L}_{\rm SM}$ is the leading order term, the SM Lagrangian. The new physics effects are encoded in the values of the Wilson coefficients, C_i, of each higher-dimensional operator. These operators can be related to specific models via integrating out the heavy degrees of freedom of the high-energy theory [27–30]. The observable effects of an operator of dimension d are suppressed by $(E/\Lambda)^{d-4}$, where $E < \Lambda$ is the typical energy of the process (in general $\sqrt{s}$). Therefore, the leading new physics contributions are expeced to be given by dimension-six operators. (The only operator in $\mathcal{L}_5$, the main effect of which is to generate Majorana neutrino masses, is irrelevant for the analysis presented here.) A complete basis of dimension-six operators, consistent with independent conservation of baryon and lepton number was first presented in Ref. [31]. It contains a total of 59 types of dimension-six operators (2499 if the flavour indices are taken into account).

The FCC-ee measurements of electroweak precision observables (EWPO) and of Higgs boson observables, summarized in the previous two sections, carry a large potential sensitivity improvement on the effects of a representative set of the dimension-six interactions. The most representative set chosen for this study includes the following ten operators entering EWPO in the basis of [31]:

$$\begin{gathered}\mathcal{O}_{\phi D} = \left|\phi^\dagger D^\mu \phi\right|^2, \qquad \mathcal{O}_{\phi WB} = \left(\phi^\dagger \sigma_a \phi\right) W^a_{\mu\nu} B^{\mu\nu}, \\ \mathcal{O}^{(1)}_{\phi\psi} = (\phi^\dagger \overleftrightarrow{D}_\mu \phi)(\overline{\psi}^i \gamma^\mu \psi^i), \qquad \mathcal{O}^{(3)}_{\phi F} = (\phi^\dagger \overleftrightarrow{D}^a_\mu \phi)(\overline{F}^i \gamma^\mu \sigma_a F^i), \qquad \mathcal{O}_{ll} = \left(\bar{l}\gamma_\mu l\right)\left(\bar{l}\gamma^\mu l\right), \end{gathered} \tag{1.13}$$

where ϕ is the scalar doublet, ψ runs over all the SM fermion multiplets, while F only refers to the SM left-handed fermion doublets. Some of the above also affect Higgs boson observables. Additional interactions, absent in EWPO, enter Higgs boson observables, for example:

$$\begin{gathered}\mathcal{O}_{\phi G} = \phi^\dagger \phi G^A_{\mu\nu} G^{A\,\mu\nu}, \quad \mathcal{O}_{\phi W} = \phi^\dagger \phi W^a_{\mu\nu} W^{a\,\mu\nu}, \quad \mathcal{O}_{\phi B} = \phi^\dagger \phi B_{\mu\nu} B^{\mu\nu}, \quad \mathcal{O}_{\phi\Box} = (\phi^\dagger\phi)\Box(\phi^\dagger\phi), \\ \mathcal{O}_{\tau\phi} = (\phi^\dagger\phi)(\bar{l}^3 \phi \tau), \qquad \mathcal{O}_{b\phi} = (\phi^\dagger\phi)(\bar{q}^3 \phi b), \quad \mathcal{O}_{t\phi} = (\phi^\dagger\phi)(\bar{q}^3 \tilde{\phi} t). \end{gathered} \tag{1.14}$$

DRAFT FOR ADVISORY COMMITTEE - DO NOT DISTRIBUTE

For simplicity, the expected sensitivities to the above-mentioned dimension-six operators presented here are estimated with a fit in which only one operator is present at a time. While these results are technically not model-independent, they still serve to illustrate the expected sensitivity improvement of future experimental data.

The projected sensitivity to new physics obtained from the FCC-ee electroweak precision measurements is illustrated in Fig. 1.9. These results assume that the intrinsic uncertainty of SM theory calculations will be reduced according to Ref. [32]. The improvement of the SM parametric uncertainties due to the more precise measurements of the SM inputs at the FCC-ee is also taken into account, together with the expected advance in the determination of the strong coupling constant from lattice calculations. The sensitivities to the ratios C_i/Λ^2 are reported as the 95% probability bounds on the *interaction* scale, $\Lambda/\sqrt{C_i}$, associated to each operator. (This interaction scale must not be confused with the mass scale of new particles, in the same way as the Fermi constant $G_F^{-\frac{1}{2}}$ does not represent the scale where new degrees of freedom, i.e. the W boson, enter in the electroweak theory.) These bounds are compared to the results obtained from current electroweak precision data [33, 34]. In general, an overall improvement in the sensitivity to C_i/Λ^2 of $\sim$ 10-20$\times$ is expected. Not surprisingly, an even stronger constraining power could be achieved if theory uncertainties were further reduced, as show in the right panel of Fig. 1.9.

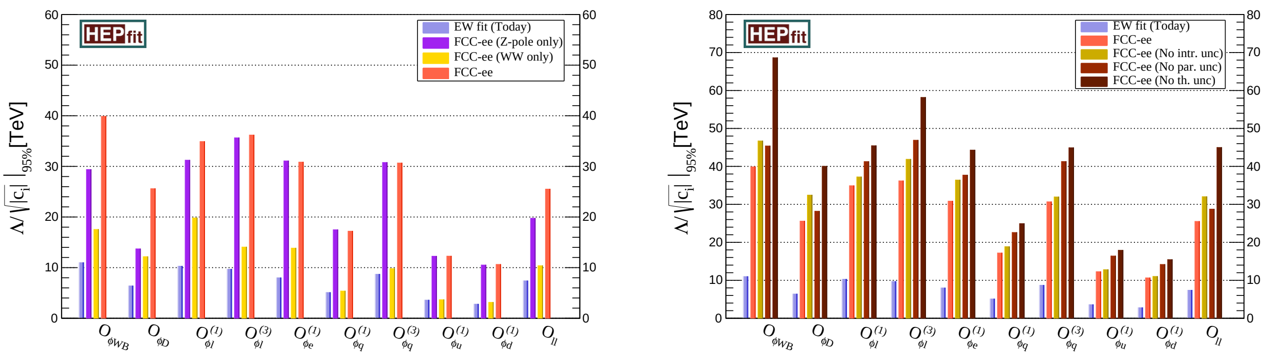

Figure 1.9: Left: Expected improvement of the current EW constraints using the FCC-ee Z-pole data only (Z lineshape, partial decay widths, and asymmetries), the FCC-ee measurements at the WW threshold only (W mass, width and the invisible Z width), as well as using the whole set of EWPO at the FCC-ee. Right: For the results using the full FCC-ee dataset, comparison of sensitivities using the future SM theory uncertainties and those neglecting either the intrinsic errors, the parametric ones, or both.

The left panel of Fig. 1.10 shows similar results for the case of a fit to the precise measurements of the Higgs boson observables. The corresponding limits on the interaction scale are compared to those from current LHC data [35]. The overall sensitivity to C_i/Λ^2 can be, again, as large as $\sim$ 20 times that of current data. The experimental uncertainties for the Higgs boson are expected to be larger than those from SM calculations, in most cases. More FCC-ee data would therefore allow the sensitivity to be improved even further. Finally, the right panel of Fig. 1.10 compares both EWPO and Higgs boson constraints and shows also the resulting bounds obtained with the combination of both sets of observables. In these simplified fits to each interaction individually, the EWPO and Higgs boson constraints appears to be very much complementary.

These fits must be used carefully when translated into specific scenarios, as they are not fully model-independent. The results, however, clearly demonstrate the important step that the FCC-ee represents with respect to any existing experiment, in terms of the physics potential in precision studies of the electroweak sector.

DRAFT FOR ADVISORY COMMITTEE - DO NOT DISTRIBUTE

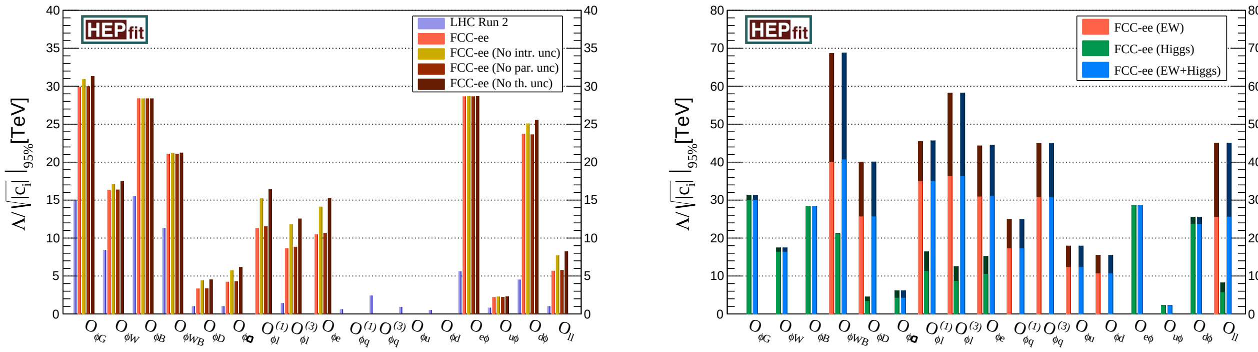

Figure 1.10: Left: FCC-ee Higgs constraints on the different interactions in Eqs. (1.13) and (1.14), compared to the current LHC Run 2 results. The impact of the different types of SM theory uncertainties are also shown (neglecting intrinsic, parametric and both uncertainties, respectively). Right: Comparison of the separate EW and Higgs constraints, as well as the results combining both in the same fit. Darker shades of each color indicate the results neglecting all SM theory uncertaintities.

1.4.2 Constraints from Precision Measurements in Specific Models

Composite Higgs models

The 4-Dimensional Composite Higgs Model (4DCHM) of Ref. [36] describes the intriguing possibility that the Higgs particle may be a composite state arising from some strongly interacting dynamics at a high scale. This realisation would solve the hierarchy problem of the Standard Model (SM) owing to compositeness form factors taming the divergent growth of the Higgs boson mass upon quantum effects. Furthermore, the measured Higgs boson mass could well be consistent with the fact that such a (now composite) object arises as a pseudo Nambu-Goldstone Boson (pNGB) from a particular coset of a global symmetry breaking. Models with a Higgs state as a pNGB generally also predict modifications of its couplings to both bosons and fermions of the SM, hence the measurement of these quantities, at either a hadronic or leptonic collider, represents a powerful way to test its possible non-fundamental nature [37, 38].

New neutral massive gauge bosons predicted by the 4DCHM, i.e., companion states to the Z boson of the SM, hereafter denoted by $\mathrm{Z}'_{2,3}$, with mass larger than $\sim$ 3 TeV could escape detection at the LHC owing to the small Z'_i couplings to both light quarks and leptons [39], combined with possibly very large widths of the Z'_i states. Such additional EW gauge bosons would however enter the $\mathrm{e}^+\mathrm{e}^- \to \mathrm{t}\bar{\mathrm{t}}$ cross section [40], in a twofold way. On the one hand, their presence can be felt through mixing effects with the Z state of the SM that would modify the $\mathrm{Zt}\bar{\mathrm{t}}$ and the $\mathrm{Z}\ell^+\ell^-$ couplings. On the other hand, new Feynman diagram topologies with the propagation of such $\mathrm{Z}'_{2,3}$ states would also enter top-pair production and appear as effective $\gamma\mathrm{t}\bar{\mathrm{t}}$ coupling modifications. The modification of the $\mathrm{Z}\ell^+\ell^-$ couplings would also affect other processes, specifically $\mathrm{e}^+\mathrm{e}^- \to \mu^+\mu^-$.

To evaluate the sensitivity of the FCC-ee to these models, a benchmark point A was identified by the following choice of 4DCHM gauge sector parameters: $f = 1.6$ TeV, $g^* = 1.7871$, $g_0 = 0.6095$, and $g_{0Y} = 0.3494$ [36], to evade the latest projected bounds of the HL-LHC searches for Z' gauge bosons and to be compatible with current EWPO measurements. With these parameters, the Z' masses amount to $m_{\mathrm{Z}'_2} = 2.98$ TeV and $m_{\mathrm{Z}'_3} = 3.07$ TeV, and their widths are all of the order of 20-30% of their masses. As shown in Fig. 1.11, the large statistics offered by the FCC-ee would reveal very significant deviations in almost all observables mentioned above for this benchmark point with respect to the SM: top-quark left and right couplings to the Z (4σ), effective top couplings to the photons (8σ), Higgs boson couplings to the Z boson and to the b quark (13σ), or $\mathrm{e}^+\mathrm{e}^- \to \mu^+\mu^-$ cross sections above the Z pole ($> 20\sigma$). With such a pattern of significance, these measurements in principle allow the model to be completely

DRAFT FOR ADVISORY COMMITTEE - DO NOT DISTRIBUTE

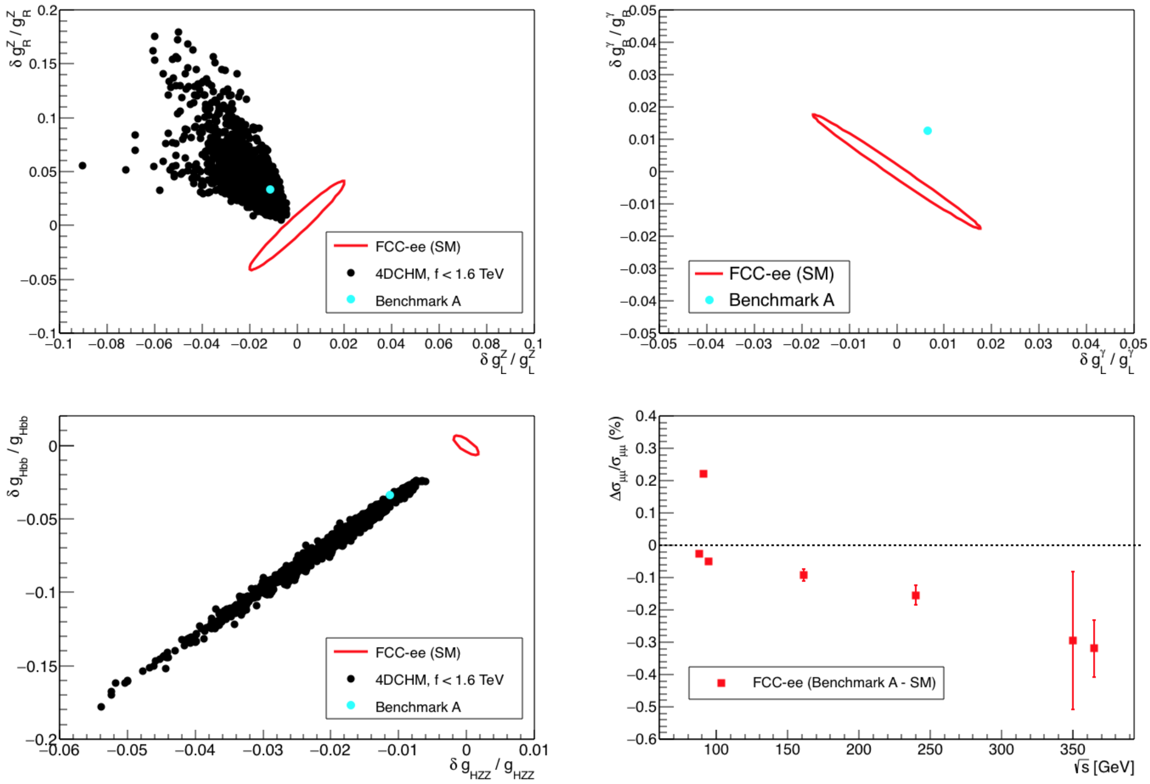

Figure 1.11: Predicted deviations of the top-quark left and right couplings to the Z (top left) and effective couplings to the photon (top right), of the Higgs boson couplings to the Z boson and the b quark (bottom left), and of the dimuon cross section as a function of the centre-of-mass energy (bottom right) for the 4DCHM benchmark point A (represented by a cyan marker in the first three graphs) with respect to the SM, centred at (0,0) in the first three graphs, and at 0 in the fourth. The FCC-ee measurement uncertainties are displayed either as red ellipses or as error bars. The black markers in the top-left and bottom-left plots show the deviations predicted by other 4DCHM parameter sets, with $f < 1.6$ TeV.

and uniquely characterised. For example, the Z$'$ masses would be predicted with a precision of 50 GeV (2%), the scale f with a precision of 130 GeV (8%), and the coupling constant g^* with a precision of 0.14 (8%) with the sole $\mu^+\mu^-$ observables.

Right-Handed Neutrinos

Neutrino oscillations demonstrate that neutrinos have mass [41]. As such, they provide the only established laboratory evidence for physics beyond the SM and open the way to a deeper understanding of particle masses, as well as possible solutions to outstanding issues in particle physics such as the origin of the baryon asymmetry in the universe or of dark matter. A minimal and natural way to account for the observed smallness of neutrino masses is the existence of both Dirac and Majorana neutrino mass terms, leading to the existence of right-handed neutrinos [42–47]. For these reasons, in the discussion of future projects, the sensitivity to right-handed neutrinos (also named “sterile neutrinos”) has become one of the benchmarks for discovery potential. Right-handed neutrinos lead to spectacular signatures at the FCC-ee, both from their impact on precision measurements and from possible observation of right-handed neutrino decays, making it the most powerful machine for their discovery.

It has been argued that the right-handed neutrino mass scale M might have a common origin with the electroweak scale [48–51]. In general, a comparatively small value of M gives rise to an

DRAFT FOR ADVISORY COMMITTEE - DO NOT DISTRIBUTE

approximate $B - L$ symmetry, which is exactly what happens when all neutrino masses are zero, and also avoids large radiative corrections to the Higgs boson mass. Reviews of how comparatively light right-handed neutrinos can address the fundamental puzzles of the baryon asymmetry of the universe and dark matter can be found in Refs. [52–67]. Model classes that allow for a low scale see-saw are the "inverse see-saw models" [42,43,68,69], "linear see-saw models" [44,46,70–76]), and "minimal flavour violation" [47,77]. A recent review on collider phenomenology of neutrino mass models can be found in Ref. [78].

Right-handed neutrinos impact precision measurements through their mixing to their left-handed counterparts, with a mixing angle Θ. This mixing produces heavy and light mass eigenstates. The light neutrinos states, while remaining mostly left-handed, acquire a small sterile component yielding an apparent violation of the unitarity of the PMNS matrix [79]. The PMNS non-unitarity alters the couplings of the light neutrinos to the weak currents, thereby systematically shifting all the observables in which neutrinos are involved [80–86] and leading to a very specific pattern of deviations from the SM.

The single most important observable is the Fermi constant G_{F}, which is measured very precisely in muon decays $\mu \to \mathrm{e}\nu_\mu\nu_\mathrm{e}$, while being an input parameter for the electroweak precision observables. In the FCC-ee era, with many of these observables measured at the 10^{-5} precision level or better, a reduction of the neutrino coupling of that magnitude will be visible. Other observables that can be measured with great precision to test the PMNS matrix (non)unitarity include the charged current branching ratios, in particular $\tau \to \ell\nu_\ell\nu_\tau$ and $\mathrm{W} \to \ell\nu_\ell$), rare lepton-flavour-violating processes ($\ell \to \ell'\gamma$, $\ell \to 3\ell'$), as well as weak cross sections for processes like $\mathrm{e}^+\mathrm{e}^- \to$ HZ, ZZ, and $\mathrm{W}^+\mathrm{W}^-$. For example, with 1.5×10^{11} tau lepton pairs produced, the tau leptonic branching ratios should be measurable to a relative precision of better than 10^{-5}. Based on Ref. [80], the sensitivity from the FCC-ee precision measurements in the plane (Θ^2, M) is shown by the horizontal blue lines in Fig. 1.12. Two comments are in order: first,

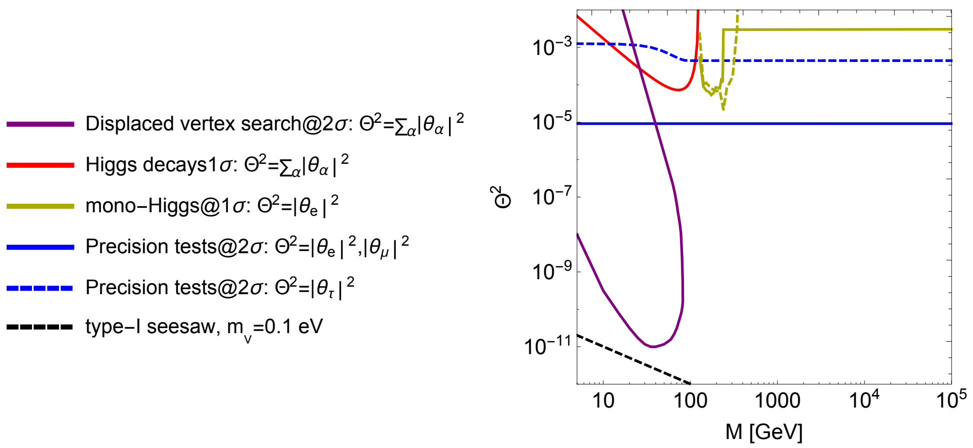

Figure 1.12: Sensitivities of the different signatures to the active-sterile mixing and masses of sterile neutrinos at the FCC-ee, from Ref. [87]. In addition to the main signatures described in the text, sensitivity from Higgs decays and mono-Higgs production is also shown

the combination of lepton universality and EWPO available will allow access to the three lepton flavour mixing angles separately. Secondly, the sensitivity to heavy neutrinos from precision measurements extends well beyond 100 TeV; this is a particular example of BSM physics for which decoupling is not at work.

Heavy neutrinos N with masses M below m_Z and active-sterile mixing Θ below the present constraints [88] naturally have long lifetimes ($\simeq 3\ [\mathrm{cm}]/|\Theta|^2(M\ [\mathrm{GeV}])^6$), which can give rise to visible displaced secondary vertices in the detector, especially when the decay is semi-leptonic: $\mathrm{N} \to \ell\mathrm{q}\bar{\mathrm{q}}$. Searches for heavy neutrino decays with detached vertices are most efficient during the Z pole run due

DRAFT FOR ADVISORY COMMITTEE - DO NOT DISTRIBUTE

to the larger luminosity and production cross section from $Z \to \nu N$ decays. These searches [89–91] can reach sensitivities to active-sterile mixing parameters $|\Theta|^2$ down to and below $\sim 10^{-11}$, as shown by the purple line in Fig. 1.12, and by the orange line in the left panel of Fig. 1.13. The search benefits

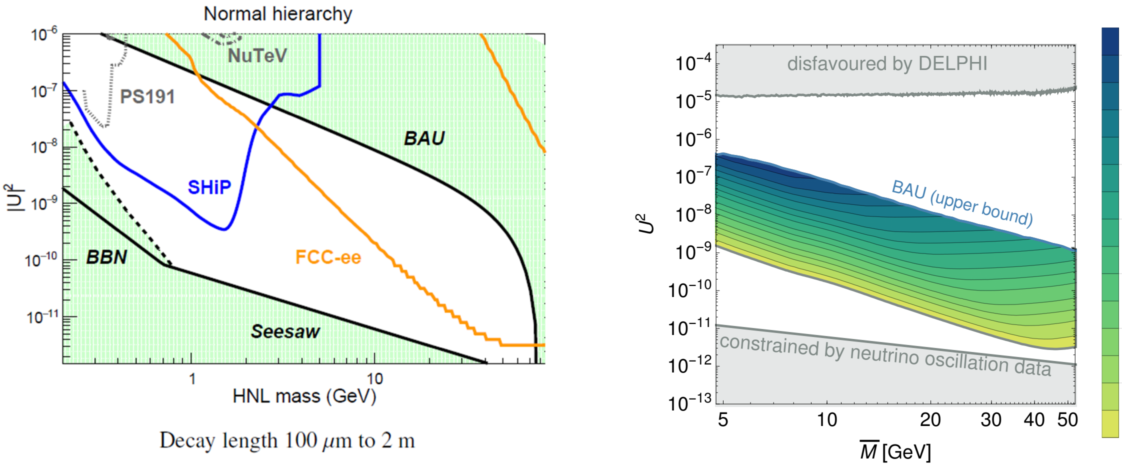

Figure 1.13: Left: the region of sensitivity to the right-handed neutrinos in the displaced vertex search, put in perspective with the lower energy searches in neutrino beams or beam dump experiments (from Ref. [89], updated for the CDR FCC-ee conditions), and with theoretical constraints. Right: detail of the parameter space showing by colour code the number of events expected at the FCC-ee within the parameter space (thick black line) consistent with the leptogenesis hypothesis (from Ref. [92]); constraints from the DELPHI searches [88] and from neutrino oscillation data are shown. In both plots, normal mass ordering is assumed, and $U \equiv \Theta$.

from the suppression of the SM background due to the displaced vertex of the heavy neutrino decay. The small beam pipe radius and the clean experimental conditions are additional advantages. The sensitivity could be improved to some extent by a larger tracking volume, but the dominant factor remains the huge luminosity at the Z pole. The right panel of Fig. 1.13 indicates the number of events that would be observed as a function of M and Θ. In some regions of the phase space, several hundred signal events are expected to be observed, which would allow a first determination of the mass and lifetime of the right-handed neutrino and establish its relative decay rate into the three lepton flavours. This discovery, which would be made early in the life of the FCC-ee, would certainly have an impact on both detector design and motivation for FCC-hh, for which *(i)* dedicated displaced vertex triggers would be necessary; and *(ii)* the right-handed neutrinos would be produced most abundantly in W leptonic decays, thereby giving access to both initial and final state lepton charge and flavour.

1.4.3 Direct Observation of Other Rare Processes

With a 10^5-fold increase of luminosity at the Z pole with respect to LEP, the FCC-ee can potentially produce 5×10^{12} Z at the two interaction points. Such a large number allows a multitude of rare Z hadronic and leptonic decays to be studied or searched for. By 2025, the main two players in the field of rare b-flavoured hadrons or τ decays will be the upgraded LHCb experiment at CERN and the Belle II experiment at KEK. Beyond this horizon, the very large statistics at the Z pole, the clean experimental environment similar to that of the Belle II experiment and the production of all species of heavy flavours with a large boost as in the LHCb experiment, make the FCC-ee a natural perspective for flavour physics. The unique physics potential is discussed here with two illustrations of opportunities in quark and lepton sectors: the search for lepton-flavour-Violating (LFV) Z decays and the measurement of a rare decay of b hadron, $\bar{B}^0 \to K^{*0}(892)\tau^+\tau^-$ — which can complement and substantially improve the knowledge

DRAFT FOR ADVISORY COMMITTEE - DO NOT DISTRIBUTE

and results anticipated from the current and planned b-physics programs of the LHCb upgrade and the Belle II experiment.

Lepton Flavour Violating Z Decays

The observation of flavour-violating Z decays, e.g. $\mathrm{Z} \to \mathrm{e}\mu$, $\mu\tau$, or $\mathrm{e}\tau$, would provide indisputable evidence for physics beyond the SM. These decays are forbidden in the SM by the GIM mechanism [93] and their branching fractions are still predicted to be extremely small (below 10^{-50}) when the SM is minimally extended to incorporate flavour violation in the neutral lepton sector induced by the leptonic mass mixing matrix [94]. Sizeable rates for these LFV $Z \to \ell_1^{\mp}\ell_2^{\pm}$ processes could hence reflect the existence of new particles such as right-handed neutrinos. The search for LFV Z decays is also complementary to the direct search for heavy neutral leptons.

A phenomenological study [95] addresses the potential for the FCC-ee to probe the existence of sterile neutral fermions in the light of the improved determination of neutrino oscillations parameters, the new bounds on low-energy LFV observables as well as cosmological bounds. This work also addresses the complementarity of these searches with the current and foreseeable precision of similar searches at lower energy experiments. The best sensitivity to observe or constrain LFV in the $\mathrm{e}\mu$ sector is then obtained by the experiments based on the muon-electron conversion in nuclei [96]. In contrast, the study of the decays $\mathrm{Z} \to \mathrm{e}\tau$ and $\mathrm{Z} \to \mu\tau$ provides invaluable and unique insight in the connection to the third generation.

The current limits on the branching ratios of charged lepton flavour violating Z decays were established by the LEP experiments [97–99]. More recently, the ATLAS experiment improved the bound for $\mathrm{e}\mu$ final states [100]. Typical upper limits on the branching fractions are at the level of 10^{-5} to 10^{-6}. The production at FCC-ee of 5×10^{12} Z decays provides improved limits by several orders of magnitude and probes BSM physics scenarios for branching fractions down to 10^{-9} [101].

Electroweak Penguins in b-quark Transitions

The processes involving a quark transition $\mathrm{b} \to \mathrm{s}\ell^+\ell^-$ (ℓ denotes here an electron or a muon) are currently receiving substantial phenomenological [102–105] and experimental [106–108] interest. The departures from the SM predictions observed in these studies question, in particular, the lepton universality in quark-based transitions and may even suggest BSM physics with gauge-mediated processes or leptoquark transitions. Should these deviations be confirmed, observables involving the third generation charged lepton τ may enhance the observed effects and shed new light on the new physics involved. In that respect, the $\mathrm{B_s} \to \tau^+\tau^-$ and $\bar{\mathrm{B}}^0 \to \mathrm{K}^{*0}(892)\tau^+\tau^-$ decays are obvious candidates to study. The presence of neutrinos in the final states makes the experimental search for and reconstruction of these decays particularly challenging at hadron colliders. At the FCC-ee, however, the excellent knowledge of the decay vertices of multi-hadronic τ decays allows the kinematics of these decays to be fully and unambiguously reconstructed. Identification of the different hadron species in the tracking system of the detector would be an additional advantage to further reduce the background.

About 1000 events with a reconstructed $\bar{\mathrm{B}}^0 \to \mathrm{K}^{*0}(892)\tau^+\tau^-$ decay are expected at the FCC-ee, which opens the way to the measurement of the angular properties of the decay [109] and therefore to a much refined characterisation of the potentially underlying new physics. Figure 1.14 displays the reconstructed B^0 mass distribution of simulated SM signal and background events in a sample of 5×10^{12} Z decays in the CLD detector design. The signal purity and yield obtained at the FCC-ee are unequalled at any current or foreseeable collider and are bound to increase in a correlated manner with any improvement to the charge-particle track impact parameter resolution.

DRAFT FOR ADVISORY COMMITTEE - DO NOT DISTRIBUTE

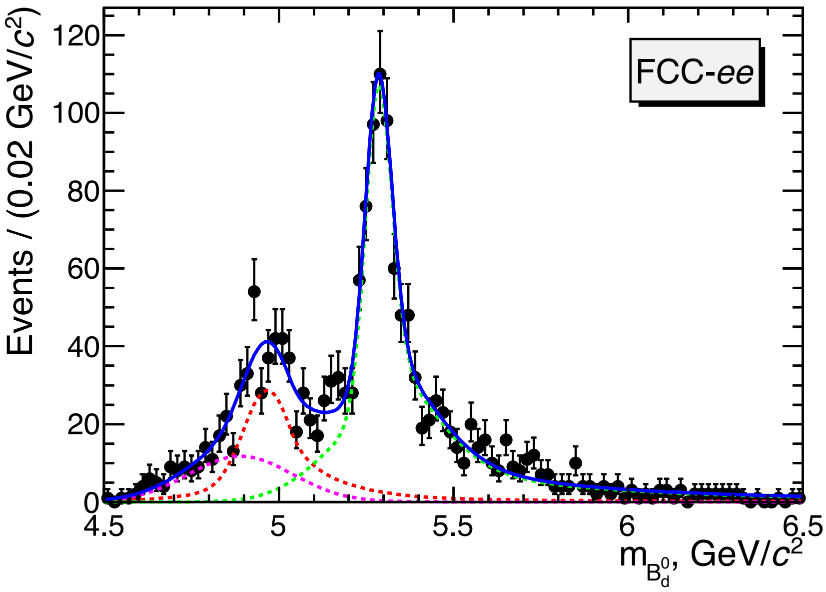

Figure 1.14: Invariant mass of $\bar{B}^0 \to K^{*0}(892)\tau^+\tau^-$ reconstructed candidates (dots with error bars). In the selected events, the τ particles decay into three prongs $\tau^- \to \pi^-\pi^+\pi^-\nu_\tau$ allowing the τ decay tertiary vertex to be reconstructed. The primary vertex (Z vertex) is reconstructed from primary charged particle tracks, and the secondary vertex ($\mathrm{\bar{B}^0}$ vertex) is reconstructed with the $\mathrm{K^*(892)}$ daughter particles ($\mathrm{K^*(892)} \to \mathrm{K^+}\pi^-$). The dominant sources of backgrounds included in the analysed sample, namely $\mathrm{\bar{B}_s \to D_s^+ D_s^- K^{*0}(892)}$ and $\mathrm{\bar{B}^0 \to D_s^+ \bar{K}^{*0}(892)}\tau^-\bar{\nu}_\tau$, are modelled by the red and pink probability density functions (p.d.f.), respectively. The signal p.d.f. is displayed with the green curve.

Other Unique Opportunities in Flavour Physics

The study of the two rare decays above has shown that the statistics available at a high-luminosity Z factory, complemented by state-of-the-art detector performance, can allow their potential measurement at unequalled precision. They can also serve as a benchmark to open the way to other physics observables in quark and lepton sectors. The loop-induced leptonic decays $\mathrm{B_{d,s}} \to \mathrm{e^+e^-}$, $\mu^+\mu^-$, and $\tau\tau$ provide SM candles and are sensitive to several realisations of BSM Physics. The observation of $\mathrm{B_s} \to \tau^+\tau^-$ would be invaluable in this respect and, with 100,000 events expected, is uniquely reachable at the FCC-ee. The charged-current-mediated leptonic decays $\mathrm{B_{u,c}} \to \mu\nu_\mu$ or $\tau\nu_\tau$ offer the possibility to determine the CKM elements $|V_{ub}|$ $|V_{cb}|$ with mild theoretical uncertainties. The CP violation in mixing can be measured through semileptonic asymmetries, as yet unobserved, but the FCC-ee sensitivity is close to their SM predictions. The cleanliness of the $\mathrm{e^+e^-}$ experimental environment will benefit to the study of $\mathrm{B_s}$, $\mathrm{B_c}$ and b baryons, the decay modes involving neutral particles in the final state (π_0, $\mathrm{K_S}$, η, η',ν), as well as the many-body fully hadronic b-hadron decays. The harvest of CP-eigenstates in several b-hadron decays will allow the CP-violating weak phases to be comprehensively measured.

1.5 Requirements

1.5.1 Theory

As summarized in the previous sections, the opportunities offered by the FCC-ee luminosities at centre-of-mass energies ranging from around the Z pole to above the $\mathrm{t\bar{t}}$ threshold allow improvements between one and two orders of magnitude on the experimental accuracy of most electroweak and Higgs precision observable measurements, with respect to the achievements of previous $\mathrm{e^+e^-}$ and hadron colliders.

DRAFT FOR ADVISORY COMMITTEE - DO NOT DISTRIBUTE

This kind of improvement is particularly ambitious for the theoretical backing of the interpretation of the data in terms of new physics sensitivity. At LEP, for example, it was carefully checked that the combined use of tools dedicated to QED effects like `KKMC` [110] and of electroweak analysis tools like `ZFITTER` [111], both with complete one-loop electroweak calculations and soft-photon exponentiation, basically fulfilled the corresponding accuracy requirements. These approaches must be considerably refined for the FCC-ee. A confrontation of the standard model predictions to the FCC-ee data will deserve a systematic procedure for the extraction of electroweak precision observables from cross sections and asymmetries, with proper QED unfolding; and at least complete two-loop electroweak and three-loop QCD calculations, together with an $\sim$10% knowledge of the next perturbative order [112].

Sector decomposition and Mellin-Barnes methods, which proved to work with completion of two-loop EWPOs [113], must be developed further for numerical calculation of Feynman integrals. There are many places for further studies, e.g. optimisations at three- and four-loop level of minimal number of MB-integral dimensions, IBP reductions to master integrals, solution to the γ_5 issue and contributions at three loops, etc. The numerical methods will be supported by progress in analytical and semi-analytical approaches (methods and tools). Some four-loop QCD effects might need to be evaluated.

The complexity of the task is similar to that of the computations required for the HL-LHC data to make theoretical sense and the necessary tools have been identified [112]. These studies demand focused investment by the community in order to reach the necessary level of development. With this investment, it is estimated that all main issues should be solved in the course of the next five-to-ten years.

1.5.2 Collider

In 2013 the European Strategy for Particle Physics unambiguously recognised the importance of an electron-positron collider able to measure the properties of the Higgs boson and other particles with an unprecedented accuracy. In order to significantly increase the sensitivity to new physicsof these measurements, such an electroweak factory must deliver integrated luminosities at centre-of-mass energies from around the Z pole to above the $\mathrm{t\bar{t}}$ threshold such that the statistical precision of most electroweak and Higgs observable measurements improve by one to two orders of magnitude.

The data samples needed to achieve this ambitious goal correspond to

1. An integrated luminosity of at least 30 ab^{-1} at $\sqrt{s} \simeq 88$ and 94 GeV for the measurement of the electromagnetic coupling constant at the Z mass scale. These data are also useful for the determination of the Z decay width;
2. An integrated luminosity of at least 100 ab^{-1} at $\sqrt{s} \simeq m_{\mathrm{Z}} \simeq 91.2$ GeV in particular, for the measurement of the effective weak mixing angle and for the search for or study of rare decays. These data are also important for the determination of the Z mass and of the strong coupling constant at the Z mass scale;
3. An integrated luminosity of at least 10 ab^{-1} around the $\mathrm{W^+W^-}$ production threshold, for the measurement of the W mass and decay width, evenly shared between $\sqrt{s} \simeq 157.5$ and 162.5 GeV. These data are also important for the determination of the number of neutrino species and an independent measurement of the strong coupling constant;
4. An integrated luminosity of at least 5 ab^{-1} at $\sqrt{s} = 240$ GeV, for the measurements of the Higgs boson couplings from its decays branching fraction and the total HZ production cross section;
5. An integrated luminosity of about 0.2 ab^{-1} in a 5-GeV-wide window around the $\mathrm{t\bar{t}}$ threshold, typically shared among eight centre-of-mass energy points from ~ 340 to ~ 345 GeV, for the measurement of the top-quark mass, decay width, and Yukawa coupling to the Higgs boson;
6. An integrated luminosity of at least 1.5 ab^{-1} above the $\mathrm{t\bar{t}}$ threshold, $\sqrt{s} \simeq 365$ GeV, for the measurement of the top electroweak couplings. These data also provide a threefold improvement of the Higgs boson decay width accuracy with respect to the sole data at $\sqrt{s} = 240$ GeV, which in turn, significantly constrains the Higgs boson couplings.

DRAFT FOR ADVISORY COMMITTEE - DO NOT DISTRIBUTE

At this stage of the study, it appears that once enough luminosity is accumulated at each of these energies, the potential gain in the precision of the Higgs boson and other particle properties is not enough (if any) to justify an upgrade at larger centre-of-mass energies, e.g., $\sqrt{s} = 500$ GeV. (Of course, the appearance at the LHC of some threshold for new physics above 365 GeV may change the picture entirely.) On the other hand, many of the measurements offered by the FCC-ee between the Z pole and the $\mathrm{t\bar{t}}$ threshold are not experimentally limited by statistics and would continue to improve with double the luminosity. While the twofold symmetry of the current tunnel design (arguably tailored for the FCC-hh) limits the number of $\mathrm{e^+e^-}$ interaction points to two, a fourfold symmetry would open the possibility to enjoy four interaction points and therefore roughly double the total integrated luminosity collected in a given amount of time.

A feature unique to circular $\mathrm{e^+e^-}$ colliders is the possibility to achieve transverse polarisation for the incoming beams for precision beam energy calibration. A precision of the order of 100 keV on the centre-of-mass energy is a high-priority target at the Z pole and the W pair threshold, for absolute measurements of the Z and W masses with the promised accuracies. The measurements of the beam energy and the beam energy spread are also compulsory for the determination of most EWPOs, which show a strong dependence on these two quantities. On the other hand, the study demonstrated that longitudinal polarisation of the incoming beams provides no information that cannot otherwise be obtained with a similar accuracy from either unpolarised asymmetries or final state polarisation of particles that decay (e.g., top, tau), especially if it comes at the expense of a large loss of luminosity.

Finally, the study showed that a data sample corresponding to an integrated luminosity of at least $10\ \mathrm{ab}^{-1}$ at $\sqrt{s} \simeq m_{\mathrm{H}} \simeq 125$ GeV, with moderate centre-of-mass energy monochromatisation, would be a valuable addition (unique to the FCC-ee) to constrain the Yukawa coupling of the electron to the Higgs boson. These data would also allow the precision of the number of neutrino species to be improved by a factor two with respect to the same amount of data at the W pair threshold.

1.5.3 Detector

To be written ...

Luminosity measurement
Flavour tagging (b, c, g)
Muon momentum and direction resolution; acceptance determination
Particle identification and Particle Flow capabilities (includes magnetic field)
Comment on the possibility of large detector size.

DRAFT FOR ADVISORY COMMITTEE - DO NOT DISTRIBUTE

Chapter 2

Collider Design and Performance

Katsunobu Oide: Katsunobu Oide, 25 pages

2.1 Requirements and Design Considerations

The goal of the lepton collider is to provide e^+e^- collisions in the beam energy range of 40 to 182.5 GeV. The main centre-of-mass operating points with most physics interest are 91 GeV (Z-pole), 160 GeV (W pair production threshold), 240 GeV (Higgs production) and 350 - 365 GeV ($t\bar{t}$ threshold). The machine should accommodate at least two experiments operated simultaneously and deliver peak luminosities above 1×10^{34} cm^{-2}s^{-1} per experiment at the $t\bar{t}$ threshold and the highest ever luminosities at lower energies.

The layout of the particle collider follows the layout of the FCC-hh hadron collider infrastructure, which has been developed with a view to its integration with the existing CERN accelerator complex as injector facility. As with the hadron collider, beam with adequate quality can be provided by an upgrade of the existing injector complex. Alternatively, a dedicated optimised injector could be built. Care has been taken to ensure easy implementation of transfer lines from the SPS to a future collider tunnel.

2.2 Key Parameters and Layout

2.2.1 Layout

The design goal is to maximise the luminosity for each energy under these constraints:

- Apart from ± 1.2 km around each interaction point (IP), follow the layout of the 97.75 km circumference hadron collider [114], as shown in Fig. 2.1 .
- Have two interaction points, located at the straight sections A and G as shown in Fig. 2.1.
- Limit synchrotron radiation power 50 MW/beam at all energies.

Figure 2.1 shows the layout of the FCC-ee together with FCC-hh.

The design goals are:

- A double ring collider.
- A horizontal crossing angle of 30 mrad at the IP, with the crab-waist scheme.
- The critical energy of the synchrotron radiation of the incoming beam toward the IP is kept below 100 keV at all beam energies.

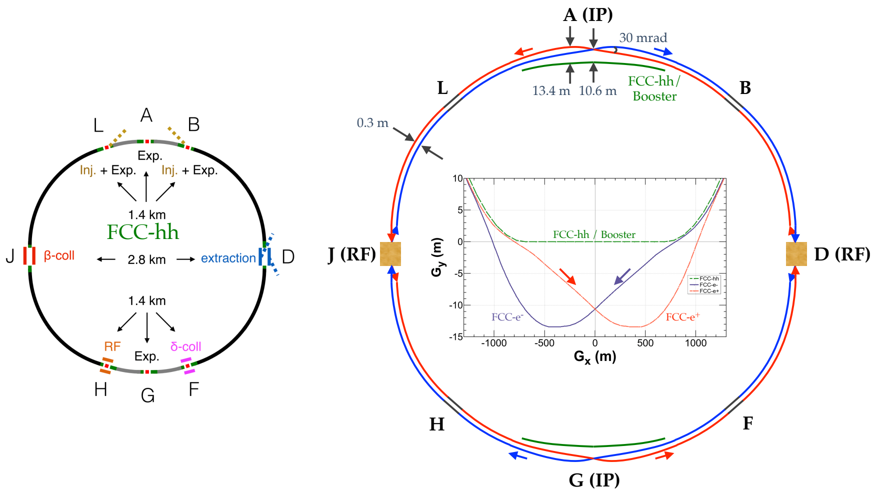

Figure 2.1: The layouts of FCC-hh (left), FCC-ee (right), and the zoom in on the trajectories across interaction point G (right middle). The FCC-ee rings are placed 1 m outside the FCC-hh footprint in the arc. The e^+ and e^- rings are horizontally separated by 30 cm in the arc. The main booster follows the footprint of the FCC-hh. The interaction points of shift by 10.6 m towards the outside of FCC-hh. The beams coming toward the IP are straighter than the outgoing ones in order to reduce the synchrotron radiation at the IP.

– A common lattice for all energies, except for a small rearrangement in the RF section. The betatron tune, phase advance in the arc cell, final focus optics and the configuration of the sextupoles are set to the optimum at each energy by changing the strengths of the magnets.
– The length of the free area around the IP (ℓ^*) and the strength of the detector solenoid are kept constant at 2.2 m and 2 T, respectively, for all energies.
– A “tapering" scheme, which scales the strengths of all magnets except for solenoids according to the local beam energy taking into account the energy loss due to synchrotron radiation.
– Two RF sections per ring placed in the straight sections at PD and PJ. The RF cavities will be common to e^+ and e^- in the case of $t\bar{t}$.
– A top-up injection scheme to maintain the stored beam current and the luminosity at the highest level throughout the experiment run. It is necessary to have a booster synchrotron in the same tunnel as the collider.

FCC-ee inherits two aspects from the previous generations of e^+e^- circular colliders The first aspect comes from the high energy colliders up to LEP2 and means that at $t\bar{t}$ there will be very strong synchrotron radiation together with the associated damping. The second which comes from high intensity colliders such as B-factories brings the feature that at Z there will be a high beam current with a large number of bunches per beam.

There are two reasons to choose a double-ring collider. Firstly, at low energies, especially at Z, more than 16,000 bunches must be stored to achieve the desired luminosity and this is only possible by avoiding parasitic collisions with a double-ring collider. Secondly, at the highest energy $t\bar{t}$, although the optimum number of bunches reduces to $\sim$30, the double ring scheme is still necessary to allow “tapering” [115]. The local energy of the beam deviates by up to $\pm 1.2\%$ between the entrance and the exit of the RF sections, with the result that the orbit deviation due to the horizontal dispersion in the arc and the associated optical distortion becomes intolerable, or the optics may even fall into an unstable region. The tapering scheme restores the ideal orbit and optics almost completely. In the case of a single ring, the tapering scheme cannot be applied to the e^+e^- beams simultaneously.

DRAFT FOR ADVISORY COMMITTEE - DO NOT DISTRIBUTE

The number of IPs is restricted by the layout of the straight sections in the FCC-hh. The straight sections around PD and PJ do not have large caverns for detectors and the intermediate straight sections at PB, PF, PH and PL are placed asymmetrically in the arcs and are not suitable to locate the RF cavities for FCC-ee. Thus two IPs are the only solution for FCC-ee given this constraint. The resulting beam optics [115] have a complete periodicity of two. The beam lines for e^+ and e^- have a mirror symmetry with respect to the line connecting the two IPs and the beam optics are identical.

The crab-waist scheme [116] is essential to boost the luminosity by the order of 10^3 at Z, compared to the previous colliders. This scheme gives a very small beam size at the IP together with a large crossing angle and small emittances, without exciting harmful synchrotron-betatron resonances associated with the crossing angle [116]. This scheme simply needs a pair of static sextupole magnets at both sides of the IP. These sextupoles are incorporated in the local chromatic correction system (LCCS) [115]. The effect of the crab-waist is produced by reducing the strengths of some sextupoles in the LCCS, so there is no need for special hardware. The optimum parameters with the crab-waist scheme including β^*s, bunch intensity, bunch length, etc., are obtained by the procedures described in the next section, which take into account beamstrahlung and various beam-beam effects.

The layout around the IP including the crossing angle, the strengths of solenoids and beam pipes are common for all energies. The polarity as well as the strengths of final quadrupoles change according to the beam energy and optimum focusing.

2.2.2 Beam Parameter Optimisation

One of the main factors determining collider performance is the beam-beam interaction, which at high energies can gain an extra dimension due to beamstrahlung – radiation in the field of the oncoming bunch [**?**, **?**]. FCC-ee apparently will be the first collider where beamstrahlung plays a significant role in the beam dynamics. Only half of the ring with one IP will be discussed in this section, because the other half will behave in the same way due to symmetry. To avoid confusion, the half-ring tunes will be marked by the superscript *.

The luminosity per IP for flat beams ($\sigma_x \ll \sigma_y$) can be written as:

$$L = \frac{\gamma}{2er_e} \cdot \frac{I_{tot}\xi_y}{\beta_y^*} \cdot R_{\text{HG}}, \tag{2.1}$$

where I_{tot} is the total beam current which in this case is determined by the synchrotron radiation power of 50 MW. Therefore L can only be increased by making ξ_y larger and β_y^* smaller while keeping the hour-glass factor R_{HG} reasonably large. The latter depends only on L_i/β_y^* ratio, where L_i is the length of interaction area which in turn depends on σ_z and Piwinski angle ϕ:

$$\phi = \frac{\sigma_z}{\sigma_x} \tan\left(\frac{\theta}{2}\right), \tag{2.2}$$

$$L_i = \frac{\sigma_z}{\sqrt{1+\phi^2}} \Rightarrow \frac{2\sigma_x}{\theta}. \tag{2.3}$$

here θ is the full crossing angle, and expressions after arrow correspond to $\phi \gg 1$ and $\theta \ll 1$, see Fig. 2.2. The beam-beam parameters for $\theta \neq 0$ become [**?**]:

$$\xi_x = \frac{N_p r_e}{2\pi\gamma} \cdot \frac{\beta_x^*}{\sigma_x^2(1+\phi^2)} \Rightarrow \frac{N_p r_e}{\pi\gamma} \cdot \frac{2\beta_x^*}{(\sigma_z\theta)^2}, \tag{2.4a}$$

$$\xi_y = \frac{N_p r_e}{2\pi\gamma} \cdot \frac{\beta_y^*}{\sigma_x\sigma_y\sqrt{1+\phi^2}} \Rightarrow \frac{N_p r_e}{\pi\gamma} \cdot \frac{1}{\sigma_z\theta}\sqrt{\frac{\beta_y^*}{\varepsilon_y}}, \tag{2.4b}$$

DRAFT FOR ADVISORY COMMITTEE - DO NOT DISTRIBUTE

where N_p is the number of particles per bunch. Note that $\xi_x \propto 1/\varepsilon_x$ (in head-on collision) transforms to $\xi_x \propto \beta_x^*/\sigma_z^2$ when $\phi \gg 1$, and ξ_y dependence on σ_x vanishes.

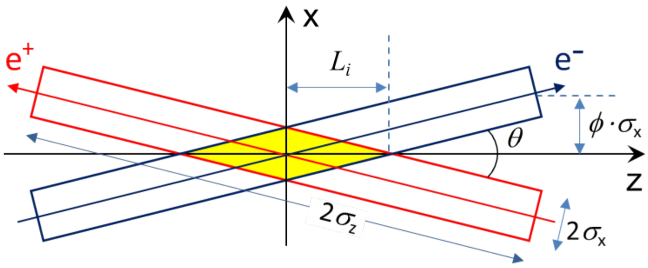

Figure 2.2: Collision with large Piwinski angle.

In the following, the main parameters that need to be optimised are listed first. The vertical emittance should be as small as possible, but there are two restrictions: $\varepsilon_y \geq 0.002 \cdot \varepsilon_x$ and $\varepsilon_y \geq 1$ pm. In addition, at Z there is some contribution to ε_y (0.2 – 0.3 pm) coming from the detector solenoids. It follows that ε_x should also be minimised, but there is no particular reason to drop below 0.4 nm. An important parameter for the luminosity is β_y^*, whose minimum value is 0.8 mm and it is limited by the dynamic aperture. It is assumed that ξ_y can be easily controlled by N_p, which implies that the number of bunches is adjusted to keep I_{tot} unchanged. In addition, β_x^*, RF voltage (which determines the bunch length and the synchrotron tune) and the betatron tunes are relatively free parameters.

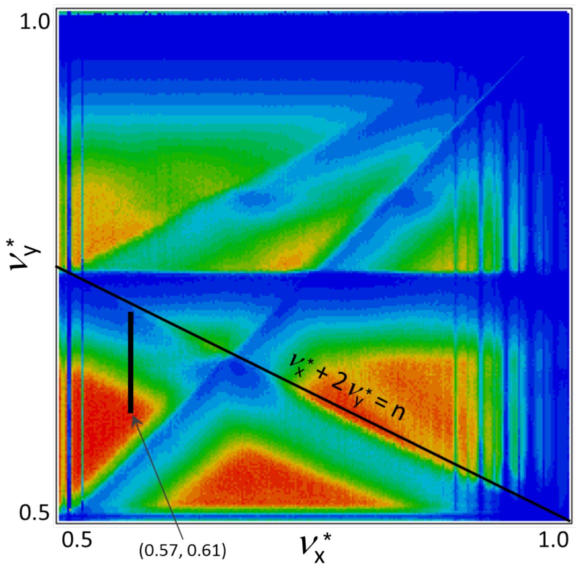

Figure 2.3: Luminosity at Z as a function of betatron tunes. The colour scale from zero (blue) to 2.3×10^{36} cm^{-2}s^{-1} (red). The black narrow rectangle shows the footprint at (0.57, 0.61).

Since FCC-ee is designed for a wide range of energies, parameter optimisation looks different at the various energies. To find the area of good working points at low energy (45.6 GeV) a scan of betatron tunes was performed in a simplified model: linear lattice and weak-strong simulations (without coherent instabilities). The results are presented in Fig. 2.3. Since $\xi_x \ll \xi_y$, the footprint looks like a narrow vertical strip, with the bottom edge resting on the working point. Particles with small vertical betatron amplitudes have maximum tune shifts and are in the upper part of the footprint, so the resonances in Fig. 2.3 seem to be shifted down. The good region is reduced to a red triangle bounded by the main coupling resonance $\nu_x^* = \nu_y^*$, sextupole resonance $\nu_x^* + 2\nu_y^* = n$, and half-integer resonance $2\nu_x^* = 1$

DRAFT FOR ADVISORY COMMITTEE - DO NOT DISTRIBUTE

with its synchrotron satellites. All other higher-order coupling resonances are suppressed by the crab waist, and therefore are not visible. As seen from the plot, the range of permissible ν_x for large ξ_y is bounded on the right by 0.57 – 0.58.

At low energies, the main problems associated with the beam-beam interaction come from the two new phenomena found in simulations: coherent X-Z instability [**?**, **?**, **?**] and 3D flip-flop [**?**], the latter occurs only in the presence of beamstrahlung. Both instabilities are bound with the horizontal synchro-betatron resonances – satellites of half-integer. Even high-order resonances (not visible in Fig. 2.3) are dangerous and they cannot be avoided completely. In any case, it is necessary to move away from low-order resonances, so ν_x^* is chosen close to the upper limit (thus $\nu_{x,y}$ move further from the integer, which facilitates tuning of the linear optics). Another requirement is that ξ_x must be substantially less than the distance between neighboring satellites, which is equal to the synchrotron tune. In other words, it is required to reduce the ratio ξ_x/ν_s^*.

The first step is to reduce β_x^*. However, because of the absence of local horizontal chromaticity correction in the interaction region, attempts to make β_x^* too small lead to a decrease in the energy acceptance. β_x^* can be reduced to 15 cm at Z, but this is not enough to suppress the instabilities. The next step is to reduce ξ_x for a given β_x^*, whilst trying to keep ξ_y unchanged. Obviously, this can only be done by increasing σ_z. The most efficient way is to increase the momentum compaction factor α_p, because not only does ξ_x decrease (due to larger σ_z) but also ν_s^* grows. In addition, larger α_p raises the threshold of microwave instability to an acceptable level. The only drawback of this approach is that ε_x grows with the power of 3/2 with respect to α_p. For the luminosity, ε_x is not so important by itself, but ε_y should be small and it is normally proportional to ε_x. However, the natural emittance at Z with small α_p and FODO arc cells with $90^\circ/90^\circ$ phase advances is very small – less than 90 pm. Therefore, even a threefold increase still allows $\varepsilon_y = 1$ pm to be achieved. Thus a lattice where doubling of α_p is achieved by reducing the phase advance per FODO cell in the arcs to $60^\circ/60^\circ$ was chosen (see Section 2.4.1).

Turning to the dependence on RF voltage: $\sigma_z \propto 1/\sqrt{U_{RF}}$, $\nu_s^* \propto \sqrt{U_{RF}}$. The requirement to keep ξ_y unchanged means that N_p/σ_z is constant. Therefore, if U_{RF} is lowered, ξ_x decreases by the same factor that σ_z grows by (not quadratically as it may seem). As a result ξ_x/ν_s^* does not change, but by lowering ν_s^* the order of synchro-betatron resonances located in the vicinity of working point is increased. U_{RF} is made small for this reason and one can find betatron tunes where neither instability manifests itself. For example, the working point is located between high order resonances $2\nu_x^* - 10\nu_s^* = 1$ and $2\nu_x^* - 12\nu_s^* = 1$.

At low energies beamstrahlung leads to a significant increase in the energy spread and, correspondingly, the bunch lengthening. If N_p is large enough to achieve high ξ_y, then σ_z becomes several times larger; in this case it scales as $\sigma_z \propto \sqrt{N_p}$. Accordingly, ξ_y and luminosity also grow $\propto \sqrt{N_p}$ while ξ_x remains constant. This means that by increasing N_p we do not reach the instability threshold, but only increase the energy spread. In general, N_p can be limited by several factors: ξ_y, beam lifetime (depends on the energy spread and energy acceptance) and the impedances. The result is close to all these limits, which corresponds to a proper optimisation.

As the energy increases, σ_x grows and the bunch lengthening due to the beamstrahlung decreases, therefore the Piwinski angle drops. In addition, the damping decrements grow with γ^3. All this leads to an increase in the instability threshold. For example, at 80 GeV it is already possible to work in a lattice with small momentum compaction. However, at $W^\pm$ there is one more important requirement. In order to obtain a resonant depolarisation, which is necessary for the energy calibration, the synchrotron tune must be larger than 0.05 (see Sect. ?.?). To achieve such a ν_s the momentum compaction has to be increased, therefore the same $60^\circ/60^\circ$ lattice was chosen as for Z. Furthermore, the RF voltage must be increased to 750 MV, so the only window for a good working point can be found between $2\nu_x^* - 4\nu_s^* = 1$ and $2\nu_x^* - 6\nu_s^* = 1$. In order that instabilities do not arise near these resonances, one must have $\beta_x^* \leq 20$ cm. Here it should be noted that with increasing energy, obtaining small beta functions becomes more difficult as this leads to a reduction in the dynamic aperture and momentum acceptance.

DRAFT FOR ADVISORY COMMITTEE - DO NOT DISTRIBUTE

Consequently, β_y^* was increased to 1 mm. Since U_{RF} is large enough, single-cell cavities used at Z will be replaced by multi-cell ones, thus restricting the capacity to damp HOM. An important consequence is that the number of bunches should not be smaller than 2000 and therefore the luminosity at $W^{\pm}$ is limited by this factor.

The possibility of further increasing ν_s to 0.075 was also considered, in accordance with the desire to improve the conditions for resonant depolarisation. In this case ν_x^* falls between low order resonances $2\nu_x^* - 2\nu_s^* = 1$ and $2\nu_x^* - 4\nu_s^* = 1$ and to avoid coherent instabilities it is necessary to reduce β_x^* to 15 cm. The momentum acceptance drops accordingly and, as a consequence, luminosity decreases. On the other hand, the number of bunches for this option is larger (2500), though they are shorter. This option is not worse for HOM and the luminosity is about the same as for 2000 bunches with $\nu_s = 0.05$. However, to obtain $\nu_s = 0.075$ it is necessary to double U_{RF}, which will require a revision of RF staging scenario. Therefore, the current primary option is $\nu_s = 0.05$.

Polarisation is not an issue at 120 GeV (Higgs production) and the optimum parameters are selected as follows:

1. The $90^\circ/90^\circ$ lattice, which provides small emittances.
2. The RF voltage is made small, but adjusted so that RF acceptance still exceeds the energy acceptance and this makes $\nu_s^* \approx 0.018$.
3. To be separated from low-order synchro-betatron resonances, ν_x^* is selected in the range of 0.56 – 0.58 with the condition that $\nu_x^* \approx 0.5 + \nu_s^* \cdot (m + 0.5)$, and $\nu_y^* = \nu_x^* +$ (0.03 – 0.04).
4. A β_x^* at which the coherent instabilities disappear is then sought; in this case, 30 cm is enough.
5. With the given ε_x and β_x^*, the length of interaction area $L_i \approx 0.9$ mm, and this defines the optimum β_y^*. However, obtaining small β_y^* at higher energies is more difficult, so 1 mm was chosen.
6. The lattice optimisation was performed for the selected β^* in order to maximise the dynamic aperture and energy acceptance.
7. A fine scan of betatron tunes was performed to choose the exact working point.
8. Then quasi-strong-strong simulations were performed with an asymmetry of 3% in the bunch currents (3% is determined by the required beam lifetime and the injection cycle time). At such energies, single high-energy beamstrahlung photons become significant and they impose a limit on N_p. The bunch population is scanned, while the restriction is the lifetime of the weak bunch. The maximum N_p and luminosity are determined in this way .

At the top energy (175 – 182.5 GeV) the coherent instabilities are suppressed by very strong damping, but another problem becomes dominant: the lifetime limitation by single high-energy beamstrahlung photons [?]. Thus, in contrast to low energies, β_x^* should be increased in order to make σ_x larger and thereby weakening the beamstrahlung. With increased σ_x, $L_i \approx 2$ mm is obtained and β_y^* should be about the same (or slightly smaller). Note that an increase in ε_x is not profitable since a small ε_y is required for high luminosity, so the $90^\circ/90^\circ$ lattice is used.

2.3 Design Challenges and Approaches

Based on existing technologies for e^+e^- circular colliders developed through the last half century, the FCC-ee will achieve the best ever luminosities at each energy. Although some components need final touches to their design or prototyping in the phase after the CDR, the fundamental feasibility of their construction has already been proved in other colliders and storage rings.

2.3.1 Synchrotron Radiation

The synchrotron radiation (SR) is a key feature for any e^+e^- storage ring. It is worth comparing the characteristics of FCC-ee with those of LEP2, the highest energy e^+e^- ring ever operated and PEP-II HER, one of the e^+e^- colliders with the highest beam current (see Table 2.2 [117]).

DRAFT FOR ADVISORY COMMITTEE - DO NOT DISTRIBUTE

Table 2.1: Machine parameters of FCC-ee for different energies.

		Z	$W^{\pm}$	Zh	$t\bar{t}$	
Circumference	[km]	97.756				
Bending radius	[km]	10.760				
Free length to IP ℓ^*	[m]	2.2				
Solenoid field at IP	[T]	2.0				
Full crossing angle at IP	[mrad]	30				
SR power / beam	[MW]	50				
Beam energy	[GeV]	45.6	80	120	175	182.5
Beam current	[mA]	1390	147	29	6.4	5.4
Bunches / beam		16640	2000	328	59	48
Average bunch spacing	[ns]	19.6	163	994	2763[1]	3396[??]
Bunch population	[10^{11}]	1.7	1.5	1.8	2.2	2.3
Horizontal emittance ε_x	[nm]	0.27	0.84	0.63	1.34	1.46
Vertical emittance ε_y	[pm]	1.0	1.7	1.3	2.7	2.9
Arc cell phase advances	[deg]	60/60		90/90		
Momentum compaction	[10^{-6}]	14.8		7.3		
Arc sextupole families		208		292		
Horizontal β^*_x	[m]	0.15	0.2	0.3	1.0	
Vertical β^*_y	[mm]	0.8	1.0	1.0	1.6	
Horizontal size at IP σ^*_x	[μm]	6.4	13.0	13.7	36.7	38.2
Vertical size at IP σ^*_y	[nm]	28	41	36	66	68
Energy spread (SR/BS)	[%]	0.038/0.132	0.066/0.131	0.099/0.165	0.144/0.196	0.150/0.192
Bunch length (SR/BS)	[mm]	3.5/12.1	3.0/6.0	3.15/5.3	2.75/3.82	1.97/2.54
Piwinski angle (SR/BS)		8.2/28.5	3.5/8.7	3.4/5.8	1.1/1.6	0.8/1.0
Length of interaction area L_i	[mm]	0.42	0.69	0.90	2.1	1.8
Hourglass factor R_{HG}						
Crab sextupole strength	[%]	97	87	80	50	50
Energy loss / turn	[GeV]	0.036	0.34	1.72	7.8	9.2
RF frequency	[MHz]	400			400 / 800	
RF voltage	[GV]	0.1	0.75	2.0	4.0 / 5.4	4.0 / 6.9
Synchrotron tune Q_z		-0.0250	-0.0506	-0.0358	-0.0818	-0.0872
Long. damping time	[turns]	1273	236	70.3	23.1	20.4
RF acceptance	[%]	1.9	2.3	2.3	3.5	3.36
Energy acceptance (DA)	[%]	$\pm$1.3	$\pm$1.3	$\pm$1.7	-2.8 +2.4	
Polarisation time t_p	[min]	15000	900	120	18.0	14.6
Luminosity / IP	[10^{34}/cm^{2}s]	230	28	8.5	1.8	1.55
Horizontal tune Q_x		269.139	269.124	389.129	389.104	
Vertical tune Q_y		269.219	269.199	389.199	389.175	
Beam-beam ξ_x/ξ_y		0.004/0.133	0.010/0.115	0.016/0.118	0.088/0.148	0.099/0.126
Allowable e^+e^- charge asymmetry	[%]	$\pm$5	$\pm$3			
Lifetime by rad. Bhabha	[min]	68	59	38	37	40
Actual lifetime by BS	[min]	>200	>200	18	24	18

While the total radiation power is higher than that of LEP2 by a factor of 2, the critical energy and the energy loss per arc length are only 20% and 10% higher, respectively. The power dissipation per arc length is less than 1/4 of PEP-II. Thus it is likely that the level of synchrotron radiation can be handled by existing technology.

Another aspect of the SR is the radiation toward the detector at the IP. This issue is addressed by the beam optics around the IP which suppresses the critical energy of the SR photons from the dipoles upstream of the IP to below 100 keV [115], from ~480 m from the IP. The highest critical energy of photons experienced at LEP2 was 83 keV at ~270 m from the IP [118]. Thus the criterion for FCC-ee sounds reasonable. The suppression of the SR toward the IP is achieved by asymmetric beam optics around the IP. The detailed analysis of the effect of SR for the detector is given in Section **??**.

DRAFT FOR ADVISORY COMMITTEE - DO NOT DISTRIBUTE

Table 2.2: Comparison of synchrotron radiation between FCC-ee, LEP2, and PEP-II at their highest energies.

		FCC-ee	LEP2	PEP-II (HER)
Highest beam energy	[GeV]	182.5	104.6	9.0
Bending Radius	[km]	10.760	2.584	0.167
Synchrotron radiation loss per turn	[GeV]	9.05	4.07	0.0034
Critical energy in the arc dipole	[MeV]	1.06	0.83	0.0082
Beam current / specie	[mA]	5.5	3	1960
Radiation power per beam	[MW]	50	12.2	6.8
Total radiation power per arc length	[kW/m]	1.2	1.1	5.5

2.3.2 Tapering

The tapering method is essential to maintain the beam orbit and the optics at the design values with the high synchrotron radiation loss around the ring, especially at $t\bar{t}$. Here it is assumed that all dipoles and quadrupoles have independent trim windings to facilitate the tapering [115]. Sextupoles are paired more or less locally and have independent power supplies. The magnitude of the trims reach $\pm1.2\%$ near the RF cavities. These trim windings are also useful for the correction of the orbit and the beam optics. While most of the dipoles and quadrupoles use the “twin aperture" scheme described below, trim windings can be installed independently for the two beams.

2.3.3 Dynamic Aperture, Beam Lifetime, Top-up Injection

FCC-ee will be the first circular collider where beamstrahlung dominates the luminosity performance. Thus the first requirement is that the collider optics must have sufficiently large dynamic momentum acceptance to hold a particle that loses its energy in a single photon emission due to beamstrahlung. The second requirement arises because beamstrahlung also increases the equilibrium momentum spread of the beam by multiple random emission of photons, therefore the dynamic momentum aperture must ensure the quantum lifetime. Generally speaking, at higher energy such as $t\bar{t}$, the first effect is more critical than the second one.

The dynamic aperture must be large enough to capture the injected beam for the top-up injection. There are at least two schemes: off-axis-on-momentum and on-axis-off-momentum injections. They need transverse on-momentum or off-momentum dynamic apertures, respectively. The dynamic aperture of the optics that has been designed is sufficient for both injection schemes at all energies [119].

There are two major processes which determine the beam lifetime. One is the radiative Bhabha scattering at the IP, which is proportional to the luminosity divided by the number of particles stored in the ring. The other is the lifetime given by the beamstrahlung and the dynamic momentum acceptance. The latter depends on the optimisation of the beam parameters as discussed in the previous section. The resulting lifetime as shown in Table 2.1 matches the capacity of the injector. The injection must be done with a “bootstrap" procedure, in which the imbalance of the charges of both beams is kept within a certain relative difference, i.e. $\pm5\%$ at Z and $\pm3\%$ at higher energies, as described in the previous section.

2.3.4 Low Emittance Tuning and Optics Correction

To maintain the vertical emittance below the design criteria is also necessary to reach the high luminosity, as well as being important to ensure beam polarisation at Z and $W^{\pm}$. It is assumed that the emittance ratio is $\varepsilon_y/\varepsilon_x \geq 0.2\%$ and that $\varepsilon_y \geq 1$ pm at all energies. The latter condition is important since the vertical emittance generated by the fringe field of the solenoids together with the crossing angle reaches

DRAFT FOR ADVISORY COMMITTEE - DO NOT DISTRIBUTE

0.2 pm at Z, where the effect is the largest.

The tuning scheme described later uses skew quadrupole fields generated by trim windings on arc sextupoles to control the vertical emittance generated by the misalignments in the arc. The x-y coupling and dispersion can be measured using beam position monitors (BPMs) at each quadrupole in either a turn-by-turn or multi-turn mode. The method is like those developed at other colliders such as LHC and B-factories, as well as at light sources. The misalignment tolerances and the precision of the diagnostics is comparable to those that have been achieved in the aforementioned machines. Special care will be needed for the error correction of the final quadrupoles and the local chromaticity section, where the β-functions become very high, up to 6,000 m.

The correction of the beam optics including the β-functions and horizontal dispersion will be important both for the low emittance tuning and the dynamic aperture. The trim windings on all of the quadrupoles equipped for the tapering will be used for optics corrections.

2.4 Optics Design and Beam Dynamics

2.4.1 Lattices

The beam optics was established for the baseline in 2016 [115], then further revised to include several modifications such as $60^\circ/60^\circ$ phase advance at Z and $W^\pm$, twin-aperture quadrupoles [120], a section for inverse-Compton spectrometer [121], etc. [122, 123]. In the description below, the beam energy at $t\bar{t}$ is 182.5 GeV, unless otherwise specified.

The arc optics are based on FODO cells with $90^\circ/90^\circ$ (Zh and $t\bar{t}$) and $60^\circ/60^\circ$ (Z and $W^\pm$) phase advances. A FODO cell has the best packing factor of dipoles, which is a crucial condition for a high energy collider. Since twin-aperture quadrupoles are used, both horizontally focusing (QF) and defocusing (QD) quadrupoles must have the same length, thus the spacing between quadrupoles must be the same.

The number of cells was determined so that the goal of the horizontal emittance could be achieved. Generally speaking, although a smaller emittance is favorable for higher luminosity, it requires a shorter cell length. A shorter cell reduces the horizontal dispersion and the momentum compaction factor. Then the quadrupole and sextupole magnets would become stronger and longer which would degrade the dipole packing factor. A smaller momentum compaction can lead to beam instabilities due to collective effects and the beam-beam effect. A thinner quadrupole magnet with a stronger field will degrade the dynamic aperture due to the synchrotron radiation. Thus the current number of FODO cells is already close to the maximum. The resulting packing factor of dipoles in the arc is 81.8%. Trim windings on sextupole magnets will be used as horizontal/vertical dipole and skew quadrupole correctors to avoid having dedicated correctors and thereby improve the packing factor. Using a combined function dipole may have benefits for the emittance and momentum compaction factor by increasing the horizontal damping partition, but the resulting momentum spread is not suitable for polarisation and this idea has therefore been rejected.

Non-interleaved families of sextupole pairs, with a $-I$ transformation between sextupoles [124], are placed in the FODO cells. As the phase advance is different between high and low energies, the locations of the usable sextupoles depend on the experiments. There are three types of the arrangement of a sextupole around a quadrupole as shown in Fig. 2.4: no sextupole, a singlet sextupole, and a doublet sextupole. Whilst a doublet is used at higher energies, only one of them is used at lower energies if the same location is required. A singlet sextupole is installed where a sextupole is only needed for the lower energy. To achieve a better dipole packing factor where possible, the spaces not needed for a sextupole are filled with dipoles. Thus there are three dipole lengths but with the same bending radius. The resulting lattice has a super period of 35 FODO cells as shown in Fig. 2.5. Within the super period, the β-functions are almost periodic in each cell, since the focusing due to dipoles is weak. On the other hand, the horizontal dispersion has a modulation within a super period. Studies of such a modulation on

DRAFT FOR ADVISORY COMMITTEE - DO NOT DISTRIBUTE

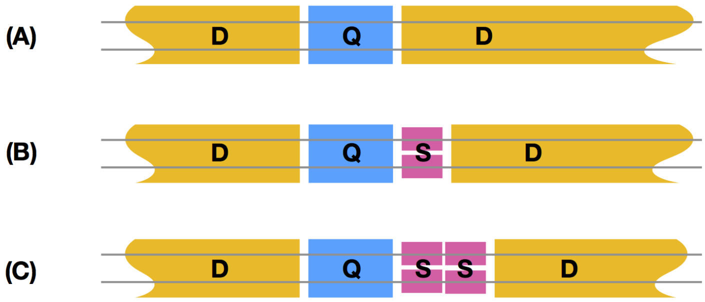

Figure 2.4: Three arrangements of a sextupole around a quadrupole. D: twin-aperture dipole, Q: twin-aperture quadrupole. S: single-aperture sextupole. (A) no sextupole, (B) single aperture, singlet sextupole only for $60^\circ/60^\circ$, (C) single aperture, doublet sextupole for either $60^\circ/60^\circ$ or $90^\circ/90^\circ$. In the case of (C), only the pieces next to the quadrupole are powered for $60^\circ/60^\circ$. As the result, three lengths of the dipoles are needed to maintain the distance between quadrupoles constant.

the dynamic aperture have so far not shown any effect. All sextupole pairs are independently powered, and there are 294 and 208 independent pairs per half ring for $90^\circ/90^\circ$ and $60^\circ/60^\circ$, respectively. The non-interleaved scheme of sextupoles has been applied at B-factories and successfully operated for more than 15 years [125, 126]. At KEKB, the number of pairs was 52 per ring.

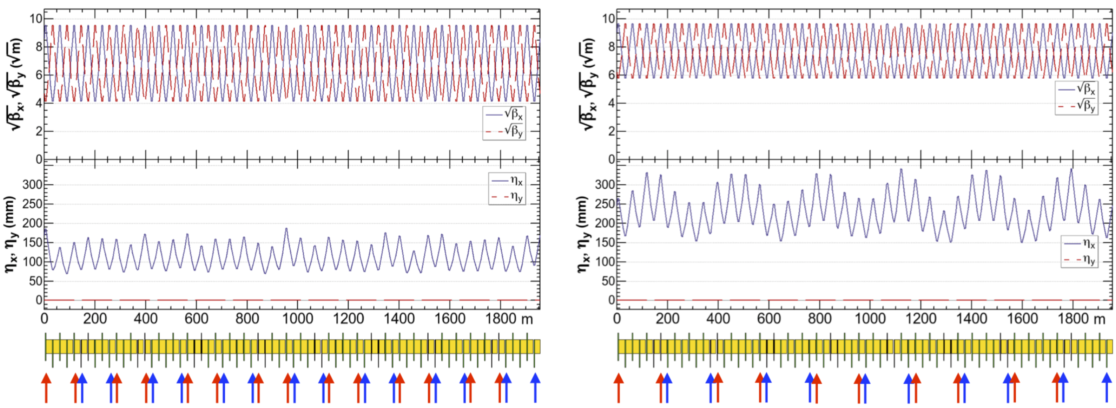

Figure 2.5: The beam optics of the arc super cell of FCC-ee, for two phase advances. Left: $90^\circ/90^\circ$ (for Zh and $t\bar{t}$) right: $60^\circ/60^\circ$ (for Z and $W^{\pm}$). The upper and lower rows show $\sqrt{\beta_{x,y}}$ and dispersions, respectively. The locations of the focusing and defocusing sextupoles, SF and SD, are indicated by red and blue arrows, respectively, for each phase advance. Every two sextupoles are paired with $-I$ transformation between them.

2.4.2 Interaction Region

One of the beam optics challenges for the collider is providing the dynamic aperture with small β-functions down to $\beta^*_{x,y}$ = (0.15 m, 0.8 mm) at the IP for Z. Although these values are still higher than those in modern B-factories [127], the associated vertical chromaticity around the IP is comparable, since the distance, ℓ^*, from the face of the final quadrupole magnet to the IP is much longer than those in B-factories. Also especially at the $t\bar{t}$ energy, the beamstrahlung caused by the collisions requires a very wide momentum acceptance of $-2.8\% + 2.4\%$. The transverse on-momentum dynamic aperture must be larger than $\sim 12\sigma_x$ to enable top-up injection in the horizontal plane.

Figure 2.6 shows the optics in the interaction region (IR) for $t\bar{t}$. It has a local chromaticity correction system (LCCS) only in the vertical plane at each side of the IP. The sextupole magnets pairs

DRAFT FOR ADVISORY COMMITTEE - DO NOT DISTRIBUTE

for the LCCS have one at each side of the IP and only the inner ones at (b,c) have non-zero horizontal dispersion [128]. The outer ones at (a,d) perform two functions: cancelling the geometrical nonlinearity of the inner ones, and generating the crab-waist at the IP by choosing their phase advance from the IP as $\Delta\psi_{x,y} = (2\pi, 2.5\pi)$, as described in [115]. The incorporation of the crab sextupoles into the LCCS saves space and reduces the number of optical components. The optimum magnitude of the sextupole depends on the luminosity optimisation. As the crab sextupoles are dispersion-free [128], they can be adjusted to any ratio up to the "full crab-waist" without causing unnecessary side effects.

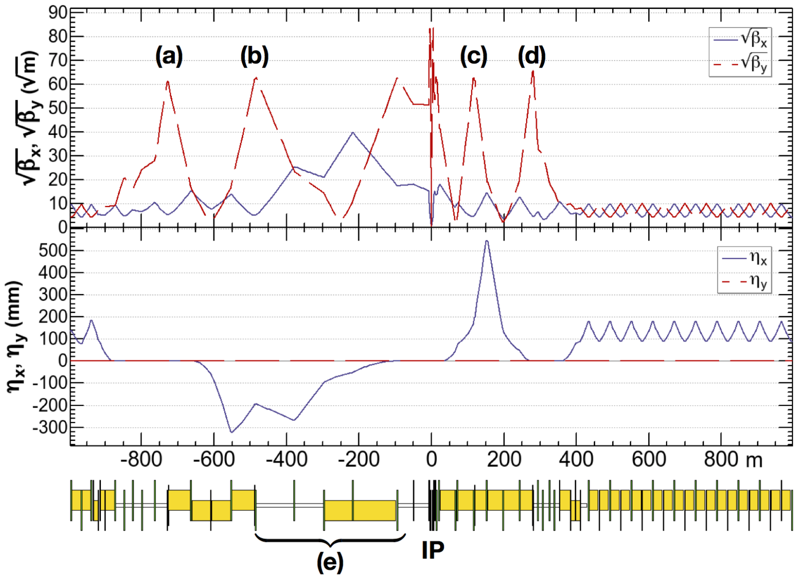

Figure 2.6: The beam optics of the FCC-ee IR for $t\bar{t}$. Upper and lower rows show $\sqrt{\beta_{x,y}}$ and dispersions, respectively. The beam passes from the left to the right in this figure. The optics is asymmetric to suppress the synchrotron radiation toward the IP. Dipoles are indicated by yellow boxes, and those in region (e) have a critical energy of the SR photon below 100 keV at the $t\bar{t}$. Sextupoles for the LCCS are located at (a–d), and sextupoles at (a,d) play the role of crab sextupoles.

The beam lines in the interaction region are separate for the two beams and there are no common quadrupoles in the IR. As a working assumption [129] ℓ^* is chosen to be 2.2 m, which is sufficient for two independent final quadrupoles with a 30 mrad crossing angle. This is the subject of further study and will depend on the detailed design of the detector and its interface with the machine. The solenoids are common for two beams, and they are compensated locally with counter solenoids to cancel the $\int B_z dz$ between the IP and the faces of the final quadrupole, as shown in Fig. 2.7. The vertical orbit, vertical dispersion, and x-y couplings do not leak out for any particle at any energy. So far in the study, such a perfect compensation has been assumed. The vertical emittance increases due to the fringe field of the compensating solenoid in combination with the horizontal crossing angle. The increase becomes largest at the Z energy as it is assumed that the solenoid field is independent of the beam energy. The increase of the vertical emittance is below 0.2 pm for 2 IPs and a realistic profile of B_z shown in Section 2.5.

The optimised $\beta^*_{x,y}$ discussed in Section 2.2 has to be smaller at low energies. To reduce β^*_x at the Z from $\beta^*_{x,y} = (1$ m, 1.6 mm) at $t\bar{t}$ to (0.15 m, 0.8 mm) at Z, the final vertical focusing quadrupole QC1, which is placed at $\ell^* = 2.2$ m from the IP, is split into three pieces. The polarities and the strengths of these pieces depend on the beam energy. For instance, all three pieces provide vertical focusing at $t\bar{t}$, and only the first piece provides vertical focusing while the remaining two focus horizontally at Z. The field strengths are limited to the same value, 100 T/m, at all beam energies. With this triple splitting, the centre of focusing for each plane moves closer towards the IP at the Z, which reduces the increment of the chromaticity for the smaller β^*. Comparing left and right of Fig. 2.7, it can be seen that the beam

DRAFT FOR ADVISORY COMMITTEE - DO NOT DISTRIBUTE

sizes at Z through this region are still smaller than those at $t\bar{t}$. The peak value of β_y is almost unchanged even though β_y^* is reduced by 1/2. The peak of β_x at Z is about 3 times higher, while β_x^* becomes 1/6 of the value at $t\bar{t}$.

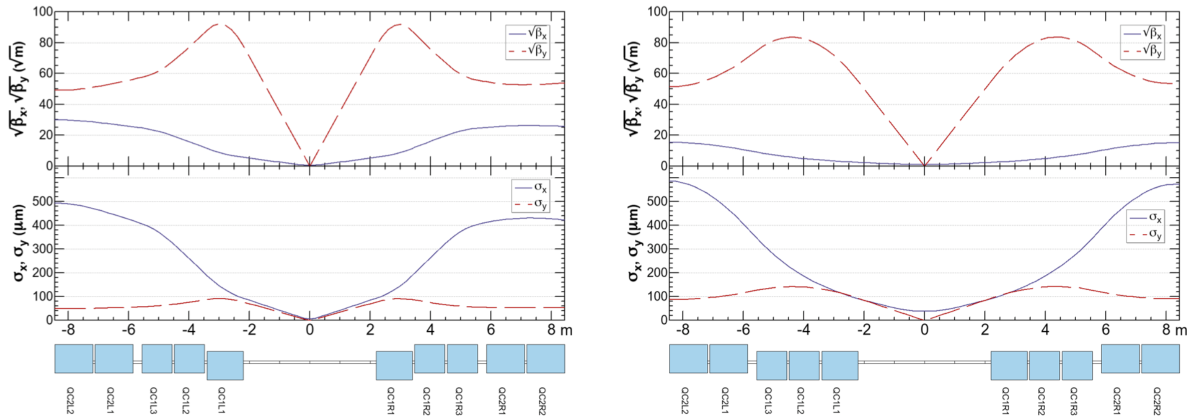

Figure 2.7: The $\sqrt{\beta_{x,y}}$ and beam sizes around the IP at Z (upper left), $W^{\pm}$ (upper right), Zh (lower left), and $t\bar{t}$ (lower right). The beam sizes assume the equilibrium emittances listed in Table 2.1. The final quadrupoles QC1(L/R) are longitudinally split into three slices. While all slices of QC1 are vertically focusing at $t\bar{t}$, only the first ones are at Z. Note that the inner radius of the beam pipe is larger than 15 mm through these quadrupoles.

The critical energy of SR photons from the dipoles up to 500 m upstream of the IP is set below 100 keV at $t\bar{t}$. There are no dipole magnets upstream of the IP for up to 100 m.

2.4.3 RF Section and Other Straight Sections

Figure 2.8 shows the beam optics for the half ring for $t\bar{t}$. The RF sections are located in the long straight sections around PJ and PD as shown in Fig. 2.1. At $t\bar{t}$, an acceleration voltage of ∼5.3 GV per section is needed, so the length of the RF section will be about 1 km. Both beams pass through a common RF section at $t\bar{t}$. A combination of electrostatic separator and a dipole magnet only deflects the outgoing beam to avoid SR shining toward the RF cavities. The quadrupoles within the RF section are common to both beams, but are still compatible with the overall tapering scheme, if their strengths are symmetrical about the middle point of the RF section.

The staging of the RF system adds cavity modules step by step as the energy increases, starting at Z up to $t\bar{t}$, and the beam line in the RF section needs minimal modification as more modules are installed. Most of the RF cavities and cryomodules are reused at the various stages.

The straight section (a) in Fig 2.8 has space for a spectrometer which will use inverse Compton scattering from a laser to measure the beam energy and the polarisation. This section has a free space of 100 m immediately after the dispersion suppressor dipole at the entrance of the inner ring and therefore the beam optics is different to that of (b).

Other use of the intermediate straight sections in the middle of the arc has not been fully determined and the optics for them have not been finalised. Some of them can be used for injection, dump, collimation, etc.

2.4.4 Dynamic Aperture

The dynamic aperture (DA) has been estimated using the computer code SAD [130], taking into account the effects listed in Table 2.3. The synchrotron radiation from the dipoles improves the aperture, especially at $t\bar{t}$, due to the strong damping, whereas the radiation loss in the quadrupoles for particles with

DRAFT FOR ADVISORY COMMITTEE - DO NOT DISTRIBUTE

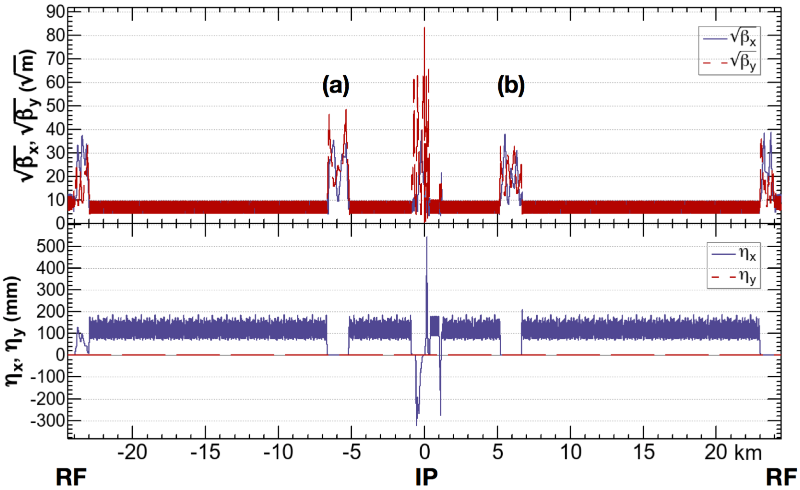

Figure 2.8: The beam optics of the FCC-ee half ring for $t\bar{t}$. Upper/lower plots show $\sqrt{\beta_{x,y}}$ and horizontal/vertical dispersions, respectively. These plots start and end in the middle of the RF sections, and the IP is located at the centre. Sections marked by (a,b) correspond to the intermediate straight sections B, F, H, L in Fig. 2.1.

large betatron amplitudes reduces the dynamic aperture. This is due to the synchrotron motion induced by the radiation loss as described in Ref. [115]. This effect is most noticeable in the horizontal arc quadrupoles and therefore the length of the arc quadrupoles must be sufficiently long. The final focus quadrupole has another effect resulting from the SR which makes the transverse damping unstable. The vertical motion for a $\beta_y^* = 0.8$ mm at Z is unstable for $\Delta y \gtrsim 30\sigma_y$ due to the large β_y and the strong field gradient in the quadrupole.

Table 2.3: Effects taken into account during the optimisation of the dynamic aperture.

Effect	Significance
Synchrotron motion	**Essential**
Radiation loss in dipoles	**Essential** – improves the aperture, esp. at Zh and $t\bar{t}$
Radiation loss in quadrupoles [a]	**Essential** – reduces the aperture
Radiation loss in sextupoles	minimal
Tapering	**Essential**
Crab-waist	transverse aperture is reduced by $\sim 20\%$ for 100% strength
Maxwellian fringes [131]	small
Kinematic terms	small

[a] See Appendix **??**

The DA has been optimised by particle tracking with a downhill simplex method scripted within SAD and varying the sextupole settings. All the effects listed in Table 2.3 were included in the optimisation. The goal of optimisation is to determine a weighted area covered by the initial conditions in the z-x plane, detailed in Ref. [115]. The results are shown in Fig. 2.9. The transverse apertures in the x-y plane, shown in Fig. 2.10, are evaluated after the optimisation for the z-x plane.

The resulting DA satisfies the requirements for both beamstrahlung and top-up injection, at least without field errors and misalignments. The optimisation was done for each energy. The number of initial conditions that can be studied is limited by the computing resources available. A larger number is always better, but when n_z and the number of revolutions from Fig. 2.9 were doubled, the resulting

DRAFT FOR ADVISORY COMMITTEE - DO NOT DISTRIBUTE

change in the DA was tiny.

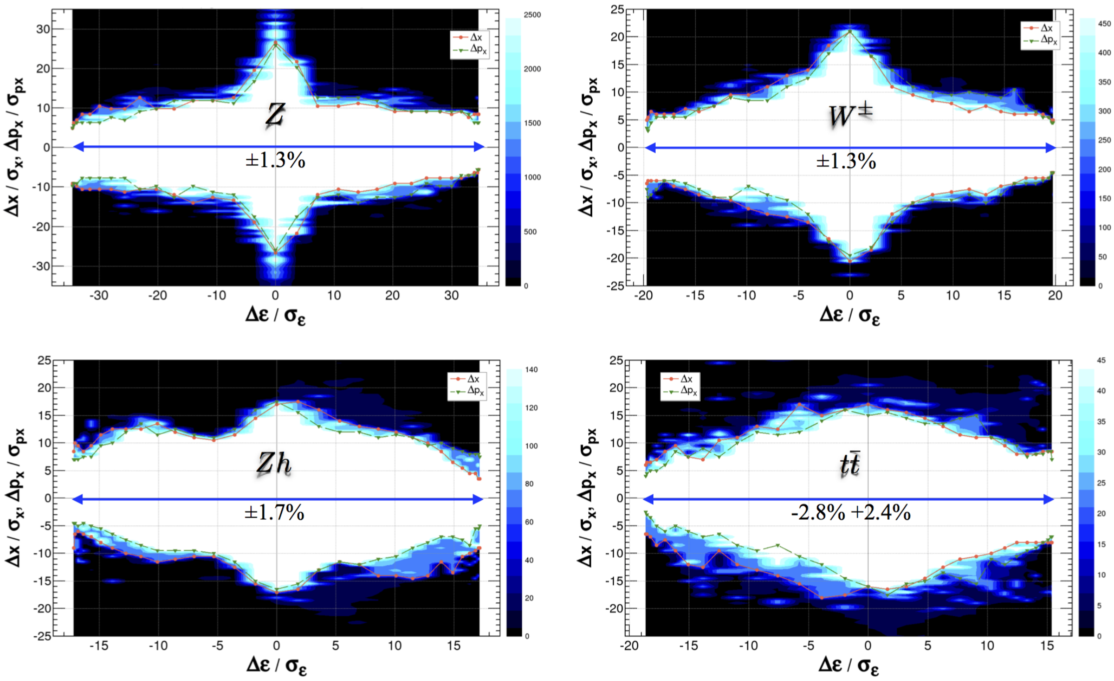

Figure 2.9: Dynamic apertures in z-x plane after sextupole optimisation with particle tracking for each energy. The initial vertical amplitude for the tracking is always set to $J_y/J_x = \varepsilon_y/\varepsilon_x$. The number of turns corresponds to about 2 longitudinal damping times. The resulting momentum acceptances are consistent with the luminosity optimisation shown in Table 2.1. Effects in Table 2.3 are taken into account. The momentum acceptance at $t\bar{t}$ is "asymmetric" to match the distribution with beamstrahlung.

So far all sextupole pairs have been used independently in the optimisation, thus the degree of freedom for the optimisation is 296 for Zh and $t\bar{t}$, and 210 for Z and $W^{\pm}$, respectively, including the sextupoles for the local chromatic correction. The super period periodicity of 2 for the ring is kept. It has not been verified whether the large number of sextupole families is really necessary.

The purpose of a wide momentum acceptance is to capture the particles which emit a beamstrahlung photon at the IP. Since the primary energy change is always negative, the momentum acceptance can be wider on the negative side and somewhat narrower on the positive side. The acceptance on the positive side can be determined by the damping and the diffusion during a synchrotron motion half cycle thus:

$$A_+ \approx -A_- \exp(-\alpha_z/2\nu_s) + 3\sigma_{\delta,\mathrm{BS}}\sqrt{1 - \exp(-\alpha_z/\nu_s)}\,, \qquad (2.5)$$

where α_z, ν_s, $\sigma_{\delta,\mathrm{BS}}$ are the longitudinal damping rate per turn, the synchrotron tune and the equilibrium momentum spread including the beamstrahlung, respectively. The size of the diffusion has been set at 3σ. At $t\bar{t}$ if $A_- = -2.8\%$, then $A_+ = +2.4\%$, as shown in Table 2.1. The optimisation of the DA at $t\bar{t}$ has been done for such an asymmetric momentum acceptance. Since this effect is weak at lower energies, symmetric acceptances have been applied.

There are a number of effects that are not included in the optimisation process, mainly due to their stochastic nature, which will need a large number of samples to simulate. Table 2.5 lists such effects, which are evaluated separately after the optimisation. Among them, the quantum fluctuation should have significant effects and the radiation fluctuation of the SR in the lattice should be simulated together with the beamstrahlung, since they have comparable magnitudes.

DRAFT FOR ADVISORY COMMITTEE - DO NOT DISTRIBUTE

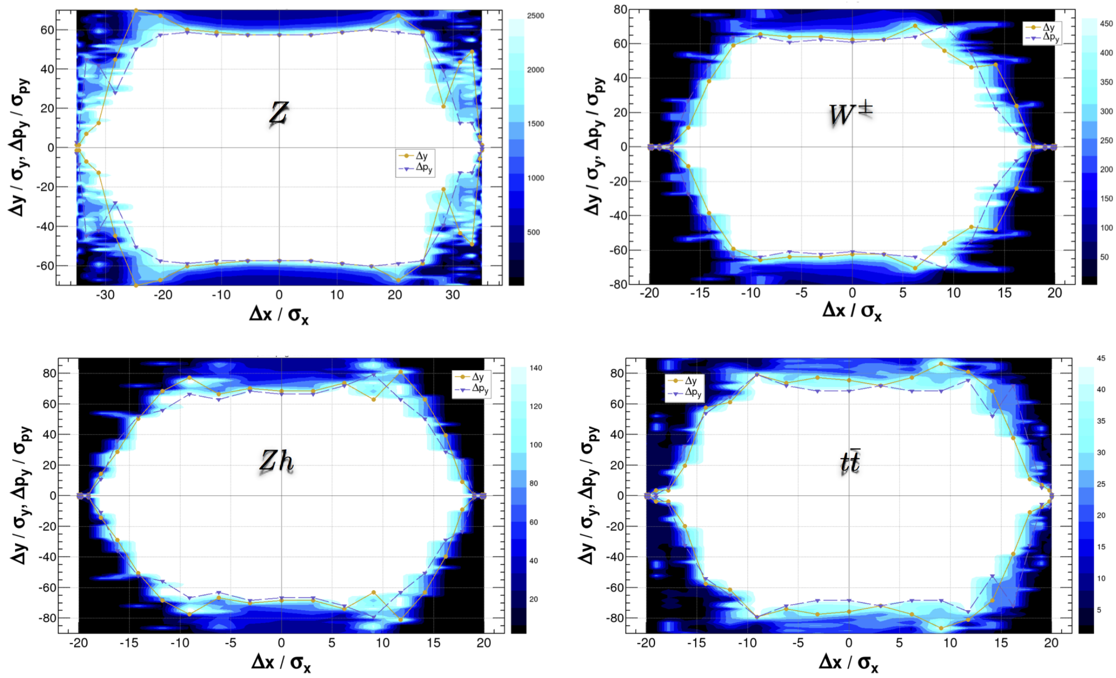

Figure 2.10: On-momentum transverse dynamic apertures after an optimisation of sextupoles at each energy. The initial momentum offset is set to 0. All of the effects in Table 2.3 were taken into account.

Table 2.4: On-momentum transverse dynamic and physical apertures at each energy. The narrowest physical aperture is given by the beam pipe of the final quadrupole with 15 mm inner radius as shown in Fig. 2.7. All effects in Table 2.3 were included for the DA.

Energy	Dynamic		Physical	
	$\Delta x/\sigma_x$	$\Delta y/\sigma_y$	$\Delta x/\sigma_x$	$\Delta y/\sigma_y$
Z	± 35	± 58	± 37	± 170
$W^{\pm}$	± 22	± 55	± 23	± 133
Zh	± 18	± 67	± 34	± 144
$t\bar{t}$	± 19	± 70	± 43	± 107

2.4.5 Tolerances and Optics Tuning

Due to the very low emittance budget and the small β^* at the interaction point, the FCC-ee is a very challenging accelerator to correct when misalignments are introduced in the simulations. These errors produce a very large vertical dispersion (several hundred meters without any correction applied) and coupling, which compromise the target emittance, in particular at high energy. Several correction methods and algorithms were developed in order to preserve the emittances as close as possible to their design values.

Horizontal correctors were installed at every focusing quadrupole and vertical correctors at every defocusing quadrupole. Beam Position Monitors (BPM) were placed at each quadrupole, including at the doublet of the IPs. Skew quadrupole correctors with a trim quadrupole are placed at the sextupoles to correct the beta-beat and rematch the horizontal dispersion. Special skew quadrupoles were installed in the interaction region to compensate the tilt of the doublet quadrupoles at the IPs.

The vertical dispersion distortion was corrected with orbit correctors via the Dispersion Free Steering method [132] first and with skew quadrupoles with the help of response matrices. The linear cou-

DRAFT FOR ADVISORY COMMITTEE - DO NOT DISTRIBUTE

Table 2.5: Effects evaluated separately after the optimisation of DA.

Effect	Significance at $t\bar{t}$
Detector & compensation solenoids	minimal, if locally compensated at the IP
Beam-beam effect with beamstrahlung	Overall beam lifetime satisfies the requirement (strong-weak model)
Radiation fluctuation	**Essential**, evaluated together with beamstrahlung
Multipoles of final quadrupoles	minimal for the proposed design of the magnets
Multipoles of other magnets	minimal for the proposed design of the magnets
Misalignments of magnets with corrections	**Essential**

pling was corrected by adjusting the linear coupling resonance driving term parameters, as tested at the ESRF [133]. Trim quadrupoles were used to rematch the phase advances between the BPMs, again using response matrices. Satisfactory results for the misalignment tolerance were found when the magnets were misaligned as defined in Table 2.6.

Table 2.6: Tolerance for Arc quadrupoles, sextupoles and quadrupoles of the IPs.

Magnet type	Hor. displacement Δx μm	Vert. displacement Δy μm	Tilt $\Delta\theta$ μrad
Arc quadrupoles	100	100	100
Sextupoles	100	100	0
IP quadrupoles	50	50	50

1000 seeds were tested with the correction algorithm using the input misalignments listed in Table 2.6 and 70% of them converged, with the following results for the emittances:

$$\epsilon_y = 0.099\text{pm} +/- 0.013 \quad (2.6)$$

$$\epsilon_x = 1.52\text{nm} +/- 0.01 \quad (2.7)$$

$$\epsilon_y/\epsilon_x = 0.0065\% \quad (2.8)$$

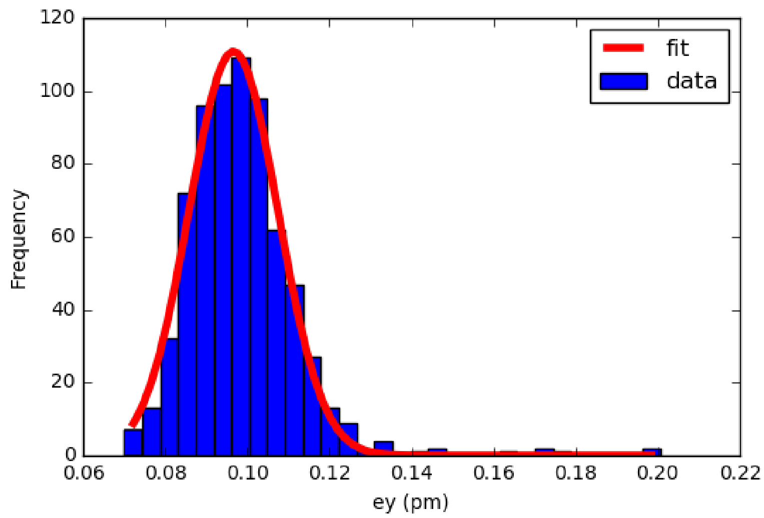

Figure 2.11: Statistical distribution of the vertical emittance for 700 different seeds resulting from the input misalignments given in Table 2.6. Initially 1000 seeds were tested and 70% of them converged.

DRAFT FOR ADVISORY COMMITTEE - DO NOT DISTRIBUTE

2.5 Machine Detector Interface

2.5.1 Overall Layout of the Interaction Region

Together the requirements of the detector and of the accelerator at the collision point make the IR one of the more challenging parts of the overall design. The challenge is to maximise performance in terms of integrated luminosity with a tolerable level of the related background for the experiments. This includes minimising synchrotron radiation in the IR. The interaction region has a flexible design to allow running at different energies. The IR optics scales with the energy, allowing a common IR layout for all energies.

To reach the target luminosity of $2 \times 10^{36}\mathrm{cm}^{-2}\mathrm{s}^{-1}$ at the Z-pole it is necessary to have the crab-waist collision scheme together with pushing the beam current to the limit. The main guideline for the IR optics has been to keep the synchrotron radiation (SR) backgrounds acceptable for the detector and the process has been guided by experience from LEP2. There, the highest local critical energy was 72 keV for photons emitted 260 m from the IP [134]. Consequently, the main guideline in the IR design has been to keep critical energies from bending magnets up to 500 m from the IP below 100 keV for the incoming beam and have the first dipoles located at least 100 m from the IP. An additional goal for the optics design that comes from considerations of synchrotron radiation, is to keep all critical energies around the ring below 1 MeV in order to minimise neutron production. An asymmetric optics has been designed to meet these goals for the critical energy of the synchrotron radiation photons in the presence of the crossing angle as large as 30 mrad, which is required by the crab-waist scheme. The asymmetry allows the beam to come from the inner ring to the IP, then it is bent strongly after the IP to merge back close to the opposite ring as shown in Figure 2.1. The distance between the IP with FCC-hh beamline is 10.6 m. Outside the IR, the FCC-ee and FCC-hh trajectories are on the same orbit but an additional tunnel is necessary for ~1.2 km around the IP in order to allow for the crab-waist collision scheme with a large crossing angle.

An expanded horizontal view of the IR layout is shown in Fig. 2.12, for the region $\pm 2.5\,\mathrm{m}$ around the IP. As is shown in the figure, the interaction region is symmetric and the two beam pipes are merged together close to the IP. The distance between the IP and the entrance of the first quadrupole ℓ^* is 2.2 m.

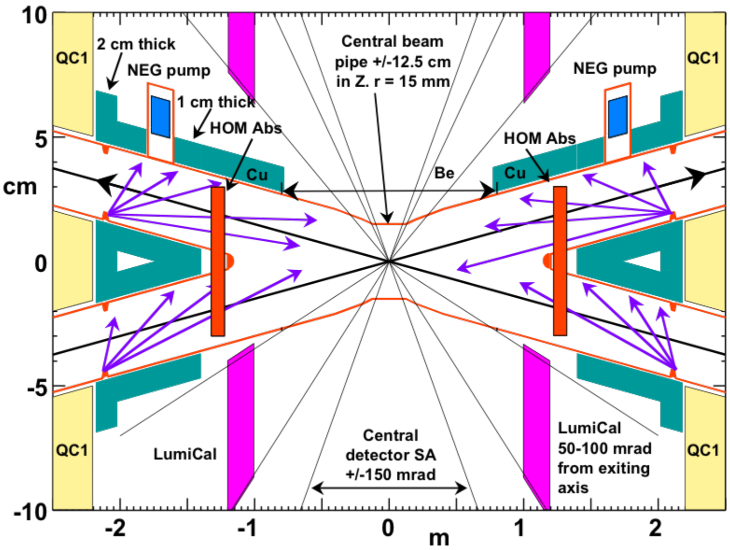

Figure 2.12: An $x-z$ view of the FCC-ee IR layout for $\pm 2.5\,\mathrm{m}$ from the IP. Note the expanded vertical scale.

The vacuum beam pipe aperture, which is circular and has a constant radius of 15 mm is shown in red on Fig. 2.12. The first final focus quadrupole QC1 is shown in yellow. Synchrotron radiation mask tips which intercept SR scattered particles are also shown on the plot, they are located in the

DRAFT FOR ADVISORY COMMITTEE - DO NOT DISTRIBUTE

horizontal plane just in front of QC1 at 2.1 m from the IP. The horizontal aperture will be 12 mm at the mask tips. Section 2.5.4 describes how synchrotron radiation is handled in the collider. The luminosity monitor which is placed longitudinally between 1.074 and 1.19 m from the IP, is shown in magenta. A description of the luminosity monitor is given in Section 2.5.3.

To reduce multiple scattering effects in the luminosity monitor, the vacuum chamber located in the range of $\pm 0.9\,\mathrm{m}$ from the IP, will be made from beryllium, followed by a copper vacuum chamber throughout the final focus doublet. The vacuum chamber inside the superconducting final focus is warm. The central vacuum chamber will also have a 5 µm gold coating to shield the detector and luminosity monitor from scattered synchrotron radiation photons. Outside the vacuum chamber, between the luminosity monitor window and QC1, 1 cm of Tantalum (or some other high Z material such as Pb or W) shielding (shown in green on Fig. 2.12) will be installed to protect the detectors. It has been confirmed by a full GEANT4 simulation of the sub-detectors (see Section 2.5.5 that this high-Z material shielding is sufficient and it is necessary, especially at the top energy.

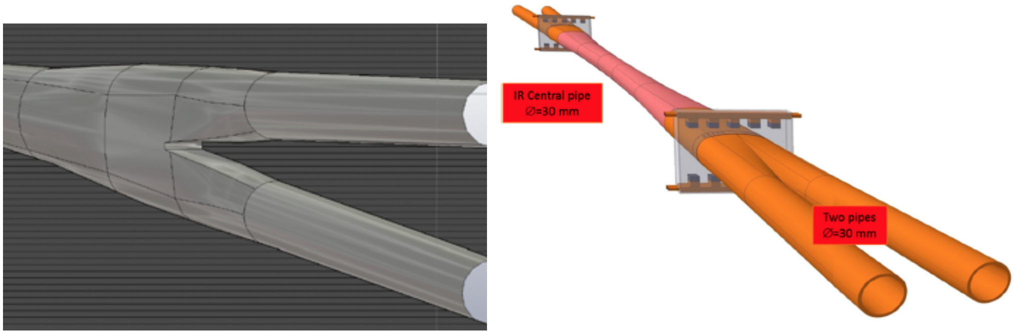

Figure 2.13: Left: 3D CAD view of the IR vacuum chamber in the region where two beam pipes merge; right: beam pipe with HOM absorbers.

The geometry of the beam pipe in the IR is constant and smooth and particular care is taken where the two separate beam pipes merge. This region, shown on the left in Fig. 2.13, was designed using CST [135] and HFSS [136] with CAD to analyse electro-magnetic fields in the IR correctly. These studies show that the cut-off frequency of electro-magnetic fields generated or trapped in the IR is at a safe value. High order mode (HOM) absorbers have also been studied following the PEP-II experience [137]. The right plot of Fig. 2.13 shows the vacuum chamber in the IR with a sketch of the HOM absorbers. A detailed analysis of this study is presented in Section 2.6.18. The HOM absorber design includes a water cooling system to avoid heating. The beam pipe will be at room temperature and water cooling is planned in the IR, inside the final focus quadrupoles and through the IR.

2.5.2 Magnet Systems

The magnetic elements required in the vicinity of the IP are the main detector solenoid and the final focus quadrupoles. The main detector solenoid is a cylinder with half-length 4 m and a diameter of around 3.8 m and has a peak strength of 2 T (see Chapter 1 for more details). The value of 2 T was chosen as a good compromise between the physics performance and the requirement for the vertical emittance to be in the pm region. Due to the crab-waist design, the first final focus quadrupole, QC1, is inside the main detector solenoid. Further requirements can be formulated as follows:

1. Leave adequate space for the detectors: in the present design magnetic elements reach up to angles of $\pm$ 100 mrad, and the luminosity counter sits unobstructed in front of all magnetic elements;
2. The integrated field seen by the electrons and positrons crossing the IP should vanish to minimise emittance blow-up due to coupling between transverse planes. Field compensation should be better

DRAFT FOR ADVISORY COMMITTEE - DO NOT DISTRIBUTE

than 1% to avoid any noticeable increase in emittance (if the compensation is off by 0.1% then the resulting vertical emittance blow up would be 0.1 pm per IP – the effect is quadratic);

3. Vertical emittance blow-up due to fringe fields in the vicinity of the IP should be much smaller than the nominal emittance budget and particular attention is given to the low energy run where the emittance blow-up is worse, aiming at a fraction of the nominal vertical emittance of 1 pm for two IPs (the effect is cumulative across the interaction points);
4. The final focus quadrupoles should reside in a very low field region to avoid transverse beam coupling; the maximum integrated solenoid field at the final focus quadrupoles should be less than about 50 Tm at each side of the IP.
5. Very good field quality of the final focus quadrupoles, smaller than 1×10^{-4} for all multipoles.

Requirement No. 4 necessitates the use of a set of screening solenoids. Requirement No. 3 necessitates the use of a compensating solenoid placed as close as possible to the IP. This is because it is not possible to have a very long screening solenoid which crosses the IP, due to requirement No. 1. It has been possible to fit the compensating solenoids in the region before the screening solenoids, given that the range of ± 1.23 m from the IP has some free space. Requirement No. 5 is very stringent due to the close proximity of the final focus quadrupoles to the two beams; at a distance of 2.2 m (at their tips) the distance between their magnetic centres is only 6.6 cm, so significant magnetic crosstalk will be present. Finally, requirement No. 2 is the least stringent, as it can be satisfied by tuning the overall level of compensation, so no specific design provision is needed.

The magnetic design of the IR satisfies all these requirements and it is symmetrical with respect to the mid plane of the detector, it is shown in Fig. 2.14. The first element at 1 m from the IP is the luminosity counter, followed by the compensating solenoid (from 1.23 m to 1.95 m), followed by the screening solenoid (starting at 2 m). The detector solenoid (diameter about 3.8 m) is outside this volume. The first of the final focus quadrupoles can be seen inside the compensating solenoid, starting at a distance of 2.2 m.

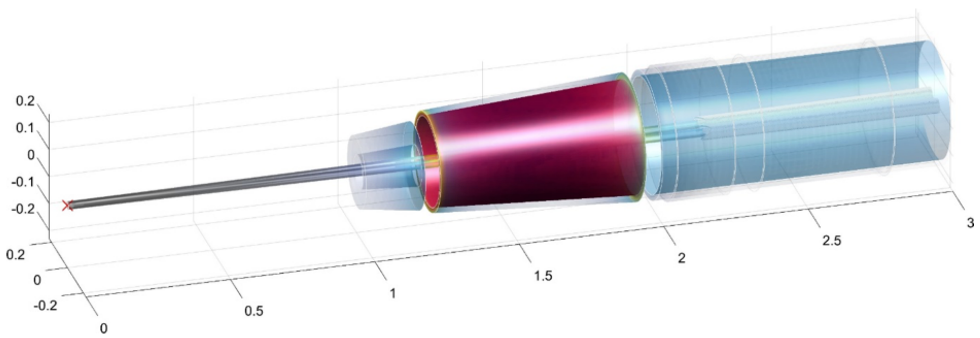

Figure 2.14: A 3D sketch of the IR magnetic system in the first 3 m from the IP (zero in the plot).

This design gives an overall emittance blow-up at Z energies of 0.4 pm for two IPs. The design fulfils requirement No. 1 in the sense that all magnet coils are at an angle of less than 100 mrad from the IP. Requirement No. 2 is met by trimming the total current of the screening and compensating solenoids until the total Bdl seen by electrons is arbitrarily close to zero. The current design has an integrated solenoid field inside the quadrupoles of less than 10 mTm and this can be improved further, if needed.

The very stringent requirements of the final focus quadrupoles are satisfied by using canted-cosine-theta technology. It is an iron-free design with crosstalk and edge effect compensation, giving a field quality of better than 0.1 units for all multipoles (requirement No. 5). Dipole and skew quadrupole correctors can be incorporated without increasing the length of the magnetic system.

A full magnetic analysis has been performed, including a misalignment analysis. The resulting field files have been processed using the full SAD optics analysis in order to have reliable emittance

DRAFT FOR ADVISORY COMMITTEE - DO NOT DISTRIBUTE

blow-up results. Also, a full engineering analysis (mechanical, thermal) has been performed and no issues which require attention were found.

JPo
Check this statement before publication

2.5.3 Luminometer

A precise measurement of the luminosity is delivered by the luminosity calorimeter inside the detector. The measurement is performed in an angular range between 65 and 85 mrad with an accepted cross section of 12 nb. This value of the cross section does not provide enough statistics for a fast luminosity measurement. Therefore Bhabha events at lower angles have to be used. The events have to pass close to the beam through the beam pipe and eventually be detected outside the experiment. The cross section in the µb range which will provide an event rate of 1 kHz at 10^{33} $\mathrm{cm}^{-2}\mathrm{s}^{-1}$ can be used. Larger cross sections are provided by single bremsstrahlung events, which are in the mb range, although they suffer from higher beam background.

2.5.4 Synchrotron Radiation

Two independent approaches have been used for the evaluation of the SR from dipoles and the final focus (FF) quadrupoles, in order to define the IR beam pipe dimensions and to place masks and shielding at the correct locations. The MDISim [138] code is used to evaluate SR from near and far bends, whilst a modified version of SYNC_BKG is used to evaluate SR from the FF quads and to design the IR masks and shielding. In this second method, macro-particles of the beam are traced through sliced magnets, MDISim combining the standard tools MAD-X, ROOT and GEANT4. See Ref. [139] for a detailed description of the two methods and studies.

The left plot of Fig. 2.15 shows a 3D MDISim display of a Gaussian positron beam at 175 GeV for five thousand particles tracked from 510 m to the IP in GEANT4 with the standard electro-magnetic processes. The plot on the right shows the resulting distribution of the photons generated.

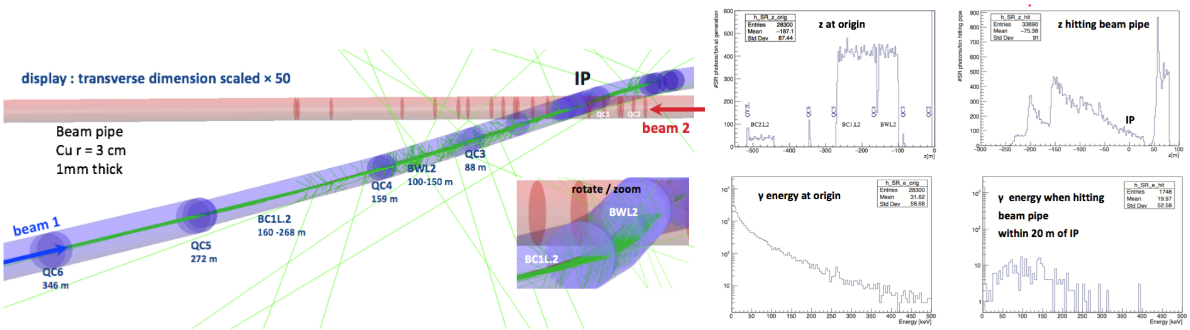

Figure 2.15: MDISim simulation. 3D display (left) ; distribution of the IR photons generated (right).

The main sources of the SR background in the IR regions are the photons from the last bending magnets and photons emitted by higher amplitude particles in the insertion quadrupoles. Several methods are employed to reduce SR backgrounds to tolerable limits. The first method, mentioned above, has been to impose a minimum distance between the bending magnets and to set the maximum critical energy of the radiation for the incoming beam. The SR radiation flux reaching the detectors can be further reduced by the combination of fixed and movable masks (collimators), as well as reducing X-ray reflections by optimising internal surfaces. Fixed mask tips are planned for 2.1 m upstream of the IP, just in front of the first final focus defocusing quadrupole, in order to intercept the radiation fan and prevent the photons from striking the central Be beam pipe directly. The next level of SR background comes from photons that strike near the tip of these masks, forward scatter through the mask and then strike the central beam pipe. At the top energy, most of these scattered photons will penetrate the Be beam pipe and then cause background in the detector. To reduce the effect on the experiment of this SR source, it is proposed to

DRAFT FOR ADVISORY COMMITTEE - DO NOT DISTRIBUTE

add a thin layer of high-Z material, for example gold, to the inside of the Be beam pipe. This is under study and it has been found that at the top energy, any reasonable thickness of gold (up to 10 μm) is not very effective due to the high energy of the scattered photons from the mask tip while at the Z energy the tip-scattered photons are so few and so soft that a gold layer is probably not needed. However, a layer of high conductivity metal will be needed (especially at the Z) in order to minimise beam pipe heating from image currents. Table 2.7 gives a partial summary of the SR study with details of the photon rate from the last soft bend upstream of the IP for all the running energies of the collider. Quadrupole radiation has not been considered in this study.

Table 2.7: Summary table of the SR coming from the last soft bend upstream of the IP. The second column refers to the number of photons incident at 500μm from mask tip and with an energy >1 keV, the third and fourth columns give the incident number of photons in the central beam pipe per beam crossing and per second, respectively. Note that this table is calculated for an older version of the beam optics with the highest energy of 175 GeV. The optics in Section 2.4 has the critical energy below 100 keV at 182.5 GeV beam energy.

E_{beam} GeV	$E_{critical}$ keV	incident γ/crossing (500μm from tip)	incoming on central pipe/crossing	γ rate on central pipe (Hz)
182.5	113.4.	3.32×10^9	1195	1.18×10^8
175	100	3.06×10^9	1040	1.25×10^8
125	36.4	1.05×10^9	10.3	1.01×10^7
80	9.56	6.11×10^8	0.18	7.02×10^5
45.6	1.77	9.62×10^7	1.92×10^{-4}	9.58×10^3

KO
This table should be updated for the newest lattice.

2.5.5 Beamstrahlung, Radiative Bhabha Scattering

Numerical simulations of particle losses in the IR due to beamstrahlung, radiative Bhabha and Touschek scattering, have been made for the different running conditions. Particle tracking has been performed with SAD [130] for these processes and Guinea-Pig++ [140] has been used as the radiative Bhabha scattering generator. Particles have been tracked over a sufficiently large number of turns to determine the IR loss maps. These particle loss distributions are then tracked into the sub-detectors with a full GEANT4 simulation. For the beamstrahlung background, the beam-beam element was inserted at both IPs and tracking for one thousand turns with the full lattice was done. The beamstrahlung lifetime was estimated from the particles lost. The result was shorter than that obtained with the analytical formula and in agreement with expectations, given the approximations in the simulation. Particle losses are mainly concentrated within 5 m around the IP in the vertical plane and the losses mainly happen in the first few turns.

Radiative Bhabha particles were generated in Guinea-Pig++, tracked in SAD for the 45.6 GeV and 175 GeV lattices. At 45.6 GeV, the radiative Bhabhas are all lost in a region up to about 70 m downstream of the first IP. At 175 GeV, the radiative Bhabhas are lost mainly in the first half of the ring and high energy particles that are eventually lost, reach the second IP. Detailed studies have been made to analyse the losses in the detector at 175 GeV and evaluate the need for collimators to intercept this background source.

Touschek scattering is also under study in order to determine loss maps and lifetime at all running energies but especially for the high intensity run at 45.6 GeV. This effect is not a major concern for beam induced background into the detectors.

DRAFT FOR ADVISORY COMMITTEE - DO NOT DISTRIBUTE

2.6 Collective Effects

2.6.1 Introduction

One of the major issues for the lepton collider is collective effects due to electromagnetic fields generated by the interaction of the beam with the vacuum chamber, which can produce instabilities, tune shifts and spread, bunch lengthening, etc., thus limiting the machine operation and performance. This chapter focuses on the impedance model and collective effects at Z running: some important sources of impedance have been included in the model to study both single bunch and multi bunch instabilities, to predict their effects on the beam dynamics and to find a possible solution for their mitigation. Another critical aspect for the future lepton collider is the electron cloud which will be discussed in the last section of this chapter, together with possible strategies to suppress its effects.

2.6.2 Impedance Budget

In this section, the contributions to the total impedance budget of some important vacuum chamber components are presented. The beam parameters used for these studies are summarised in Table 2.1.

2.6.3 Resistive Wall

Among the several sources of wakefields, a critical contribution for the lepton machine design is the resistive wall (RW) impedance. This is produced by the finite conductivity of the copper chamber and whose value is increased by coating films of non-evaporable getter (NEG) materials [141]. This coating is required to mitigate the electron cloud build up in the machine and to improve the vacuum pumping [142]. The essential properties of the NEG are a low Secondary Electron Yield (SEY), a low desorption yield and a very high pumping speed. At high current, the RW impedance is responsible for low single bunch intensity thresholds, for both the microwave instability in the longitudinal plane and the transverse mode coupling instability (TMCI) in the transverse plane. It has been observed [143] that the thickness of the coating plays a fundamental role in the beam dynamics while the conductivity of the material only plays a marginal role: the RW impedance decreases for a thinner coating and this results in higher single bunch instability thresholds, thus improving the beam stability during machine operation. In this analysis, the vacuum chamber is assumed to be circular with 35 mm radius and four layers: a first 100 nm thin NEG film with resistivity $\rho_{NEG} = 10^{-6}$ Ωm, a second 2 mm thick layer of copper, then 6 mm of dielectric and finally iron with resistivity $\rho = 10^{-7}$ Ωm. The total loss factor at nominal intensity is about 210 V/pC for a bunch length of 3.5 mm.

JGU
I wonder if this subsection should move to the Collider Technical Systems, chapter 3

2.6.4 RF Cavities and Tapers

For the Z case, the RF system consists of about 56 single cell cavities at 400 MHz (see Fig. 2.16) which will be arranged in groups of 4 cavities and connected by 14 double tapers. The number and the design of these cells have been optimised for strong HOM damping and low longitudinal loss factor [144, 145]. For a Gaussian bunch with a nominal bunch length of 3.5 mm, wakefield simulations using the ABCI code [146] estimated a loss factor of 0.3297 V/pC for each cavity. By taking into account the 2.5 m long tapers used to connect the cavities to the beam pipe, there is an additional loss factor of 0.4372 V/pC for a single double taper (in and out considered independently). In total, the loss factor for 14 4-cell cavities at 400 MHz with double tapers will be 24.58 V/pC.

JGU
I wonder if this subsection should move to the Collider Technical Systems, chapter 3

2.6.5 SR Absorbers

Synchrotron radiation (SR) is a source of heating and photoelectrons in the machine. Sufficient RF power is needed to replace the energy lost to the SR and, to cope with the extra heating and potential background, SR absorbers are required. Due to their large number, SR absorbers may be a very important source of wakefields. In order to reduce their contribution to the machine impedance budget, it was

JGU
I wonder if this subsection should move to the Collider Technical Systems, chapter 3

DRAFT FOR ADVISORY COMMITTEE - DO NOT DISTRIBUTE

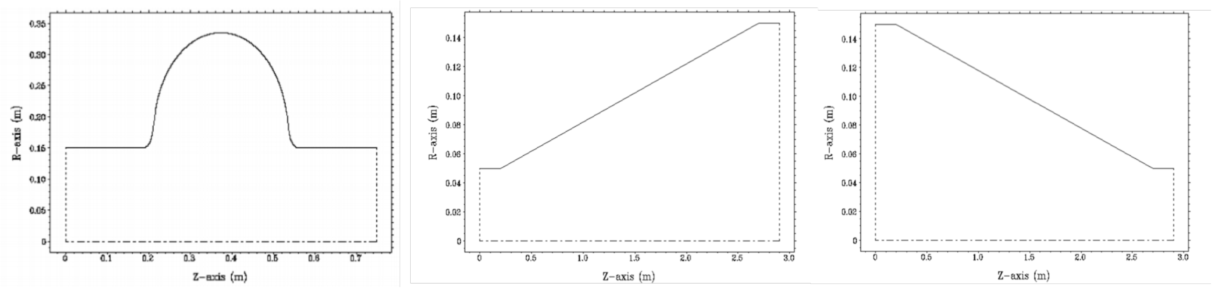

Figure 2.16: 400 MHz single cell cavity and tapers used in ABCI.

decided to use a circular vacuum chamber with 35 mm radius with a rectangular antechamber on each side, as in the SuperKEKB beam pipe [147].

Absorbers will be installed inside the chamber winglets every 4-6 meters to intercept the radiation that would otherwise strike the beam chamber. These metallic devices are shaped like a trapezoid, with a total length of 30 cm and placed at about 42.5 mm from the beam axis, as shown in Fig. 2.17. Placing slots for vacuum pumps just in front of each absorber facilitates the efficient capture of the synchrotron radiation and the molecular desorption. The pumping slots have a racetrack profile with a length of 100-120 mm and a width of 4-6 mm. A cylindrical volume and a flange will be installed to support a NEG pump behind the slots. Numerical simulations of the beam chamber profile with one absorber insertion have been performed using CST [135]. These impedance studies do not include pumping slots and pumps. Simulations show that below 3 GHz the longitudinal impedance is purely inductive, giving a longitudinal broadband impedance $\frac{Z}{n} \simeq 1$ mΩ for 10000 absorbers in the ring.

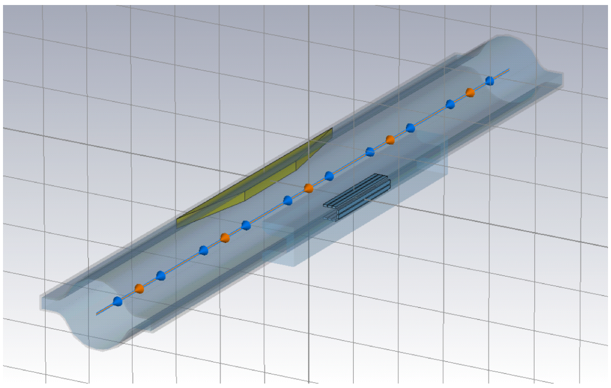

Figure 2.17: 3D model of the FCC-ee chamber and an SR absorber with pumping slots used for CST simulations.

2.6.6 Collimators

In order to suppress the background and to cut off the beam halo, 20 collimators (10 for each plane) with a design very similar to those of PEP-II [148] and SuperKEKB [149] are used in the simulations. The 3D models used for CST simulations are shown in Fig. 2.18. With the minimum apertures of 5 mm and 2 mm for horizontal and vertical collimators respectively, the total loss factor is about 38.36 V/pC for the nominal bunch length of 3.5 mm.

JGU
I wonder if this subsection should move to the Collider Technical Systems, chapter 5

KO
I think the evaluation of the impedance of collimators should be written here, but technical specs can be moved to somewhere else.

JPo

DRAFT FOR ADVISORY COMMITTEE - DO NOT DISTRIBUTE

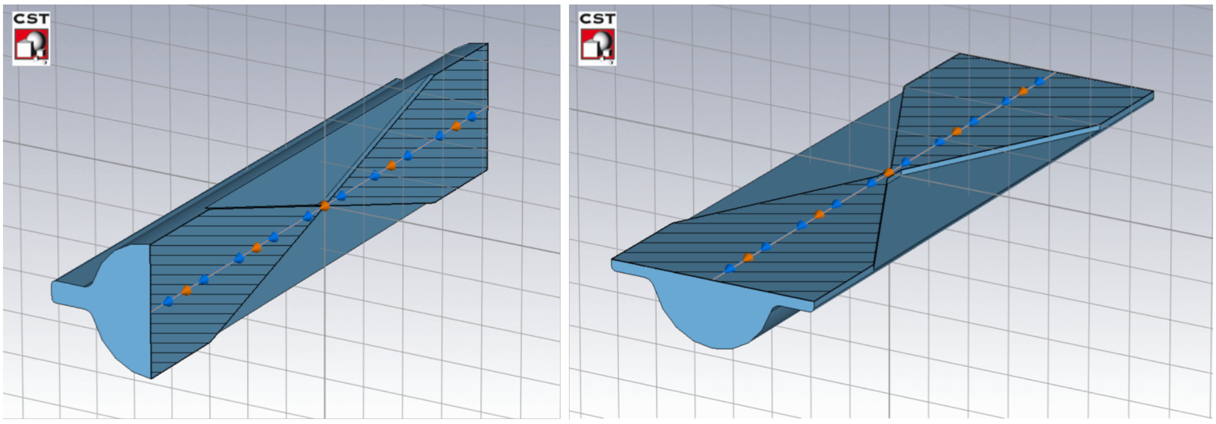

Figure 2.18: CST projection view of the vertical collimator (left) and the horizontal collimator (right).

2.6.7 Beam Position Monitors

Diagnostic elements like ∼4000 four-button Beam Position Monitors (BPMs) are planned to be installed in the machine. In order to avoid a special type of winglet-to-circular tapers, these elements will be installed directly on the beam pipe with a rotation angle of 45°. The geometry has been optimised from the impedance and heat transfer point of view [150]: the button has a diameter of 15 mm and a thickness of 3 mm. A BPM design with a conical button, similar to the one used in SIRIUS [151], is also being considered in order to push the frequencies of higher order modes trapped in the BPM structure to higher frequencies. CST simulations in the time domain have been performed and the total loss factor is about 31.47 V/pC for 4000 elements in the ring.

JGU
I wonder if this subsection should move to the Collider Technical Systems, chapter 3

KO
I think the evaluation of the impedance of BPMs should be written here, but technical specs can be moved to somewhere else.

2.6.8 RF Shielding

In addition to the previous components, 8000 bellows with RF shields will be installed before and after each BPM. Since the conventional finger-type RF shielding showed a non-negligible impedance contribution compared to the RW type [152], it was decided to use the comb-type bellows and flanges similar to those of SuperKEKB [153]. A 3D model was built using the CST code (see Fig. 2.19). In this case, the RF shielding consists of 10 mm long nested teeth, 1 mm wide, 0.5 mm radial thickness and a 2.14 mm gap between adjacent teeth, corresponding to a gap of 0.57 mm between the nested teeth. This design also includes small fingers to ensure electrical contact. The total loss factor of the bellows has been computed using CST and found to be about 49.01 V/pC for 8000 elements.

JGU
I wonder if this subsection should move to the Collider Technical Systems, chapter 3

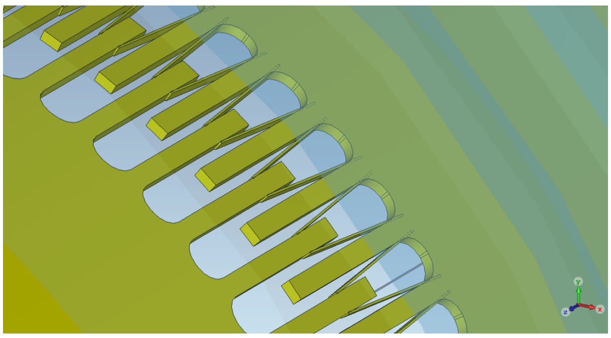

Figure 2.19: Inside view of the RF shielding with small fingers between the teeth.

DRAFT FOR ADVISORY COMMITTEE - DO NOT DISTRIBUTE

2.6.9 Overall Impedance Budget

As already mentioned, in order to evaluate the contribution of all the machine components to the longitudinal impedance budget, ABCI and CST simulations in time domain were performed for a Gaussian bunch with nominal length of σ_z=3.5 mm. Figure 2.20 shows the longitudinal wake potentials of each component. The RW wake potential has been obtained analytically as the convolution between the wake function computed by ImpedanceWake2D [154] and a 3.5 mm Gaussian bunch. There is a factor of about 9 between the RW contribution and that of the other components, showing that the RW is the main source of impedance in the machine. Table 2.8 summarises the corresponding loss factors. The total dissipated power is about 13.4 MW at the nominal intensity, about a factor 3.7 smaller than the total SR power dissipated by the beam of about 50 MW. The loss factors have been evaluated at 3.5 mm, but the bunch length at nominal current is longer due to the bunch lengthening effect, thus giving a lower dissipated power. However, other impedance sources will add their contributions.

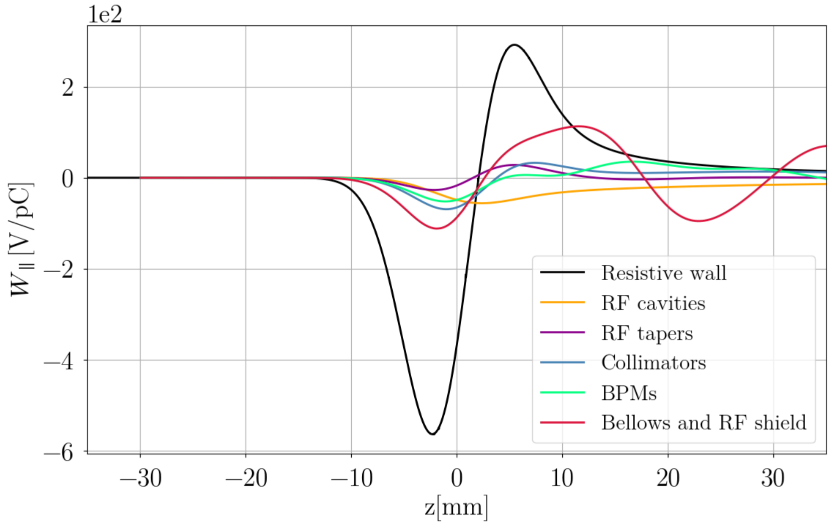

Figure 2.20: Longitudinal wake potentials for the nominal bunch length σ_z=3.5 mm due to several vacuum chamber components compared with the RW contribution (black line).

Table 2.8: Power loss contribution of the main FCC-ee components at nominal intensity and bunch length, in the lowest energy case of 45.6 GeV.

Component	**Number**	$k_l[V/pC]$	$P_l[MW]$
Resistive wall	97.75 km	210	7.95
RF cavities	56	18.46	0.7
RF double tapers	14	6.12	0.23
Collimators	20	38.36	1.45
Beam Position Monitors	4000	31.47	1.19
Bellows	8000	49.01	1.85
Total		**353.4**	**13.4**

2.6.10 Single Bunch Instabilities

The following sections focus on the most important effects of the RW on the single bunch dynamics: the Microwave Instability (MI) and the Transverse Mode Coupling Instability (TMCI) in the longitudinal and transverse planes, respectively. The beam parameters used for the simulations are listed in Table 2.1. Numerical simulations have been performed by using the macroparticle tracking code PyHEADTAIL [155].

DRAFT FOR ADVISORY COMMITTEE - DO NOT DISTRIBUTE

2.6.11 Microwave Instability

One important effect of the longitudinal wakefield on the single bunch dynamics is the increase of the bunch length with the bunch intensity, as shown on the left in Fig. 2.21. At nominal intensity, the bunch length obtained from numerical simulations is about 5.86 mm and this value is in good agreement with the analytical predictions by the Haissinski equation [156], as shown in Fig. 2.22.

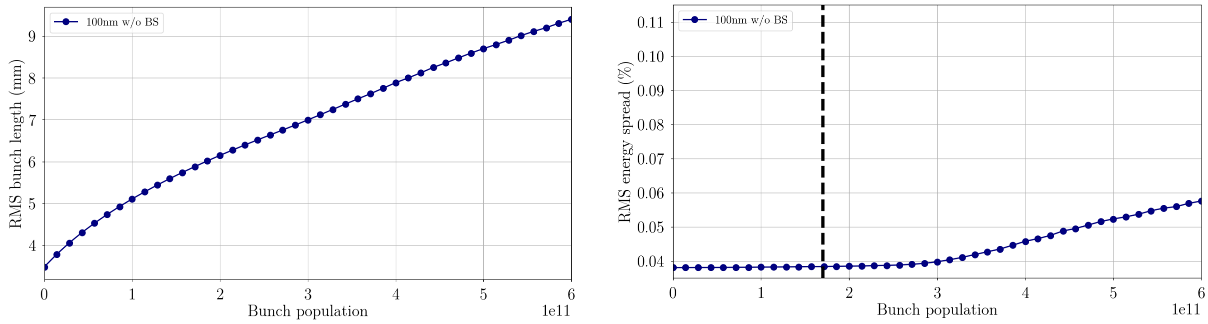

Figure 2.21: RMS bunch length (left) and RMS energy spread (right) as a function of the bunch intensity obtained from numerical simulations.

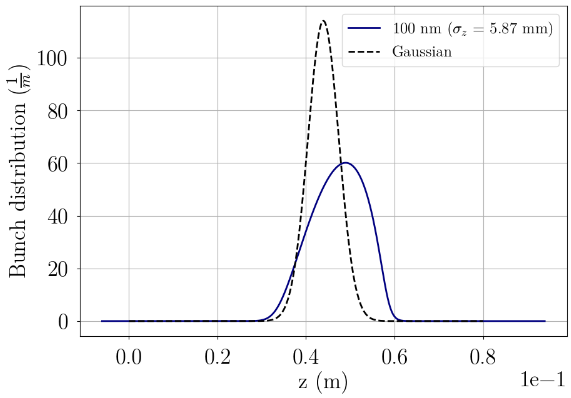

Figure 2.22: Bunch shape distortion obtained from Haissinski equation at nominal intensity. The dashed black line represents the Gaussian equilibrium shape.

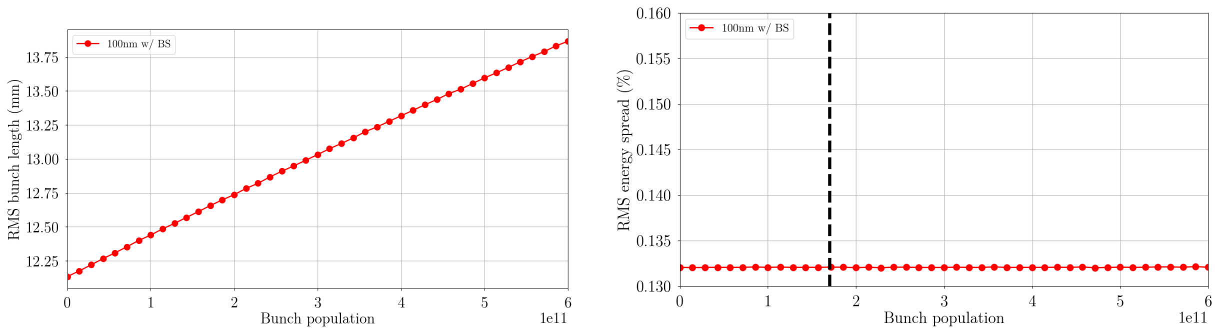

Figure 2.23: RMS bunch length (left) and RMS energy spread (right) as a function of the bunch intensity obtained from numerical simulations, with beamstrahlung.

Another important effect concerns the energy spread which starts to increase with the bunch intensity above the instability threshold. On the right of Fig. 2.21 the energy spread obtained from simulations as a function of the bunch population is shown. In the case of a 100 nm NEG coating, the MI threshold is about a factor 2 higher than the nominal bunch intensity. It is important to note that operation with

DRAFT FOR ADVISORY COMMITTEE - DO NOT DISTRIBUTE

beamstrahlung allows a much longer bunch and a higher energy spread, thus helping to increase the MI threshold and to operate in stable conditions (see Fig. 2.23).

2.6.12 Transverse Mode-coupling Instability

It is known from the theory [157] that the betatron frequencies of the intra-bunch modes shift when the bunch intensity increases and the instability occurs when the mode frequency lines merge. Unlike the longitudinal case, in the transverse case above the instability threshold, the bunch is lost and this makes the transverse mode-coupling instability (TMCI) very dangerous for the beam. Figure 2.24 shows the real part of the tune shift of the first two radial modes (with azimuthal number from -2 to 2) as a function of the bunch population, obtained with the analytical Vlasov solver DELPHI [158]. This computation takes into account the bunch lengthening due to the longitudinal wake shown in Fig. 2.21. As in the longitudinal case, the TMCI threshold is about a factor 2 higher than the nominal bunch intensity and it is increased by about a factor 3 in the case of operation with beamstrahlung.

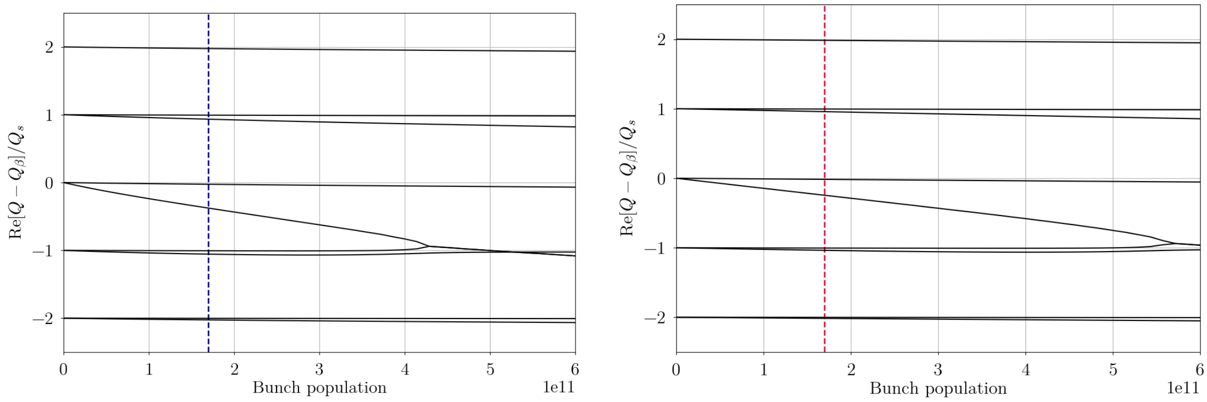

Figure 2.24: Real part of the frequency shift of the first coherent oscillation modes as a function of the bunch population without (left) and with (right) beamstrahlung.

2.6.13 Multi Bunch Instabilities

2.6.13.1 Transverse resistive wall coupled bunch instability

For the multibunch dynamics, the most critical situation is related to the transverse coupled bunch instability due to the long range RW wakefield. By considering the beam motion as sum of coherent oscillation modes, the growth rate of the lowest azimuthal mode $m = 0$ for a Gaussian bunch is given by

$$\alpha_{\mu,\perp} = -\frac{cI}{4\pi(E_0/e)Q_\perp} \sum_{q=-\infty}^{\infty} Re\left[Z_\perp\left(\omega_q\right)\right] \tag{2.9}$$

where the form factor due to the bunch shape [159] is assumed equal to 1 and

$$\omega_q = \omega_0\left(qN_b + \mu + Q_\perp\right) \tag{2.10}$$

each μ is an integer number from 0 to $N_b - 1$ representing a coupled bunch mode. The instability happens when α_μ is positive, i.e. modes will be unstable for negative frequencies. By considering the most dangerous mode, which is the one with the coherent frequency ω_q closest to zero and negative, and by using a single betatron frequency line as an approximation instead of the sum over q, for the vertical plane with a fractional part of the tune of 0.22, the growth rate given by Eq. 2.9 is about 435 s^{-1}, corresponding to about 7 turns. There are several unstable modes that need to be damped. The rise times

DRAFT FOR ADVISORY COMMITTEE - DO NOT DISTRIBUTE

of these modes are in the range of few milliseconds, corresponding to few turns in the case of FCC-ee. Therefore, robust feedback is necessary to cope with the fast instability.

2.6.14 Bunch-by-bunch Feedback Requirements

The bunch-by-bunch feedback systems will be based on the experience on lepton circular colliders in the last two decades. There has been a common approach to these systems for PEP-II, KEKB, DAΦNE, and, later, for SuperB and SuperKEKB. The teams have worked together to find the best solutions to common problems and limits. Feedback systems for circular light sources are apparently very similar, but they have to cope with different performance requirements and beam currents. From previous lepton colliders it is clear that it is necessary to damp the beam oscillations by "simply" getting the position displacement (transverse and longitudinal) for each bunch on every turn and after computing the correction signal, applying it to the selected bunch as early as possible. The systems will be designed to work in the time domain without considering in detail which modes are active in the ring. Working bunch-by-bunch leads to a basically digital design.

From the beam dynamics point of view, three possible cases can be considered:

a) slow or very slow instabilities (growth rates slower than 10 revolution turns)
b) fast instabilities (growth rates up to 3 revolution turns)
c) extremely fast instabilities (growth rates around 1-2 turns o even less).

There are some preliminary requirements to consider before looking at the various cases. First of all, it is necessary to have a very good β function at the pickups to have an adequate signal to noise ratio before processing. To have the best performance from the voltage applied to each bunch also requires a good β at the kicker. If the tune value is too small ($< .10$), the computation of the correction signal will be too slow because additional acquisitions will be necessary to fill the response filter.

In order to maintain the standard mixed analogue and digital technologies developed for feedback in the past, the only possibility is case a) which is based on the well known approach and for which many components are commercially available. Nevertheless these systems process up to a few thousand buckets. It should be noted that usually all the bucket signals are acquired and handled even if they are empty – this makes the real time computation simpler and faster. Consequently for case a) new and more powerful processing units have to be built to cope with the very high harmonic number (of the order of 100k). Another issue can rise due to the possible very low frequency of the modes that have to be damped and therefore the kickers and power amplifiers feeding the correction signal must have the appropriate bandwidth. Consequently both kickers and the power amplifiers have to be checked carefully to verify that they will work at the low frequencies. Based on experience at other colliders it is planned to have a damping rate of 10 turns for this feedback system.

A different scheme must be implemented for case b) which concerns instability growth rates of up to 3 turns. One feedback system alone is not guaranteed to have enough power to damp the oscillations. Experience of implementing two complete feedback systems in the horizontal plane at DAΦNE in 2007 is described in [160, 161]. This work demonstrates that the feedback damping rate is mainly limited by noise from the pickup entering the loop.

High beam current makes the signal to noise ratio worse, leading to feedback saturation. Moreover saturation or excess feedback gain can induce growth of the bunch dimensions. This effect is more dangerous in the vertical plane and it can also be amplified by the beam-beam interaction. Implementing four systems spaced by a quarter of a revolution can avoid the gain saturation limit. The goal of such a scheme is to achieve a feedback damping rate of the order of 10/4=2.5 turns.

Finally considering case c) which has an instability growth rate of the order of 1-2 turns or even less, a very different design scheme is necessary because the solution for case b) is not sufficient. To achieve a faster damping rate it is necessary to apply the correction signal much earlier than with the

DRAFT FOR ADVISORY COMMITTEE - DO NOT DISTRIBUTE

previous scheme (kicking in one revolution period). Again four systems are necessary but in this case the kicker has to be installed a quarter of a revolution downstream of the pickup. The correction signal has to arrive at the kicker before the bunch to be effective and this can be possible because the path along the chord (for the signal) is shorter than the path along the arc (for the beam). A speed of light signal transmission system is necessary. The new hollow optical fibre technology is the current state-of-the-art transmission solution. With this scheme, the feedback damping rate can be pushed up to 0.625 revolution turns (10/4/4=0.625). In conclusion, instability growth rates of the order of one turn require a signifcant R&D programme to implement the innovative design proposed above. Less critical instability growth rates can be handled by a more moderate R&D program.

It is worth noting that the three feedback design options each have a different impact for the impedance budget. The first option only requires one cavity kicker for the longitudinal case and two strip-line kickers for the transverse planes. Whereas both the b) and c) options need four cavity kickers and eight strip-line kickers consequently increasing the ring impedance. However all feedback (transverse and longitudinal) systems can be implemented using the design which is appropriate for the instability growth rate.

2.6.15 Interaction Region Impedance Budget

This section presents the results of studies of the impedance for the interaction region (IR) of the machine, with an evaluation of the power loss due to geometrical and resistive wall impedances and trapped modes. A sketch of the IR is shown in Fig. 2.25 [162]. Its length (from the interaction point to the first quadrupole QC1) is about 2.2 m.

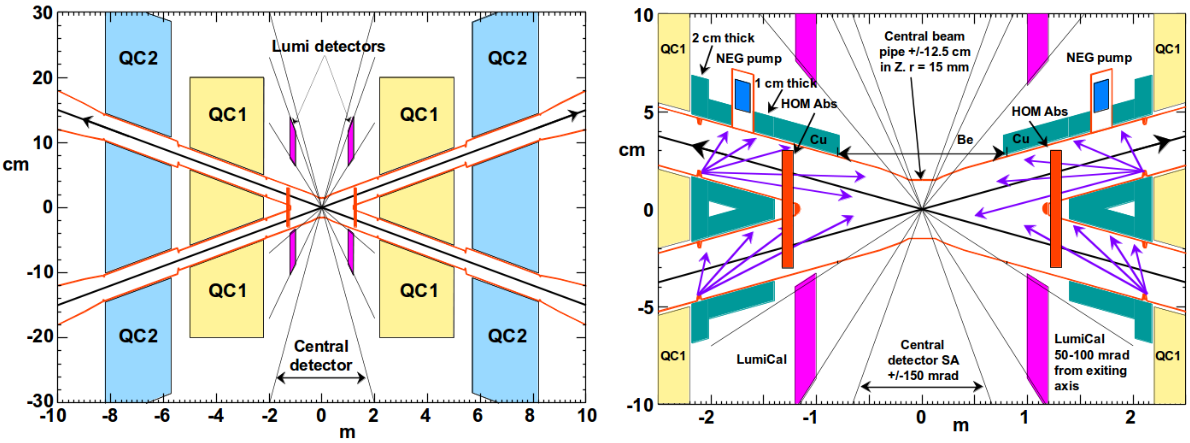

Figure 2.25: A sketch of the interaction region.

2.6.16 IP Resistive Wall

For a circular pipe with radius b, the power loss per unit length due to resistive wall is given by

$$\frac{P_{loss}}{L} = \frac{1}{T_0}\frac{N^2e^2c}{4\pi^2 b\sigma_z^{\frac{3}{2}}}\sqrt{\frac{Z_0}{2\sigma_c}}\Gamma\left(\frac{3}{4}\right)n_b \qquad (2.11)$$

where N is the bunch population, e the elementary charge, σ_z the bunch length, σ_c the conductivity of the material, Z_0 the vacuum impedance and n_b the number of bunches. Assuming a 15 mm radius pipe made of 1.2 mm thick beryllium at $\pm$80 cm and elsewhere 2 mm thick copper, the power loss in the IR due to RW is 513.5 W/m.

DRAFT FOR ADVISORY COMMITTEE - DO NOT DISTRIBUTE

2.6.17 Synchrotron Radiation Masks

In the IR, synchrotron radiation (SR) masks are placed before and after each quadrupole, in order to protect the vacuum chamber from photons generated by the last magnet located 100 m from IP. These masks are 2 cm long with a 1 cm long ramp back to the larger radius at each end and produce a variation of 2 mm in the pipe radius (from 15 mm to 13 mm in QC1 and from 20 mm to 18 mm in QC2). Geometric impedances and wake potentials computed with the ABCI code indicate a power loss of about 3.8 W per bunch. [REFERENCE]

2.6.18 Trapped Modes

Another important source of heating in the IR is from High Order Modes (HOMs) that can remain trapped in the IR because of small variations in the beam pipe geometry which unintentionally generate cavities. In order to reduce the HOMs' effects, the geometry of the IR beam pipe was optimised from the impedance point of view. Various models have been considered [137] and a smooth geometry was designed, with a relatively small impedance from HOMs and only one trapped mode. Wakefield and eigenmode calculations have been carried out by using the CST and HFSS [136] codes, respectively, revealing the presence of the mode at 3.5 GHz with an impedance much lower than that from the other models. In order to mitigate its effects, longitudinal slots oriented perpendicular to the HOM electric field lines are placed in the top and bottom walls of the beam pipe, so that the mode field can escape through them and be absorbed by a water-cooled absorber installed above and below the slots. In the case of a bunch length of 2.5 mm and a beam current of 1.45 A, the electromagnetic power due to the trapped mode and all the other propagating modes was found to be approximately 5 kW at each end of the central pipe connection. This power will be mainly absorbed in the HOM absorbers, which require further optimisation.

2.6.19 Electron Cloud

Electron cloud (EC) effects are one of the main performance limitations for both hadron and lepton machines [163, 164]. In the case of the FCC-ee, the positron beam can produce primary electrons by ionisation of the residual gas in the vacuum chamber or by photoemission due to SR. These primaries are attracted and accelerated by the positron beam and the electron accumulation in the vacuum chamber can cause the heating of the pipe walls and instabilities, beam losses, emittance growth and vacuum and diagnostic degradation.

2.6.20 Electron Density Threshold for the Single Bunch Head-Tail Instability

Electron cloud single bunch head tail instability has been analysed and observed in several machines [165, 166]. This instability depends on the electron density near the beam and the threshold is given by

$$\rho_{th} = \frac{2\gamma Q_s}{\sqrt{3} Q r_e \beta C} \tag{2.12}$$

with r_e the classical electron radius, C the machine circumference, Q_s the synchrotron tune, $\beta_{x,y} = \frac{C}{2Q_{x,y}}$ the average beta of the machine and $Q = min\left(\frac{\omega_e \sigma_z}{c}, 7\right)$ with ω_e the frequency of the electron oscillation near the beam centre [167]. Table 2.9 summarises the electron density thresholds at four energies, using the baseline beam parameters shown in Table 2.1.

In the FCC-ee, the number of photons emitted per positron per meter is equal to 0.085/p.m at 45.6 GeV, with a critical energy $E_c \simeq$ 19 keV, and 0.329/p.m at 175 GeV, with $E_c \simeq$ 1 MeV. Numerical simulations show that about 95% of these photons are absorbed by the SR absorbers installed in the rectangular antechambers. Therefore, by assuming a photoelectron yield $Y = 0.02$ the number of photoelectrons per meter produced by the passage of a bunch is $10^7(Z)$ - 10^8 $(t\bar{t})$. Given the cham-

DRAFT FOR ADVISORY COMMITTEE - DO NOT DISTRIBUTE

Table 2.9: Electron density threshold for the fast head-tail instability at four energies.

Energy [GeV]	**45.6**	**80**	**120**	**175**
Electron frequency $\frac{\omega_e}{2\pi}$ [GHz]	393.25	395.23	392	385.93
Electron oscillation $\frac{\omega_e \sigma_z}{c}$	28.84	24.85	25.88	22.24
Electron density threshold $\rho_{th}[10^{10}/\mathrm{m}^3]$	**2.31**	**11.92**	**12.6**	**30.8**

ber cross-section, this translates into a photoelectron density from a single bunch of about $10^9/\mathrm{m}^3(Z)$ - $10^{10}/\mathrm{m}^3$ ($t\bar{t}$) which is comparable with the instability threshold. However, further investigations with numerical simulations are needed. As mentioned in the previous section, in order to mitigate the electron cloud build up in the positron ring, the vacuum chamber will be coated with a thin film of NEG materials, which have a low SEY. Another possibility to reduce the build up in the machine is to introduce gaps in the bunch train in compliance with the RF requirements.

2.7 Energy Calibration and Polarisation

Beam polarisation is an important parameter for operation at the Z and W, in view of the beam energy calibration. This task, leading to precision measurements ($<$100 keV) of the Z mass and width and of the W mass and width ($<$500 keV) has been assigned highest priority by the physics group. These challenging goals can be achieved but require a few hardware elements and careful control and monitoring of the operating conditions.

The running mode is proposed as follows. Resonant depolarisation (RDP) of a transversely polarised beam provides an exceptionally accurate measurement of the beam energy, to the level of 0.1 MeV or better. Such an improvement of the accuracy requires continuous monitoring of the beam energy during luminosity data taking, with for example O(200) non-colliding 'pilot' bunches per beam, to be injected at the beginning of each fill and polarised using wigglers, before the rings are filled for luminosity running. This will allow tracking of the effects of the ground motion (tides, Geneva lake level, and other geological variations): given the very small momentum compaction factor (at the level of a few 10^{-5}), the range of energy variations, both daily and seasonally, is expected to be larger than 100 MeV. These will have to be compensated continuously by corresponding changes of the RF frequency.

The depolarisation kicker(s) must be able to impose a spin rotation of up to 3×10^{-4} radian per passage of the particles. This corresponds to a maximum kick of 3×10^{-3} Tm which has to be applied during a pulse of a few nanoseconds so as to act on a single bunch without influencing the others. An electrostatic RF kicker similar to that of the TBI feedback kicker of the LHC would seem adequate. The exact disposition of the system of kickers is under study.

Polarimeters are needed to monitor the polarisation level continuously with a precision of 1% every few seconds; they will also provide independent and continuous beam energy monitoring at a level of 10^{-5}. Since the two beams are in different magnetic channels, sizeable differences in beam energy between positron and electrons are expected, requiring a polarimeter and a depolariser for each beam. Independent monitoring of the beam energy will be most useful. First concepts based on Compton scattering have been proposed. The Compton polarimeter can be implemented in the last dipole of the dispersion suppressor in the short straight sections H and F with a laser, of alternate circular polarisation, hitting the inside incoming beam upstream of the dipole and segmented electromagnetic calorimeters observing both the recoil electrons (or positrons) and the photons to observe the shifts in position and intensity upon laser polarisation reversal.

Wigglers will be needed for polarised beam operation at the Z pole. Electron (and positron) beams polarise spontaneously in storage rings due to the emission of synchrotron radiation up to an equilibrium

DRAFT FOR ADVISORY COMMITTEE - DO NOT DISTRIBUTE

level of 92.4%. The build-up time of polarisation P τ_P scales like

$$\tau_P \propto \frac{\rho^3}{E^5}$$

where ρ is the beam radius. Compared to LEP1, the polarisation time is increased by a factor $\sim$43 to around 250 hours which is excessively long. The rise time may be lowered to $\sim$12 hours using wigglers. Such a rise time would allow a 10% (5%) beam polarisation to be obtained in 90 (45) minutes, which would be sufficient for the energy calibration by RDP. The use of wigglers is also limited by the induced energy spread. A possible set of wigglers has been specified as 8 units per beam with a maximum field of 0.7 T for the strong pole (B^+), a length of the strong pole of L^+ 0.43 m and ratios $L^-/L^+ = B^+/B^+ = 6$, where the $-$ sign refers to the weak pole. For these wiggler parameters, a polarisation of 10% can be obtained in 1.8 hours.

The LEP observations indicate that the maximum tolerable energy spread is around 60 MeV (compared to the 440 MeV spacing of the integer spin resonances). For such a limit, spontaneous polarisation with a rise-time of around 10 hours should be observable without wigglers at the W operation point and this has been confirmed by spin simulations. At LEP, the larger energy spread prevented the build-up of polarisation at the W threshold.

The interpolation of the average beam energy as determined by RDP to the IPs requires an understanding of all sources of energy loss and energy gains: RF cavity voltages and phases, energy loss by synchrotron radiation and beamstrahlung or impedances. The effect of RF voltage and phase uncertainties is eliminated if the RF of each beam is concentrated in one straight section, for example the electron RF in straight section D and the positron RF in straight section J. In such a configuration the energy gain by the RF is simply determined by the total energy loss, uncertainties due to the distribution of RF gains across the ring are eliminated. The energy offset at any of the IPs only depends on the energy loss between the RF system and the IP. The energy loss in the arcs at 45 GeV, of 9 MeV per quadrant, is expected to be known to better than one part per mil (9 keV) and will not introduce a significant uncertainty.

If the RF of each beam is distributed over two straight sections, then voltage and phase errors lead to energy shifts at the IPs, anti-correlated between the two experiments. This correlation may be used to control systematic uncertainties in case such a solution has to be adopted. The average energy loss by beamstrahlung is of the order of 300 keV (at the Z) and could potentially induce a difference between the pilot and the colliding bunches.

The beam energy spread must be determined with a relative precision of better than 0.2%. This can be done every few minutes by the experiments themselves by looking at the collinearity of the muon pairs. Independent monitoring of the related beam length should be implemented with e.g. a streak camera.

Opposite sign dispersion at the IPs must be monitored and its effect on the average centre of mass energy should be eliminated as much as possible by regular luminosity optimisation to maintain the beams head-on. This has to be done with a precision for the impact parameter between the beams of 1% of the beam sizes at the IP.

Longitudinal polarisation in collisions is not part of the FCC-ee baseline. It can be used for precise left-right asymmetry measurements at the Z pole and for polarisation asymmetries at the other energies. However, the high luminosity allows the same information to be gained by other means. Such an option would become interesting for polarisation levels of 30% or more. Given the topping up of the rings with unpolarised beams, this would lead to a considerable loss in luminosity. Spin rotators would have to be installed around each IP where data taking with longitudinal polarisation is expected. Reaching a high level of polarisation and at the same time having a reasonable polarisation time requires cancellation of depolarising effects at a level of perfection much better than achieved in LEP. Various ideas have been investigated, such as Siberian snakes in the storage ring itself, or injection of a polarised beam from the

DRAFT FOR ADVISORY COMMITTEE - DO NOT DISTRIBUTE

JPo: Is there a conclusion and reference for theses investigations?

booster or from a dedicated polarising damping ring along with Siberian snakes.

2.8 Injection and Extraction

2.8.1 Top-up Injection

Beam particles in the collider rings are continuously lost due to radiative Bhabha scattering in the collisions, resulting in a rather short beam lifetime. There is a technique called *Top-up injection*, which is widely employed in lepton colliders and light sources. It keeps the beam current essentially constant by injecting electrons/positrons on top of a circulating beam to compensate for the beam current loss. It may be necessary to mask the physics data acquisition during the injection period [**?**]. However, the masking period can be short and thus the luminosity production efficiency is maximised with the constant, maximum beam currents. In addition, the stability of the machine is maximised: the constant beam current generates a constant heat load from synchrotron radiation on the accelerator components. Therefore, it is crucial to incorporate the top-up injection in the collider design.

The following conditions are taken into account in the design. Firstly, a straight section of about 1.6 km is available, which is sufficiently long. Secondly, the beam clearance, i.e., the distance between the circulating (injection) beam orbit and the septum blade must be larger than or equal to 5σin units of the circulating (injection) beam size. The injection system of SuperKEKB, for example, is designed with 3$\sigma$and 2.5σclearances for the circulating and injection beams, respectively [**?**]. The rather large clearances in the FCC design have been chosen to ensure robust injection with low losses. Thirdly, it is assumed that the transverse emittance of the injection beam is equal to that of the collider ring. The injector chain can provide beams with transverse emittance smaller than or equal to that of the collider ring. The design, therefore, includes additional margins to benefit from this situation.

The conventional injection scheme widely used in electron storage rings is applicable to FCC-ee. A septum and a dynamic orbit bump are used in this scheme. The injected beam which is initially separated by the septum blade merges into the circulating beam thanks to synchrotron radiation damping.

It is noted that the dynamic aperture of the collider ring is rather limited due to strong chromaticity correction sextupoles. In order to facilitate top-up injection, the beta function at the septum is enlarged, which has the effect of reducing the septum blade thickness in units of beam sigma.

Figure 2.26 shows a possible layout of the injection straight section together with the optical functions and beam orbits. The beta function at the septum is increased to 2000 m, which sets the dynamic aperture requirement to 13.6σ and 16.0σ for $t\bar{t}$ and Z operation modes respectively, assuming a septum with 3.5 mm-thick blade. The injection beam needs to be properly matched [**?**].

In the above layout, the required kicker deflection angle is 20.6 μrad and 11.5 μrad for $t\bar{t}$ and Z, respectively, which corresponds to 0.012/0.0017 Tm. These integrated fields can easily be achieved with ferrite kickers as are commonly used. A modest septum deflection angle of about 5 mrad (3.0/0.8 Tm) is sufficient to separate the injection beam line and the collider orbit.

One of the important issues in top-up injection is disturbance of the stored beam, arising from non-closure of the orbit bump. Additional kickers have to be installed and fine-tuned to accomplish satisfactory bump closure.

There will always be differences in the bunch charges of the circulating beam since the top-up injection is performed at the repetition rate of the booster. Beam-beam simulations (see Section 2.2.2) show that the tolerance for the charge difference should be set at ±5%. A feedback system for the filling pattern has to be implemented to keep the bunch charges in the injector chain as constant as possible.

Finally, a few alternative injection schemes have been studied and they have proved to be viable (see [119]).

KO: Added one paragraph and a figure, 28/4/2018.

DRAFT FOR ADVISORY COMMITTEE - DO NOT DISTRIBUTE

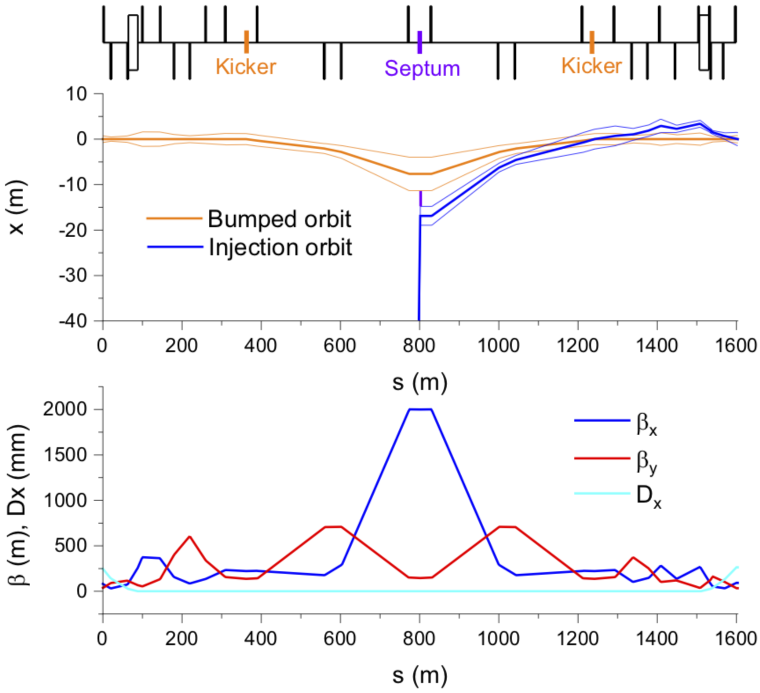

Figure 2.26: Injection straight section layout (top), the optical functions (middle) and the beam orbits (bottom) together with 5σ envelopes are shown.

2.8.2 Extraction and Beam Dump

The extraction system is designed to remove the electron and positron beams from the main ring and transport them to the external beam dump. The extraction kickers and Lambertson septum deflect the beam downwards by 12 mrad. In order not to melt the dump absorber material, the beam is spread over the front surface of the dump in a spiral pattern by means of horizontal and vertical dilution kicker magnets. Graphite has been chosen as the main material for the beam dump because of its high melting temperature. A cylinder with 40 cm radius and a length of 500 cm was chosen as shape of the absorber. With 57 turns of the spiral, which keeps the dilution sweep frequency below 200 kHz, the maximum energy deposition density in the graphite from the beam of electrons is found to be 130 J/cm^3, which is equivalent to 76 J/g. The peak temperature rise in the graphite due to the impact of an electron beam is $\sim$ 100 $^\circ$C. The energy density deposited in the graphite in the horizontal-longitudinal (x-z) plane is shown in Fig. 2.27.

2.9 Operation and Performance

The 14 year life-cycle of the collider, will comprise five operation phases that are separated by RF system re-configuration periods. Each operation phase is dedicated to one energy working point.

The physics goals require the following integrated luminosities, summed over two interaction points (IPs): 150 ab^{-1} at and around the Z pole (88, 91, 94 GeV centre-of-mass energy); 10 ab^{-1} at the WW threshold ($\sim$ 161 GeV with a $\pm$few GeV scan); 5 ab^{-1} at the HZ maximum ($\sim$ 240 GeV); 1.5 ab^{-1} at and above the $t\bar{t}$ threshold (a few 100 fb^{-1} with a scan from 340 to 350 GeV, and the rest at 365–370 GeV [168, 169].

To estimate the time required for accumulating these target values, and to develop a time line for operation the following assumptions have been made. 200 days per year scheduled for physics, which corresponds to roughly 7 months of regular operation minus 13 days for machine development and technical stops. Profiting from the top-up-injection constant-current mode of operation, a "Hübner factor" of 0.75 is applied. This empirical factor relates the product of the peak (or average luminosity)

DRAFT FOR ADVISORY COMMITTEE - DO NOT DISTRIBUTE

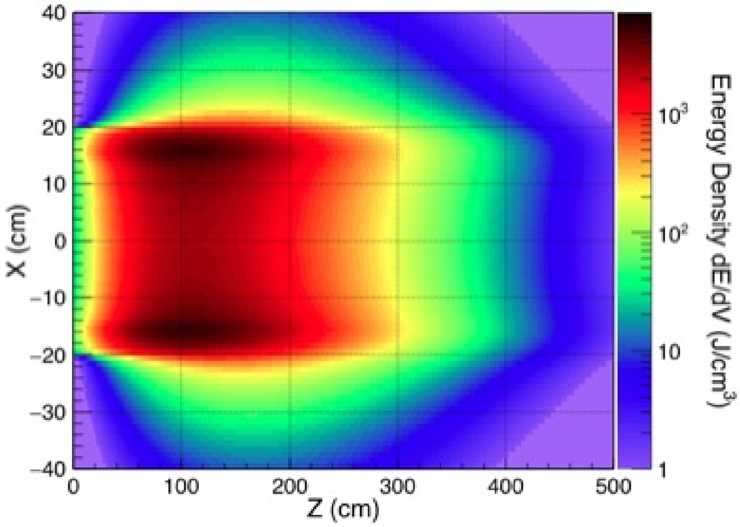

Figure 2.27: The energy deposition on the beam dump for FCC-ee.

and the scheduled time for physics collisions with the luminosity actually integrated. In the case of FCC-ee no time is lost for acceleration, and the Hübner factor reflects the relative downtime due to technical problems and associated re-filling time. The assumed value of 0.75 is lower than the value ~ 0.8 achieved with top-up injection at KEKB.

The machine operation is expected to start with Z running, similar to LEP-1, as this requires the lowest RF voltage, implying the smallest amount of RF installation and the associated minimum impedance. Based on the LEP-1 experience, it is pessimistically supposed that, on average, only half the design peak luminosity is obtained in the first two years of Z operation.

The upgrades from the Z machine to the W and H machines requires installing no more than 65 cryomodules per winter shutdown, which remains comparable to winter activities at LEP, or, more precisely, which is no more than two times the number of cryomodules installed during a winter shutdown at LEP. Therefore, the machine configuration between the Z, W and H running, can be re-adjusted during the regular winter shutdowns. These winter shutdowns offer an effective time window of about 3 months per year for scheduled work in the tunnel. However, longer periods are needed between Higgs and top operation to allow for, in particular, the transverse rearrangement of all ($\sim$100) cryomodules and the installation of about 100 new RF cryomodules in the collider and another $\sim$ 100 cryomodules for the booster. The number of cryomodules to be installed or rearranged in this transition significantly exceeds the amount of work done in a typical LEP winter shutdown. For this reason, a one year shutdown is proposed for this final reconfiguration, so that there is a distinction between a phase 1 operation (Z, W, and H), and a phase 2 operation ($t\bar{t}$).

Conservatively, it is assumed that there will be another year at half the design luminosity after this one-year shutdown, for the first year of top running. This first year of the phase-2 operation is performed at a beam energy of 175 GeV, requiring somewhat fewer RF cavities than 182.5 GeV. It is noted that LEP-2 needed much less than one year to reach and exceed its design luminosity.

2.9.1 Possible Running Schedule

Table 2.10 presents the peak luminosity, integrated luminosity per year, physics goals and the resulting running time for the different modes of operation, based on the assumptions laid out above. This yields the time line shown in Fig. 2.28.

Phase 1 comprises two years of running-in, and the full Z pole operation, W threshold scans, and Higgs production modes. It can be accomplished within 8 years. After one additional year of shutdown

DRAFT FOR ADVISORY COMMITTEE - DO NOT DISTRIBUTE

and upgrades, operation phase 2, covering the top quark studies, would last for another 5 years. The entire FCC-ee physics programme could be achieved within 14 years.

After phase 1 there could be a natural breaking point, where one might decide, e.g., not to upgrade towards phase 2, but instead to install the next hadron collider.

Table 2.10: Peak luminosity per IP, total luminosity per year (two IPs), luminosity target, and run time for each FCC-ee working point.

working point	luminosity $[10^{34}\ \mathrm{cm}^{-2}\mathrm{s}^{-1}]$	tot. lum./year $[\mathrm{ab}^{-1}]$ / year	goal $[\mathrm{ab}^{-1}]$	run time [years]
Z first two years	100	26	150	4
Z other years	200	52		
W	32	8.3	10	~ 1
H	7.0	1.8	5	3
RF reconfiguration				1
$t\bar{t}$ 350 GeV (first year)	0.8	0.20	0.2	1
$t\bar{t}$ 365 GeV	1.5	0.38	1.5	4

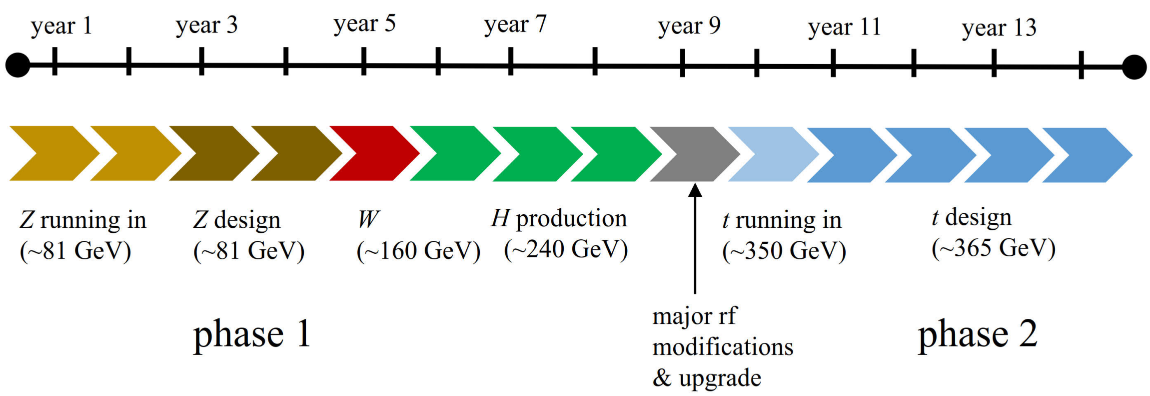

Figure 2.28: FCC-ee operation time line. The energy values shown in parentheses refer to the centre-of-mass collision energy.

2.9.2 Machine Protection

JGU
I moved this to chapter 3!

2.10 Monochromatisation

Direct s-channel Higgs production in e^+e^- collisions, with a collision energy around 125 GeV, allows the measurement of the Hee Yukawa coupling, provided that the centre-of-mass energy spread can be reduced to about 5–10 MeV to be comparable to the width of the standard model Higgs boson, without too much reduction in luminosity. The natural collision-energy spread at 125 GeV due to synchrotron radiation is about 50 MeV.

The decrease of the collision energy spread to the desired level can be accomplished by means of monochromatisation [170]. The monochromatisation is most efficiently achieved by introducing non-zero horizontal dispersion of opposite sign at the interaction point for the two colliding beams in colli-

DRAFT FOR ADVISORY COMMITTEE - DO NOT DISTRIBUTE

sions without a crossing angle. This requires either a change of beam-line geometry in the interaction region or the use of crab cavities to compensate for the existing angle. The monochromatisation magnitude is defined as the parameter λ:

$$\lambda = \sqrt{\frac{D_x^{*2}\sigma_\delta^2}{\varepsilon_x \beta_x^*} + 1}\ , \tag{2.13}$$

where β_x^* denotes the horizontal beta function at the IP. A value of λ equal to 10 would correspond to the desired collision energy spread around 5 MeV.

Monochromatisation at 125 GeV c.m. energy could result in a useful Higgs event rate and at the same time provide the energy precision required to measure the width of the Higgs resonance [171].

In the other operation modes, beamstrahlung primarily affects the energy spread and bunch length. In the case of monochromatisation, it is the horizontal emittance which blows up due to beamstrahlung. This is a new effect, not present in past monochromatisation proposals. The horizontal emittance increase may degrade the luminosity performance, but it also weakens the beamstrahlung.

For the FCC-ee, the impact of the monochromatisation on the luminosity and energy spread including the effect of beamstrahlung in the longitudinal and horizontal plane needs to be analysed. Numerical studies were performed along these lines to optimise the interaction-point beam parameters at 62.5 GeV beam energy, in particular the values of β_x^*, D_x^* and the number of particles per bunch. The maximum achievable luminosity for a given value of λ. is displayed in Fig. 2.29. The target value of the collision energy spread, σ_W, of about 5.6 MeV, is obtained with an optimised horizontal IP dispersion of 30.8 cm, along with $\beta_x^* = 1.96$ m, $\beta_y^* = 1$ mm, $N_b = 3.7 \times 10^{10}$, $n_b = 23184$ bunches per beam, $\epsilon_x \approx 200$ pm, $\epsilon_y \approx 1$ pm. The corresponding luminosity per interaction point (IP) is about 1.3×10^{35} cm^{-2}s^{-1} [172].

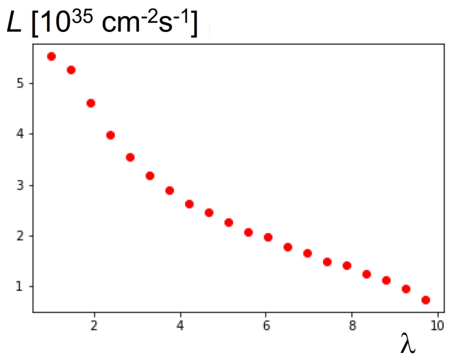

Figure 2.29: Optimum luminosity at 125 GeV as a function of the monochromatisation parameter λ.

This translates into an integrated luminosity of almost 2 ab^{-1} per IP per year. For a c.m. energy spread around 5 MeV, commensurate with the natural width of the Higgs boson, the cross section of $e^+e^- \rightarrow H$ is about 290 ab [173]. Assuming this value, the monochromatised FCC-ee would produce approximately 500 s-channel Higgs bosons per IP per year.

2.11 Running at Other Energies

The FCC-ee can produce further important physics results by running at additional centre-of-mass energies. Worth mentioning are operating points in the vicinity of the Z pole and a push for highest energy.

Of considerable interest is the operation just above or below the Z resonance peak, allowing a high-precision measurement of the electromagnetic coupling constant α_{QED}, based on the muon forward-backward asymmetry $A_{\text{FB}}^{\mu\mu}$ [174]. This method does not rely on the experimental determination of the vacuum polarisation and provides a direct evaluation of α_{QED} at $\sqrt{s} \sim m_Z$. The present uncertainty in $\alpha_{\text{QED}}(m_Z^2)$ of order 10^{-4} will limit the potential for new physics explorations at the FCC-ee. The goal

DRAFT FOR ADVISORY COMMITTEE - DO NOT DISTRIBUTE

of an α_{QED} run would be to reduce this uncertainty by at least a factor 5 to $2{\times}10^{-5}$. It is expected that achieving this would require one year of dedicated operation.

Similar to LEP-2, the energy could be pushed to the maximum by installing more RF systems and increasing the RF voltage. For $t\bar{t}$ running at a c.m. energy of 365 GeV the RF system (common for both beams) occupies a total length of about 2 km and provides a voltage of ∼10 GV. Filling the two straight sections D and J, which have a combined length of 5.6 km, completely with RF cavity cryo-modules, the total RF voltage could be increased to around 30 GV. This voltage would support collision energies up to 475 GeV or beyond. At constant RF power the beam current would drop to about 2 mA at 475 GeV. Taking into account the increase of the transverse emittance with beam energy, the luminosity per IP is estimated at about 5×10^{33} cm^{-2}s^{-1} for a collision energy of 475 GeV. Even 500 GeV may be within reach with similar performance, especially if higher-gradient 800 MHz RF cavities can be deployed. Further investigation of beamstrahlung effects at highest beam energies is required because they may introduce additional constraints.

DRAFT FOR ADVISORY COMMITTEE - DO NOT DISTRIBUTE

Chapter 3

Collider Technical Systems

3.1 Requirements and Design Considerations

3.2 Main Magnet System

Attilio Milanese: Attilio Milanese, 5 pages

3.2.1 Introduction

The requirements for the main magnets are quite similar to those of LEP: the arcs contain many long, low field, bending magnets interleaved with short straight sections, with quadrupoles and auxiliary magnets. As such, there are many features of the resistive magnet system used in LEP and in other large lepton machines (HERA electron ring and SLC) which can be retained, for example, modular cores with aluminium busbars threaded through them. However, it is possible to exploit the dual aperture system, with dedicated magnets based on a twin aperture layout. Combining the rings not only halves the total quantity of main magnets, but by exploiting magnetic coupling, it also allows a 50% power saving from not having two separate sets of magnets.

Short prototypes have been built of both the main dipoles and the quadrupoles, in order to confirm the magnetic coupling. Optimisation and an analysis of various industrial manufacturing procedures will be done at a later stage.

Other magnets, such as correctors, sextupoles, polarisation wigglers or those for the top up injector, are beyond the scope of this report. A scheme for trimming the excitation of the main bending magnets is an interesting option to replace some horizontal correctors. The design of a combined quadrupole-sextupole has started, along the lines of the more common combined dipole-quadrupole magnet. For the moment this is left as an additional conceptual development, pending further discussions with beam physicists. More details about concepts for the main magnet system can be found in [175, 176].

3.2.2 Main Dipole Magnets

Table 3.1 summarizes the key requirements of the bending magnets, together with the main parameters as illustrated on the cross-section shown in Fig. 3.1.

The design of the magnetic yoke is based on an I configuration, combining two back-to-back C layouts. In this way, the return conductor for one aperture provides the excitation current for the other gap.

As in previous large lepton machines, aluminium busbars were used instead of coils. These busbars are generously sized ($46\times$ 80 mm) to keep the current density low with a maximum value of 1 A/mm^2,

Table 3.1: Main requirements and parameters of the main bending magnets

Strength, 45.6 GeV to 175 GeV	mT	14.1 to 54.3
Magnetic length	m	21.94 / 23.94
Number of units per ring		2900
Aperture (horizontal × vertical)	mm	130× 84
Good field region (horizontal)	mm	±10
Field quality in GFR (not counting quad. term)	10^{-4}	≈1
Central field	mT	54
Expected b_2 at 10 mm	10^{-4}	≈3
Expected higher order harmonics at 10 mm	10^{-4}	<1
Current	kA	3.65
Current density	A/mm^2	1.0
Resistance per unit length (total two apertures)	μΩ/m	14.4
Power per unit length (total two apertures)	W/m	192
Total power, 81.0 km (connections included)	MW	15.5
Inter-beam distance	mm	300
Iron mass per unit length	kg/m	219
Aluminium mass per unit length	kg/m	19.9

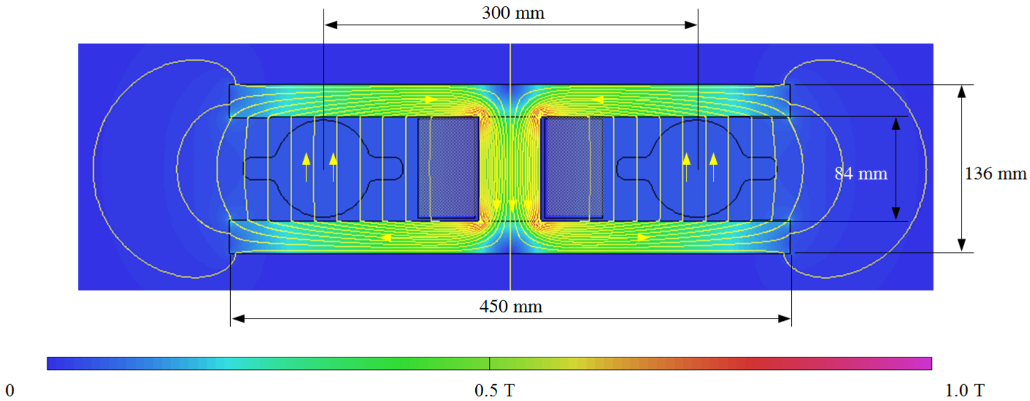

Figure 3.1: Cross-section of the main bending magnet; the flux density corresponds to 54 mT in the gap; the outer outline of vacuum chambers with side winglets is also shown.

even at the highest beam energy. These busbars can be threaded through several cores and welded to each other, as in LEP. Direct cooling with water is not necessary, but it might be useful to avoid adding Joule heating (up to about 200 W/m) to the tunnel air.

As magnetic lengths of up to about 24 m are needed, a modular structure for the bending magnets with 6-8 m long cores is proposed. The final length will be optimised on the basis of manufacturing and handling considerations. The elastic deflection due to their weight is not critical, as it can be compensated, if needed, by adding a pre-camber in the opposite direction during manufacture, as was done for the SPS dipoles.

Besides the I layout, the geometry of the yoke has an elongated aspect ratio of the poles: this keeps the cross-section compact and at the same time it takes the low field in the air gap and amplifies it in the iron. Therefore, a dilution in the longitudinal direction (for example with concrete, as in LEP) is not necessary in this case, as it would bring more complications than savings in materials.

Another key feature which makes a compact yoke possible is the small size of the good field region: in this case, the size of the vacuum chamber is not dictated by the size of the beam (which is consistent with the good field region) but by other considerations, such as impedance and absorption of

DRAFT FOR ADVISORY COMMITTEE - DO NOT DISTRIBUTE

synchrotron radiation. Furthermore, it has been agreed with the accelerator physicists that the quadrupole term b_2 can be disregarded in the expansion for field quality, as a systematic linear component can be compensated in the arc quadrupoles. A strong b_2 term at low (few tens of mT) dipole fields was considered an issue for LEP. This comes from two main effects: a change in relative permeability of the iron between the inside and outside at different excitation currents, and the remanent field coming from the coercivity. As the FCC-ee will be operated at constant current with a top up injector, the second effect can be disregarded: even if the machine were to operate at low energy after a high energy run, there will be time for full degaussing or preconditioning. The first effect is being evaluated with prototypes, using a noble material (pure iron ARMCO) and a less noble one (S275JR construction steel). The option preferred for the machine appears to be a low carbon steel: it is cost effective and it still features stable permeability over time. Tight specifications on the magnetic properties, in particular the coercivity, could possibly be relaxed, as they can be compensated by shuffling the cores during installation, instead of the more classical shuffling of laminations in the yokes. This is possible due to the large number of cores in the machine. Instead of being based on punched laminations, the prototypes are based on machined iron plates, held together by precise cylinders. In the prototypes, the central cylinders give satisfactory results for mechanical assembly tolerances; magnetically they can concentrate the flux further up to 1.5 T, at the highest excitation current.

The overall dimensions of the cross section are compatible with vacuum chambers which have the side winglets, as shown in Fig. 3.1. For one of the two beams, the synchrotron radiation points towards the central part of the dipole, in particular towards an aluminium busbar. This is not a particular concern because this component can be made radiation hard by using a suitable material for the ground insulation (for example, an inorganic coating). Furthermore, aluminium has the advantage of becoming less activated than heavier metals.

At the highest beam energy, the total electric power needed for the bending magnets, including the connections, is $\sim$16 MW. As in LEP, the busbars of the dipoles come near to each other (to mutually compensate their magnetic effect) and are then bent away to bypass the straight sections.

Two prototypes with a magnetic length of 1 m have been manufactured at CERN so far. For convenience these models had copper busbars, but this had no effect on the magnetic response. At the time of writing, full magnetic measurements are being made: these will be reported in [177]. Preliminary results from the first prototype confirm the expected magnetic coupling and show an interesting hysteresis effect on field quality (which is not a concern for this application) during ramp down.

There are several lines of development for the bending magnets after this initial conceptual phase. The first, after the magnetic measurements of the two short prototypes, is a possible further refinement of the cross-section, with the addition of $\pm 1\%$ trimming in the two apertures, to cope with the synchrotron radiation sawtooth. Then, options for materials and manufacturing techniques will be analysed from an industrial viewpoint. Topics will include cost effective low carbon steel, inorganic coating of aluminium busbars, machining of poles, automated assembly and dimension control of yokes and welding of busbars, etc. In parallel, the details of the interconnections between neighbouring dipole cores and around the short straight section will need to be studied in more detail, together with the supports and the related alignment strategy and finally, the integration with all other components (like vacuum chambers, radiation absorbers and vacuum pumps).

3.2.3 Quadrupoles

Table 3.2 lists the main requirements for the quadrupoles, together with the parameters as illustrated on the cross-section shown in Fig. 3.1.

These quadrupoles cannot be considered to be low field magnets because although the beam, which is quite small with respect to the physical aperture, sees at most 100 mT (that is, 10 T/m at 10 mm), the pole tip field reaches 0.42 T. This has an impact on the Amp-turns and the power consumption and it

DRAFT FOR ADVISORY COMMITTEE - DO NOT DISTRIBUTE

Table 3.2: Main requirements and parameters of the main bending magnets

Maximum gradient	T/m	10.0
Magnetic length	m	3.1
Number of twin units per ring		2900
Aperture diameter	mm	84
Radius for good field region	mm	10
Field quality in GFR (not counting dip. term)	10^{-4}	$\approx$1
Current	A	222
Current density	A/mm^2	2.4
Number of turns		2$\times$64
Resistance per twin magnet	mΩ	164
Power per twin magnet	kW	8.1
Power, 2900 units (with 5% cable losses)	MW	24.6
Iron mass per magnet	kg	4400
Copper mass per magnet (two coils)	kg	700

will be even more critical for large aperture sextupoles where the field grows quadratically from the centre.Therefore, a twin aperture layout providing significant power savings is also particularly interesting for the quadrupoles, even if they are relatively short compared to the dipoles.

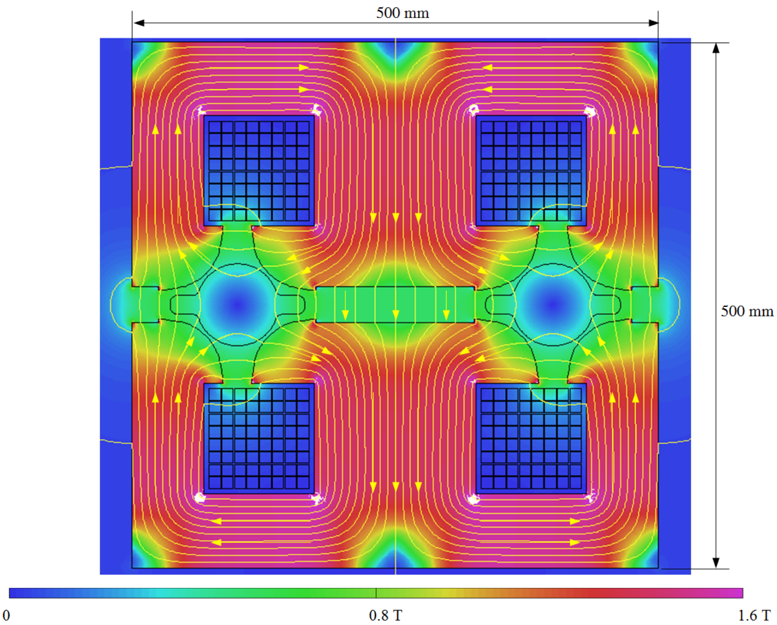

Figure 3.2: Cross-section of FCC-ee main quadrupole, for a 10 T/m gradient.

The magnetic coupling is achieved with a layout which resembles two figure-of-8 quadrupoles next to each other and in which the Amp-turns are concentrated in only two instead of four poles. Two simple racetrack coils excite the yoke, which is split in two halves and separated by a central non-magnetic spacer. In this way, a 50% power saving with respect to separate units is possible, with however, a polarity constraint: the two beams see a focusing and a defocusing field respectively. This has now been fully taken into consideration in the lattice design and individual trimming at the % level which could be provided by either additional windings on the poles, or by small stand-alone correctors.

The starting point of the design was the inter-beam distance of 300 mm defined by the geometry of the twin aperture bending magnet. Copper is favoured over aluminium as the conductor and it is

DRAFT FOR ADVISORY COMMITTEE - DO NOT DISTRIBUTE

operated at low current densities (< 2.5 A/mm^2) to help limit the power consumption, which, at 25 MW is still larger than that of the dipoles. This figure includes a tentative 5% for cable losses. The electrical parameters of the magnets and power converters, such as current and resistance, will have to be optimised at the circuit level. Cooling with demineralised water is needed with several circuits per coil in parallel. The details will depend on choices at a more general level, such as the temperature increase needed in the water to allow for partial recuperation of heat.

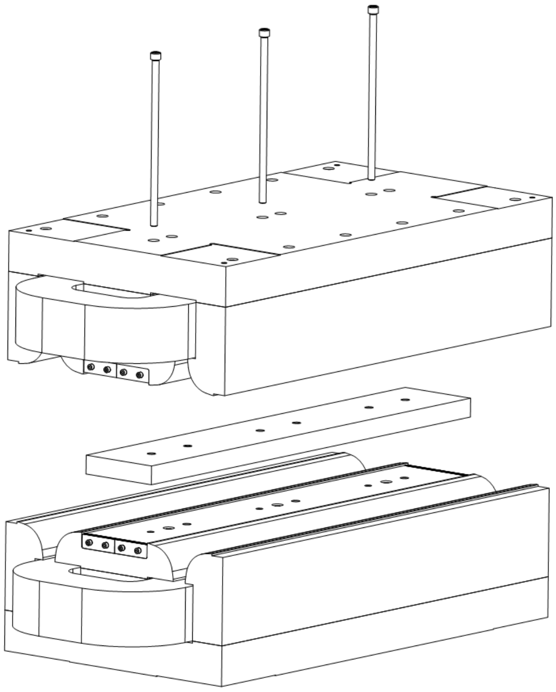

Figure 3.3: Exploded view of quadrupole prototype, with also end pole shims to adjust the integrated field quality.

From a magnetic viewpoint, the cross-section of Fig. 3.1 breaks many of the canonical symmetries used in a quadrupole. As such, the optimisation of the pole tip with 2D and 3D finite element models has been particularly challenging, in particular the minimisation of the unwanted dipole and sextupole components. A symmetric (at least at the pole tip) configuration was adopted for the manufacture of the 1 m long prototype, which was built by milling and grinding solid iron blocks and using a stainless steel spacer for the central part. An exploded view of the prototype is shown in Fig. 3.3 and a photograph of it is shown in Fig. 3.4. This manufacturing technique might not be the most suitable for the production of a large series, which in this case can probably be based on punched laminations, but it offers the flexibility of modifying individual details, for example on the pole tip, when iterations are needed.

The results of magnetic measurements of this first prototype will be used to refine the design, in particular at the pole tips. Individual trimming of the two apertures can be added after these refinements, possibly with embedded dual plane dipole correctors, obtained by separate windings over each pole.

3.2.4 Interaction Region and Final Focus

KO filled

This subsection is filled.

FCC-ee has two interaction regions, each with a detector solenoid which has a field of 2 T. The collider will run at different energies with optimised values of $\beta^*_{x,y}$ for the different operating points (see Table 2.1). The distance between the IP and the first quadrupole is 2.2 m and this determines the requirements for the final focus quadrupoles.

The philosophy is to design the simplest (in terms of magnetic elements) high performance sys-

DRAFT FOR ADVISORY COMMITTEE - DO NOT DISTRIBUTE

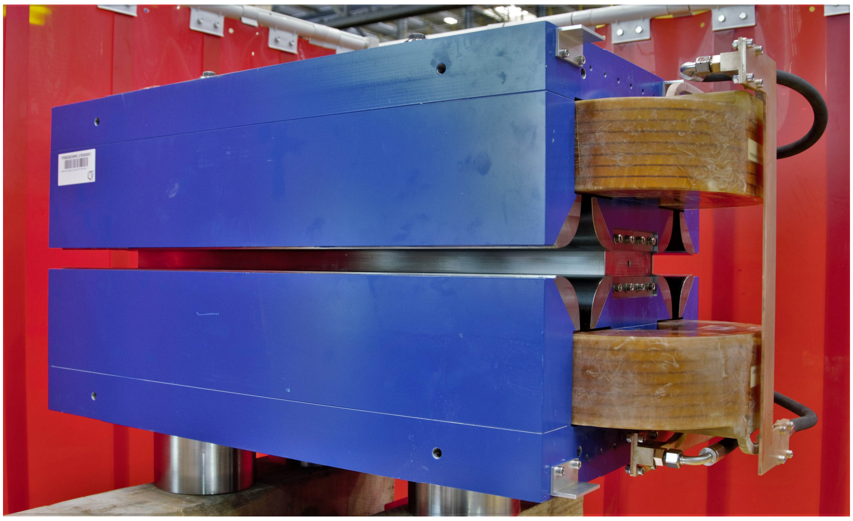

Figure 3.4: Picture of 1 m long quadrupole prototype.

tem, using state-of-the-art techniques whenever possible. The proximity of the final focus (FF) magnetic elements to the interaction point (IP), where the solenoid field of the detector magnet is strong, necessitates the use of two further magnetic elements. The first is a screening solenoid, which ensures that the solenoidal field seen by the beam at the FF quadrupoles is less than 0.05 T.m. The second element is a compensation solenoid which ensures that the integrated field seen by electrons and positrons traversing the detector is zero. Both of these are essential for good performance of the accelerator (the inevitable emittance blow up caused by passing through the IP needs to be within the total emittance budget). An iron-free design was chosen for the magnetic elements close to the IP, so the system does not suffer from non-linearities at different field strengths. Therefore the principle of superposition of the magnetic fields can always be applied, simplifying the design considerably. The iron yoke of the detector solenoid will extend to ± 4 m from the IP. The strength of the detector solenoid will be the same at all beam energies, therefore the screening and compensating solenoids will also have constant strength. The FF quadrupoles (which are split into 5 individually-powered units in the vicinity of the IP) will have different strengths for each energy point. Because the detector solenoid will always be operated at the same field, the emittance blow-up requirements are more stringent when running at the Z.

JPo
I assume that the yoke runs for the length of the magnet and is not just located at the edges, as the original text implied. However, is this number compatible with the length of the solenoid (± 3.6 m) given in the table below?

All magnetic elements will be installed within two cryostats (one per side). The beam pipe in the vicinity of the IP will be warm and liquid cooled. It will be possible to remove each cryostat and beam pipe assembly during assembly/dismantling of the detector, therefore there must be a flange at the end of the cryostat closest to the IP. NbTi has been chosen for the superconducting cable material for all of these interaction region magnets. It meets the performance requirements and the technology is well mastered at CERN. The temperature of the cryostat will be 4.2K, as there is no need for operation below the helium Lambda point. The heat load in the vicinity of the IP and when running at the Z energy, which is the most challenging point, will be around 100 W/m in normal operation. However, for full beam intensity at the Z energies with no collisions (and, therefore, no bunch lengthening due to beamstrahlung) this figure will become as high as 600 W/m.

3.2.4.1 Compensation scheme

As mentioned above, the compensation scheme comprises a screening solenoid and a compensating solenoid on each side of the IP. The main parameters are given in Table 3.1. The cable technology will be NbTi. For the compensation solenoid, which requires a high field, a standard LHC 13 kA Rutherford cable could be used. The screening solenoid can use eight individual LHC cable strands of 0.85 mm diameter bundled together.

DRAFT FOR ADVISORY COMMITTEE - DO NOT DISTRIBUTE

Table 3.1: Solenoids and compensation scheme parameters, given for one side (positive z). The paramters for the main detector solenoid are also listed for completeness.

	Start position (m)	Length (m)	Outer diameter (mm)	Current (A - turns)
Detector solenoid	0	3.6	400	3900 A - 1000
Screening solenoid	2.0	3.6	400	3900 A - 1000
Compensation solenoid	1.23	0.77	246-398 (tapered)	10600 A - 300

3.2.4.2 *Final Focus Quadrupoles*

The Canted Cosine Theta (CCT) technology without an iron yoke has been chosen for the FF quadrupoles. This technology provides excellent field quality and has many possibilities for customisation of the field which is necessary for cross talk compensation (the tips of the FF quadrupoles closest to the IP are only 66 mm from the beams). At the same time, the advent of numerically controlled machines (CNC machines) for the manufacture of the magnet formers, presents significant cost savings compared to conventional methods. The main parameters of the five individual elements of the FF quadrupoles on one side of the IP (positive Z) and for the electron beam only are shown in Table 3.2. The inner diameter of the beam pipe in the vicinity of QC1 is 30 mm and around QC2 it is 40 mm. The FF quadrupoles have an inner diameter of 40 mm and an outer diameter of 68 mm (truncated to 66 mm for the first FF element, QC1L1). The beam pipe around the IP is warm and its temperature is regulated by water flow. There is enough space for the insulation vacuum and one layer of radiation screen between the beam pipe and the quadrupole (which is operated at 4.2 K). The maximum field gradient is 100 T/m, although the design can easily be modified to accommodate considerably higher gradients (150 T/m) to give more flexibility if needed. Each element is positioned so that its magnetic centre is along the ideal beam trajectory. In FCC-ee the angle between electrons and positrons at the IP has been chosen as 30 mrad which means that the minimum distance between the magnetic centres of the e^+ and e^- QC1L1 magnets is 66 mm (see Fig.3.5).

JPo
I have understood
Please check that I have understood this correctly

Table 3.2: Final focus quadrupoles parameters.

	Start position (m)	Length (m) (m)	B' @Z (T/m)	B' @$W^\pm$ (T/m)	B' @Zh (T/m)	B' @$t\bar{t}$ (T/m)
QC1L1	2.2	1.2	−78.60	−96.16	−99.98	−100.00
QC1L2	3.48	1	+7.01	−40.96	−99.94	−100.00
QC1L3	4.56	1	+28.40	+22.61	+26.72	−100.00
QC2L1	5.86	1.25	+2.29	+40.09	+23.75	+58.81
QC2L2	7.19	1.25	+9.05	+3.87	+39.82	+68.18
QC1R1	−2.2	1.2	−79.66	−100.00	−99.68	−99.60
QC1R2	−3.48	1	+5.16	−37.24	−92.78	−99.85
QC1R3	−4.56	1	+36.55	+24.02	+5.87	−99.73
QC2R1	−5.86	1.25	+7.61	+45.51	+36.45	+63.03
QC2R2	−7.19	1.25	+4.09	+3.95	+44.43	+77.91

DRAFT FOR ADVISORY COMMITTEE - DO NOT DISTRIBUTE

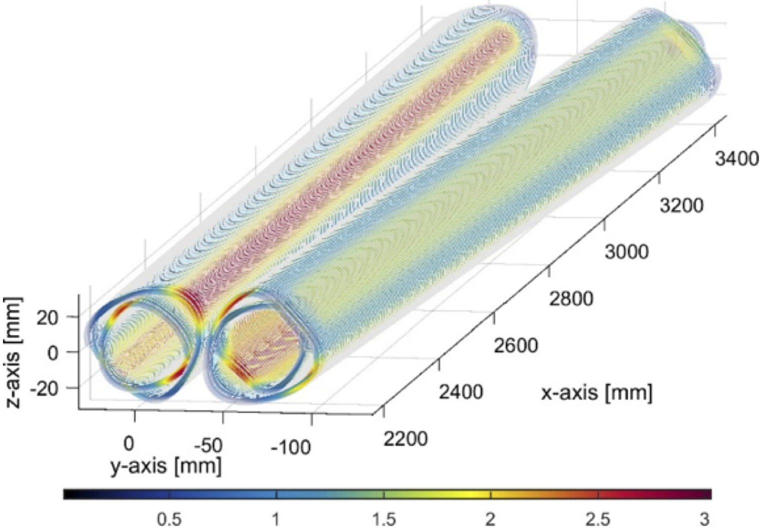

Figure 3.5: The position of the two QC1L1 magnets near the IP (QC1L1P on the left and QC1L1E on the right). The colours correspond to the magnitude of the magnetic field at the surface. There is a horizontal angle of 30 mrad between the two beam pipes (not shown here). The tips of the quadrupoles are 2.2 m from the IP. The axes are in mm and they follow the positron beamline and the IP is at the origin (0,0,0).

3.2.4.3 Field quality of QC1L1

The field quality requirements become less stringent as one moves further away from the IP. It is planned to use the same technology for all elements and the following paragraphs will concentrate on the most critical elements, QC1L1. These magnets are 1.2 m long, at the tip they are located 66 mm from their counterpart for the other beam and they are 102 mm apart at the far end. The magnet has an inner aperture of 40 mm diameter and an outer diameter of 64 mm. The beam pipes for both electrons and positrons have an inner diameter of 30 mm in the vicinity of QC1L1. A traditional CCT design has excellent field quality but there are small edge effects, which cancel out if one integrates through the whole length of the magnet. However, in a region of rapidly varying optics this cancellation alone does not ensure excellent performance and therefore the edge effects have been corrected locally using a novel technique based on the addition of multipole components [?].

Furthermore, the significant amount of crosstalk between the two quadrupoles which are sitting in close proximity has been corrected. The result is a quadrupole magnet with integrated multipole components of less than 10^{-5}, as can be seen in Table 3.3. It should be noted that these multipole values do not take into account the effect of imperfections like misalignments and mechanical tolerances. It is therefore assumed that crosstalk and edge effects are perfectly compensated and the final field quality will be dominated by mechanical tolerances and misalignments.

A misalignment analysis has also been performed. Mechanical alignment of the two quadrupoles (QC1L1E and QC1L1P) should be better than 30 µm (a strict but achievable requirement for objects a few centimetres apart). The multipoles affected by a misalignment in x are B_3 (0.8 units for a misalignment in x of 100 µm). For misalignment in y, the multipoles affected are A_2 and A_3 (2.2 units and 0.7 units for a misalignment of 100 µm in y respectively). A beam misalignment of up to several millimetres will only have a dipole effect with no higher order multipoles (due to the homogeneity of the field resulting from the CCT design). To a large extent, winding alignment and machining errors average out, with the final accuracy depending on the systematic machining accuracy. These errors need to be measured after a prototype magnet has been constructed. No problems are expected to arise from the machining accuracy.

DRAFT FOR ADVISORY COMMITTEE - DO NOT DISTRIBUTE

Table 3.3: Integrated field errors in units of 10^{-4} after correction for the effect of crosstalk from the adjacent quadrupole in the absence of imperfections. Calculation performed at 10 mm (2/3 aperture). All multipoles can be corrected to better than 0.05.

n	B_n	A_n	n	B_n	A_n
2	10000	0.01	7	0.03	< 0.01
3	0.01	0.03	8	0.02	< 0.01
4	-0.03	-0.01	9	< 0.01	< 0.01
5	-0.01	-0.01	10	< 0.01	< 0.01
6	-0.03	0.02			

3.2.4.4 Corrector magnets

The FF quadrupole design has no multipole components apart from B_2, the main quadrupole field, so any correctors are for effects other than the imperfections of the FF quadrupoles themselves. There is room for many corrector elements (four can be easily fitted per quadrupole). An important consideration for the FF quadrupole design is that steering and skew quadrupole correctors should be installed as close to QC1L1 as possible and in this case they will be fitted as extra rings over QC1L1. Correctors of adequate strength can be installed without affecting the packing factor. Due to the close proximity of the other beam, each corrector has to have its own crosstalk compensator to ensure zero crosstalk with the other beam.

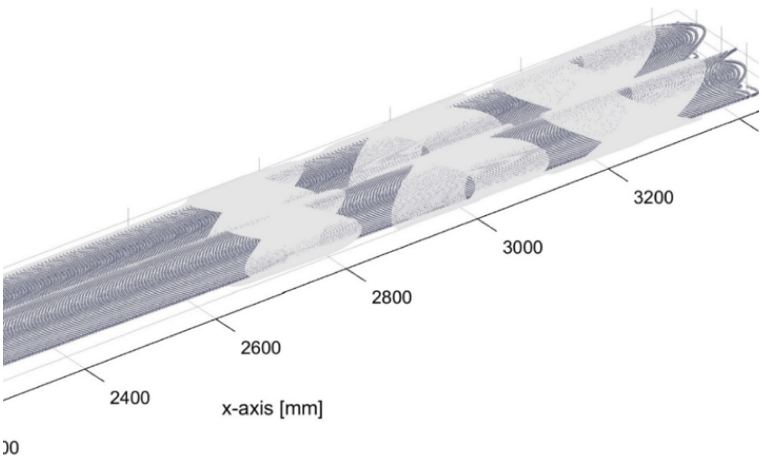

Figure 3.6: The position of the A_2, A_1 and B_1 correctors, fitted as extra rings on top of the QC1L1 magnets.

3.2.5 Auxiliary Magnets

3.3 Vacuum System and e-Cloud Mitigation

Roberto Kersevan: Roberto Kersevan, 4 pages

3.4 Radiofrequency System

Olivier Brunner: Olivier Brunner, 5 pages

DRAFT FOR ADVISORY COMMITTEE - DO NOT DISTRIBUTE

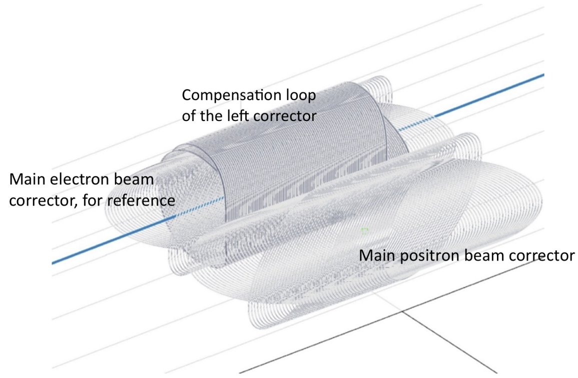

Figure 3.7: Detail of a horizontal dipole corrector. The individually powered correctors for the electron and positron beams are shown, together with the positron beam corrector compensation coil (fitted outside the main electron beam corrector), which is powered in series with the main positron beam corrector.

3.4.1 Overview

3.4.1.1 Introduction

The parameter range for the e^+e^+ collider is large, operating at centre-of-mass energies from 90 GeV to 365 GeV with beam currents ranging between 1.39 A and 5.4 mA, at fixed synchrotron radiation power of 50 MW per beam. These are challenging parameters for the radiofrequency (RF) system due to the voltage requirements and beam loading conditions. The system, is equally distributed between the two opposite straight sections at PD and PJ as shown in Fig. 3.8.

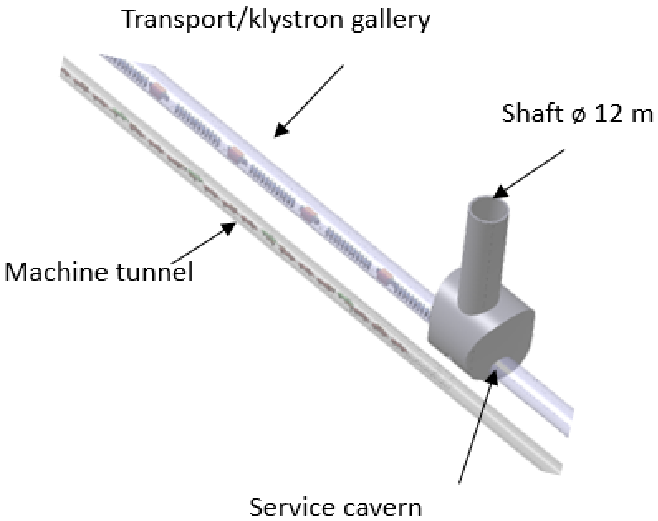

Figure 3.8: A schematic view of RF system at point D and J

DRAFT FOR ADVISORY COMMITTEE - DO NOT DISTRIBUTE

3.4.1.2 System parameters

The main centre-of-mass operating points are around 91 GeV (Z-pole), 160 GeV (W pair production threshold), 240 GeV (Higgs resonance) and 365 GeV (above top-antitop ($t\bar{t}$) threshold). Therefore, the system needs to evolve in five steps, combining eight months of operation periods with four months of interleaved shutdowns during which the hardware upgrades for energy increase can take place.

In order to produce the integrated luminosity at each energy step, the machine would operate four years at the Z-pole, one year at the W pair production threshold, three years at the Higgs resonance and four years at the highest energy, one year at the $t\bar{t}$ threshold ($t\bar{t}$1), followed by three years at 182.5 GeV per beam ($t\bar{t}$2). The system parameters are summarised in Table 3.3 [178].

Table 3.3: Machine parameters.

Parameter	**Z**	**W**	**H**	**$t\bar{t}$1**	**$t\bar{t}$2**
Beam Energy [GeV]	45.6	80	120	175	182.5
Beam current [mA]	1390	147	29	6.4	5.4
Number of bunches	16640	2000	328	59	48
Beam RF voltage [MV]	100	750	2000	9500	10930
Runtime [year]	4	1	3	1	4

The RF voltage requirement spans from 0.1 to 11 GV. Running at the Z-pole, the collider is an Ampere class, heavily beam loaded machine, while at the $t\bar{t}$ energy it becomes a high energy machine. Having a single design that can meet all four cases is not efficient [179]. For the Z-pole machine, the cavity shape must be optimised with respect to higher order modes (HOM). This favours low frequency, low shunt resistance and a low number of cells per cavity. For this energy step, there will be a 400 MHz continuous wave (CW) RF system made up of 52 single-cell Nb/Cu cavities per beam is considered. This frequency is also the natural choice for the FCC-hh, which can use the LHC as injector which also operates at this frequency. The 400 MHz system can be built with today's well-known technology. It also provides an opportunity to re-use a large part of the hardware and infrastructure for a subsequent hadron collider.

High acceleration efficiency is necessary to optimise the system size and cost for the highest energy. About 2600 cells are required to produce a total RF voltage of 11 GV. At this energy, the small number of bunches and the low beam loading suggest the possibility of a common RF system for both beams. This can be accomplished by re-aligning the cavities used for the Higgs production on a common beam axis and installing additional cavities to produce the extra 7 GV. For this, the relatively modest CW RF power per cavity offers the possibility to use 800 MHz bulk Nb five-cell cavities. Although these cavities must be operated at 2 K, this choice provides a better acceleration efficiency and a significantly reduced overall footprint, hence potentially significant cost savings. Higher frequencies have been excluded due to transverse impedance considerations and power coupler limitations for CW operation.

3.4.1.3 RF for the booster

A fast repetition rate booster [180] of the same size as the collider must provide beams for top-up injection at collision energy to achieve the luminosity goals. The booster's rated voltage corresponds to the energy loss per turn resulting from synchrotron radiation emission. The RF configuration of the booster ring for each step is shown in Table 3.5. In order to optimise the cryogenic system and cryogen distribution, the same technology as for the collider will be used. Since the booster has a low duty factor, less than 10 % (ratio of average to peak power), a compact RF power system can be used. The low beam loading allows for multi-cell cavities at all energies and a staged installation.

DRAFT FOR ADVISORY COMMITTEE - DO NOT DISTRIBUTE

3.4.2 Superconducting Cavities

3.4.2.1 Cavity materials

A detailed analysis of performance data for different RF frequencies, temperatures and materials for the superconducting cavities [181] has led to a recommendation for Nb/Cu technology. A well-focused R&D programme on Nb thin-film coated Cu cavities could decrease the surface resistance at high RF fields by factors of two to three. As a result, the technology could be operated at 4.5 K, which makes it competitive with bulk Nb operated at 2 K. This choice also facilitates the re-use of the existing RF power system for the hadron machine, which requires a high RF acceleration efficiency with several hundred kW power input per cavity and for which a lower transverse impedance is certainly beneficial. R&D is focusing on Nb/Cu produced by the high power impulse magnetron sputtering technique, which will improve the micro-structure of the coating due to the larger energy made available during film growth. Any progress on substrate manufacturing and preparation will have an immediate impact on the final RF performance, as it was demonstrated by the seamless cavities produced for the HIE ISOLDE project, where the Q slope was substantially reduced compared to their welded counterparts [182].

The A15 compounds have the potential to outperform niobium as their BCS surface resistance is much lower due to the higher critical temperatures. Nb_3Sn cavities obtained by thermal diffusion of Sn in bulk Nb have a similar performance at 4.5 K to state of the art bulk Nb cavities at 2 K. A programme aimed at the synthesis of Nb_3Sn films on copper substrates is ongoing at CERN and has already produced high quality films on small samples [183, 184].

3.4.2.2 Manufacturing

The number of cavities needed justifies investing in novel, cost-effective manufacturing technologies ensuring the best reproducibility whilst minimising the performance limitations. In addition to the traditional fabrication methods, notably spinning and deep drawing of the half-cells, electro-hydraulic forming (EHF) [185] turns out to be particularly suitable for series production.

For bulk Nb and Nb-coated elliptical cavities alike, minimising the electron-beam welded joints by seamless construction helps to reduce the performance limitations arising from defects and irregularities of the welding seams and the area in their vicinity, as well as reducing possible contamination originating from them. Efforts are ongoing to push the technology beyond existing limits to produce seamless cavities within the very tight required tolerances [186]. It can be expected that such Nb coated cavities will have superior and less scattered electro-magnetic performance [182]. Surface treatments are necessary in order to eliminate the surface layer damaged during cavity fabrication and to achieve the smoothest possible substrate for Nb coatings. Efforts are ongoing to achieve full electro-polishing of seamless cavities in order to achieve these goals.

3.4.2.3 RF power couplers

For the proposed configuration of the Z-pole and W-threshold machines to be achieved, the RF coupler technology must also be pushed forward to increase their CW power transfer capability: the higher order mode couplers will have to deal with high beam loading and must extract kilowatts of RF power. Progress with the fundamental power couplers will be essential to limit the cost and size of the RF system. The target value for fixed couplers is 1 MW CW per power coupler at 400 MHz [187]. Fixed power coupler (FPC) design must ensure that their coupling coefficient to the different machines can be adapted easily. The machine parameters and time line imposes the use of 'adaptable' power couplers. The external Q of the coupler must be easily adapted 'in situ', without venting the cavities. Fundamental power couplers for superconducting cavities are among the most important and most complex auxiliary systems. They must simultaneously deliver RF power to the beam and separate the cavity ultra-high vacuum, ultra-low temperature environment from air-filled, room temperature transmission lines, as illustrated in Fig. 3.9.

DRAFT FOR ADVISORY COMMITTEE - DO NOT DISTRIBUTE

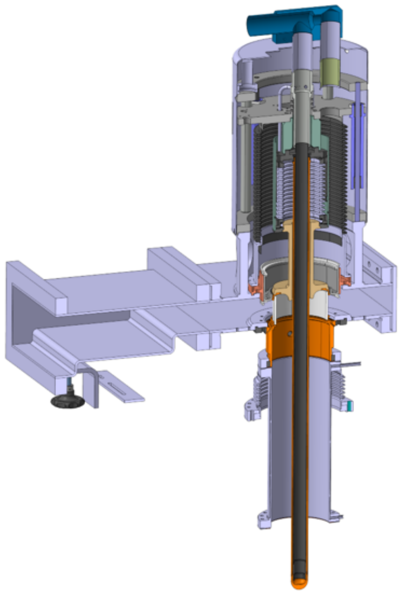

Figure 3.9: Schematic of the complex LHC power coupler.

3.4.3 Powering

3.4.3.1 High efficiency klystron development for FCC

The need to provide two times 50 MW of continuous RF power sets the overall scale of the system. Improving energy efficiency and reducing energy demand is crucial for such a particle collider. Therefore, highly efficient RF power sources need to be conceived [180].

The High Efficiency International Klystron Activity (HEIKA) [188] was initiated at CERN in 2014 to evaluate and develop new bunching technologies for high efficiency klystrons [189–191]. Results point to efficiency increases from 65% to potentially above 80%, resulting also in significant operation cost reductions [192]. One critical step towards the realisation of these devices is the development and use of a software called KlyC [193] to optimise system designs with high accuracy and short iteration times.

Table 3.4 displays the main parameters obtained for a 800 MHz high efficiency klystron, optimised for the lepton collier and a scaled version at 400 MHz adapted for HL-LHC (i.e. the parameters of LHC klystron modulator were preserved). Their bunching technology is based on the core stabilisation method (CSM) described in [193]. The gain and power transfer curves of the 800 MHz tube, simulated by KlyC for different voltages are shown in Fig. 3.10. The tube has a comfortable dynamic range, preserving efficiency above 65% for the output power range from 0.6 MW to 1.7 MW and a comfortable 3-dB bandwidth of 4 MHz at 1.35 MW.

Table 3.4: Design parameters of klystrons operating at 400 and 800 MHz

Frequency	**Beam voltage**	**Beam current**	**Peak RF power**	**Efficiency**	**Power gain**	**Tube length**
400 MHz	54 kV	9 A	357 kW	73.5%	38.5 dB	1.26 m
800 MHz	134 kV	12.6 A	1.35 MW	80.0%	38 dB	1.74 m

3.4.4 Feedback

Longitudinal instabilities caused by the cavity fundamental impedance will be the major issue when running at the Z-pole. Their growth rate is much faster than than synchrotron radiation damping and

DRAFT FOR ADVISORY COMMITTEE - DO NOT DISTRIBUTE

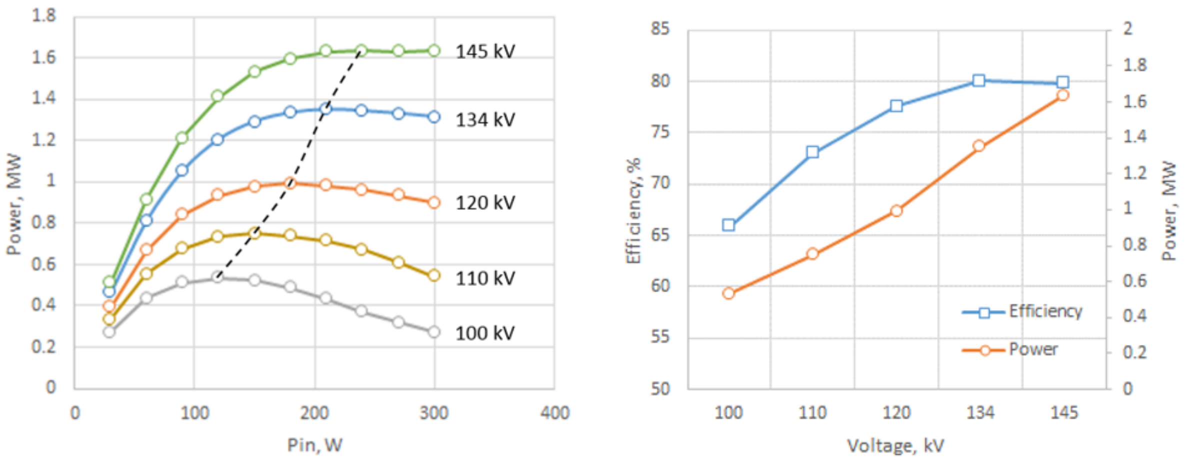

Figure 3.10: The power gain curves simulated by KlyC for different voltages (left) and the transfer curves for saturated power (right). The dashed line in the left plot traces the saturated power.

strong feedback around the cavities will therefore be required to maintain stability and damp the coupled bunch instabilities for high intensities [194]. A direct RF feedback will be supplemented by a bunch-by-bunch longitudinal feedback giving extra impedance reduction.

3.4.5 Low-Level RF

Most of the LLRF issues for FCC-ee have been faced in PEP-II [195]. Modern LLRF designs implement most of the signal processing in the digital domain and even stronger performance will be achieved in the future with continuously growing processing power.

3.4.6 Staging

The RF system will be upgraded in steps, with rising maximum voltage, as shown in Table 3.3. First of all, 26 cryomodules, consisting of 4 single-cell cavities each will be installed for the Z-pole machine. Each cavity will be fed by about 1 MW CW RF power to generate the 2×50 MW beam power. There are a number of possible solutions for the production of the required RF power, but as the space in the tunnel is restricted, the large, bulky power equipment will be installed on the surface. The underground areas will only accommodate the RF power amplification, the DC power distribution, the fast servos and control and the protection systems. Given the perspective of the energy upgrades, using a combination of two or four medium-size RF power sources seems very attractive.

During a shutdown period at the end of the Z-pole campaign, these cryomodules will be replaced by 26 four-cell cavity cryomodules for the W-threshold machine operation. The RF power sources, the control systems and the RF power distribution will remain unchanged. The step between the W and H machines requires the installation of 42 additional four-cell four-cavity cryomodules to produce the RF voltage of 2 GV/beam. The fast RF feedback requirements and the large number of bunches favour a single cavity per power source. The RF power system initially installed for the Z machine will be reconfigured to adapt to the new power requirement per cavity and additional new RF power stations will complete the installation. The detailed powering scheme and the associated workload must be carefully studied to be in line with the available time frame and the pre-installation effort must be spread over several winter shutdowns (e.g. cabling and installation campaigns).

For the highest beam energy of 182.5 GeV the existing RF system would be re-arranged. It would be shared between the two beams, to double the RF voltage available for either beam. The sharing of cavities by the two beams is possible due to the small number of bunches in this mode of operation. The

DRAFT FOR ADVISORY COMMITTEE - DO NOT DISTRIBUTE

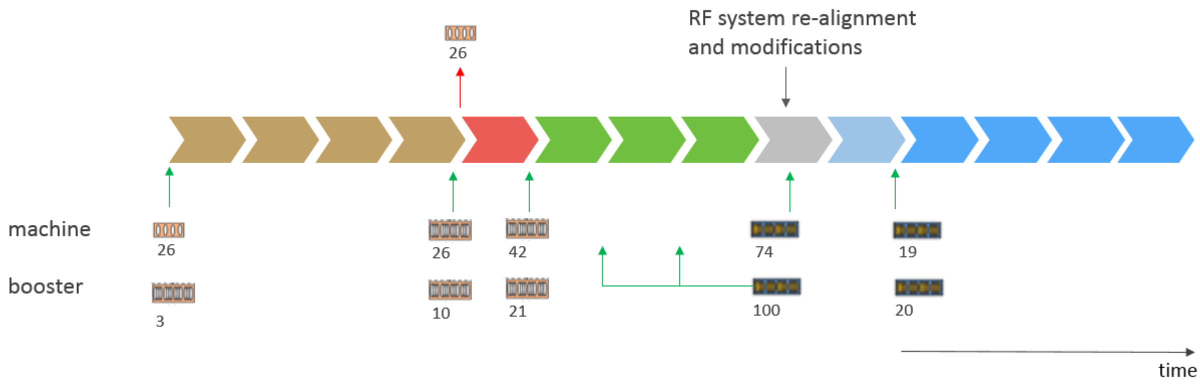

Figure 3.11: Proposed FCC-ee staging schedule. The figures underneath indicate the numbers of cryomodules to be installed during the various shutdowns. Each solid arrow represents an 8 month running period which are interleaved with the 4 month long shutdowns.

Table 3.5: Detailed RF configuration of each machine and booster ring.

	Z		*W*		*H*		$\mathbf{t\bar{t}_1}$		$\mathbf{t\bar{t}_2}$	
	per beam	booster	per beam	booster	per beam	booster	2 beams	booster	2 beams	booster
Total RF voltage [MV]	100	140	750	750	2000	2000	9500	9500	10930	10930
Frequency [MHz]	**400**									
RF voltage [MV]	100	140	750	750	2000	2000	4000	2000	4000	2000
E_{acc} [MV/m]	5.1	8	9.6	9.6	9.8	9.8	10		10	
# cell / cav	1	4	4		4		4		4	
V_{cavity} [MV]	1.92	12	14.4	14.4	14.7	14.7	15		15	
# cavities	52	12	52	52	136	136	272	136	272	136
# CM	13	3	13	13	34	34	68	34	68	34
T operation [K]	4.5		4.5		4.5		4.5		4.5	
dyn losses/cav [W]	14	11	210	26	202	29	210	30	210	30
stat losses/cav [W]	8		8		8		8		8	
Q_{ext}	4.4 10^4		6.6 10^5		1.9 10^6		4 10^6		4.7 10^6	
P_{cav} [kW]	962		962		368		175		149	
Frequency [MHz]	**800**									
RF voltage [MV]							5500	7500	6930	8930
E_{acc} [MV/m]							19.8	20	19.8	19.8
# cell / cav							5		5	
V_{cavity} [MV]							18.6	18.75	18.6	18.6
# cavities							296	400	372	480
# CM							74	100	93	120
T operation [K]							2		2	
Dyn losses/cav [W]							66	10	66	10
Stat losses/cav [W]							8		8	
Q_{ext}							3.9 10^6		5.6 10^6	
P_{cav} [kW]							176		155	

68 RF cryomodules will be moved transversely and separators will be installed at the entrance and exit of each RF straight section. The system will be completed with additional 800 MHz five-cell four-cavity cryomodules installed in series to produce the extra voltage. These 2 K cryomodules will be connected to form long cold segments in order to minimise the warm beamline sections and the relatively modest

DRAFT FOR ADVISORY COMMITTEE - DO NOT DISTRIBUTE

power requirement per cavity will allow for the gradual introduction of less powerful and less expensive RF power sources. A one-year shutdown will be necessary to cope with this major intervention. It will be followed by one-year of an intermediate operation stage at 175 GeV. The main changes to the RF unit's configuration in tandem with the required beam-energy changes are depicted in Fig. 3.11. The main RF parameters for each stage are detailed in Table 3.5.

3.4.7 Beam-cavity Interaction and Beam Dynamics Issues

JGU: Not sure where to put this section

Sufficient current must be stored in both beams in order to maximise the luminosity at the different energies. Higher-order mode (HOM) losses, single- and coupled-bunch instabilities that might seriously affect the final performance of the machines, have been studied in detail [196, 197]. Most of these issues appear to be more prominent in the 'high-current - low-energy' operation at the Z pole and to a lesser extent at the W threshold.

The microwave instability thresholds have been computed with the BLonD code, a macro-particle tracking code developed at CERN for longitudinal beam dynamics simulations [198]. Its latest release accurately computes synchrotron radiation effects for leptons and very high energy hadrons [199]. At nominal beam current, the machine impedance leads to increased energy spread and bunch length, despite the strong synchrotron radiation damping, but does not result in unstable growth [200]. This is consistent with previous analyses [201, 202].

An analytical approach was used to calculate the coupled-bunch instability thresholds [203]. Although the single-cell cavity for the Z-pole machine must be further optimised, its longitudinal impedance spectrum above the cut-off frequency of the pipe sits well inside the coupled-bunch stability zone, as shown in Figure 3.12. HOMs should be damped according to the calculated limit for the impedance spectrum below the cut-off frequency. Further analysis needs to focus on the cavity fundamental-driven coupled-bunch instabilities and on the potential impact of the large detuning angle.

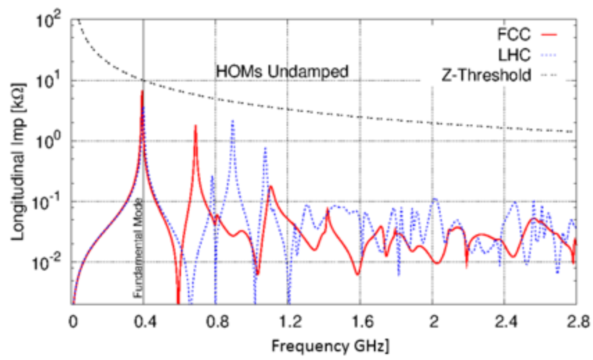

Figure 3.12: Comparing the Z machine coupled bunch instability threshold with longitudinal impedance of FCC single-cell cavity. HOM damping should make sure that the impedance remains below 10 kΩ

The cavity design and the beam configuration are closely intertwined. The calculated power loss map of a reference single cell cavity for filling schemes with distances between the first two bunches of consecutive trains larger than 100 RF buckets as a function of the cavity resonant frequencies, is shown in Fig. 3.13. Regions with acceptable power losses are shown in green. The dark vertical line corresponds to the position of HOM of a reference single-cell cavity design with the maximum frequency shift of 5 MHz. It can be observed, for example, that bunch spacings of 10 ns and 17.5 ns are not favourable for operation. The frequency range for calculations is limited by the fundamental mode frequency (400.79 MHz) and the cut-off frequency (765 MHz).

DRAFT FOR ADVISORY COMMITTEE - DO NOT DISTRIBUTE

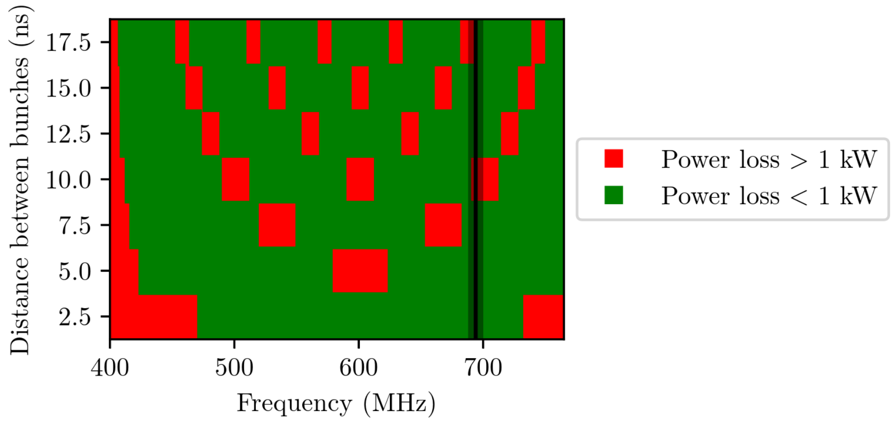

Figure 3.13: Calculated power loss map for single cell cavity. Frequency ranges with acceptable power losses below 1 kW for different bunch spacing are shown in green. Regions with power losses above 1 kW are shown in red. The dark vertical line corresponds to the position of HOM of the single-cell cavity design with the maximum frequency shift of 5 MHz. The bunch spacings of 10 ns and 17.5 ns are not acceptable for this HOM due to high power losses (see, overlap of red with black regions). The frequency range for the calculations is limited by the fundamental mode frequency (400.79 MHz) and the cut-off frequency (765 MHz).

A detailed analysis of the HOM power and damping requirements has been performed for all FCC-ee machines with the current cavity designs and cryomodule arrangements, including beam pipes and tapers [196, 197]. The tapered connection between the cavity and the beam pipe can significantly contribute to the high-frequency part of the impedance spectrum (above 3 GHz) and must be carefully designed. For the Z machine, it is envisaged to install intermediate tapers inside each cryomodule and longer tapers in warm sections, where transition to the small beam pipe radius is necessary [196]. A judicious combination of bunch spacings and cavity designs allows the HOM power per cavity to be kept below a few kilowatts, which is acceptable for the LHC-like superconducting hook couplers.

3.5 Beam Transfer Systems

3.5.1 Overview

3.5.2 Injection

3.5.3 Extraction

3.5.4 Dumping

Brennan Goddard: Brennan Goddard, 2 pages

3.6 Collimation Systems

3.6.1 Overview

3.6.2 Collimation

3.6.3 Protection

3.6.4 Dump and Masls

Roberto Kersevan: Roberto Kersevan, 4 pages

DRAFT FOR ADVISORY COMMITTEE - DO NOT DISTRIBUTE

3.7 Other Systems

3.7.1 Overview

3.7.2 Beam Diagnostics Requirements and Concepts

Schmickler or Höfle: Schmickler or Höfle, 3 pages

Miguel Jimenez/Mar Capeans: Miguel Jimenez/Mar Capeans, 3 pages

3.7.3 Powering

3.7.4 Wigglers

3.7.5 Wire Septum

3.7.6 Multipole Kicker

3.7.7 X-ray Interferometer

3.7.8 Machine Protection

In the Z running mode a total energy of 4 MJ is stored in the FCC-beams. This is more than two orders of magnitude lower than the energy stored in the LHC or FCC proton beams, and even lower than the energy stored in a linear-collider bunch train, e.g., at ILC or CLIC. While a linear collider dumps such a beam several times per second, or hundred times per second, beam dumps at the FCC-ee will be a rare exception. An appropriate machine protection system, with an early detection of beam instabilities or relevant technical failure modes, will trigger a beam abort, and safely extract the FCC-ee beams to their corresponding beam dumps, before any damage to machine components can occur.

Unavoidable collision-related beam losses will continually impact machine components, however. For a beam lifetime of 20 minutes, in all operation modes the total beam loss power is less than 20 kW. If these losses are limited to a few locations, the latter require appropriate shielding and cooling measures.

The energy stored in the magnets is tremendously reduced compared with the energy stored in the high-field superconducting magnets of the LHC or FCC.

3.7.9 Controls Requirements and Concepts

3.8 Radiation Environment

3.8.1 Reference Radiation Levels

Radiation levels in the collider scale with energy and, as LHC has shown, degradation of components exposed to radiation can become a show stopper. Two complementary approaches are needed: the reduction of the dose to equipment by shielding and develop fault tolerant or radiation resistant electronics and equipment. A structured approach for radiation hardness assurance (RHA) will ensure that the electronics and materials developed perform to their design specifications after exposure to the radiation in the collider environment.

Radiation to electronics (R2E) is an issue in the design of any high energy and high intensity machine [?]. Radiation effects in electronic devices can be divided into two main categories: cumulative effects and stochastic effects (Single Event Effects - SEE). Cumulative effects are proportional to the total ionising dose (TID) - the damage induced by ionising radiation, and the 1 MeV neutron-equivalent fluence which concerns displacement damage. On the other hand, SEE, which are proportional to the high energy hadron fluence (HEH, i.e. hadrons with energies $>$ 20 MeV), are due to the direct or indirect ionisation by a single particle which is able to deposit sufficient energy to disturb the operation of the device. SEE can only be defined by their probability to occur and the effect strongly depends on the device, the intensity and the kind of radiation field. The FCC-ee staging schedule which has long operational phases at energies of 45.6, 80 and 120 GeV, before the 175 GeV ultimate design energy

DRAFT FOR ADVISORY COMMITTEE - DO NOT DISTRIBUTE

is achieved, gives confidence for the selection process of rad-hard equipment. In addition, the use of the shielded alcoves for the electronics will reduce the radiation levels, thus increasing the equipment lifetimes and reducing the probability of stochastic effects.

Monte Carlo (MC) simulation is an indispensable tool to evaluate the impact of radiation on the machine equipment, but it relies on both a refined implementation of physics models of the particle interaction with matter and an accurate 3D-description of the region of interest. In this context, FLUKA [?, ?] which is widely employed at CERN, is a well benchmarked, multi-purpose and fully integrated particle physics MC code for calculations of particle transport and interactions with matter. FLUKA is employed in the majority of CERN technical and engineering applications such as machine protection, energy deposition calculations, damage to accelerator elements and shielding design. For a high intensity and energy machine like FCC, typical sources of radiation are luminosity debris, direct losses on collimators and dumps and, particularly for the ee collider, synchrotron radiation.

A FLUKA model of half an arc cell has been created REFERENCE [3]. The geometry consists of a 25 m long half FODO cell, with five absorbers 24 cm long. The latter are shaped with an inner radius of 25 mm. While the geometry parameters can still be optimised and probably will change slightly, they will not have a major impact on radiation to equipment or the critical radiation levels for the electronics.

JPo
This did not make sense - is it radius, diameter or something else?

FLUKA was set up to sample from the 175 GeV electron beam synchrotron radiation spectrum taking into account the photon angular distribution and polarisation. Photonuclear production was enabled and variance reduction techniques were applied to obtain a statistically meaningful result. Figure 3.14 shows the dose distribution in the beam plane. Qualitatively, similar distributions have been found for the HEH and 1-MeV neutron equivalent fluence.

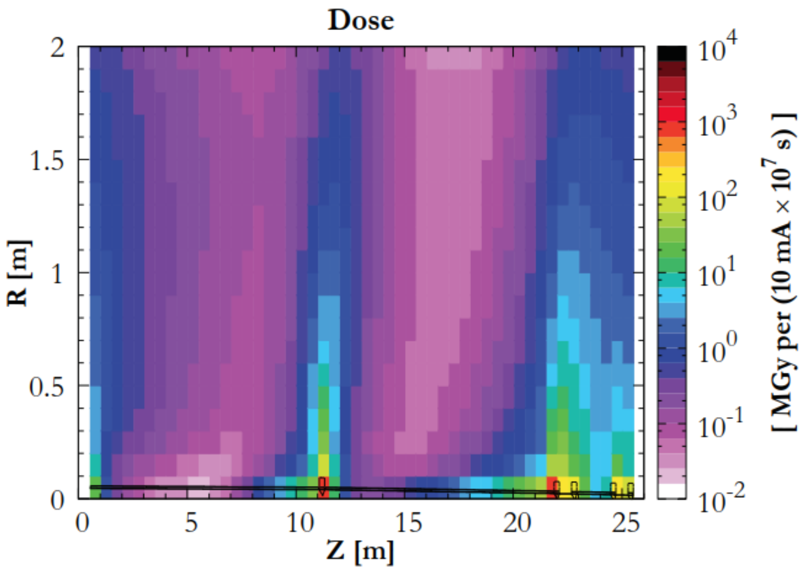

Figure 3.14: Dose distribution in a half-FCCee arc cell. Results were normalised for 10^7 seconds in data taking and a beam current of 10 mA.

The pattern in Fig, 3.14 shows hot spots along the beam pipe corresponding to the interconnects where the synchrotron radiation absorbers are placed. The results show that equipment installed in certain locations in the tunnel will be affected by the TID effects which will limit the equipment lifetime, in addition to experiencing SEE failures. In particular, the TID values of the order of 100 kGy - 1 MGy are an enormous challenge for the electronics in the vicinity of the FCC-ee machine and they will limit the use of commercial-off-the-shelf (COTS) components, which typically have limits in the 50 Gy - 1 kGy range. Therefore, the quantity of active electronics needs to be minimised and based on radiation-hardened by design components, as is the case for high-criticality space missions, high-energy physics

DRAFT FOR ADVISORY COMMITTEE - DO NOT DISTRIBUTE

experiments or ITER. The impact of the radiation-hardened design on the cost, availability and lead time of the components is significant.

3.8.2 Radiation Hardness

As is the case for the present LHC machine, the power converters, beam position and loss monitors (BPM and BLM) and quench protection system (QPS) have to be close to the accelerator itself. Such equipment is mainly based on commercial-off-the-shelf (COTS) components and therefore the equipment needs to be qualified for use in the radiation environment [**?**].

The FCC RHA strategy is founded on a *full-availability* approach based on: (i) a remote control approach, moving the processing tasks from the equipment under control and (ii) failure self-diagnosis, online hot swapping and remote handling. Therefore system designs are based on a modular approach that will allow switching to a redundant sub-system without any impact on operation. This will be particularly beneficial for transient errors, which can typically be corrected with a reset. The approach will also relax the constraints on the error qualification limits, which will be obtained through accelerator radiation testing.

In the case of events which cause permanent effects such as hard SEEs (occurring stochastically) or cumulative damage, online hot-swapping will need to be complemented by the substitution of the faulty board. This procedure will need to be carefully optimised, especially for cumulative damage, where similar sub-systems exposed to similar radiation levels are expected to fail at around the same time. Therefore, remote handling and the possibility of replacement of faulty units with spares which have been stored in radiation-safe areas, is one way to mitigate the risk.

The proposed scheme will bring benefits from the use of a selected set of semiconductor components that can be used in different sub-systems. The related procurement and qualification processes can be optimised and the impact of variability in sensitivity across batches and deliveries can be reduced. In specific cases, the use of radiation-hardened solutions at component level (e.g. FPGA) can be considered in combination with the use of COTS devices.

3.8.3 Radiation-hard Technology Trends

In parallel with the rapid advance of electronics development and market trends, intensive work on radiation hardening is ongoing for electronics, components, materials and detectors with the main focus on HL-LHC. Continuous technology scouting and early technology analysis throughout the FCC design phase will be an important activity.

Communication links

A reliable, high performance communication link is a fundamental component of a new collider. It helps to move processing and control logic away from the radiation areas. Possibilities include fibre optic links and wireless technologies. A first study has been carried out on an Ethernet based solution.

The basic building blocks of such a system can be seen in Fig. 3.15. In this case, three components need to be radiation tolerant: the Ethernet physical layer component (PHY), a transceiver that bridges the digital world (including processors); field-programmable gate arrays (FPGAs); and application-specific integrated circuits (ASICs), which bridge to the analogue world. The MAC is usually integrated in a processor, FPGA or ASIC and controls the data-link-layer portion of the OSI model. Finally, an FPGA, a processor or an ASIC is needed to implement the application protocol. This solution will allow rates of several tens of Mbps with a low packet loss/failure factor to be reached.

Preliminary studies to evaluate the feasibility of using such a system to reliably transmit data over long distances in a radiation environment have been conducted [**?**]. This solution would use either hard or soft processors which are part of a microcontroller or FPGAs so that the system is able to conduct additional operations. The processor-based solution is not only chosen for the simplification of the

- JPO: [illegible] — JGu - This is not a second pillar.
- JPO: [illegible] — JGu: I suggest that we edit this part, which is not entirely clear. There are more than 2 "pillars". Also, I miss the fault-tolerant electronic design, which is the actual design rather than failure self-detection, which is a precondition for fault tolerant design. The fault-tolerance is described in the subsequent sentence.
- JPO: [illegible] — Is it accelerator or accelerated ?
- JPO: Add to glossary.
- JPO: [illegible] — Please check this statement.
- JPO: [illegible] — It is not clear to me if the processors are part of a microcontroller and part of an FPGA or the FPGAs are an alternative to the hard/soft processors. It is probably clear to an expert but it would probably be better

DRAFT FOR ADVISORY COMMITTEE - DO NOT DISTRIBUTE

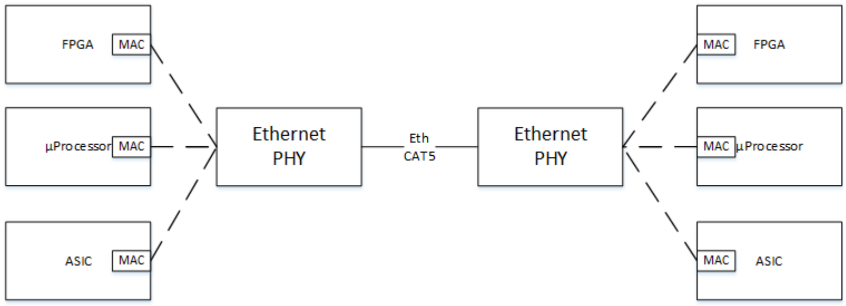

Figure 3.15: Ethernet Subsystem.

implementation of transmission protocols, but also for the processing of the input/output data. In order to achieve higher radiation tolerance in terms of single event upset, the best choice would be the use of a radiation tolerant flash-based FPGA with a radiation mitigated soft-core processor implementing the application protocol.

CMOS Technologies

Most of the on-detector application-specific integrated circuits (ASICs) being developed for HL-LHC make use of CMOS technologies in the 130 and 65 nm nodes. The study of radiation tolerance of these technologies has revealed that parasitic oxides used in the manufacturing processes are responsible for a significant degradation which limits their application. This is the case even in the pixel detector of HL-LHC REFERENCE [16-18], where the current plan is to replace the inner detector layers after 5 years of operation. As an example, Fig. 3.16 shows the dramatic degradation in the current capability of small size 65 nm transistors. This study is now extended to 40 and 28 nm technologies, where preliminary results show different phenomenology and demonstrate slightly more promising radiation tolerance.

CMOS technologies have been shifted from planar to bulk FINFETs starting from a nominal gate length of about 22 nm and have now reached the 7 nm pattern size. The literature consistently [REFERENCE] shows that TID tolerance has decreased with this miniaturisation due to radiation-induced leakage currents in the neck region of these devices, a characteristic that cannot be addressed by any design technique. This evidence shows that the construction of reliable electronics systems for FCC detectors cannot simply rely on the improved radiation performance which accompanies miniaturisation, a concept exploited largely for LHC and HL-LHC. The situation calls for an R&D programme on technologies and front-end systems, possibly nurturing new concepts such as disposable detectors.

DRAFT FOR ADVISORY COMMITTEE - DO NOT DISTRIBUTE

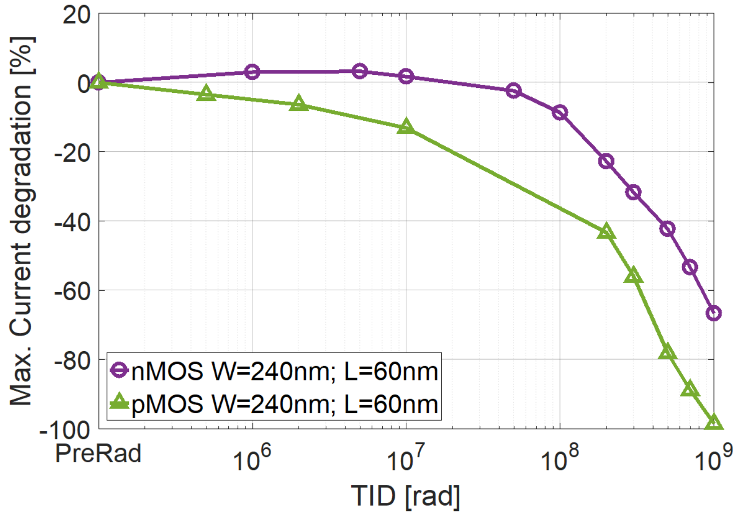

Figure 3.16: Percent degradation of the current capability for small-size nMOS and pMOS transistors in the 65 nm technology node up to 10 MGy.

DRAFT FOR ADVISORY COMMITTEE - DO NOT DISTRIBUTE

Chapter 4

Civil Engineering

4.1 Requirements and Design Considerations

The civil engineering design and planning is a key component in the establishment of the feasibility of the project. The tunnel for the collider will be one of the longest in the world; only water supply tunnels with smaller diameters are longer, and it will be similar in scope to the recently completed Gotthard Base Tunnel in Switzerland. Civil engineering typically accounts for around one third of the overall cost of large scale physics projects, therefore particular emphasis is placed on the civil engineering design and planning. Since the launch of the study, a variety of options for the machine layout have been considered, ranging from 40-100 km circular colliders to less conventional, racetrack shaped designs. The layout is now fixed on a quasi-circular layout with a circumference of 97.75 km. In addition to the machine tunnel, approximately 8 km of by-pass tunnels, 22 shafts, 16 large caverns and 12 new surface sites are required.

The emphasis for the underground structures has been on locating the machine within the natural boundaries defined by the geological formations of the Geneva basin with as short as possible connections to the SPS or LHC. The construction methods, and hence the technical feasibility of construction, have been studied and deemed achievable. For the access points and their associated surface structures, the focus has been on establishing possible locations that are realistic from social and environmental perspectives.

4.2 Layout and Placement

4.2.1 Collider Layout

The principal structure required for the collider is a 5.5 m internal diameter, 97.75 km long tunnel, comprising straight sections and arcs. In addition, large caverns are required at each of the four points (A, B, G and L) which house the experiments; these caverns have a maximum clear span of 35 m, which is at the limit of what is possible, given the ground conditions. At each of the access points around the ring, a service cavern with a span of 25 m is required. These caverns are connected to the surface via shafts with diameters ranging from 10 m to 18 m. Auxiliary structures in the form of by-pass tunnels and alcoves are required to house electrical equipment and connecting tunnels.

As the civil engineering infrastructure for the ee machine must also be compatible with the hh machine, and their lattice designs diverge as they approach experiment points A and G, portions of the tunnel must be wider to accommodate the two.

The excavation of the underground structures will produce approximately 10 million cubic metres of spoil. This will primarily be made up of sedimentary deposits, a mixture of marls and sandstone, a small fraction of the tunnel (approximately 5%) will be excavated in limestone.

Figure 4.2 shows a 3D schematic of the underground design.

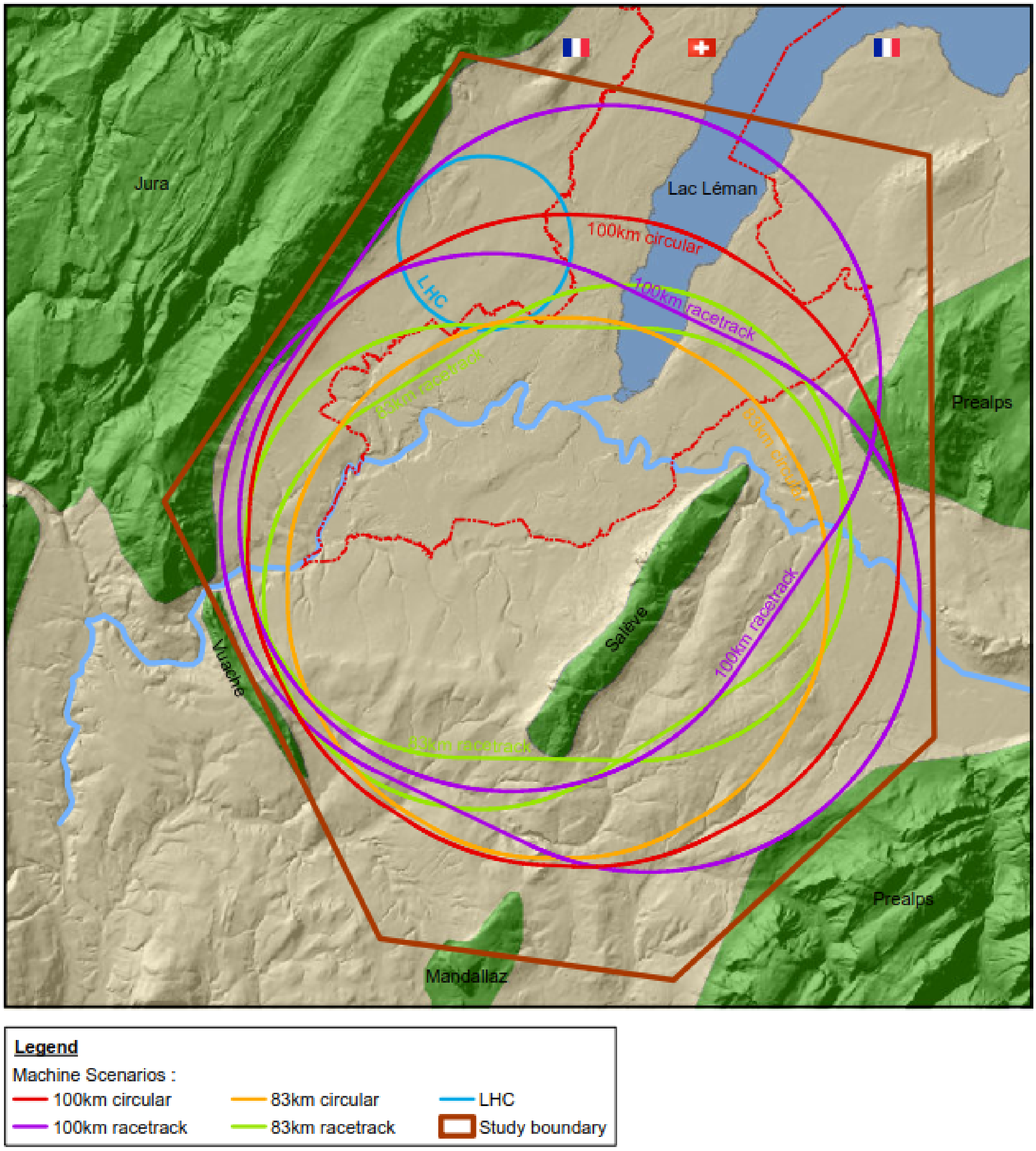

Figure 4.1: Boundary of the study (red polygon) with different machine placement scenarios.

4.2.2 Collider Placement

Experience from the construction of LEP and LHC, has shown that the sedimentary rock in the Geneva Basin, known as molasse, provides good conditions for tunnelling. During the excavation of the tunnel for LEP, water ingress from the limestone formations in the Jura mountains caused significant problems. For this reason, one of the primary aims when positioning the FCC tunnel was to maximise the fraction of the tunnel in the molasse and minimise that in the limestone. Another primary concern was to orientate the tunnel in a way that limited the depth around its perimeter, therefore minimising the depth of the shafts. These concerns, along with the need to connect to the existing accelerator chain, led to natural boundaries in the form of the Jura range to the north-west, the Vuache mountain to the south-west and the

DRAFT FOR ADVISORY COMMITTEE - DO NOT DISTRIBUTE

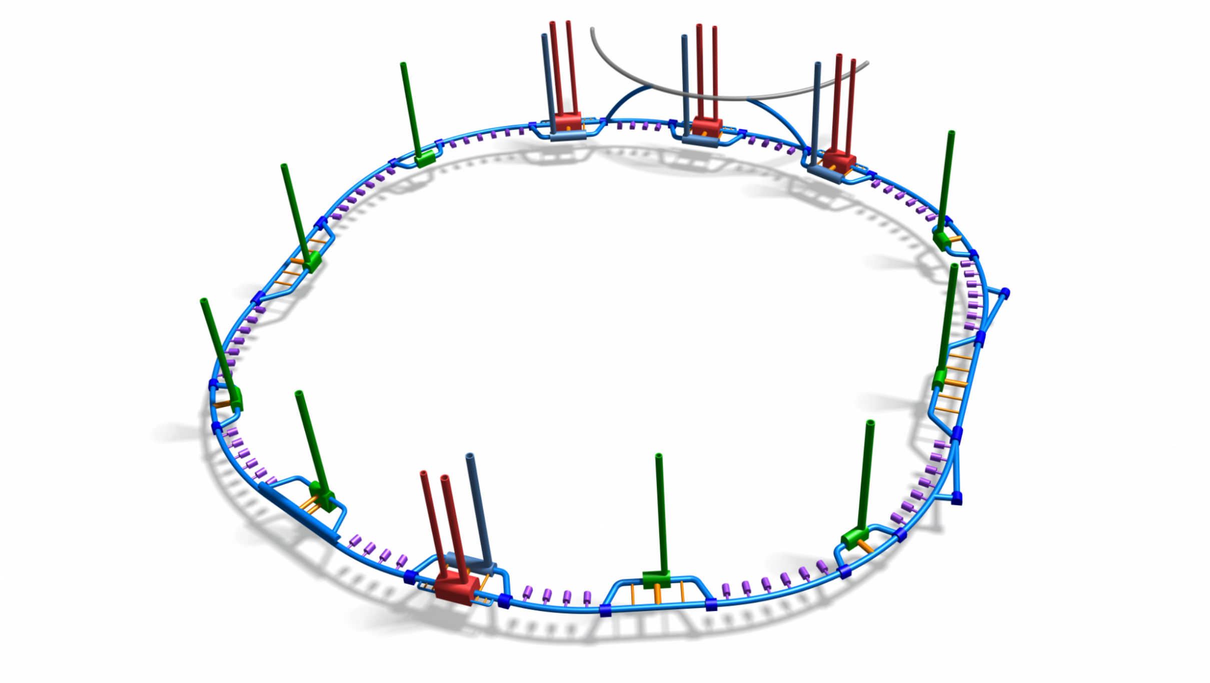

Figure 4.2: Three-dimensional schematic of the underground infrastructure (not to scale).

Pre-Alps to the south-east and east. An additional boundary is placed to the north due to the increasing depth of Lake Geneva in that direction. Figure 4.1 shows the boundary of the study in red.

In order to evaluate different layouts and positions within the boundary area, a bespoke digital tool incorporating a 3D geological model was developed. The Tunnel Optimisation Tool (TOT), developed specifically for the FCC study, is based on an open source driven Geographical Information system (GIS). GIS systems enable multiple sets of data to be arranged spatially, together with a physical or topographical map, and the ensemble can then be manipulated, managed and analysed as one. For TOT, this means that the user is able to input any size, shape and position of the tunnel and quickly see how this interacts with the geology, the terrain, the environment and the surface structures in the study area.

The geological data for the tool were collected from various sources including **[REFs for all used data]**, but not limited to: previous underground projects at CERN, the French Bureau de Recherches Géologiques et Minières (BRGM), existing geological maps and boreholes for geothermal and petroleum exploration. The data was processed to produce rock-head maps that formed the basis of the TOT. All of the geological data for the study has come from previous projects and existing data and no ground investigations have been conducted yet specifically for the FCC project.

The machine studies demonstrated that it was necessary to have a circumference of $\sim$100 km in order to meet the physics goals. Using the TOT, the alignment of the tunnel has been optimised based on criteria such as: geology along the tunnel, overburden, shaft depth and surface locations. The location has been refined by making small variations in the position to avoid the limestone of the Jura and Pre-Alps, whilst also minimising tunnelling in the water-bearing moraine layer and also keeping overburden to a minimum. A good solution for the location of the machine has been found in which the tunnel is located primarily in the molasse (90 %). This avoids the limestone of the Jura mountains and the Prealps but passes through the Mandallez limestone formation, which is unavoidable. The tunnel passes through the moraines under the lake at a depth where the moraines are believed to be well consolidated, and whilst there will be some additional challenges during excavation, the long term stability of the tunnel is not a major concern. The topographical and geological profile of the tunnel in the chosen position is shown in Figure 4.3.

DRAFT FOR ADVISORY COMMITTEE - DO NOT DISTRIBUTE

The tunnel position places the shafts in reasonable positions with acceptable depths of less than 300 m apart from Shaft F which requires special attention as it is 558 m deep. In this case it has been necessary to replace the shaft with an inclined tunnel.

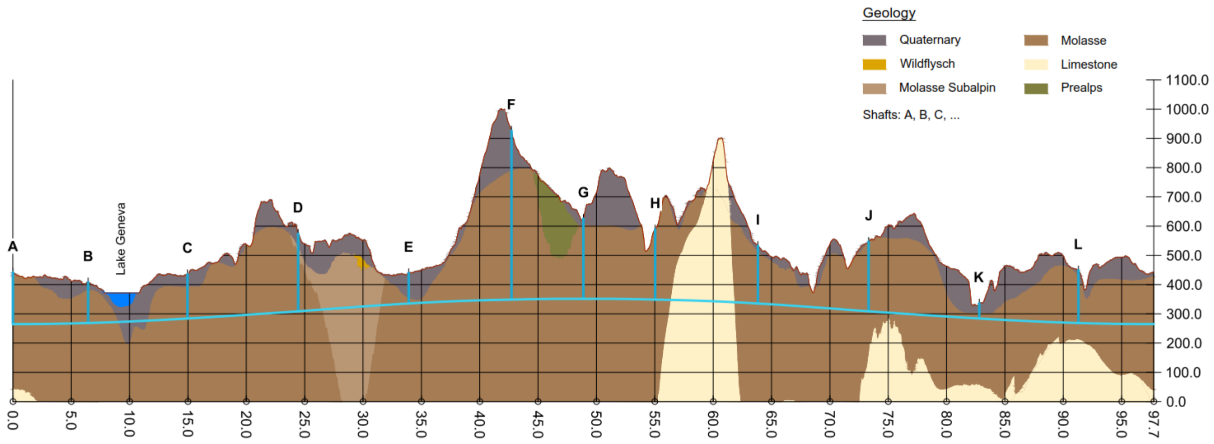

Figure 4.3: Geological alignment

4.2.3 Future Site Investigations

Based on the available geological data for the region, the civil engineering is deemed feasible, however, in order to confirm this and provide a comprehensive technical basis for the design, extensive ground investigations are required. These investigations will take the form of non-invasive techniques such as walkover surveys and geophysics, and also invasive techniques, such as boreholes. A combination of in-situ tests, such as the standard penetration test (SPT) and permeability test, in combination with laboratory testing on the samples, will give a comprehensive understanding of the geological situation.

In order to confirm the feasibility, the initial site investigations must encompass the highest risk areas: the crossing of Lac Leman, the Rhone and the Arve valleys. In addition, each access point location should be investigated. This can be conducted via geophysical investigations and could lead to a recommendation for the alignment to be adjusted to reduce the construction cost and risk.

4.3 Underground Structures

4.3.1 Tunnels

A 5.5 m internal diameter tunnel is required to house all the necessary equipment for the machine. Figure 4.4 shows the cross-section of the empty tunnel but with the air supply and smoke extraction ducts, which have been integrated into the civil engineering design. The smoke extraction duct structure comprises a 70 mm thick steel structure with passive fire protection on both sides, connected to the lining using post-drilled anchors. The air-supply duct in the floor is a pre-cast structure and the rest of the floor will be cast in concrete around it. Separation walls with fire safety doors spaced 440 m apart are required along the entire length of the machine tunnel.

The tunnel will be constructed with a slope of 0.2% in one plane, this is in part to optimise the geology intersected by the tunnel and the shaft depths, but also to facilitate the use of a gravity drainage system.

It is anticipated that the majority of the machine tunnel will be constructed using tunnel boring machines (TBMs), but the sector passing through the Mandallaz limestone formation will be mined. For the TBM excavations, different lining designs have been developed corresponding to the "good" or "poor" conditions of the rock. For TBM excavation in a sector with "good" conditions, a single pass

DRAFT FOR ADVISORY COMMITTEE - DO NOT DISTRIBUTE

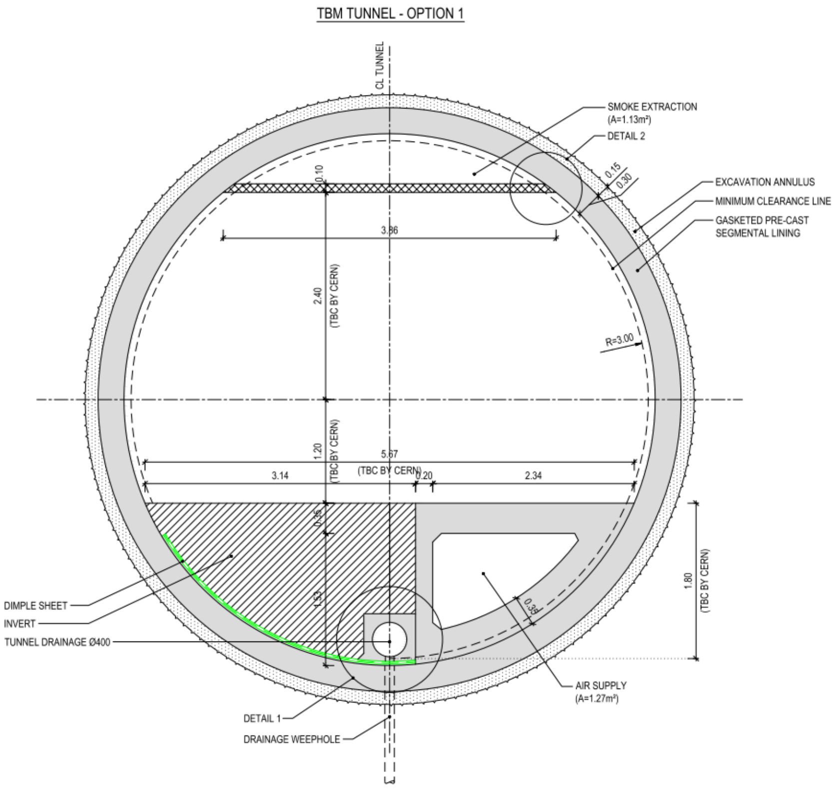

Figure 4.4: Machine tunnel cross-section in "good" molasse

pre-cast lining is adopted. This is the fastest and cheapest construction method but is reserved for sectors that are completely located in molasse with a good rock coverage and hence a low risk of water inflow. For sectors in "poor" conditions to be excavated with a TBM, an optional second cast in-situ lining can be incorporated. This reduces the risk of water flow in sectors which are located in the molasse, but where the depth of rock to the water bearing layers is minimal. Construction under the lake presents another situation which is the same as for "poor" conditions but with a thicker initial pre-cast lining. Table 4.1 shows the lining and excavation parameters for each of the TBM lining cases.

As mentioned in Section 4.2.1, widening of the tunnels is required on each side of the experiment caverns at Points A and G. These enlargements extend for 1.1 km on either side of the caverns. For construction purposes, the enlargements will be created in a "stepped" design as shown in (Figure to be added); this allows the formwork to be re-used for optimal lengths whilst at the same time not constructing an excessive volume. The widest part of the enlargement will have a span of 18.14 m. These enlargements can either be constructed by allowing the TBM to pass through to the experiment cavern and then excavating the additional volume required with a roadheader, or stopping the TBM before the start of the enlargement and then excavating the entire volume with a roadheader. The costs and construction rates for these two methods are comparable and the method chosen will be based on compatibility with the construction schedule as a whole.

It is necessary to excavate the tunnel under Lake Geneva in water bearing moraines between sectors B and C (see Figure 4.3). In order to achieve this, it is necessary to employ an Earth Pressure Balanced Tunnel Boring Machine (EPB TBM). During excavation with this type of machine, the excavated material behind the cutter face is pressurised to support the tunnel face. Consequently, the excavation can be achieved safely and efficiently in the wet and unstable conditions. It is anticipated the layer of moraines to be excavated is impermeable enough that the tunnel would not be affected by the fluctuating depth of the lake and hence would not disrupt the machines once in operation, however, this risk must be

DRAFT FOR ADVISORY COMMITTEE - DO NOT DISTRIBUTE

Table 4.1: Proposed TBM cross-section parameters

Parameter	**TBM tunnel in "good rock"**	**TBM tunnel in "poor" rock**	**TBM tunnel in moraines**
Minimum internal diameter (m)	5.5	5.5	5.5 m
Characteristic compressive concrete strength for pre-cast concrete, fck (Mpa)	50	50	50
Pre-cast concrete thickness (m)	0.30	0.30	0.45
Reinforcement density for pre-cast concrete	Steel fibre (50%) and bars at 80 kg/m^3	Steel fibre (50%) and bars at 80 kg/m^3	150 kg/m^3
Gasketed segments	yes	yes	yes
Cast insitu concrete thickness (m)	None	0.25	0.25
Characteristic compressive concrete strength for in-situ concrete, fck (Mpa)	-	40	40
Reinforcement for in-situ concrete	-	local reinforcement cages	local reinforcement cages
Total radial construction tolerance (m)	0.10	0.10	0.10
Excavation diameter (m)	6.3	6.8	7.1

evaluated once additional ground investigations have been conducted.

In addition to the machine tunnel, auxiliary tunnels are required for by-passes, connections, beam dumps and transfer lines. These have similar requirements to the machine tunnel and depending on their diameter and position in relation to the TBM launch points, will be constructed using a TBM or roadheaders.

4.3.2 Shafts

There are 22 large diameter shafts included in the design: one at each of the 12 access points for service connections (12 m diameter), at the 4 experiment points, an additional 2 shafts connecting into the experiment caverns (15 m and 10 m diameters) and finally, 2 shafts located near to the existing CERN accelerators. The latter are required to facilitate the removal of spoil during construction of the connection to the LHC or SPS. At least one of the access shafts requires a diameter of 18 m to accommodate magnet lowering; the possibility of having an elliptical shaft with a maximum width of 18 m, in place of a circular shaft of diameter 18 m, is under consideration as this requires less material. However, this was only deemed economically efficient in the molasse as extra reinforcement would be required to support the inherently less strong elliptical shape in the moraines. Therefore, it is anticipated that the magnet lowering shaft(s) will be circular in the moraine layer and elliptical in the remaining depth in the molasse.

The shafts range in depth from 52 m to 274 m and as previously mentioned, the shaft at Point F has been replaced with an inclined access tunnel. This inclined tunnel has a length of 2750 m and a gradient of 15%. This is deemed a better solution than a 558 m vertical shaft as it would be faster and cheaper to construct (although not considerably), the lift system would not be feasible in a shaft of that depth, and a better location for the access portal can be found with the inclined access.

Internal structures in the form of staircases and lift shafts are required within the service shafts. Figure 4.5 shows the layout of these items; the lift shafts and the staircases are pre-fabricated concrete structures. The initial excavation for each shaft will be through a layer of glacial deposits known as moraines and this will be achieved either by using a diaphragm wall or a vertical shaft sinking machine (VSM). The remainder of each shaft will be constructed using traditional excavation techniques with

DRAFT FOR ADVISORY COMMITTEE - DO NOT DISTRIBUTE

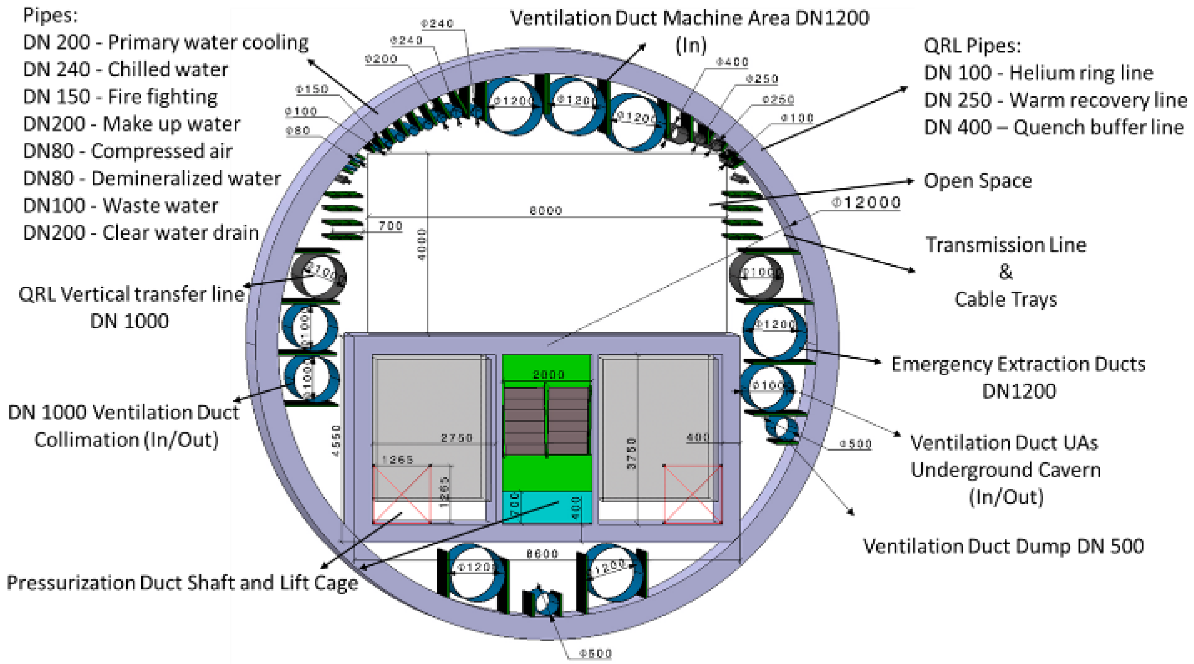

Figure 4.5: Service shaft cross-section

JPo
Add shotcrete to the glossary

shotcrete followed by a cast in-situ lining.

4.3.3 Alcoves

Alcoves for electrical equipment are required every 1.5 km around the machine circumference. These are 25 m long, 6 m wide and 6 m high, located on the inside of the ring at 90°to the machine. The excavation for these will be carried out after the machine tunnel drives, this will be followed by the inner lining work for the alcoves before the secondary lining of the machine tunnel.

4.3.4 Experiment Caverns

Very large span caverns are required at each of the four experiment points to accommodate the detectors. The dimensions for the caverns at A and G are 66 m×35 m×35 m (L×W×H), and at L and B, where the secondary experiments will be housed, 66 m×30 m×35 m (L×W×H). The caverns will be constructed at depths of up to 274 m in the molasse layer. The exact construction sequence is yet to be confirmed, however, it will include benched excavations using a rockbreaker and roadheader with the primary support being provided by rock bolts, cable bolts and some layers of steel fibre concrete. During the widening of the crown area of the experiment cavern, additional girder lattices and layers of steel fibre reinforced shotcrete will be installed. The lattice girders for the various excavation steps can be bolted together to ensure continuous rock support along the excavated area. The final lining will be concrete, cast in-situ. A proposed excavation sequence is shown in Figure 4.6.

JPo
Add rockbreaker and roadheader to the glossary

4.3.5 Service Caverns

A service cavern with dimensions of 100 m×25 m×15 m (L×W×H) is required adjacent to the experiment caverns at Points L, A, B and G, and also at the remaining 8 access points. These will be constructed in a similar manner to that for the experiment caverns. At the experiment points, the spacing between the two caverns is 50 m as this allows the structures to be independent and hence minimises the structural support needs and reduces the risk and complexity during construction.

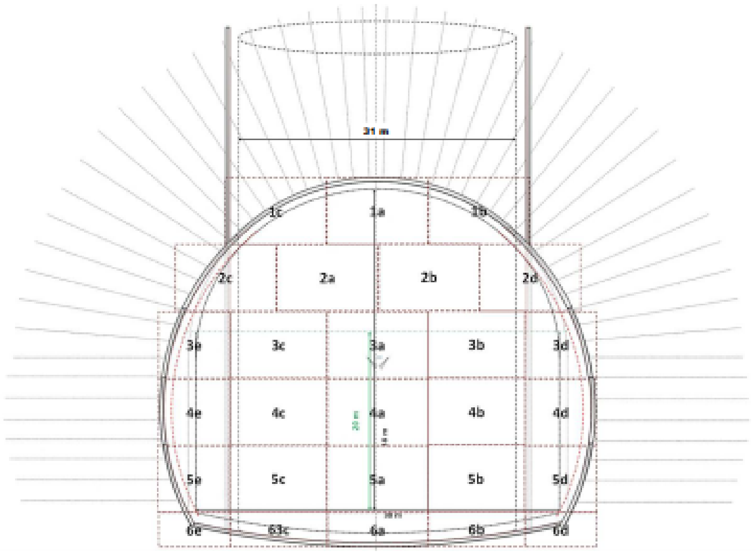

Figure 4.6: Excavation sequence for an experiment cavern

4.3.6 Junction Caverns

There are three types of junction caverns which are required for structural purposes when tunnels of similar size connect, for example a by-pass tunnel connecting to the machine tunnel. There are 26 locations which require a junction cavern, ranging in length from 30 m to 400 m and with a cross section of 16.3 m×8.3 m (W×H). The longest junction caverns also serve as reception points or crossing points for the TBMs. A 400 m long junction cavern is also required for each of the beam dumps to accommodate the dump beamline up to the point where it is possible to have a separate tunnel for the dump line.

4.4 Surface Points

4.4.1 Experiment Surface Site

The conceptual design for surface sites range from classical sites similar to the LHC (for example see Fig. 4.7 which shows the CMS site) to semi-underground installations. Specific designs will reflect the particular machine and environmental requirements.It is anticipated that each site will be approximately 6 hectares in size. In most cases it is expected that there will be a large shaft head building, which will also act as the detector assembly hall during installation. The surface sites will also be used for assembly and temporary spoil storage sites during construction and therefore their location is critical to minimise the impact of the project on the surroundings. Every effort will be made during the design process to minimise the visual, environmental and acoustic impact of these sites, which could mean building parts of the site below ground.

Using TOT, it has been possible to quickly assess surface sites for suitability, by evaluating the proximity to existing structures, protected areas and transport links. With the chosen collider placement, it has been possible to locate site A near to the CERN Meyrin campus on existing CERN land. Points L, A and B are in Switzerland and point G is located in France. Table 4.2 lists the anticipated structures and their dimensions for a typical surface site.

4.4.2 Technical Surface Site

The 8 access points without experiments will require surface sites for the technical facilities. The requirements are similar to those for the experimental surface sites except that the shaft head building is smaller. All the technical sites are located in France apart from point C, which is in Switzerland.

DRAFT FOR ADVISORY COMMITTEE - DO NOT DISTRIBUTE

Table 4.2: Proposed Structures at a typical Experiment Site

Structure Name	Structure Type	Material	Dimensions

4.4.3 Access Roads

It is preferable for the sites to be accessible via existing roads, however, it is anticipated that additional roads and even tunnels or bridges may be necessary for the more remote sites. The large dipole magnets and detector components will need to be transported along these roads, as well as the vehicles and machinery for construction, hence the roads must be able to withstand heavy loads. For costing purposes, it has been assumed a new 5 km road is required for each surface facility.

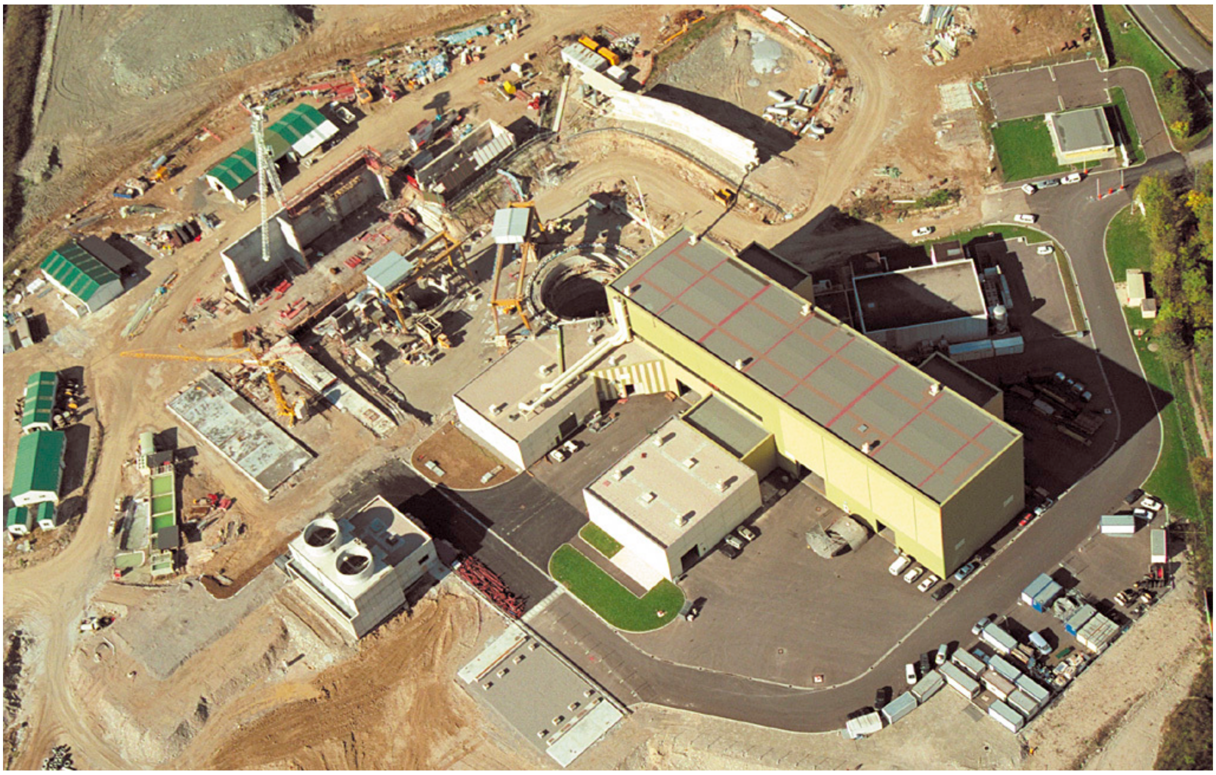

Figure 4.7: Photograph of the CMS surface site during construction

DRAFT FOR ADVISORY COMMITTEE - DO NOT DISTRIBUTE

Chapter 5

Technical Infrastructures

Volker Mertens: Volker Mertens, 20 pages

5.1 Requirements and Design Considerations

The Technical infrastructure comprises a large and diverse set of services, to enable and support the operation of the accelerator and the experiments. These include the supply with electrical energy and cryogens, the removal of heat from water and air, facilities to transport people and material, the geodetic network, survey and alignment, control of accelerator equipment, data acquisition, computing and networking, as well as access control and other safety relevant functions.

As customary for other facilities at CERN, the FCC will make as much use of the existing chain of pre-accelerators as possible, but it will require a specific linac, damping rings and transfer lines. As a new large-scale accelerator facility, the FCC will require a set of new infrastructure systems. Some of them, like computer networks, will integrate with the existing infrastructure; others, like the supply of electrical energy, will be extend the existing facilities.

Building a large facility which crosses borders in a densely populated area like the Geneva basin requires that a wide range of conditions and regulations are respected, in terms of environmental and socio-cultural compatibility. The whole FCC, including its technical infrastructure, must be designed and built for safe, high-performance operation, with high reliability and availability in mind. The equipment will generally be energy- and cost-effective. Future-oriented, yet technically solid approaches are be chosen to ensure enduring high performance and affordable operation.

5.2 Piped Utilities

5.2.1 General introduction to piping systems

The piping systems for the FCC will consist of:

- industrial water and demineralized water: for the cooling of technical equipment for accelerators and detectors such as electronic racks, cryogenic equipment, etc.;
- Chilled water: for cooling of ventilation systems (air handling units);
- Drinking water: for sanitary purposes and make up of raw water circuits;
- Raw water: for fire fighting purposes;
- Waste water: reject and drain of waste water from underground and surface premises;
- Compressed air.

5.2.2 Cooling plants

The cooling plants using raw water will remove most of the heat generated by the accelerator equipment, the detector and in the technical areas; it is foreseen to install one plant in each Point.

The water cooling plant will consist of:

– a primary circuit, using raw industrial water, and cooled by means of open wet cooling towers; some equipment, in particular cryogenics systems, will be directly cooled by the primary circuit;
– a secondary circuit: connected via a heat exchanger to the primary system, it will use in most cases demineralized water in a closed loop.

Distribution circuits will be grouped according to the equipment typology to be cooled and having similar pressure rates. The depth of the underground premises with respect to the surface, being up to 400 m, will require the implementation of an underground cooling station in the cavern of each Point where a heat exchanger will separate the circuit coming from the surface (with a static pressure above 40 bar) from the distribution circuit in the underground; wherever possible this separation will correspond to the separation between primary and secondary circuit but it will be also applied for other circuits such as those of cryogenic equipment in the underground. The decoupling of the surface from the underground circuit will allow a safer operation of the underground circuit as well as a strong cost reduction for pipes at a lower NP rating.

For operability and maintenance purposes, the cooling stations, both on surface and in underground, shall be accessible during the run of the accelerator.

In Points A, C, E, G, I and K, a cooling area in the underground cavern, shall host the secondary circuit station cooling each adjacent sector as well as other equipment such as the cryogenics and the Experiment (where existing); in Points B and L, a similar area will be dedicated to the cooling of the Experiment and in Point H to the cooling of the RF. The secondary circuit in each sector shall also cool the air handling units in the alcoves in addition to the accelerator equipment.

Primary circuits will use raw industrial water with a make up of drinking water to compensate for evaporation, losses and blowdown; continuous water treatment against legionella, scaling and proliferation of algae will also be included. The drinking water make up is assumed to be provided by the local water supplier from the network located outside each Point.

Secondary circuits will use demineralized water having a maximum conductivity of 0.1 ÎijS/cm in a closed loop and, to keep the conductivity under control, a set of demineralization cartridges will be implemented in each circuit. The demineralized water shall be produced in a centralised station; however, given the long distances, it will not be possible to foresee an automatic refill pipework from this station via the tunnel to all the circuits in the different Points without decreasing excessively the quality of the water. In case of leak, refill will be made by transporting in tanks the required volume of water from the production to the concerned point.

The level of redundancy of the primary and secondary circuits is defined at N+1 for pumps and cooling towers to ensure continuous operation in case one equipment will stop; no redundancy is needed for plate heat exchangers, power and control cubicles. At present, it is not foreseen a secured power supply for the cooling plants since, in case of general power failure and therefore stop of all accelerator equipment, no cooling activity is needed until the restart of the accelerator. In order to allow essential cryogenic equipment to be kept at low temperatures also during mandatory yearly stop for maintenance and cleaning, some cooling towers with a smaller capacity shall be installed in backup to the main ones.

A dedicated plant shall be installed within the each cooling tower to concentrate the chemicals in the water rejected from cooling towers and to recycle most of the water; it shall allow to decrease around 50% of the make up needs and more than 70% of the rejected volume with respect to the volumes currently needed.

DRAFT FOR ADVISORY COMMITTEE - DO NOT DISTRIBUTE

At a later stage of the project, the recovery of the waste heat from the cooling towers shall be studied in order to reduce the environmental impact of the project; in particular, studies shall be made both for internal use of the low temperature heat as well as for use in the area surrounding each Point.

5.2.2.1 Operational parameters

The design parameters for the cooling plants are:

- primary circuit: 40°C at the inlet of the cooling towers and 25°C at the outlet of the cooling towers;
- secondary circuit: 27°C at the inlet of the heat exchanger and 42°C at the outlet of the heat exchanger.

The temperature difference between inlet and outlet is 15 K with a tolerance of about 0.5°K. In the following tables the cooling powers installed in each Point are detailed according to the equipment.

The pipework diameter in the tunnel is optimized with respect to the pressure loss of the circuit taking into consideration its length; this allows to reduce the required pressure rate of the pipeline or to avoid installing booster pumps at specific intervals in the sectors.

Tables 5.1 and 5.2 report the total powers and the nominal diameter for the circuits in surface and in the underground of each Point.

Table 5.1: Cooling powers and diameters for circuits on surface of the FCC Points

Point		**Total Point**	**Cryogenics**	**Exper.**	**Power Con-verter**	**Gen. Services**	**Chilled water**	**Undergr. circuit**
A	P [MW]	20.6		0.5	0.25	2.0	2.4	15.5
	ND	600		100	80	200	200	400
B,L	P [MW]	4.0				2.0	2.0	
	ND	350				200	200	
C,K	P [MW]	25.8			0.4	2.0	2.5	21.0
	ND	650				200	250	450
D,J	P [MW]	59.7	27			2.0	7.7	23.0
	ND	800	500			200	400	450
E,I	P [MW]	26.2			0.4	2.0	2.5	21.4
	ND	700			80	200	250	450
F	P [MW]	4.0				2.0	2.0	
	ND	200				200	200	
G	P [MW]	22.0		0.5	0.2	2.0	4.6	14.7
	ND	600		100	80	200	300	350
H	P [MW]	4.0				2.0	2.0	
	ND	200				200	200	

5.2.3 Chilled water

The cooling for ventilation plants (dehumidification or air cooling) will require the installation of chilled water production stations in each Surface Point and some distribution circuits on surface and in the underground up to the air handling units. No chilled water is needed, at present, in the sectors.

The chilled water is foreseen to be produced at a temperature of 6°C and return at 12° C; chillers shall be water cooled and connected to the cooling towers of each Point. The cooling power needed and the number of chillers are indicated in the following table 5:

DRAFT FOR ADVISORY COMMITTEE - DO NOT DISTRIBUTE

Table 5.2: Cooling powers and diameters for circuits in underground of the FCC Points

Point		Total underground	Cryogenics	Exper.	RF	Tunnel (left)	Tunnel (right)
A	P [MW]	15.5		0.5		7.5	7.5
	ND	400		100		500	500
C,K	P [MW]	21.0				9.9	11.1
	ND	450				500	600
D,J	P [MW]	23.0	1.8		21.2		
	ND	450	150		500		
E,I	P [MW]	21.4				11.1	10.3
	ND	450				600	600
G	P [MW]	14.7		0.5		7.1	7.1
	ND	350		100		500	500

As for the cooling circuits, the redundancy level is defined to ensure continuous operation in case of breakdown of one single element (chiller or distribution pump); in case of a general power failure, a buffer tank in each production circuit will ensure sufficient autonomy of part of the plant for a limited period of time; the distribution pumps shall therefore be connected to the secure electrical network.

Table 5.3 presents the total powers and the main characteristics of the chilled water circuits of each Point.

Table 5.3: Main characteristics of chilled water circuits

Point	Cooling power [kW]	Flow rate [m3/h]	Number of chillers	Cooling power/ chiller [kW]
A	1780	255	3	900
B,L	1500	215	3	800
C,K	1850	115	3	900
D,J	5760	827	4	2000
E,I	1860	267	3	1000
F	1490	214	3	800
G	3460	497	4	1200
H	1490	214	3	800

5.2.4 Drinking water

Drinking water will be used for personnel use and for make up to cooling towers and it is foreseen to be provided by the local drinking water network adjacent to each Point; in case the drinking water network surrounding one Point will not have enough capacity to provide the required flow for the make up of cooling towers, only the water for this use will be provided from the closest Point having such capacity and via a pipeline in the tunnel; in such case, the same pipe shall also be used for fire fighting purposes in the concerned sector.

5.2.5 Fire fighting network

It is foreseen to install a water network dedicated to fire fighting purposes in the underground premises, caverns and tunnel, composed by a pipe connected to fire hoses at regular length intervals and having

DRAFT FOR ADVISORY COMMITTEE - DO NOT DISTRIBUTE

Storz connections; in case of major damages to this pipe, some isolation valves installed along the sector will allow to isolate the damaged part and keep operational the rest of the circuit by the fire brigade. This pipe is foreseen to be kept dry, to avoid stagnation and corrosion, during normal operation and, in case of fire, water will be supplied from surface by opening isolation valves. Each sector can be supplied by both adjacent Points, in order to guarantee a redundant supply.

Surface premises shall be protected by a hydrant network and, where needed, by dedicated water hoses inside the buildings.

Water supply is, for the time being, foreseen to be ensured by existing public water network in proximity of each FCC Point; in case this network will not be able to ensure the requested water flow, volume of water or the level of redundancy, two options shall be taken into consideration: the installation of water tanks in the concerned surface point or the supply of water from the adjacent Point via the pipe installed in the tunnel.

5.2.6 Reject water

Two systems of raising pumps for clear water and for sewage will be installed in the underground of each Point and connected to the local drainage network of the Surface Point; all equipment located in the underground (tunnel or caverns) must be redundant in order to avoid affecting operation in case of breakdown. Dedicated alarms for high level and too high level will be implemented in all basins.

The main parameters (e.g. temperature, pH) of the rejected water will be monitored before release from the Point.

In case the rejected water should not comply with the needed level of quality, should present a risk of environmental pollution, compensatory measures, such as retention basins, shall be taken.

5.2.7 Compressed air

The compressed air for all equipment and the actuators shall be provided via dedicated compressed air stations located in each surface Point and supplying surface and underground premises. A level of redundancy of N+1 is foreseen to ensure the reliability and maintainability of the plants.

5.3 Heating, Ventilation, Air Conditioning

5.3.1 Design

The ventilation installations are designed to:

- supply fresh air for people,
- provide heating and ventilation,
- maintain a suitable temperature at the surface of the different equipment,
- dehumidify the supplied air to prevent condensation,
- allow smoke and gas extraction,
- purge the air of the tunnel before access,
- filter the exhaust air.

5.3.2 Indoor conditions

The indoor conditions to be ensured by the ventilation system are the following:

- FCC Tunnels (with maximum heat load): max 32°C
- Experimental Caverns: 18/32°C - from floor to vault;

DRAFT FOR ADVISORY COMMITTEE - DO NOT DISTRIBUTE

– Surface buildings with controlled temperature: 18°C during winter, 25°C during summer.

It has to be noted that, for surface buildings, the values indicated are mean values at heights where people and equipment are foreseen.

The relative humidity does not need to be regulated except for some specific areas (Faraday cage, clean rooms or other laboratories) that might request a humidity regulation system and whose design will be performed at a later stage. The dew point will however be kept below 12°C to avoid condensation.

The outdoor conditions for Geneva region considered to dimension the air handling equipment are 32 °C for dry bulb temperature and 40% for RH during summer and -12°C for dry bulb temperature and 90% for RH during winter.

As a general principle, a free cooling and air recycling approach will be adopted in order to reduce the electrical consumption.

5.3.3 Ventilation of underground premises

In general, the underground caverns are ventilated by air handling units located on the surface and therefore accessible at any time; redundant units (Level N+1) have been foreseen everywhere in order to avoid impacting the operation of the accelerator in case of breakdown. Air is supplied for each sector from both endpoints in order to ensure air supply also in case of a duct failure; the same configuration is also adopted for the extraction. All points supply and extract air for both adjacent sectors. In case of failure of one unit, the other one would accelerate to ventilate both adjacent sectors

One of the two units dedicated to air extraction will not be equipped with filters since these units will be used to extract smoke, which could clog the filters. All systems related to safety issues will be powered by the secure electrical network.

5.3.4 Machine tunnels

The FCC tunnel needs to be sectorized with walls and fireproof doors in order to better handle propagation of smoke in case of fire, or of helium gas, in case of rupture of cryogenic equipment or of its distribution line. Therefore, the selected ventilation scheme is the semi-transversal one, i.e. the air is supplied via a dedicated duct all along the sector and extracted either by the tunnel itself, or by an emergency extraction duct.

The air supply duct runs in the concrete slab and supplies air to the tunnel about every 100 m via some diffusers at the floor level, whereas for the emergency extraction, a circular segment duly isolated at the upper part of the tunnel, is used as a duct. The inlet diffusors and extraction grills are offset with respect to each other in order to ensure a better distribution of the air in the tunnel and to avoid shortcuts between supply and extraction. Fire resistant dampers will be installed at every connection with diffusors and grills for the extraction: in case of fire or helium release, they will allow to better manage the ventilation in the concerned compartment of the tunnel.

During normal operation, all the extraction dampers and doors in the whole sector are open. In case of smoke or helium release detection, only the dampers at the extraction duct in the affected compartment and in the adjacent ones will be kept open; the doors of these compartments will be closed and for the other compartments,the air supply will still be ensured and, the extraction will be done via different air handling units on the surface.

5.3.5 Experimental caverns

For the ventilation of the Experimental caverns, the air is blown via diffusers at floor level (or at the different floor levels) and extracted via one or more ducts located on the vault; dedicated gas extraction system shall be installed where needed.

DRAFT FOR ADVISORY COMMITTEE - DO NOT DISTRIBUTE

5.3.6 Other premises

Local cooling air handling units will be added in areas housing equipment with high heat dissipation. These units will be fitted with coils cooled by chilled water produced on the surface.

5.3.7 Operational modes

Different modes are foreseen for the ventilation systems depending on the operating conditions, as presented in table 5.4.

All motors for ventilators are foreseen to be equipped with variable speed drives in order to adjust flow rates, to adapt the working conditions to the operational needs and to achieve the requested dynamic confinement between adjacent areas, where requested.

Table 5.4: Operational modes for ventilation systems

Run	No access, accelerators running and equipment powered, full air recycling.
Shutdown	Open access, accelerator stopped, maintenance interventions, fresh air/partial recycling.
Purge	Where needed, before allowing access to personnel, accelerator stopped, fresh air

5.3.8 Working parameters

Table 5.5 shows the main ventilation parameters of an FCC tunnel sector while those of the ventilation plants for the underground premises are reported in Table 5.6. In areas where a supply and an extraction system are installed, the air can be recycled according to the operational mode.

Table 5.5: Working parameters for the ventilation of one machine tunnel sector

Air flow from each side in Run and Shutdown mode (m3/h)	25000
Air flow from each side in Purge modes (m3/h)	50000
Number of diffusors and extraction grills per compartment	4
Air flow per diffusor (m3/h)	520
Supply duct nominal diameter (mm)	1200

Table 5.6: Working parameters AHUs dedicated to underground premises

Underground premise	Nominal flow rate [m3/h]	Duct nominal diameter [mm]	Air recycling
Shaft and safe area pressurization (m3/h)	45000	1200	No
Fresh air to Service Caverns in accelerator points (points B to F and H to L)	15000	1000	No
Ventilation of Service Caverns in experimental points (points A and G)	45000	1200	Possible
Ventilation of RF areas(point D and J)	6000	700	Possible

DRAFT FOR ADVISORY COMMITTEE - DO NOT DISTRIBUTE

The filtering level of the exhaust air before release to the atmosphere will be defined mainly according to the radioprotection constraints.

Table 5.7 shows the heat dissipation of the different equipment to be removed by the ventilation systems on surface and table 5.8 provides the same loads in the underground.

Table 5.7: Main heat dissipation on surface in each Point

Point		**Cryogenics**	**Experiments**	**Power Converters**	**Gen. Services**
A	P [kW]		50	7	500
B,L	P [kW]			14	500
C,K	P [kW]			14	500
D,J	P [kW]	1100		14	500
E,I	P [kW]			14	500
F	P [kW]			7	500
G	P [kW]		50	7	500
H	P [kW]			7	500

Table 5.8: Main heat dissipation in underground in each Point

Point		**Dump**	**Cryogenics**	**Experiments**	**RF**	**Tunnel right**	**UW**
A	P [kW]			50		375	200
B	P [kW]					493	
C	P [kW]		140			557	200
D	P [kW]	50	120		2210	557	
E	P [kW]					515	200
F	P [kW]					356	
G	P [kW]			50		356	200
H	P [kW]					515	
I	P [kW]					557	200
J	P [kW]		120		2210	557	
K	P [kW]					493	200
L	P [kW]					375	

5.3.9 Ventilation of surface buildings

Each surface building will be ventilated with a dedicated air handling unit. Where the building size requires, several units in the same building are foreseen; each of them being in charge of a part of the building.

At present, no redundant units are considered necessary in these buildings; should this be needed, redundancy can be easily implemented. All surface buildings will be equipped with a mechanical system on the roof to extract smoke (400°C, 2 hours).

5.3.10 Safety

In general, smoke extraction is foreseen in all the facilities presenting an important risk because of the fire loads or to ensure the safety of personnel. In case of fire, in addition to the automatic actions, the fire brigade will be able to switch off or reconfigure manually the ventilation control system.

DRAFT FOR ADVISORY COMMITTEE - DO NOT DISTRIBUTE

All the supply air handling units are equipped with smoke detection sensors downstream of the ventilator in order to avoid injection of smoke in the underground areas.

The concrete module of the lift and staircase in the shafts is kept in overpressure with respect to the surrounding areas in the underground and therefore will be used as safe area in case of emergency.

According to standards, a pressure cascade among areas at higher level of activation and areas with a lower one has to be ensured; therefore the machine tunnel is foreseen to be at a lower pressure with respect to the experimental caverns as well as to ancillary areas. Volumes with higher risk activation are separated from less activated areas by airlocks that are kept pressurized by dedicated fans installed in the less activated areas.

Exhaust air ducts will have branches to connect the air monitoring equipment for radioprotection monitoring before release to the atmosphere.

5.4 Electricity Distribution

5.4.1 Electrical Network

The concept for the design of the FCC-ee electrical network is driven by three factors:

1. The estimated electrical power requirements as presented in Table **??**
2. The location and type of equipment to be supplied and
3. The expected level of electrical network availability and operability.

The electrical network is composed of a transmission and a distribution level. The transmission level transmits the power from three sources to three FCC points and between the twelve FCC points. This level operates at voltages of 400 kV and 135 kV. The distribution level distributes the power from the transmission level to the end users at medium and low voltage levels comprised between 36 kV and 400 V. The present baseline uses conventional AC schemes. However, emerging new technologies based on DC schemes, which could improve the power quality and power consumption efficiency, are presented in Section **??**.

5.4.1.1 Source of electrical power supply

For the most demanding FCC-ee $t\bar{t}$ configuration, the estimated 421 MW electrical power requirement, is supplied from the European Grid. The actual configuration of the European Grid has three 400 kV sources located in the area of the collider facilities (Fig. 5.1). The three sources located in France are self-redundant and, according to RTE (Reseau Transport Electricité) each of them is capable of providing 200 MW in addition to their current load by the year 2035.

5.4.1.2 Transmission network topology

The transmission network includes:

– The 400 kV transmission lines connecting the three 400 kV sources on the European Grid to three incoming substations
– Three 400/135 kV transformer substations
– The 135 kV transmission ring composed of twelve segments connecting all twelve points
– A 135/36 kV transformer substation at each point.

Figure 5.1 shows a schematic view of the transmission network. Analysing the power requirements of the four machine configurations (Z, W, H, $t\bar{t}$) for each point and for nominal operation with beam, the highest power demands are in points PD and PJ. These points are where the radio frequency systems are located each of which requires 93 to 118 MW. The remaining nine points require less power – between

DRAFT FOR ADVISORY COMMITTEE - DO NOT DISTRIBUTE

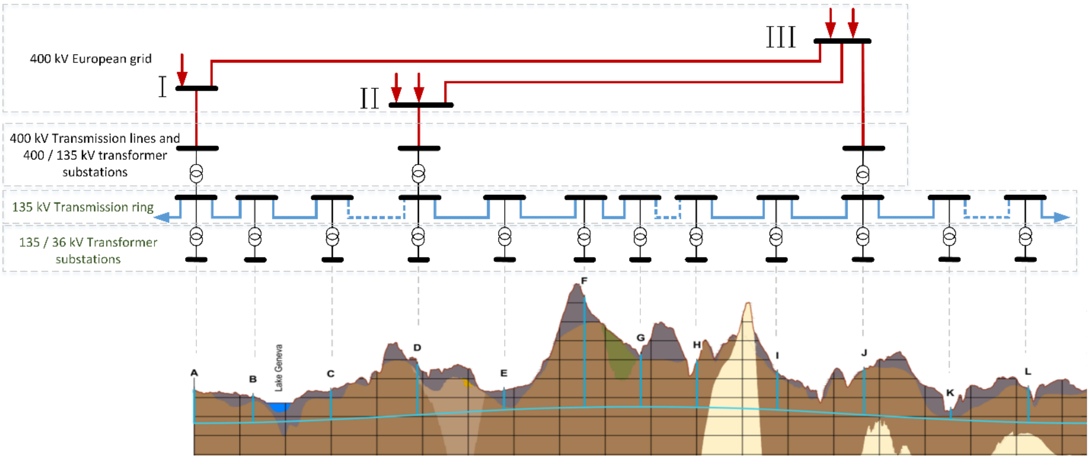

Figure 5.1: A schematic representation of the transmission network.

8 and 37 MW. Two 400 kV sources supply points PD and PJ, the third 400 kV source supplies point PA. Through the transmission line ring, each of the three incoming substations in PA, PD and PJ supplies four neighbouring points. This transmission network layout provides full redundancy and enhanced availability and operability if there is a fault on one of the transmission line segments.

Three 400 kV incoming substations are located in points PA, PD, PJ. A redundant scheme of voltage step down transformers rated at 400/135 kV, supplies the transmission line segments connecting two adjacent points. In points PB, PC, PE, PF, PG, PH, PI, PK and PL a substation will receive the incoming 135 kV transmission line segments. In all points step-down power transformers rated at 135/36 kV supply the distribution networks from the 135 kV level. Redundant step-down transformers and switchgear provide the required level of availability and maintainability. Figure 5.2 shows a simplified scheme of a 400 kV incoming substation and the connection to the two adjacent points with the corresponding step down transformers.

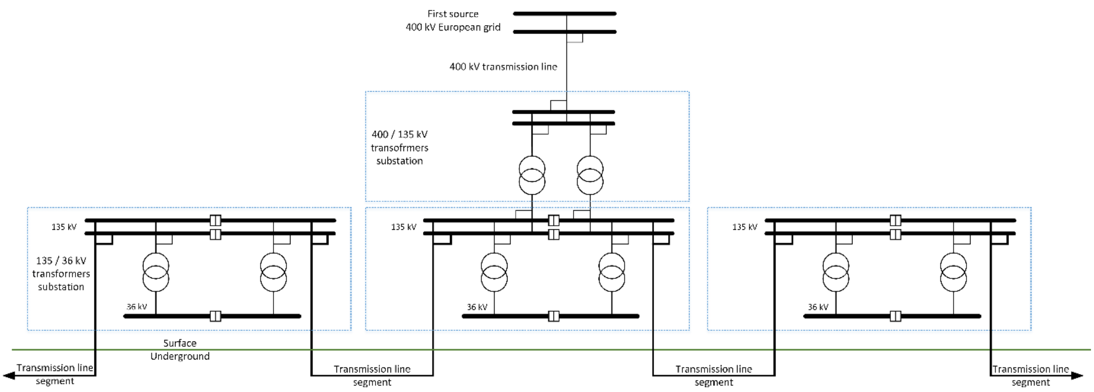

Figure 5.2: A simplified scheme of a 400 kV incoming substation and the connection to the two 135 kV substations on the adjacent points.

5.4.1.3 Distribution network topology

The distribution networks connect the transmission network to the equipment and systems installed on the surface and underground. During nominal operation, the transmission network supplies the distribution network. Alternative sources of supply are required to reach the required level of network availability and to cope with a degraded scenario such as disruption of the general or local power supply. Therefore, the distribution network includes a second source of supply, rated between 2 to 10 MVA, fed from a

DRAFT FOR ADVISORY COMMITTEE - DO NOT DISTRIBUTE

regional grid node, a third source of supply rated 1 to 5 MVA from local diesel power stations and a fourth source which provides uninterruptable power. Figure 5.3 shows the single line diagram of the baseline distribution network of one point including the alternative power sources.

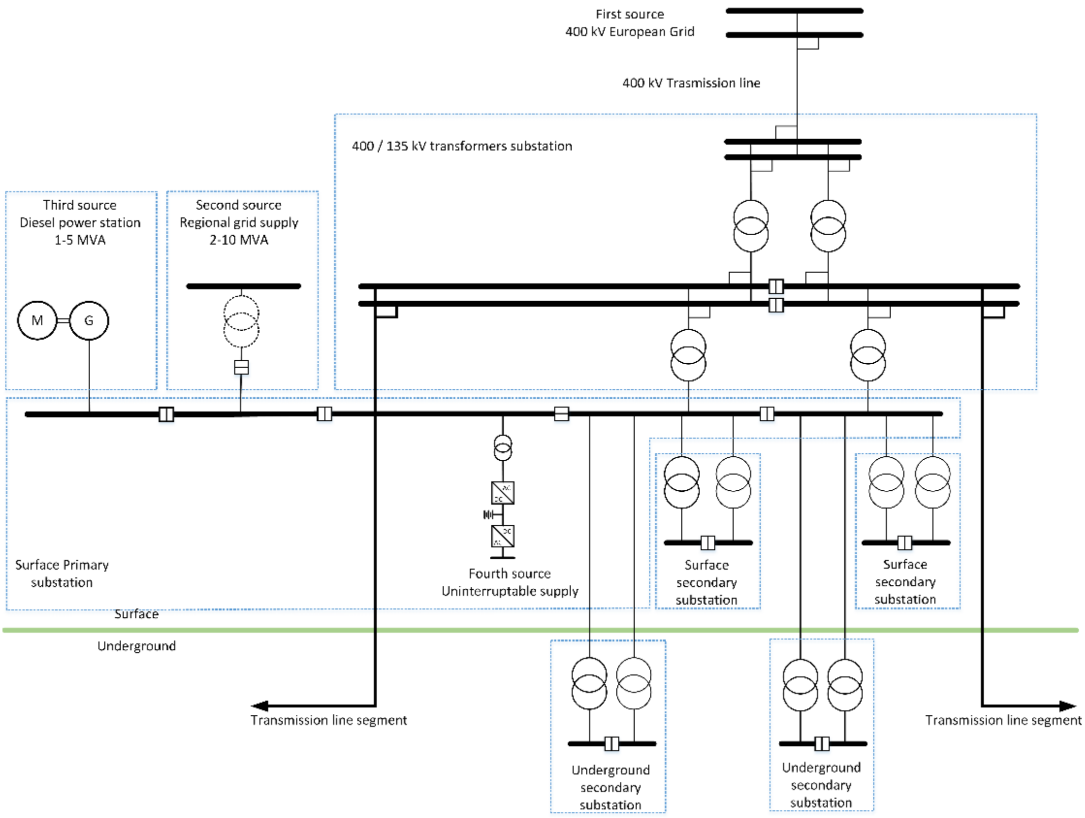

Figure 5.3: Diagram of the baseline distribution network of one FCC point including the alternative power sources.

The distribution network is composed of a primary indoor substation comprising five bus bars located on the surface level. The incoming feeders are the two redundant transformers supplied from the transmission network, the second supply from a regional source and the third supply from the local diesel power station. The out going feeders supply secondary substations. These are located either on the surface, or underground, near the load. Voltage step down transformers feed end users from the secondary substations via a maximum cable length of 750 m. The operating voltages of the distribution network are typically 36 kV for the power distribution over distances greater than 750 m. End users are supplied from the secondary substations at voltage levels between 400 V for wall plug equipment and 3.3 kV for high power motors for cooling, ventilation and cryogenic systems.

5.4.2 Power Quality and Transient Voltage Dip Mitigation

The main issues are mitigation of transient voltage dips, controlling reactive power, filtering harmonics and achieving stable voltage. The transient voltage dips, which are typically caused by lightning strikes on the 400 kV network overhead lines, often cause undesired stops of the accelerators. Due to its geographic extent, the collider will be exposed to a higher number of transient network disturbances than the current particle accelerators. The powering system design has to take into account mitigation of these transient disturbances. Extrapolation from experience in LHC operation, leads to the expectation of a total of 100 - 200 transient voltage dips per year.

The following mitigation measures are being studied:

DRAFT FOR ADVISORY COMMITTEE - DO NOT DISTRIBUTE

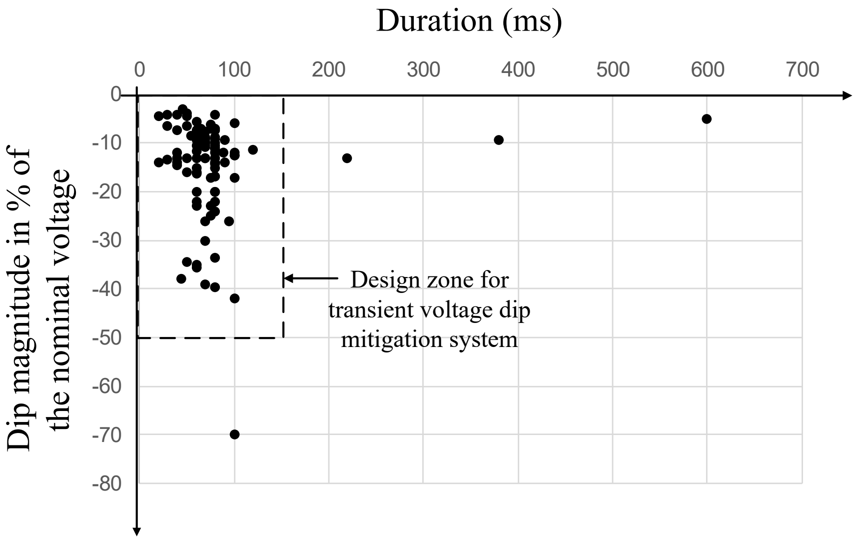

Figure 5.4: Typical distribution of transient voltage dips recorded within the existing CERN network; the design zone covers most of the transient voltage dips, which are within 0-150ms and 0-50% of magnitude.

- Dynamic Voltage Restorer (DVR) technology: the voltage will be restored by dynamic series injection of the phase voltage between the network and the loads. An integrated energy storage system would provide the required energy to restore the load voltage during transient voltage dips (see Fig. 5.5a).
- High-Voltage DC (HVDC) back-to-back link: HVDC is a well-established technology for long distance transmission of large powers and for decoupling different high voltage networks. Combined with energy storage, an HVDC system provides performance similar to a very large uninterrupted power supply (UPS). Such a system would prevent transient voltage dips in the 400 kV network from entering the collider network. In addition it would allow the control of reactive power (see Fig. 5.5b).
- Static Synchronous Compensator (STATCOM): STATCOM technology is already used for reactive and active power compensation. STATCOM would fully restore the load voltage during transient voltage dips by dynamic shunt (parallel) injection, combined with an integrated energy storage system (see Fig. 5.5c).
- Motor-Generator Set: such a system would decouple the network from the load. During transient voltage dips, the load voltage is restored by using the energy stored in a rotating mass (see Fig. 5.5d).
- Medium-Voltage DC (MVDC) distribution network: the principle of this approach is the distribution of power using DC. In combination with energy storage, this technology mitigates transient voltage dips, eliminates the reactive power, reduces the distribution losses and, compared to AC distribution, permits a larger spacing between electrical substations in the tunnel. This promising technology is still in its early stage and would require considerable infrastructure related R& D. See Section **??**.

5.5 Emergency Power

The emergency power concept is based on the management of the supply to the accelerator infrastructure. Particular emphasis is put on the supply of loads related to personnel and machine safety during a degraded situation. These include a general or local power cut, an accelerator system request or anomalous

DRAFT FOR ADVISORY COMMITTEE - DO NOT DISTRIBUTE

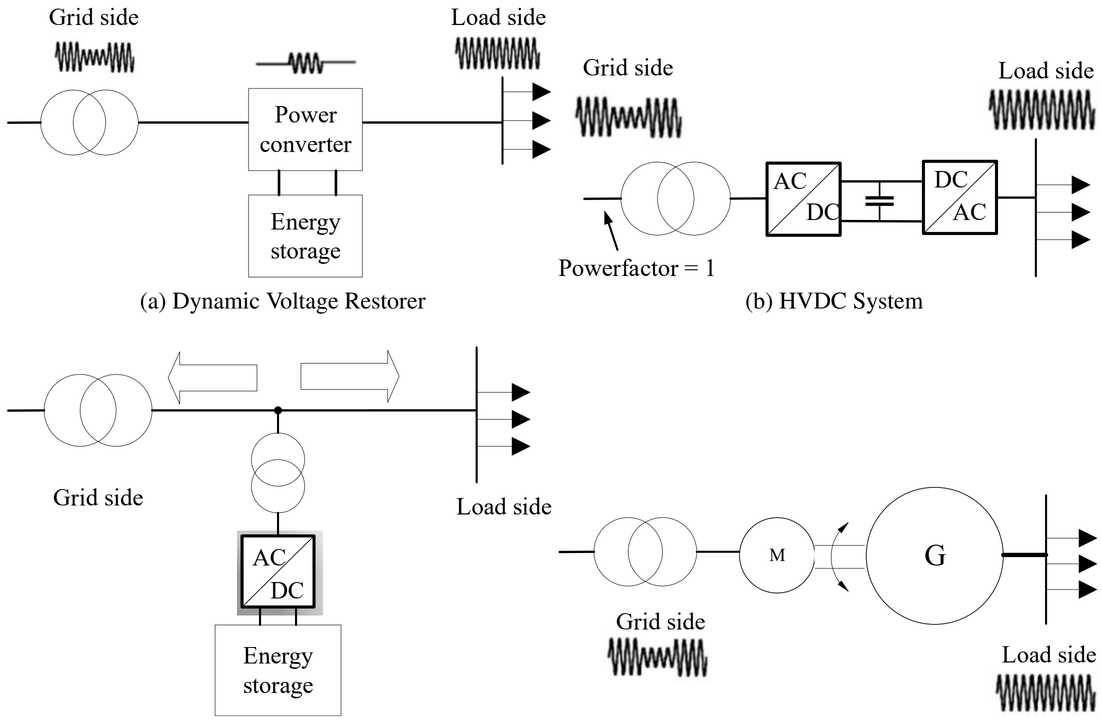

(a) Dynamic Voltage Restorer (b) HVDC System (c) STATCOM (d) Motor-Generator Set

Figure 5.5: Simplified layout of (a) Dynamic Voltage Restorer; (b) HVDC System; (c) STATCOM; (d) Motor-Generator Set.

functioning. Four classes rank each load type according to the power required in a degraded scenario. The main ranking parameters are the acceptable duration of power interruption and if it is part of a personnel, or accelerator safety system. The four classes are machine loads, general service loads, secured loads and uninterruptable loads. Table 5.10 summarises the main characteristics of the four load classes.

Machine loads are energised from the transmission line through the distribution network and do not have a second source of supply. The general services loads typically accept power cuts of several minutes and up to several hours, i.e. there is sufficient time to commute to the second source or for the main source to restore. Both the machine and general services loads do not include personnel or machine safety equipment or systems. Secured loads include personnel and machine safety equipment or systems that can sustain short power cuts up to a duration of 10 to 30 seconds. Secured loads require three sources of supply. In a degraded situation, the first level back-up is provided by the diesel power station, which typically starts up in 10 seconds. If the diesel power station is unavailable, the second level back-up supply comes from the regional grid. Uninterruptable loads include personnel and machine safety equipment or systems that require continuous and stable power supply.

A specific distribution scheme supplies uninterruptable loads. To meet safety and access requirements, UPS and batteries are located outside the tunnel and above ground. The uninterruptable network scheme is composed of two redundant uninterruptable power supply (UPS) systems supplied from the distribution network in the two adjacent points. Downstream of the redundant UPS systems, a double redundant network delivers two independent sources, each coming from an adjacent point to the end-user plug. Each piece of end-user equipment has two entries and will manage the double source of supply. Fig. 5.6 shows the functional scheme of the general services loads network and the doubly redundant uninterruptable load network.

DRAFT FOR ADVISORY COMMITTEE - DO NOT DISTRIBUTE

Table 5.9: Power Quality and Transient Voltage Dip Mitigation

	DVR	Back-to-Back	DC grid	STATCOM	Motor-Generator Set
Transient voltage dips	covered	covered	covered	covered	covered
Compensation of reactive power on the load side	Not covered, although the resulted voltage deviations on the load side can be compensated	covered	covered	covered	covered
Compensation of active power on the load side	Not covered	covered	covered	covered	covered
AC Harmonic filtering capability	Yes (although additional HF filter required)	No (additional harmonic filtering required)	No (not necessary)	Yes	No (additional harmonic filtering required)
Steady-state power losses	Very Low	High	Medium	Very Low	Medium
Technology readiness level	Available in industry	Available in industry	Design and standardisation phase	Available in industry	Available in industry
Protection aspects	Bypassed is needed	Bypassed is needed	In development	Bypassed is needed	Very high protection

Table 5.10: Load classes and main characteristics

Load class	Load type (non-exhaustive list)	Power unavailability duration in case of degraded scenario
Machine	Power converters, cooling and ventilation motors, radio frequency	Until return of main supply
General Services	Lighting, pumps, vacuum, wall plugs	Until return of main or secondary supply
Secured	**Personnel safety:** Lighting, pumps, wall plugs, elevators	10 - 30 seconds
Uninterruptable	**Personnel safety:** evacuation and anti-panic lighting, fire-fighting system, oxygen deficiency, evacuation **Machine safety:** sensitive processing and monitoring, beam loss, beam monitoring, machine protection	Interruptions not allowed, continuous service mandatory

5.6 Cryogenic System

5.6.1 Overview

The FCC-ee is based on five machines with various electron-positron beam parameters. The beams are accelerated by 400 and 800 MHz superconducting radio-frequency (SRF) cavities operating at 4.5 and 2 K respectively. The staging of the 5 machines requires a gradual increase of the number of SRF modules and consequently a staging of the cryogenics system.

DRAFT FOR ADVISORY COMMITTEE - DO NOT DISTRIBUTE

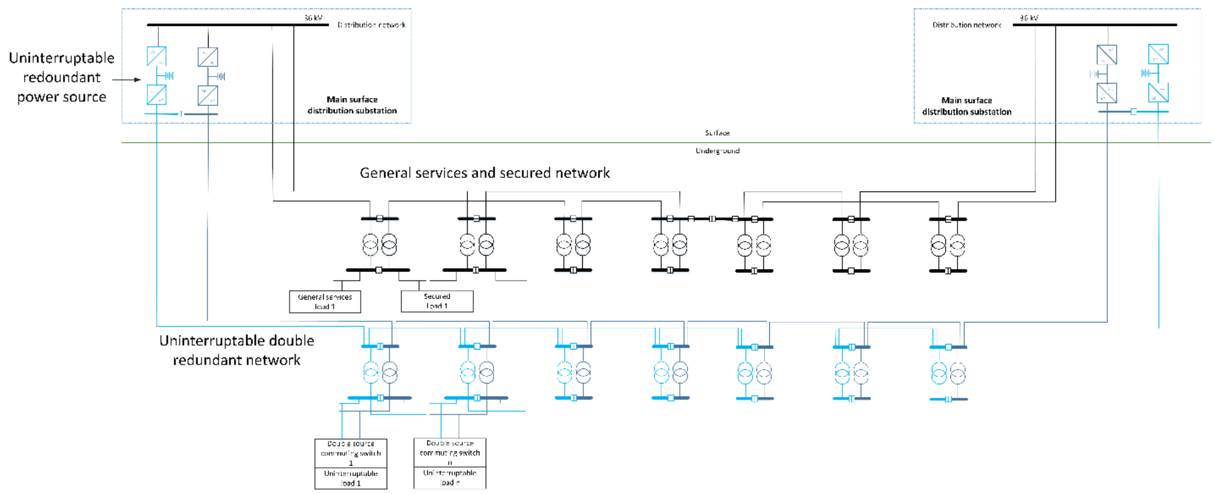

Figure 5.6: Functional scheme of the general services load network and the doubly redundant uninterruptable load network.

5.6.1.1 Functions and Constraints

The 400 MHz SRF cavities will be immersed in a saturated helium bath at a temperature of 4.5 K at 1.3 bar. The 800 MHz cavities will be immersed in a saturated superfluid-helium bath at a temperature of 2 K at 30 mbar. The first three machines (Z, W, H) are equipped with 400 MHz modules and require refrigeration at 4.5 K. The two last machines ($t\bar{t}1$ and $t\bar{t}2$) will re-use the 400 MHz modules but will be upgraded by adding 800 MHz modules and consequently require refrigeration at 4.5 and 2 K.

The cryogenic system must cope with load variations and the large dynamic range imposed by operation of the accelerator. Even if the mass of the cavities is not an issue, the cryogenic system must be able to cool down and fill the module bath, whilst avoiding thermal gradients greater than 50 K in the cryo-structure. This limit in thermal gradient also applies to the forced emptying and warm-up of the machine prior to shutdown periods.

The cooling power required at each temperature level will be produced in one or two technical sites (Points D and J) by one refrigeration plant for the Z and W, by two refrigeration plants for the H machine and by 4 refrigeration plants for the $t\bar{t}1$ and $t\bar{t}2$ machines. The cooling power will be distributed to the adjacent SRF linacs over distances of up to 1.1 km. Each extended long straight section will contain three superconducting (SC) linacs for the main electron ring, the main positron ring and the booster ring. For the $t\bar{t}1$ and $t\bar{t}2$ machines, the two main rings can be recombined and only two SC linacs are required. For reasons of simplicity, reliability and maintenance, the number of active cryogenic components distributed around the linacs is minimised. As the cryo-modules will be equipped with cold-warm transitions and also to simplify the cryo-module design, the cryogenic headers distributing the cooling power as well as all remaining active cryogenic components in the tunnel are contained in a compound cryogenic distribution line (Fig. 5.7). The cryogenic distribution line runs alongside the cryo-module linacs in the tunnel and feeds each cryo-module via a jumper connection. The tunnel is inclined at 0.3 % with respect to the horizontal which could generate flow instabilities in two-phase, liquid-vapour, flow. All fluids should be transported over large distances in mono-phase state to avoid these harmful instabilities, i.e. in the superheated vapour or supercritical regions of the phase diagram. Local two-phase circulation of saturated liquid, in a controlled direction can be tolerated over limited distances.

Equipment is installed above ground as much as possible to avoid the need for excavation of large caverns. However, certain components which must be close to the SC linacs will be installed underground. To limit the effect of gravity (hydrostatic head and relative enthalpy variation) in the deep areas (up to 266∼m), the cold part of the helium cycle below 40∼K, including cold compressors, must be located in underground caverns. For reasons of safety, the use of nitrogen in the tunnel is forbidden

DRAFT FOR ADVISORY COMMITTEE - DO NOT DISTRIBUTE

and discharge of helium is restricted to small quantities. The cryogenic system is designed for fully automatic operation between shutdown periods, during which maintenance will be performed.

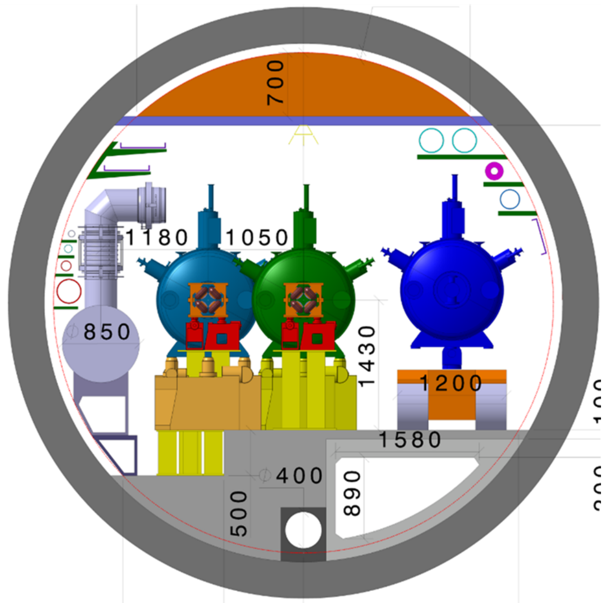

Figure 5.7: Cross section of the FCC tunnel and main FCC-ee cryogenic components.

5.6.2 Layout & Architecture

Figure 5.8 shows the the cryogenic layout of the five machines, with 2 cryogenic "islands" at points PD and PJ where all refrigeration and ancillary equipment is concentrated. Equipment at ground level includes electrical substations, warm compressor stations (WCS), cryogen storage (helium and liquid nitrogen), cooling towers, cold-boxes (UCB) and the lower cold-boxes (LCB), interconnecting lines and interconnection boxes are underground. The first machine (Z) requires limited refrigeration capacity and the refrigerator cold box can be fully integrated in the caverns. The two first machines (Z and W) require limited number of cryo-modules with can be located in a single technical site (Point J or D). Each cryogenic island houses one or two refrigeration plants which feed adjacent SC linacs, requiring distribution and recovery of the cooling fluids over distances of 1.1 km underground. Figure 5.9 shows the general architecture of the cryogenic system. The refrigeration plant for the $t\bar{t}$ machine also includes a 2 K refrigeration unit. At each cryogenic island, an interconnection box couples the refrigeration equipment to the cryogenic distribution line. When possible they also facilitate redundancy amongst the refrigeration plants.

The 800 MHz cryo-modules, which require very-low-pressure pumping, must be located close to their 2 K refrigeration unit. Consequently, the 400 MHz cryo-modules are located at the far-end of the extended straight sections, thus requiring an additional $\sim$1.4 km of cryogenic transfer line per extended straight section for the first three machines.

5.6.3 Proximity Cryogenics and Heat Loads

5.6.3.1 Temperature Levels

In view of the high thermodynamic cost of refrigeration at 2 K and 4.5 K, the thermal design of the cryogenic components aims to intercept the largest fraction of heat loads at higher temperature, hence the multiple, staged temperature levels in the system. The temperature levels are:

– 50 K to 75 K for thermal shield as the first major heat intercept, sheltering the cavity cold-mass from the bulk of heat inleaks from the environment;

DRAFT FOR ADVISORY COMMITTEE - DO NOT DISTRIBUTE

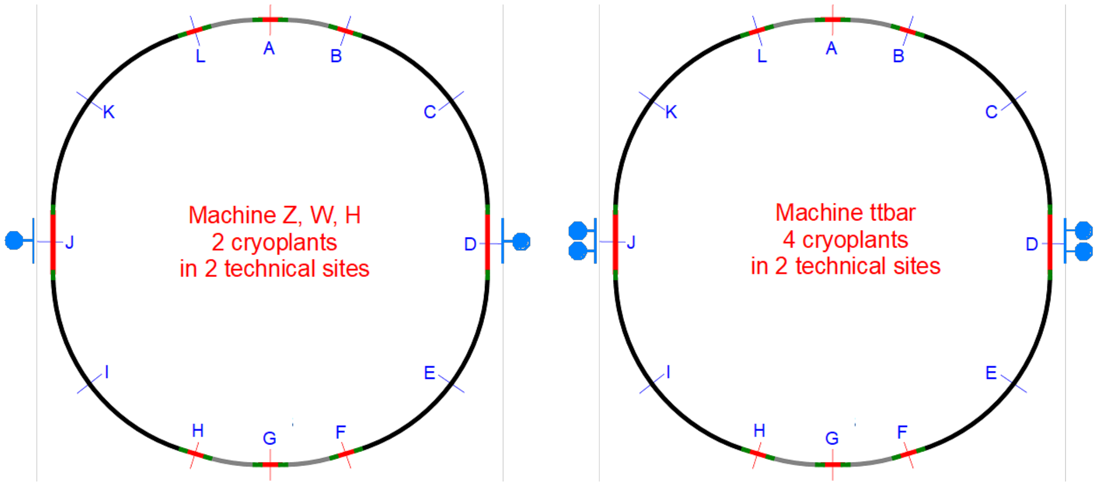

Figure 5.8: General cryogenic layout.

- 4.5 K normal saturated helium for cooling 400 MHz superconducting cavities;
- 2 K saturated superfluid helium for cooling the 800 MHz superconducting cavities.

The cryo-module and cryogenic distribution line combine several low temperature insulation and heat interception techniques which will have to be implemented on an industrial scale. These techniques include low conduction supporting system made of non-metallic fibreglass/epoxy composite, low impedance thermal contacts under vacuum for heat intercepts and multi-layer reflective insulation for wrapping the cold surface.

JGU
an industrial scale-
Explain what an industrial scale- means

For FCC-ee, the beam-induced heat load is dominated by RF losses dissipated in the cavity baths at 4.5 K (for the 400 MHz cavities) or at 2 K (for the 800 MHz cavities).

5.6.3.2 *Heat loads*

Inward static heat leaks (inleaks) are a function of the design of the cryo-module and originate from the ambient temperature environment. The thermal calculations for the cryo-modules and the distribution system are based on the thermal performance data from similar cryo-assemblies.

Beam-induced loads to the cryo-modules are mainly due to RF losses, which strongly depend on the bunch intensity and number of bunches in the circulating beams.

Table 5.11 gives the steady-state heat loads for nominal conditions for the 5 machines.

5.6.3.3 *Cooling scheme and cryogenic distribution*

The cryogenic flow scheme is shown in Fig. 5.10 for the 4.5 K and 2 K cryo-modules. The 4.5 K cavity cold-masses are immersed in saturated helium baths, which are supplied by line C through expansion valve V1. The saturation pressure is maintained by line D, which recovers the evaporated vapour. The 2 K cavity cold-masses are immersed in saturated helium baths, which are supplied by line A through expansion valve V2. The low saturation pressure is maintained by pumping the vapour through line B. Each cryo-module has a dedicated thermal shield and heat intercept circuit cooled in parallel between line E and F. The flow-rate is controlled by valve V3. Table 5.12 gives the size of the main cryogenic distribution system components.

JGU
FCC-hh??

DRAFT FOR ADVISORY COMMITTEE - DO NOT DISTRIBUTE

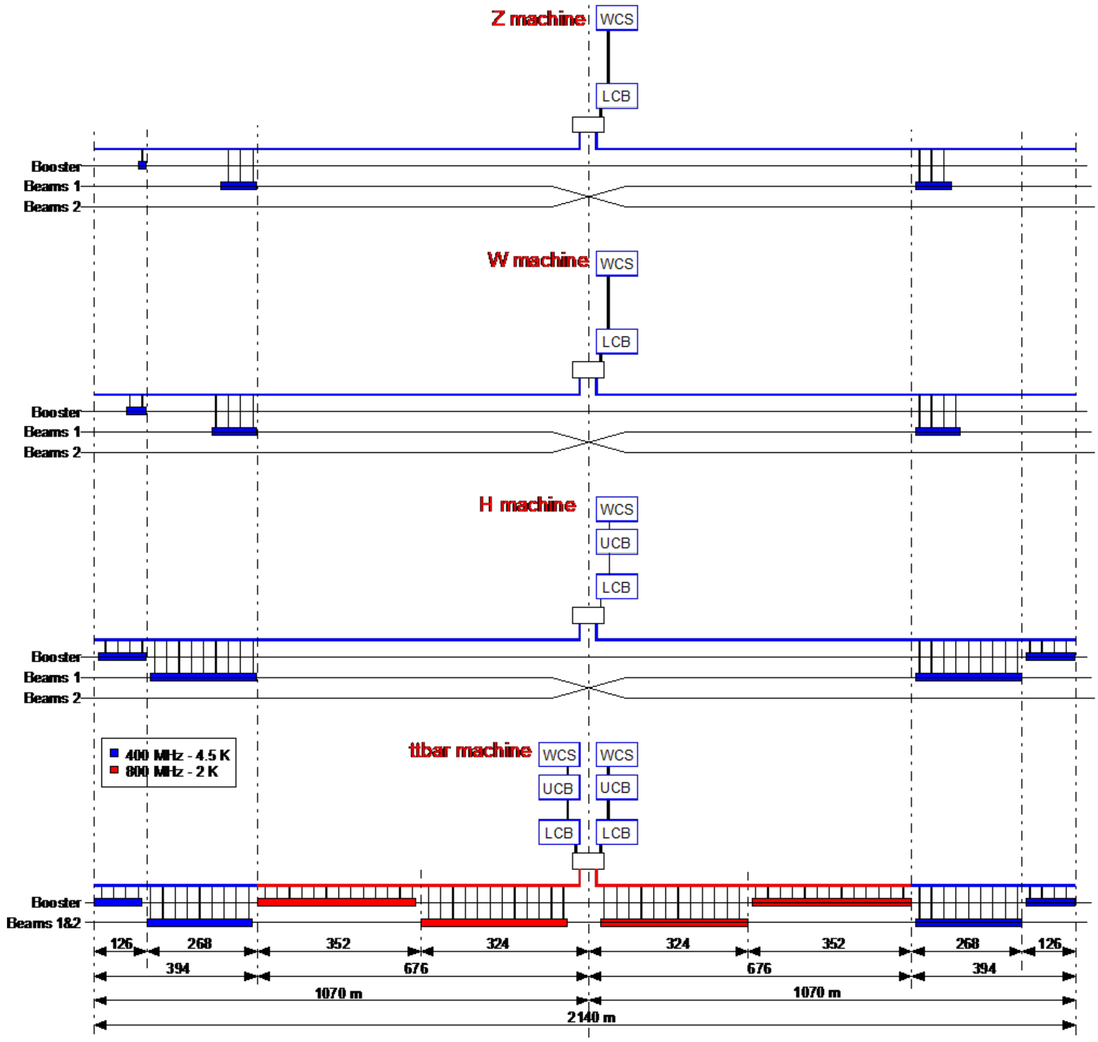

Figure 5.9: Cryogenic plant architecture.

Table 5.11: Steady-state heat loads in in FCC-ee (nominal conditions)

	Machine									
	Z		W		H		$t\bar{t}1$ ($t\bar{t}2$)			
	Per beam	Boost.	Per beam	Boost.	Per beam	Boost.	2 beams	Boost.	2 beams	Boost.
Frequency Temperature	400 MHz 4.5 k								800 MHz 2 k	
# cell / cavity	1	4	4		4		4		5	
# cavities	52	12	52	52	136	136	272	136	296 (372)	400 (480)
# cryo-modules	13	3	13	13	34	34	68	34	74 (93)	100 (120)
Dynamic losses / cav [W]	14	11	210	26	202	29	210	30	66	10
Static losses / cav [W]	8		8		8		8		8	

DRAFT FOR ADVISORY COMMITTEE - DO NOT DISTRIBUTE

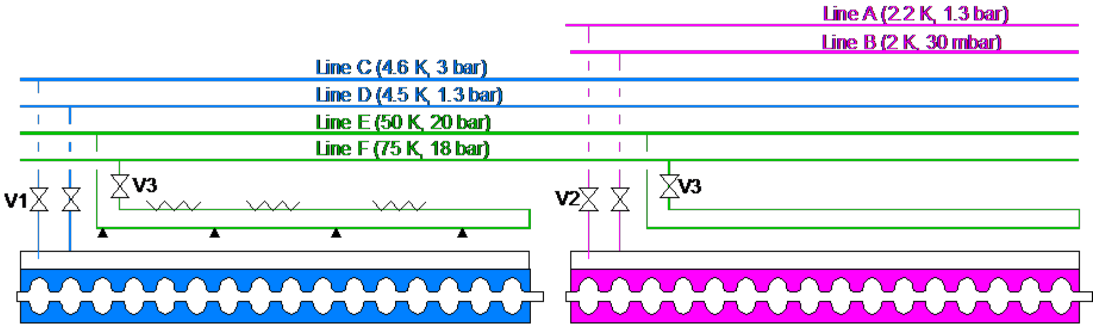

Figure 5.10: Cryogenic flow-scheme of FCC-ee cryo-modules.

Table 5.12: Dimensions of the main cryogenic distribution line components

component	Diameter [mm]
Line A	50
Line B	300
Line C	100
Line D	200
Line E	80
Line F	80
Vacuum jacket 400 MHz cryo-modules	550*
Vacuum jacket 800 MHz cryo-modules	750*
* +100 mm for bellows and flanges	

5.6.4 Cryogenic Plants

Table 5.13 gives the required nominal cooling capacity per cryogenic plant at the various temperature levels for the 4 machines, including an operational margin factor of 1.3.

Table 5.13: Nominal cooling capacity per cryogenic plant (including a 1.3 operational margin)

Temperature level	50-75 K [kW]	4.5 K [kW]	2 K [kW]	Cryoplant size [kWeq @ 4.5 K]	#Cryoplants [-]
Z machine	5.5	3.7		4	1
W machine	6.4	32		33	1
H machine	7.1	41		41	2
$t\bar{t}$1 machine	6.6	21	10	55	4
$t\bar{t}$2 machine	7.6	21	12	63	4

The cooling of the superconducting 800 MHz cryo-modules requires a refrigeration capacity of 12 kW at 2 K per cryogenic plant, a capacity larger than the state-of-the-art cryogenic plants. Specific research and development will be required concerning the design of larger cold compressors and/or on the operation of cold compressor trains in parallel. Figure 5.11 shows the upgrade scenario for FCC-ee cryogenics. In order to optimise the staging of the machine, it is proposed to use a small cryogenic plant (Cryoplant A) for the Z and W machines, then to replace this plant by a new plants (Cryoplant B) for the W machine, which could be upgraded for the $t\bar{t}$ machine, and finally, to add two cryogenic plants (Cryoplant C) for the $t\bar{t}$ machine. Figure 5.12 shows this cryogenic plants staging. The electrical power to the cryogenic plants, based on a Carnot efficiency of 28.8 % (LHC cryogenic plant value), is given in Table 5.14. In nominal operation, the electrical consumption varies from 1 MW (for the Z machine) to 50 MW (for the $t\bar{t}$2 machine).

DRAFT FOR ADVISORY COMMITTEE - DO NOT DISTRIBUTE

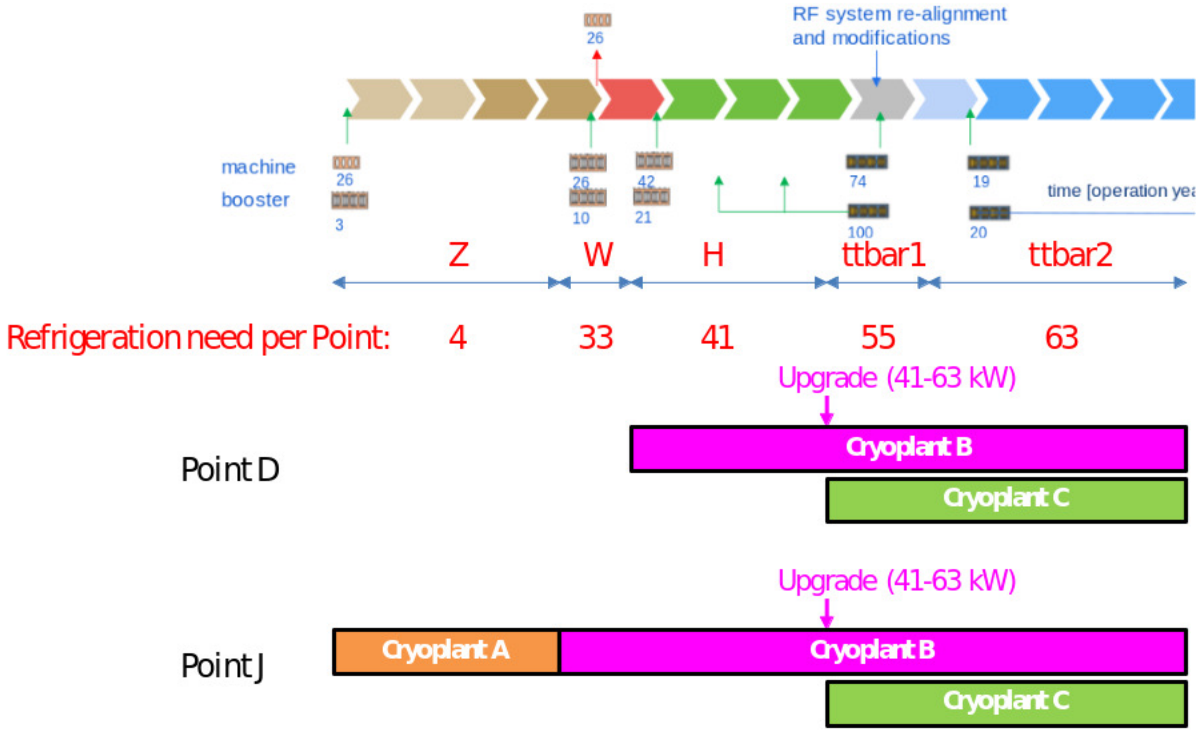

Figure 5.11: Upgrade scenario for FCC-ee cryogenics.

5.6.5 Cryogen Inventory and Storage

The cryogenics system will require helium and nitrogen. Nitrogen will be required only for the regeneration of absorbers and dryer beds; consequently, one standard 50m^3 LN_2 reservoir is planned for each technical site housing cryogenic plants (2 in total). The helium inventory is mainly driven by the cryo-module cold-mass baths, which contain 40 kg of He per cryo-module and by the helium inventory contained in the cryogenic distribution system. Table 5.15 gives the inventory of helium and its storage for the FCC-ee machines. The Z and W machines are dominated by the helium distribution inventory. The $t\bar{t}$ machine requires up to 26 t of helium which can be stored in 250m^3 medium-pressure (MP, 20 bar) storage tanks.

5.7 Equipment Transport and Handling

5.8 Person Transport

5.9 Geodesy, Survey and Alignment

5.9.1 Introduction

The FCC-ee is a circular collider of 97.75 km circumference and will be therefore the largest accelerator ever built in the world. As was already the case for the Large Electron Position (LEP) collider in the 80's, the FCC-ee will be the most demanding project in terms of positioning accuracy over such a large area. It is therefore appropriate to think about what is currently achievable and what developments have to be undertaken, in various domains, in order to achieve the physics requirements.

5.9.2 Alignment tolerances

The alignment precision requirements are the key values that will drive any survey study. The absolute accuracy in the vertical direction is the deviation to the theoretical plane of the collider, while it is the

DRAFT FOR ADVISORY COMMITTEE - DO NOT DISTRIBUTE

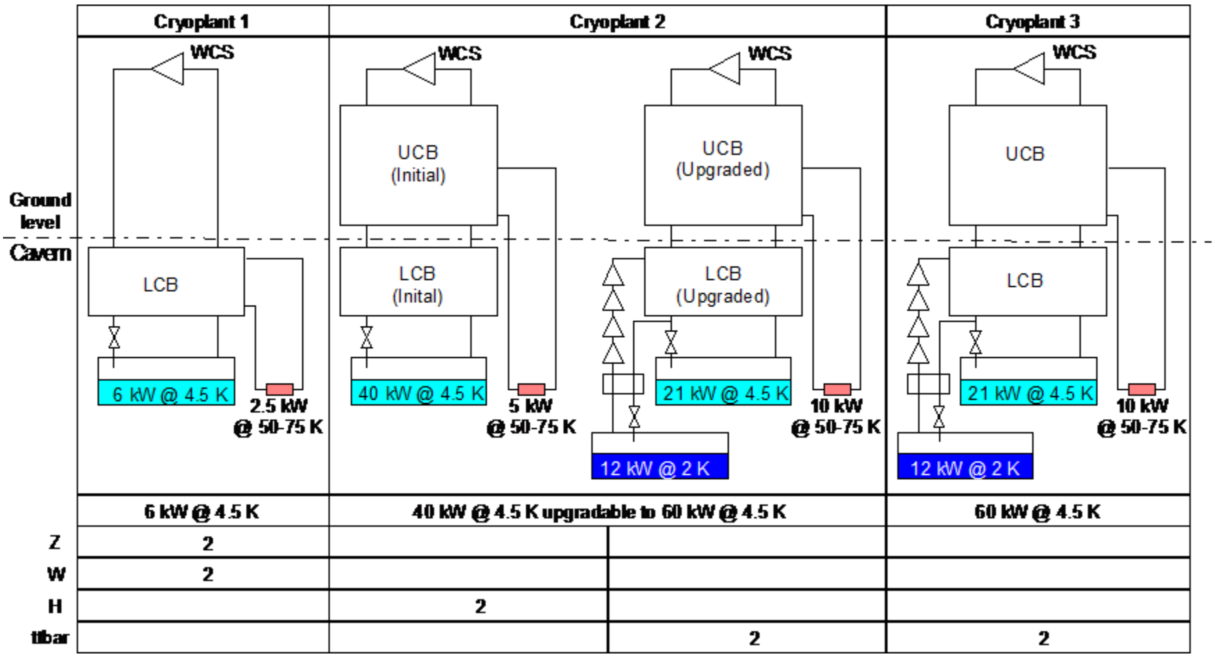

Figure 5.12: Cryogenic plant staging for FCC-ee.

Table 5.14: Electrical power to the cryogenic plants

	Installed power [MW]			Nominal power [MW]		
	per plant	per site	Total	per plant	per site	Total
Z machine	0.9	0.9	0.9	0.8	0.8	0.8
W machine	9.5	9.5	9.5	7.1	7.1	7.1
H machine	9.5	9.5	19	8.3	8.3	17
$t\bar{t}$1 machine	14	29	58	12	23	46
$t\bar{t}$2 machine	14	29	58	13	25	50

variation of its radius R with respect to the theoretical value in the transversal direction. The differential variations between several consecutive magnets represent the relative accuracy. This latter type of error has a more direct effect on the closed orbit of the particles. As it is difficult to get information for the absolute accuracy, the value of several mm, achieved for the LEP and LHC is considered, and a relative misalignment of 0.1 mm (1σ) between consecutive quadrupoles and 0.1 mrad (1σ) for the roll are the values given by the physics simulations. This error budget has to be split between mechanical errors, due mainly to the assembly process, and alignment errors, including misalignments due to ground motions or mechanical constraints.

5.9.3 Geodesy

As the area covered by the FCC is ten times larger than that of the LHC, an extension of the mean sea level equipotential surface of gravity (also called the geoid) has to be studied. The very tight relative accuracy will necessitate the determination of a geoid at the level of a few tenths of mm, which has already been demonstrated in the framework of the CLIC studies. To achieve the absolute accuracy of the surface geodetic network, Global Navigation Satellite Systems (GNSS) will be used, possibly complemented by electro-optical distance measurements. The transfer of the geodetic network points from the surface to

DRAFT FOR ADVISORY COMMITTEE - DO NOT DISTRIBUTE

Table 5.15: Inventory of helium and its storage for the FCC-ee machines

Machine	Z	W	H	$t\bar{t}1$	$t\bar{t}2$
Cryomodule [t]	1.2	1.6	4.1	11.0	12.6
Distribution [t]	3.9	3.9	7.9	8.9	8.9
Cryoplant [t]	1	1	2	4	4
Total [t]	6	7	14	26	26
Number of 250 m^3 MP storage	8	8	18	30	32

the tunnel, through shafts with a depth up to 400 m, will require new developments. The underground network will necessitate gyro-theodolite traverses, as well as accurate distance and angle measurements, and possibly offsets with respect to a stretched wire.

5.9.4 Metrological aspects

Metrological checks and alignments have to be integrated at different times in the manufacturing and assembly processes, including the fiducialisation, which is the determination of the survey reference points with respect to the component's reference axes. The techniques proposed are similar to those proposed for the CLIC, i.e. laser trackers, and photogrammetry. Co-ordinate Measuring Machines (CMM) and new sensors such as Frequency Scanner Interferometry (FSI) may be used when justified by the required accuracy. The position of the alignment targets (fiducials) has to be defined taking into account the survey needs and the experimental cavern or accelerator tunnel constraints. The equipment supports, even if they are the responsibility of their owner, have to comply with the alignment specifications and constraints.

5.9.5 Alignment of the Accelerator Components

The alignment of the accelerator components will be realised in two steps:

- the first "absolute" alignment from the underground network will be performed using standard digital level and total station measurements.
- the "relative" alignment or smoothing. Taking into account the length of the FCC cell and the required accuracy, the standard techniques of levelling and offset measurements with respect to a stretched wire cannot be used any more. The only solution that ensures the accuracy is the one proposed for the CLIC study, i.e. a permanent monitoring system based on the principle of Wire Positioning Sensors (WPS) and Hydrostatic Levelling Sensors (HLS). This solution, which fulfils the alignment tolerances, has to be heavily improved in order to get a significant cost reduction. But this solution has the advantage of providing automatically the position of all the magnets, which will be affected, without doubt, by the ground motions due to the instability of this new civil engineering structure.

5.9.6 Interaction Regions and Collimators areas

The alignment accuracy values for the interaction regions are assumed to be the same as for the LHC, i.e. 0.1 mm for the triplets located on the same side of the IP, 0.2 mm from left side of the IP to the right side and 0.5-1.2 mm from the triplets to the Experiment, all values given at 1σ. In order to achieve these specifications, survey galleries will be needed to host part of a permanent monitoring system based on the latest sensors technology available at that time. The Q0 magnet, which is located very close to the IP and therefore inside the Experiment, will be very challenging to align. A similar situation appeared for CLIC and no viable solution was found, so further research and development will have to be done. In the

DRAFT FOR ADVISORY COMMITTEE - DO NOT DISTRIBUTE

collimator areas, due to the high level of radiation, the same permanent monitoring system could be used. The challenge will be to find a solution to either allow the exchange of collimators without dismantling the survey system or to dismantle or reinstall remotely the survey system using the latest developments in robotics.

5.9.7 Experiments

The alignment accuracy values for the experiment assembly are assumed to be similar to those of Atlas and CMS i.e. 0.5 mm. The positioning of the experiment with respect to the beam line is done using a geodetic experiment network determined from the underground network. It is composed of points distributed across the whole cavern volume on the walls and floor. It is used during all the steps of the assembly and positioning of the detectors. It is measured once the cavern has been delivered, and is still empty, using mainly distances, angles and levelling measurements. The use of 3D laser tracker technology is appropriate for this type of 3D network. From this network, only the outer skin of the experiment is visible and therefore the position of the inner detectors will be reconstructed from the position of the external fiducials and the fiducialisation and assembly measurements.

5.10 Communications, Computing and Data Services

5.11 Safety and Access Management Systems

A future large-scale particle collider infrastructure will built on the industry best-practice to deploy a safety management system (SMS) which integrates all systems that contribute to a safe operation of the research infrastructure in a uniform and regulatory-compliant way. This integrated concept includes also the procedures associated to the different situations. A high-level computer-based safety management system (SMS) integrates underlying safety related functions, including fire detection, oxygen deficiency detection, smoke and helium extraction systems, fire extinction systems, access and authorization managements, door supervision and control, video surveillance, radiation monitoring, conventional environmental monitoring, evacuation signalization, supervision and control of elevators, communication with people in underground zones, emergency lighting and acoustics and communication with emergency services (fire fighting, rescue, healthcare providers, public and private security forces). The sub-systems function autonomously. The SMS provides a prioritized and homogeneous visualisation of the status of all safety relevant parameters, allows the supervisory control of all sub-systems and handles the sub-system interconnections. The SMS communicates with the sub-systems through fail-safe protocols, usually over a dedicated communication infrastructure. It guarantees that critical alarms are automatically transmitted to the competent services (e.g. fire brigade, radiation protection team) and that all incidents are recorded and suitably documented for potential examination by the authorities (auditing). Furthermore, the SMS ensures that any condition which is incompatible with safe beam operation of the accelerator (e.g. intrusion) is detected and the beam gets aborted.

Such supervisory systems are in daily operation today in all large-scale plants (e.g. particle-accelerator based ion therapy facilities, oil and gas rigs, manufacturing and processing plants). The future system shall be compliant with recognized international norms, be open and extensible, and configurable to the specific application (e.g. GIS and CAD integration, user interface designer). Processing speed is generally not critical, but the system must work extremely reliably, be highly scalable and be open to integrate a continuously growing set of diverse subsystems from different suppliers. Implementation details (e.g. localization of a central supervision point, number and position of decentral facilities to interact with the system, hard- and software choices, rights management, means to identify people requesting access to the accelerator, or to localize people in the machine) are subject to a requirements specification phase, typically once the detailed designs of the infrastructure and its individual technical systems are well known.

DRAFT FOR ADVISORY COMMITTEE - DO NOT DISTRIBUTE

Figure 5.13: Example for an SMS control centre (courtesy of Philips PKE).

Table 5.16: Examples for typical Safety Management System solutions for large-scale application cases.

Supplier	**Product**
Advancis Software & Services	PSIM
ATS Elektronik	AES5000, DLS4000
Bosch Security Systems	Building Integration System
CENARIO solutions	CENARIO
digivod	CRISP PSIM
ETM/SIEMENS	WinCC OA
Genetec	Security Center
GEOBYTE	Metropoly BOS
Honeywell	Enterprise Buildings Integrator, WINMAG plus
KÃŰTTER Security	LENEL OnGuard
PKE	AVASYS
Scanvest	ScanVis.Pro
Securiton	Universal Management System SecuriLink UMS, IPS
SIEMENS	GMA-Manager, Siveillance Vantage
Tyco Integrated Fire & Security CKS Systeme	CELIOS, C-cure 9000
WAGNER Group	VisuLAN X3

DRAFT FOR ADVISORY COMMITTEE - DO NOT DISTRIBUTE

Chapter 6

Injector complex

Yannis Papaphilippou: Yannis Papaphilippou, 10 pages

6.1 Injector Overview

The injector complex of the FCC-ee, comprises an e^+e^- LINAC (for energies up to around 6 GeV), a pre-booster ring (PBR) accelerating from around 6 to 20 GeV and a full energy booster ring (BR), integrated in the same tunnel as the collider. A basic schematic layout of the injector complex can be seen in Fig. 6.1.

Table 6.1 displays a list of parameters for the injection schemes for the different collider energies and filling modes (top-up or full filling). The baseline parameters are established based on an SLC/SUPERKEKB-like linac [?, ?] (C-band 2.8 GHz RF system) with 1 or 2 bunches per pulse and a repetition rate of 100 or 200 Hz. The full filling for Z running is the most demanding with respect to the number of bunches, bunch intensity and therefore injector flux. It requires a linac bunch intensity of 2.13×10^{10} particles for both species. The electron linac used for e^+ production should provide around a factor of two higher bunch charge, i.e. 4×10^{10} particles, allowing for a 50 % conversion efficiency. The bunch intensity requirements include a comfortable 80 % transfer efficiency throughout the injection complex.

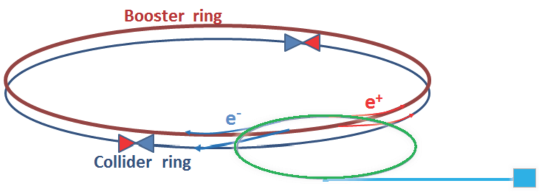

Figure 6.1: Schematic layout of the FCC-ee injector complex.

JPo have changed the ... Is this correct? I have changed the wording to make it read better

There will be multiple injection of linac bunches using a bunch to bucket transfer into the PBR which has a 400 MHz RF system. Between 50 and 1040 bunches will be injected depending on the collider running mode (Z, W, H or $t\bar{t}$). In the current baseline, the SPS, using a scheme similar to the one used for injection into LEP is considered as the PBR. Other options studied include a more compact "green field" PBR and an extension of the linac to reach an energy of 20 GeV for direct injection to the main booster. The PBR cycle length is dominated by the injection plateau and includes a fast ramp of 0.2 s up to 20 GeV and a minimum fast extraction flat top of 0.1 s. The total number of bunches required (50 to 16640 bunches) is transferred to the main booster using a maximum of 8 PBR cycles. They are injected into the bunch structure required by the collider, within the 400 MHz RF. The bunches are then accelerated with a fast ramp time of maximum 2 s, and a maximum total cycle length of up to 51.7 s, which is for the Z running. Due to the short collider lifetimes of 40 to 70 minutes, which depend on the parameter sets and different running energies, continuous top-up injection from the BR is required. In a complete filling, the bunches are accumulated in the collider within 20 min. At other times the beam is used for topping up the current, to maintain the collider lifetime limits within the 5% current drop. The filling of the two particle species in the machine is interleaved and is able to accommodate current bootstrapping [**?**].

Table 6.1: FCC-ee injector parameters.

Parameter [unit]	Z		WW		ZH		tt	
Energy [GeV]	45.6		80		120		182.5	
Type of filling	Full	Top-up	Full	Top-up	Full	Top-up	Full	Top-up
LINAC bunches	2				1			
LINAC repetition rate [Hz]	200				100			
LINAC RF freq [GHz]	2.8							
Bunch population [10^9]	2.13	1.06	1.88	0.56	1.88	0.56	1.38	0.83
No. of LINAC injections	1040		1000		393		50	
PBR bunch spacing [ns]	2.5		22.5		57.5		450	
Number of BR cycles	8				1			
No of PBR bunches	2080		2000		393		50	
PBR cycle time [s]	6.3		11.1		4.33		0.9	
PBR duty factor	0.84		0.56		0.35		0.08	
No of BR/collider bunches	16640		2000		393		50	
No of BR cycles	10	1	10	1	10	1	20	1
Filling time (both species) [sec]	1034.8	103.5	288	28.8	150.6	15.6	224	11.2

6.2 Electron Gun

The custom built RF gun has a normalised transverse emittance of $\leq$10 π.mm.mrad, and provides 6.5 nC of charge at 11 MeV. The charge is intentionally high to allow for a high charge injection for the first fill of the collider at startup. Briefly, the RF gun (see Fig.6.2) is based on a parallel coupled accelerating structure [1, 2] and has permanent magnets in the irises to reduce the size and emittance dilution. It is planned to use material based on IrCe alloy [3, 4] as the photocathode because this alloy provides acceptable lifetime with high charge extraction at high repetition rate. The design was made with the aid of the ASTRA code and some parameters are presented in Table 6.2.

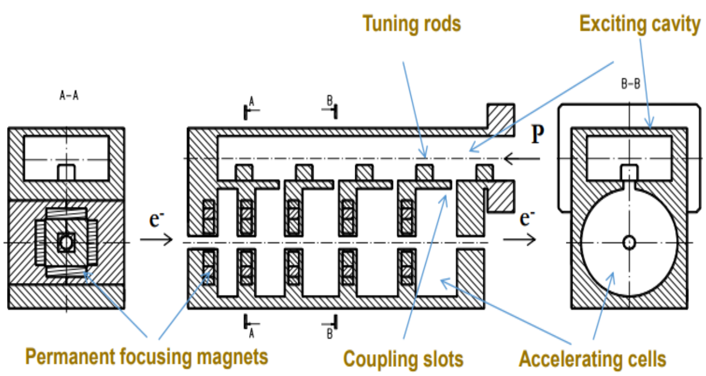

Figure 6.2: A schematic drawing of the RF gun.

DRAFT FOR ADVISORY COMMITTEE - DO NOT DISTRIBUTE

Table 6.2: Design parameters of the RF gun

Parameter	Value
Initial emittance	0.6 π.mm.mrad
Injection kinetic energy	0.1 mrad
Total charge	6.5 nC
Cathode spot size	5 mm
Initial distribution	Radially Uniform
Laser pulse duration	8 ps
Laser injection phase	variable
Magnetic field on the cathode	0 T
Peak accelerating field	100 MV/m
Focusing solenoid field	0.5 T

References

[1] A. V. Andrianov et al., "Development and low power test of the parallel coupled accelerating structure", JINST 11 P06007, 2016.

[2] Y. D. Chernousov et al., "Accelerating structure with parallel connection". Patent for invention (Russia), No. RU2472244C1, BI. 01/10/2013, No. 1.

[3] G. I. Kuznetsov, "IrCe Cathodes For EBIS", Journal of Physics: Conference Series 2, 35, 2004.

[4] D. Satoh et al., "Research and development of iridium cerium photocathode for SuperKEKB injector linac", Energy Procedia Volume 131, Pages 326-333, 2017.

6.3 Linac

The normal conducting linac will be fed by two electron sources, one will be the RF gun for the low emittance e^- beam, and the second is the thermionic gun to provide higher charge needed for creating enough positrons from a hybrid target [2,3]. The linac consists of S-Band structures which will accelerate the beam up to 6 GeV. For the option of direct injection into the top up booster, it is proposed to use C-band high gradient accelerating structures to accelerate the beams from 6 to 20 GeV. The specifications of the accelerating structures are presented in Table 6.3.

Table 6.3: Linac structures.

Cavities	S-Band	C-Band
Frequency (MHz)	2855.98	5711.96
Length (m)	2.97	1.80
Cavity mode	$2\pi/3$	$2\pi/3$
Aperture diameter (mm)	20	14
Unloaded cavity gradient (MV/m)	25	50

The wakefields [1] have been included in linac simulations, together with the misalignments and offsets which are presented in Table 6.4. The preservation of emittance and charge is ensured by an automatic orbit steering code. With ideally deployed BPMs, the impact of misalignments is cancelled out perfectly. Reliability of the linac has been studied in simulations with various charge and randomisation values.

The low energy part of the linac starts with the beam from the RF gun at 11 MeV. With the optics shown in Fig. 6.3 and the singlet, doublet, and triplet magnets not set to high fields, kicks from the misaligned quadrupoles are minimised. These settings produce the results presented in Table 6.5.

JPo: I could not understand this - have I guessed correctly?

At 1.54 GeV the linac has a bending magnet to send e^- beam for cooling in the damping ring (DR)

DRAFT FOR ADVISORY COMMITTEE - DO NOT DISTRIBUTE

Table 6.4: Linac misalignments and offsets as 1σ in Gaussian distribution

Parameter	Simulated Error
Injection offsets (h/v)	0.1 mm
Injection momentum offset (h/v)	0.1 mrad
Quadrupole misalignment (h/v)	0.1 mm
Cavity misalignment (h/v)	0.1 mm
BPM's misalignment w.r.t. cavity(h/v)	30 µm

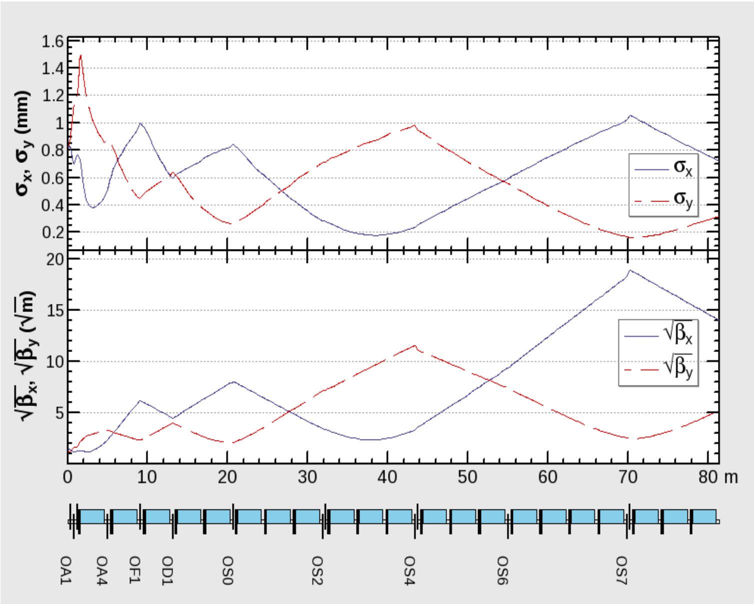

Figure 6.3: Optics of the 1.54 GeV Linac.

Table 6.5: Some parameters of the linac up to 1.54 GeV.

Parameter	Result
Length	79.1 m
Number of cavities, quadrupoles	21, 14
Injected emittance (h/v)	0.35/0.5 µm
Average extracted emit. (h/v)	6.4/5.0 nm
Transmission for 3.2 nC	100%

during e^- beam delivery to the collider. The DR removes emittance dilution due to misalignments and space charge. Electrons will be stored for 25 ms in the DR which can reduce the emittance blow up even if it is 100 times the conserved emittance. After cooling, the beam is transferred back to the linac via the turnaround loops and bunch compressor. Thus, the emittance of the beam delivered to the 1.54 GeV linac is determined by the DR cooling. Due to the relaxed emittance requirements at the entrance of the Booster, the e^- damping ring may be not necessary.

Some parameters of the 1.5 to 6 GeV part of the linac are presented in Table 6.6. In the 6 GeV linac option, the beam will be injected into a pre-booster damping ring. The transverse emittance of the beam injected in the PBR can be as big as 10/100 nm (h/v), which leaves a very large margin for the extracted emittance from the linac.

The 20 GeV linac presented in Fig. 6.5 is not just an extended version of the S-band linac, but it is re-optimised in order to increase the transmission. The drift spaces, with length L, between the cavities and steering magnets are lengthened in order to reduce the impact of BPM offsets which are proportional

JPo: I am not sure if I have understood this correctly. sending electrons for cooling 'during' transfer to the collider sounds strange. Please clarify.

JPo: Please check this whole paragraph because I have changed it substantially.

JPo: I have changed geometric to transverse as I think this is more commonly used.

DRAFT FOR ADVISORY COMMITTEE - DO NOT DISTRIBUTE

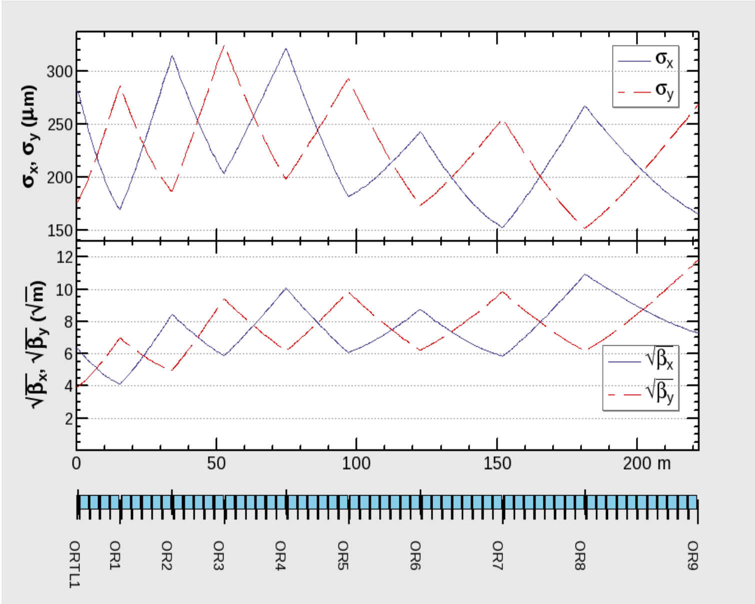

Figure 6.4: Optics of 1.54-6 GeV Linac

Table 6.6: Some parameters of the 1.54-6 GeV linac

Parameter	Value
Length	221.9 m
Injection-extraction energy	1.54 GeV-6 GeV
Injected emittance (h/v)	1.9/0.4 nm
Average extracted emit. (h/v)	1.1/0.4 nm
Transmission for 3.2 nC	100%

to σ_{BPM}/L. Furthermore, the increase in the spacing lowers the steering magnets' fields and in turn decreases the dispersion created by the steering. Consequently, the emittance dilution is decreased, however, it almost meets the requirement of the booster which is 3.4/0.3 (h/v) for 15σ acceptance. Some parameters of the 1.5 to 20 GeV part of the linac are presented in Table 6.7.

The emittance and charge requirements for all of the FCC-ee can be met with nearly perfect transmission and a factor of ten safety margin in transverse emittance at 6 GeV. Additionally, the orbit steering for the 20 GeV linac may be improved through dispersion free steering and BNS damping [4], to reduce the emittance blow up and hence the transmission loss. It should be noted that an 8% transmission loss is already envisaged and acceptable.

References

[1] K. Yokoya, "Short-Range Wake Formulas for Infinite Periodic Pill-Box", 1998, unpublished.

[2] I. Chaikovska et al., "Experimental Activities on High Intensity Positron Sources Using Channeling", Proc. IPAC'17, Copenhagen, Denmark, WEPIK002, 2017.

[3] I. Chaikovska et al., FCC-week 2017 Berlin, accessed in March 2018, https://indico.cern.ch/event/556692/contributions/2590440/attachments/1468997/2272259/e_FCCweek2017_IC.pdf

[4] T. O. Raubenheimer, A new technique of correcting emittance dilutions in linear colliders, Nucl. Instr. and Meth. A306 p. 61-64, 1991.

DRAFT FOR ADVISORY COMMITTEE - DO NOT DISTRIBUTE

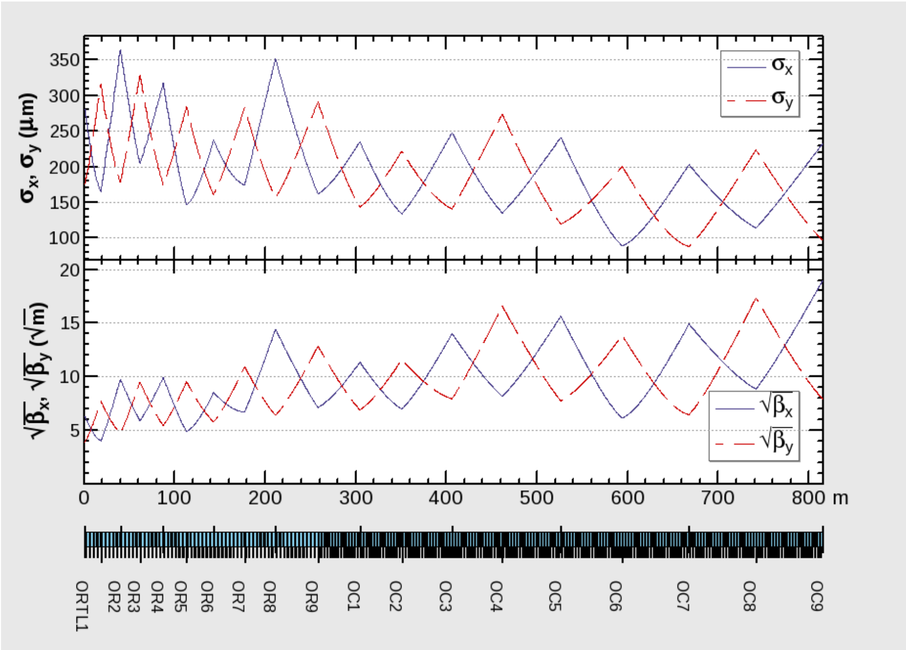

Figure 6.5: Optics of the 1.5 to 20 GeV part of the linac. Note that the C-band structures start after QR9.

Table 6.7: Some parameters of the 1.54 to 20 GeV part of the linac

Parameter	Value
Length	858 m
Injection-extraction energy	1.54 GeV-20 GeV
Injected emittance (h/v)	1.9/0.4 nm
Average extracted emit. (h/v)	4.0/0.3 nm
Transmission for 3.2 nC	92%

6.4 Positron Source and Capture System

6.5 Damping Ring

The damping ring design has been presented in [1] and some features are described in the following. The repetition rate of 200 Hz allows hosting of 5 trains, each with 2 bunches per RF pulse. After taking into account the longitudinal wakefields in the linac, the bunch to bunch spacing has been chosen as 60 ns [2]. Two bunches per RF pulse in the linac will become a train in the DR. Altogether 5 trains with a 100 ns spacing (for the kicker rise/fall time) and a bunch-to-bunch spacing of 60 ns in the linac have resulted in the requirement that the damping ring should have a circumference of at least 240 m (i.e. ∼800 ns).

The DR optics and parameters are presented in Fig. 6.6 and Table 6.8, respectively. The DR consists of 2 straight sections housing four 6.64 m long wigglers. One of the straight sections also contains a 7.44 m drift space reserved for injection/extraction and the opposite section hosts two LHC-type 400 MHz, 1.5 m long (3.5 m with cryostat) superconducting cavities. Injection of the e^+ beam from the linac [3] into the DR for a store time of 45 ms has been simulated. This storage is derived from the interleaved injection/extraction of the 5 trains.

The ±7.8% energy acceptance of the DR may be reduced to ±3.5% by lowering the voltage in order to increase the bunch length so that emittance dilution due to coherent synchrotron radiation (CSR) is avoided. For this reason, the incoming e^+ beam may be collimated at the end of the linac at ±3.5% or an energy compressor could be installed.

DRAFT FOR ADVISORY COMMITTEE - DO NOT DISTRIBUTE

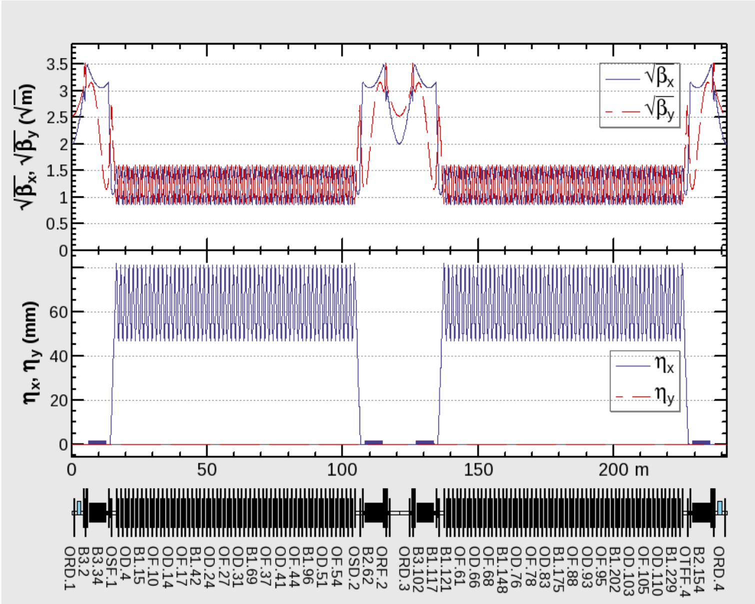

Figure 6.6: Damping ring optics.

Table 6.8: 1.54 GeV damping ring design parameters

parameter	value
Circumference	241.8 m
No. trains, bunches/train	5, 2
Train, and bunch spacings	100 ns, 61 ns
No. of cells in arc, cell length	57, 1.54 m
FODO cell phase advance (h/v)	69.5/66.1 deg
Betatron tune (h/v)	24.19/23.58
Natural emittance (h/v)	1.16/- nm
Damping time (h/v)	10.6/11.0 ms
Bending radius, wiggler field	15.5 m, 1.8 T
Energy loss per turn	0.22 MeV
RF voltage, frequency	4 MV, 400 MHz

Table 6.9: Damping ring performance without errors.

parameter	value
Transv., long. acceptance	22.4 μm, 14.7 mm
Energy spread	7.09×10^{-4}
Bucket height	8.0 %
Energy acceptance	±7.8 %
Injected emittance (h/v/l)	1.29/1.22/75.5 μm
Extracted emittance (h/v/l)	1.81/0.37 nm/1.52 μm

References

[1] S. Ogur et al., “Preliminary design of FCC-ee pre-injector complex", J. Phys.: Conf. Ser. 874 012003, 2017.

[2] F. J. Decker et al., “Long-Range Wakefields and Split-Tune Lattice at the SLC", SLAC-PUB-7259, 1996.

[3] N. Iida et al, “Beam Dynamics in Positron Injector Systems for the Next Generation b-Factories”,

DRAFT FOR ADVISORY COMMITTEE - DO NOT DISTRIBUTE

Proceedings of IPAC 2011, THYA01, San Sebastian, Spain, 2011.

6.6 Bunch Compressors

Before injection into the linac, the bunch length needs to be compressed from approximately 5 to 0.5 mm. It is proposed to have a dogleg bunch compressor comprising two triple bend acromats (TBA) to achieve this compression. A schematic drawing of the bunch compressor layout is shown in Fig. 6.7. Each dipole has a bending angle of 11.25°, and a quadrupole and sextupole are placed in mirror symmetry between each dipole. Between the two TBAs is a section for adjusting the phase advance. The quadrupole magnets are used to control the dispersion function, ensuring it goes to zero at the end of each achromat. The longitudinal dispersion properties of the bunch compressor are: $R_{56} = 0.40$ m, $T_{566} = 11.09$ mm, and $U_{5666} = 15.89$mm.

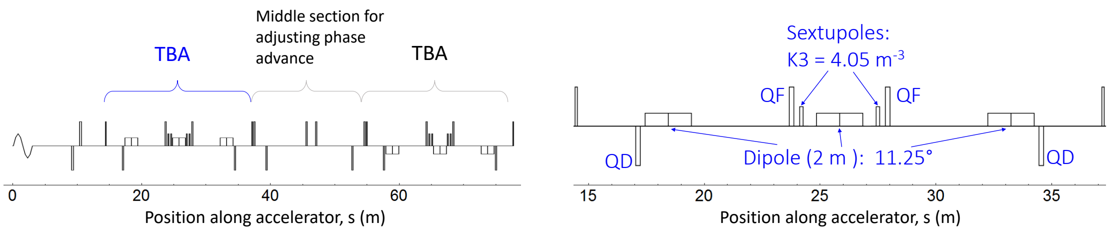

(a) (b)

Figure 6.7: (a) Magnet layout of the dogleg bunch compressor. The triple bend acromats (TBAs) are identical except that they bend in opposite directions. (b) detailed layout of one TBA.

An energy chirp is put in the beam by an S-band RF cavity upstream of the bunch compressor. The RF cavities have the following properties: $f_{RF} = 2.86$ GHz, $\phi_{RF} = 180^{\circ}$, and an accelerating gradient of 22.3 MV/m, to establish an energy chirp of $h_1 = \frac{1}{E_0}\frac{dE}{ds} = -2.75\ \mathrm{m}^{-1}$.

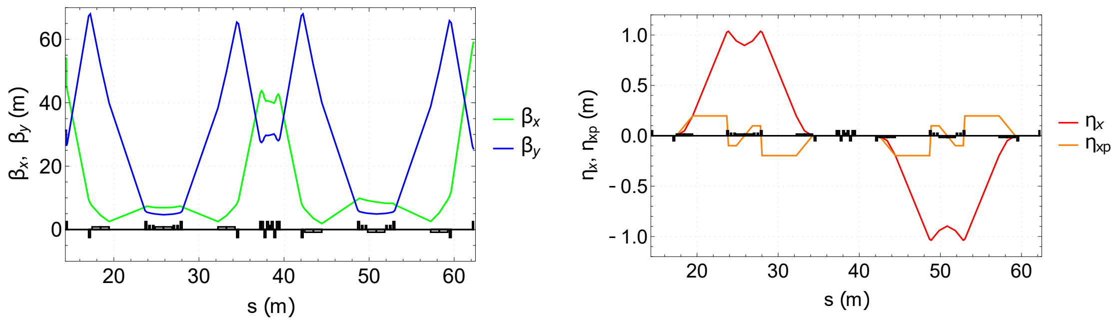

(a) (b)

Figure 6.8: (a) Beta functions through the dogleg bunch compressor, where β_x is indicated by the green line, and β_y by the blue line. (b) Horizontal dispersion function, η_x, shown by the red line, and the horizontal angular dispersion function, η_{xp} shown by the orange line.

The design presented here does not require a harmonic cavity. Instead a form of optical linearisation is used to minimise the non-linear terms encountered in bunch compression [7, 8]. Sextupole magnets are placed at a position where the dispersion is near maximum and are optimised for correcting the transverse chromaticity, rather than being optimised for cancellation of the second-order terms of the transport equations. Fortunately, despite being optimised for chromaticity, the resulting T_{566} is close to the optimum for reducing the effect of the non-linear compression terms, negating the need for a harmonic cavity [9].

DRAFT FOR ADVISORY COMMITTEE - DO NOT DISTRIBUTE

In spite of the relatively long bunch length ($\sigma_{z,f} = 0.5$ mm), coherent synchrotron radiation (CSR) has the potential to degrade the beam quality. This is because the reasonably large value for R_{56} required value necessitates a large degree of bending in a dogleg bunch compressor. Fortunately, CSR cancellation techniques [1–5] can be used to mitigate the emittance growth to within an acceptable level.

Careful control of β_x, and α_x in each dipole, as well as the phase advance between each dipole cancels out the CSR kicks (Δx_k and $\Delta x'_k$) almost completely. To compensate for the CSR kicks, an additional quadrupole magnet is needed in the section between the TBAs. A comparison of the emittance growth when this CSR kick mitigation is applied and when it is not is shown in Fig. 6.9. Initially (i.e. before the CSR kick cancellation method applied), the horizontal emittance growth was 68.3%. After the inclusion of the additional quadrupole and after the phase advance and Twiss parameters of the second TBA are manipulated, the emittance growth is reduced to 9.5% (this includes CSR in the drifts).

JPo figure (red/orange)
The colours in the figure (red/orange) are hard to distinguish. I suggest changing them for more contrast.

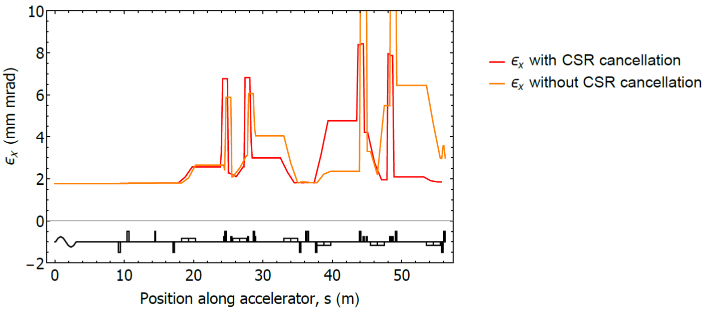

Figure 6.9: Emittance along the bunch compressor, before CSR cancellation techniques are applied (orange) and after (red).

References

[1] D. Douglas, “Suppression and Enhancement of CSR-Driven Emittance Degradation in the IR-FEL Driver,” *Technical Report JLAB-TN-98-012*, 1998.

[2] S. Di Mitri, M. Cornacchia, and S. Spampinati, “Cancellation of coherent synchrotron radiation kicks with optics balance,” *Phys. Rev. Lett.*, vol. 110, p. 014801, 2013.

[3] S. Di Mitri and M. Cornacchia, “Electron beam brightness in linac drivers for free-electron-lasers,” *Phys. Rep.*, vol. 539, 2014.

[4] R. Hajima, “A first-order matrix approach to the analysis of electron beam emittance growth caused by coherent synchrotron radiation,” *Japanese Journal of Applied Physics, Part 2: Letters*, vol. 42, pp. 974–976, 2003.

[5] Y. Jiao, X. Cui, X. Huang, and G. Xu, “Generic conditions for suppressing the coherent synchrotron radiation induced emittance growth in a two-dipole achromat,” *Phys. Rev. ST AB*, vol. 17, 060701, 2014.

[6] M. Borland, “Elegant: A flexible SDDS-compliant code for accelerator simulation,” *Advanced Photon Source Report, LS-287*, 2000.

[7] S. Thorin, M. Eriksson, S. Werin, D. Angal-Kalinin, J. McKenzie, B. Militsyn, and P. Williams, “Bunch Compression by Linearising Achromats for the MAX IV Injector,” in *Proc. of FEL2010, Malmö, Sweden*, WEPB34, pp. 471–474, 2010.

[8] Y. Sun, P. Emma, T. Raubenheimer, and J. Wu, “X-band RF driven free electron laser driver with optics linearization,” *Phys. Rev. ST AB*, vol. 17, 110703, nov 2014.

[9] T. K. Charles, K. Oide, M. J. Boland and F. Zimmerman, “Bunch compression and turnaround loops in the FCC-ee injector complex,” *Proc. of IPAC18, Vancouver, Canada*, may 2018.

DRAFT FOR ADVISORY COMMITTEE - DO NOT DISTRIBUTE

6.7 Pre-booster

Two options are under consideration for the pre-accelerator of the bunches before they are transferred to the high-energy booster: using the existing SPS (baseline) and a completely new ring.

Using the SPS as pre-booster for the FCC-ee imposes various constraints, as only certain modifications can be made to the existing machine. There were similar constraints when the SPS was used as an injector for the LEP collider [1]. The SPS is filled with FODO cells and the emittance can be minimised by tuning them to have a horizontal phase advance of around 135°. This phase advance provides an equilibrium transverse emittance of below 30 nm at 20 GeV. In addition, this phase advance ensures dispersion suppression, as the total arc phase advance is a multiple of 2π [2].

The damping time, which is around 1.7 s for the SPS at 6 GeV, is quite long and therefore it will lengthen the SPS injection plateau and consequently the whole injector cycle. Wiggler magnets with a field of 5 T and a total length of 4.5 m designed to shorten the damping times by roughly an order of magnitude are being studied. Some parameters of the SPS with and without wiggler magnets are shown in Table 6.10. In particular, the horizontal equilibrium emittance is reduced to 0.13 and 10 nm.rad at injection and extraction respectively, whereas the corresponding energy loss per turn is greatly increased to 2.7 and 47 MeV.

Table 6.10: SPS Parameters with/without wiggler magnets.

	6 GeV		20 GeV	
	Without Wiggler	With Wiggler	Without Wiggler	With Wiggler
ϵ_x (nm.rad)	2.43	0.13	27	10
τ (s)	1.7	0.1	0.04	0.02
U_0(MeV)	0.15	2.7	19	47

An alternative study of a green-field pre-booster ring has also been made. The booster requirements for dynamic aperture constrain the extracted emittance of the PBR to around 3 nm. The linear

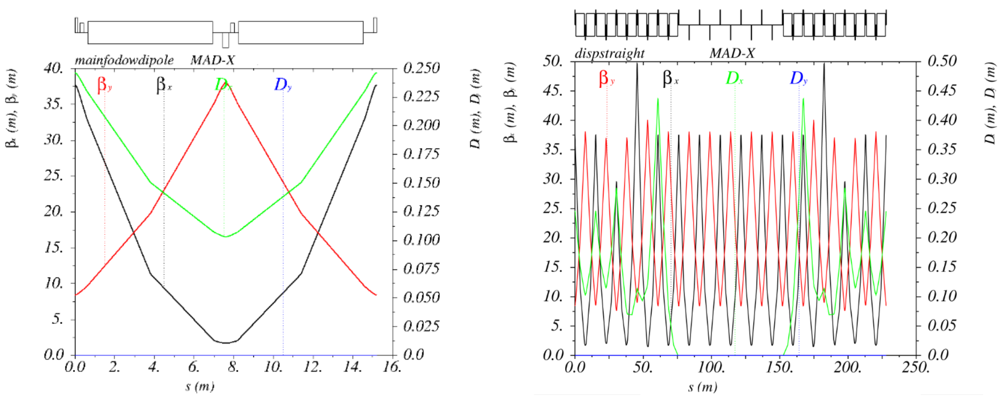

Figure 6.10: Beta functions and dispersion of the main cell (left) and straight section(right).

lattice of the PBR is based on analytic calculations and simulations. A FODO type cell has been chosen and the ring has a racetrack shape consisting of 2 arcs and 2 straight sections; each arc has 60 FODO cells with sextupole magnets in each main cell, whereas each straight section has two matching cells. The horizontal (black) and vertical beta (red) functions and horizontal dispersion (green) of a cell and one straight section are presented in Fig. 6.10.

A cell comprises two 6.3 m long dipoles located between 30 cm long quadrupoles. The dipoles have a field of 70 Gauss at injection. The chromaticity is controlled by two families of 20 cm long

DRAFT FOR ADVISORY COMMITTEE - DO NOT DISTRIBUTE

sextupoles and the total circumference is 2280 m. The damping time reduction to 0.1 s can also be achieved by using 2 T wiggler magnets.

The phase advance per cell was chosen following a study to reduce chromaticities and anharmonicities and thereby maximise dynamic aperture.

JPo: I have removed the reference to the table, since the table was commented out - is this OK?

References

[1] The LEP injector study group, The LEP injector chain, CERN-SPS/63-26.

[2] Y. Papaphilippou et al., The SPS as an Ultra-Low Emittance Damping Ring Tet Facility for CLIC, Shanghai, China, 2013.

[3] Y. Papaphilippou et al., Conceptual Design of the CLIC Damping Rings, TUPPC086, Proceedings of the 3rd International Particle Accelerator Conference 2012, New Orleans, LA, USA, 20 - 25 May 2012.

[4] B. Haerer, et. al., Status of the FCC-ee Booster Synchrotron, These Proceedings, Vancouver, Canada, 2018.

[5] CERN-BE/ABP Accelerator Beam Physics Group, MAD-Methodical Accelerator Design.

6.8 Booster

The very high target luminosities of $10^{34} - 10^{36}\,\mathrm{cm}^{-2}\mathrm{s}^{-1}$ lead to very short beam lifetimes due to beamstrahlung and radiative Bhabha scattering. As a consequence there will be a full energy booster in the same tunnel as the collider to facilitate continuous top-up injection.

JPo: I think it is beamstrahlung, not bremsstrahlung

The injection energy is determined by the field quality and reproducibility of the magnetic field in the dipole magnets in the arc sections. The current design has an energy of 20 GeV, resulting in a magnetic field of B=6 mT.

The layout of the booster follows the footprint of the FCC hadron collider, but the lepton collider rings will have an offset of about 1 m to the outside. The interaction points will even have an offset of 10.6 m as a result of the requirements for the crossing angle and synchrotron radiation mitigation around the experiments. Therefore the booster will bypass the detectors on the inside of the cavern and as for the collider, the RF sections are located in points PD and PJ.

In order not to spoil the luminosity and to reduce background coming from lost particles, the equilibrium emittance of the beam extracted from the booster must be similar to that in the collider rings. The length of the basic FODO cell was chosen to be 53 m in the separation arc and about 54 m in the long arcs. The different lengths are necessary to fit the FCC layout. In the collider, the lattice is optimised for two optics: an optics with 60° phase advance per cell is used for operation at the Z peak and the W pair production threshold (45.5 GeV and 80 GeV) and a 90° phase advance per cell will be used for H production and the $\mathrm{t\bar{t}}$ production threshold (120 GeV and 182.5 GeV). The resulting horizontal equilibrium emittances for these lattices are summarised in Table 6.11.

The radius of curvature in the arc sections is $R = 13.15\,\mathrm{km}$. At the beginning and end of each arc, a distance of 566 m is reserved for the hadron collider dispersion suppressors and therefore this region has a different radius of curvature of $R = 15.06\,\mathrm{km}$. 10 FODO cells 56.6 m long and with less bending strength are installed in the booster to follow the tunnel geometry. A quadrupole based dispersion suppressor in the last five cells is used to match the optics to the straight section FODO cells. In the straight sections around points PA, PB PF, PG, PH and PL the cell length is 50 m and in the

JPo: Please check - is it the tunnel geometry or the machine geometry?

DRAFT FOR ADVISORY COMMITTEE - DO NOT DISTRIBUTE

Table 6.11: Horizontal equilibrium emittances of the booster compared to the collider for all four beam energies. The 60° optics is used for 45.5 GeV and 80 GeV and the 90° optics for 120.0 GeV and 182.5 GeV.

beam energy (in GeV)	emittance booster (in nm.rad)	emittance collider (in nm.rad)
45.5	0.24	0.24
80.0	0.73	0.84
120.0	0.55	0.63
182.5	1.30	1.48

extended straight sections around points PD and PJ the cell length has been increased to 100 m in order to maximise the space available for RF installation. The transition of the optics from the arcs to these long FODO cells is shown in Fig. 6.11.

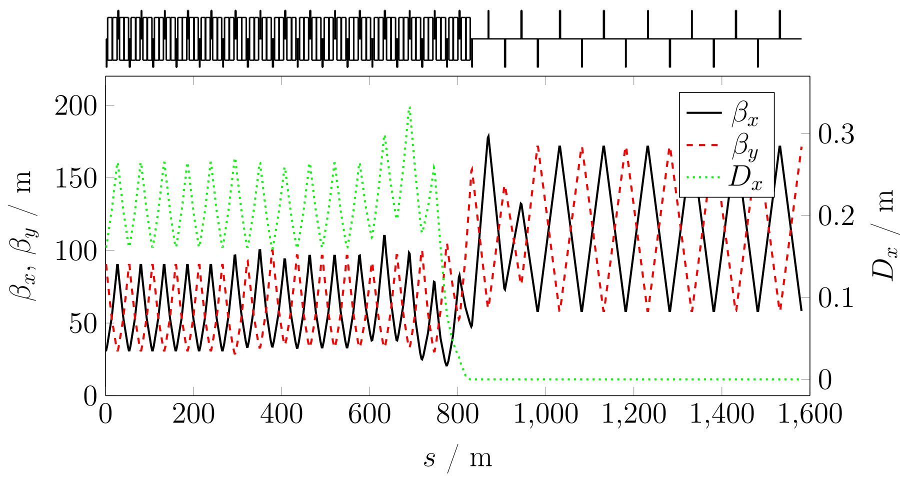

Figure 6.11: Beta functions and horizontal dispersion function of the transition from the arc lattice into a straight section with an RF installation. The first five cells are regular arc FODO cells with a length of 54 m. The following section of 566 m consists of ten FODO cells with a different bending angle to fit the geometry of the dispersion suppressor of the hadron collider. They also serve as quadrupole based dispersion suppressor and matching section to the optics of the 100 m long straight FODO cells.

Unlike the hadron collider no "tapering" (scaling of the magnet strengths to the local beam energy) is planned. Such scaling is not necessary in the booster due to the changing beam energy of the rapid cycling synchrotron .

JPo
Please check that this is correct - I was not sure what 'adequate' meant

The beam parameters at injection energy need particular examination. The damping time becomes longer than 10 s due to the weak radiation damping and this is not compatible with the booster cycle and the top-up requirements. Also the horizontal equilibrium emittance shrinks to 12 pm rad leading to emittance blow-up due to intra-beam-scattering. Therefore 16, ∼9 m long wigglers are installed in the straight sections around the points PA and PG. These normal conducting wigglers are designed so that a damping time of 0.1 s is reached and the emittance is increased to 240 pm.rad for the 60° optics and 180 pm.rad for the 90° optics. However, the additional energy loss in the wigglers needs to be compensated by the RF system and the voltage therefore needs to be at least 140 MV. The wigglers will be switched off adiabatically to reduce the energy loss during the energy ramp. As a consequence, no extra RF voltage is required for the higher beam energies and the RF voltage is the same as that in the

DRAFT FOR ADVISORY COMMITTEE - DO NOT DISTRIBUTE

collider.

Tracking studies based on the survival of the particles after 1000 turns have shown that a non-interleaved sextupole scheme provides the largest dynamic aperture. The tracking studies were performed with the PTC code which includes radiation damping and quantum excitation. Also Gaussian distributed quadrupole misalignments with σ=150 μm were introduced.

JPo mentioned before

PTC has not been mentioned before - I assume it is the name of the code

6.9 Transfer Lines

DRAFT FOR ADVISORY COMMITTEE - DO NOT DISTRIBUTE

Chapter 7

Experimental environment and detector designs

7.1 Experiment Environment

The colliding electron and positron beams of the FCC-ee cross at an angle of 30 mrad at the interaction point. The detectors are placed with their axis of symmetry (z-axis) halfway between the incoming and outgoing beam lines. Hence, each beam traverses the detector solenoid field at an angle of 15 mrad. This imposes an upper limit on the detector field strength of 2 T. In order to preserve the emittance of the beams it is necessary to have a set of two compensating solenoids in front of the final focussing quadrupoles. The compensating solenoids protrude into the detector to a distance of $|z| \simeq 1.20$ m from the interaction point. It has been decided to keep all machine elements including the compensating solenoids inside a cone with an opening angle of 100 mrad about the z-axis. The cylindrical central part of the beam pipe, which fully covers the angular range down to 150 mrad in front of the tracking detectors, has an inner radius of 15 mm and total material thickness of 1.7 mm made up of 1.2 mm of beryllium cooled by a 0.5 mm layer of water(?). At normal incidence, this corresponds to 0.47% of X_0.

The beam crossing times vary from a minimum of 20 ns at the Z pole to a maximum of 10 μs at the highest energy point, $\sqrt{s} = 365$ GeV. The unprecedented luminosity brings challenges in controlling the impact of various machine- and beam-induced backgrounds on the detector performance. The synchrotron radiation background, that sets constraints on the interaction region design and the beam-induced backgrounds due to $\gamma\gamma$ collisions are described below.

7.1.1 Synchrotron Radiation

Synchrotron radiation (SR) [175] is a potential source of background that has been already discussed in Section 2.5.4. As shown in Figure 2.12, an appropriate set of masks has been added in front of the final focus quadrupoles to protect the interaction region from direct hits of SR photons from the last bending magnet. The number of SR photons that forward scatter from the masks increases very strongly with beam energy as shown in Table 2.7. Hence, by bringing this background to a tolerable level at the highest energy, it will, by the same measure, be reduced to a negligible level at the lower energies.

It can be seen from the interaction region scheme shown in Figure 2.12, that SR masks (in red) are placed inside the beam pipe at the exit of the final focus quadrupoles (QC1) 2.1 m from the interaction point. To further limit the fraction of the SR fan that scatters off the masks and showers into the detector area, a complex scheme of shielding has been developed to minimise the impact on the detector performance. Tungsten shields (in green) are positioned outside the beam pipe. A requirement for the position of the shield comes from the need to leave the acceptance window in front of the luminometers (in magenta) unshielded, covering an angle of about 50 to 100 mrad around the outgoing beams. This constraint results in an asymmetric azimuthal coverage of the shielding material around the beam pipe in the luminometer acceptance window, $370 < |z| < 1190$ mm, leaving the vertex detector partially unshielded from SR. Figure 7.1 shows the implementation of the shield in the GEANT4 detector model used for background simulation studies. The thickness of the shield up to the rear end of the luminometer, $|z| < 1190$ mm, is limited to 1 mm whereas it becomes 15 mm with full coverage of the two beam pipes from the rear end of the luminometer up to QC1.

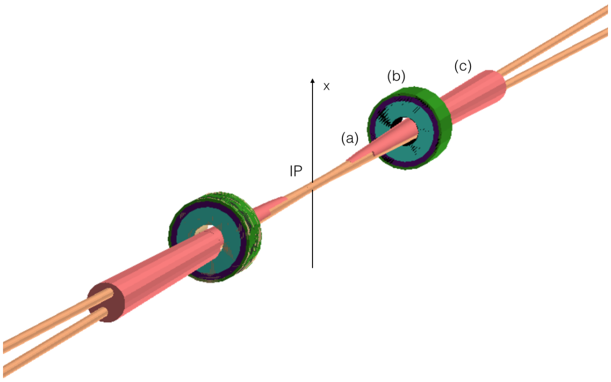

Figure 7.1: The tungsten shielding of the beam pipe from 370 mm (a) to the rear of the luminometer at 1190 mm (b) is 1 mm thick and covers only a 68° angle on the positive x-side of the beam pipe. After 1190 mm, a full 15 mm thick tungsten cone covers both beam pipes to protect the tracking detectors from synchrotron radiation.

Photons from the last bend scatter on the lower mask and partially forward scatter into the detector area. The forward scattered photons were simulated with SYNC_BKG and it was found that their energy distribution, with peaks at 70 keV and 250 keV, does not exceed 1 MeV. The photons have been propagated through a full GEANT4 simulation that accounts for the interaction region (with or without beam-pipe shielding), the luminometer (Section 7.2) and the CLD detector model (Section 7.3). While no hits were observed in the detector at lower energies, a few hits (40 per BX) were observed at $\sqrt{s} = 250$ GeV, and most (3.3×10^4 per BX) at $\sqrt{s} = 365$ GeV, reducing to only ~ 500 hits per BX with the proposed shield in place. More details are given below in Section 7.3.2, but this already shows that, with appropriate shielding, the effect of the SR on the detector is not expected to be an issue.

Pair-production Background

The production of low energy electron-positron pairs is a source of background, in particular in detector elements close to the beam-pipe. At FCC-ee, the dominant production mode is incoherent pair production (IPC), whereby an e^+e^- pair is produced in $\gamma\gamma$ interactions involving virtual or real photons from beamstrahlung. The GuineaPig (GP) [204] event generator has been used to study this background at 91.2 and 365 GeV.

Table 7.1 summarises the production rates at both energies, together with the total energy carried by the $e^\pm$ particles produced. While a large number of particles is created, only those that are emitted with a significant transverse momentum, p_T, and polar angle, θ, can enter the detector volume; the others remain trapped around the magnetic field lines of the detector field. The table also shows the number of particles with p_T and θ large enough that they can reach a typical vertex detector within a 2 T field. The kinematics of the $e^\pm$ particles produced with $E > 5$ MeV is illustrated in Fig. 7.2. The particles seen at $\theta \sim 15$ mrad correspond to those that are emitted at very small angles in the direction of the outgoing beams. The dense region at higher θ corresponds to e^- (e^+) particles that are emitted in the direction of the outgoing e^+ (e^-) beam and that are deflected towards larger polar angles by the electromagnetic field

DRAFT FOR ADVISORY COMMITTEE - DO NOT DISTRIBUTE

Table 7.1: Number of $e^{\pm}$ particles created by e^+e^- pair production per BX, total energy, and the number of these primary particles that would reach a typical vertex detector within a magnetic field of 2 T. Numbers are obtained from GuineaPig, prior to any detector simulation.

$\sqrt{s}$ [GeV]	91.2	365
Total particles	800	6200
Total E (GeV)	500	9250
Particles with $p_T \geq 5$ MeV and $\theta \geq 8^\circ$	6	290

of the bunch. Only the particles emitted within the top-right corner (black line) would reach a typical vertex detector, with a 2 T field. The effect of this background in the detector, as obtained from a full GEANT4 simulation, is discussed in Section 7.3.2. The numbers given in Table 7.1 already indicate that this background is rather moderate.

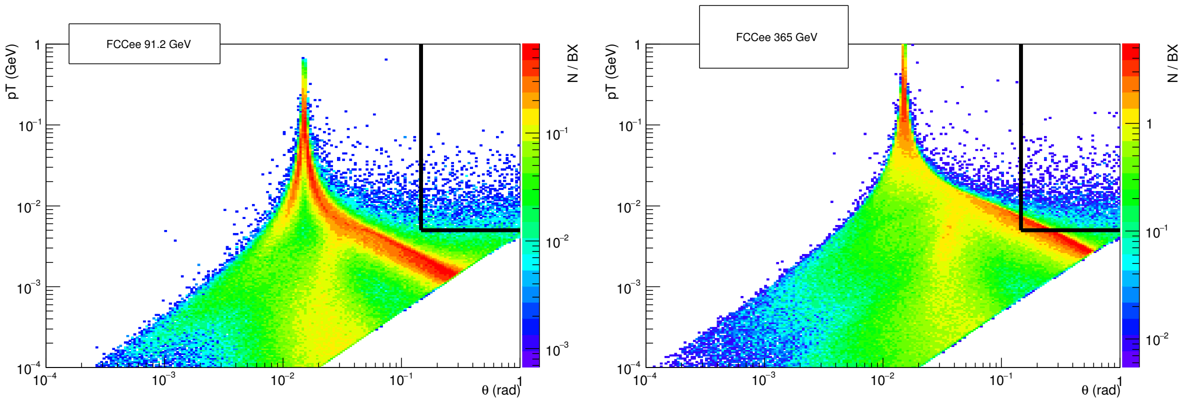

Figure 7.2: Transverse momentum versus polar angle for $e^{\pm}$ particles from IPC e^+e^- pair production, in the detector frame, for $\sqrt{s} = 91.2$ GeV (left) and 365 GeV (right). Only the particles emitted within the top-right corner (black line) would reach a typical vertex detector immersed within a field of 2 T.

Apart from creating e^+e^- pairs, $\gamma\gamma$ collisions can give rise to hadrons, resulting in jets in the detector. These interactions have been simulated with a combination of GuineaPig and Pythia6 [205]. Within the phase space considered, $\sqrt{\hat{s}} > 2$ GeV where $\sqrt{\hat{s}}$ is the invariant mass of the $\gamma\gamma$ system, this background was found to be negligible with less than 10^{-2} (10^{-3}) events produced per BX at $\sqrt{s} = 365$ (91.2) GeV.

7.2 The Luminometer

The goal of the luminosity measurement is an *absolute* normalisation of cross section measurements to a precision of 10^{-4}. Such a precision is of particular relevance at the Z energy for the precise measurement of the Z lineshape parameters. For the precise determination of the Z mass and width, both with stated goals of 100 keV, a *relative* normalisation from one energy scan point to the other of 5×10^{-5} is called for. Many sources of systematic uncertainty, including that from the geometrical definition of the detector acceptance, cancel for the relative luminosity measurement.

The reference process for the luminosity measurement is small angle Bhabha scattering, which may be complemented by that of large angle $e^+e^- \to \gamma\gamma$ production. This section describes the detector and the methodology for luminosity measurement using small angle Bhabha scattering.

DRAFT FOR ADVISORY COMMITTEE - DO NOT DISTRIBUTE

7.2.1 Luminometer Design

Following the experience with LEP [206, 207] and from more recent linear collider studies [208, 209], the luminometers will be constructed as a pair of small angle calorimeters consisting of tungsten plates interleaved with silicon readout planes finely segmented into pads. The calorimeters will be centred around (and tilted to be perpendicular to) the outgoing beam lines to precisely measure the scattering angle of the elastically scattered electrons and positrons. The small angle region is very busy and the space available for the luminometers is severely constrained. The compensating solenoids, extending to $|z| \simeq 1.2$ m, push the luminometers forwards into the detector volume. At the inner radius, the luminometers have to stay clear of the incoming beam pipe; at the outer radius, they must not interfere with the forward coverage of the tracking detectors and, hence, they must stay fully inside a cone of 150 mrad around the main detector axis of symmetry.

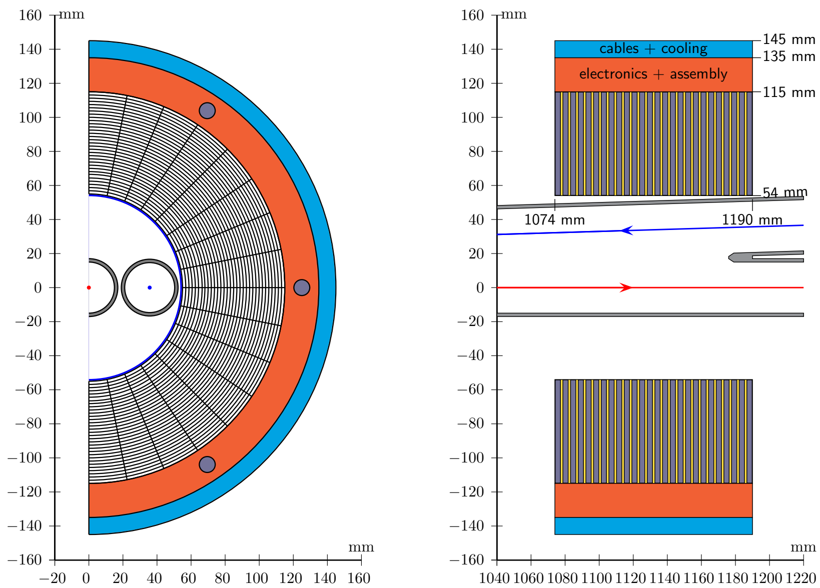

Figure 7.3: The luminosity calorimeter centred around the outgoing beam line. Front view (left), top view (right).

The proposed luminometer design is shown in Fig. 7.3. The mechanical inner radius is 54 mm, the outer radius is 145 mm. The sensitive region, instrumented with silicon sensors, extends from 55 to 115 mm. The calorimeters consist of 25 layers, with each layer comprising a 3.5 mm tungsten plane, equivalent to 1 X_0 and a silicon sensor plane inserted in the 1.0 mm gap. In the transverse plane, the silicon sensors are finely partitioned into pads. The proposed number of divisions is 32 both radially and azimuthally for 1,024 readout channels per layer, or 25,600 channels in total for each calorimeter.

The calorimeter sandwich extends along the outgoing beam line from 1074 mm to 1190 mm. The region outside the sensitive region, with radii between 115 and 145 mm, is used for services. This includes the mechanical assembly of the tungsten-silicon sandwich, front-end electronics, cables, cooling and equipment for mechanical alignment. Each calorimeter is divided vertically into two half barrels clamped together around the beam pipe. The calorimeters have a weight of about 65 kg each. Due to the compactness of the devices it will be possible to produce each silicon half-layer from a single silicon tile. This minimises potential inactive regions between sensors and facilitates precise geometrical control of the acceptance. Meticulous care is required for the design of the vertical assembly of the two half-barrels, both in order to avoid a dead region and for the precise control of the geometry. In order to decouple the luminometers mechanically from the magnetic elements of the machine which are close to the IP, it is planned that the luminometers will be supported from the rear by a mechanical system connected to the

DRAFT FOR ADVISORY COMMITTEE - DO NOT DISTRIBUTE

forward calorimeters.

The silicon sensor pads are connected to the compact front-end electronics positioned at radii immediately outside the sensors. Due to the high detector occupancy it is desirable to be able to read out the detector for each bunch crossing. This calls for the development of readout electronics with a shaping time shorter than 20 ns. Assuming that this can be accomplished within a power budget of 5 mW per channel, each calorimeter barrel will dissipate a total of 130 W, which will have to be removed by cooling. In order to maintain the required geometrical stability, the temperature of the luminometers should be kept stable and uniform within ± 1 K or better.

7.2.2 Acceptance and Luminosity Measurement

The SiW sandwich has an effective Moliere radius of about 15 mm. For a robust energy measurement, the acceptance limits should be kept of the order of one Moliere radius away from the borders of the instrumented area, effectively limiting the acceptance to the 62–88 mrad range. To ensure that the luminosity measurement only depends to second order on possible misalignments and movements of the beam spot relative to the luminometer system, the method of asymmetric acceptance will be employed [210]. Events are accepted if they are inside a narrow acceptance in one calorimeter and inside a wide acceptance in the other. Assuming that a 2 mrad difference between the wide and narrow acceptances is sufficient to accommodate possible misalignments, the narrow acceptance will then cover the angular range 64–86 mrad corresponding to a Bhabha cross section of 14 nb, at the Z pole, equivalent to about 6.4×10^{-4} events per bunch crossing.

The forward-peaked $1/\theta^3$ spectrum of the Bhabha scattering process causes the luminosity measurement to be particularly sensitive to the definition of the angular acceptance. The acceptance will be affected by any change, ΔR, in the inner and outer edges of the acceptance as follows: $\Delta A/A \approx -(\Delta R_{\text{in}}/1.6\,\mu\text{m}) \times 10^{-4}$ and $\Delta A/A \approx +(\Delta R_{\text{out}}/3.8\,\mu\text{m}) \times 10^{-4}$, where R is the radial coordinate of the reconstructed showers. Similarly, the acceptance will be affected by any change, ΔZ, in the half-distance between the effective planes of the radial measurements in the two calorimeters: $\Delta A/A \approx +(\Delta Z/55\,\mu\text{m}) \times 10^{-4}$. With the crossing beam situation, the two calorimeters are centred on different axes, and Z should be interpreted as $Z = \frac{1}{2}(Z_1 + Z_2)$, where Z_1 and Z_2 are the two distances, measured along the two outgoing beam directions, from the (nominal) IP to the luminometers.

With the method of asymmetric acceptance, a weak second order dependence of the acceptance on the interaction point position, as measured in the luminometer system, remains. The size of this effect was investigated through a high statistics study of a Bhabha event sample generated with the event generator BHLUMI [211]. The study, based on a parametrised detector response, confirmed the second order dependence as long as shifts of the IP were small enough to be covered by the difference between the wide and narrow acceptance definitions: in this case, up to shifts of about $\delta r = 0.5$ mm transversely and $\delta z = 20$ mm longitudinally. Inside this range, the changes of the acceptance observed could be parametrized as $\Delta A/A \approx +(\delta r/0.6\,\text{mm})^2 \times 10^{-4}$ and $\Delta A/A \approx -(\delta z/6\,\text{mm})^2 \times 10^{-4}$. It should be noted, that such shifts of the IP position will give rise to asymmetries in the Bhabha counting rate either azimuthally (for radial shift) or between the two calorimeters (longitudinal shifts) and hence, can be monitored and corrected for from the data. No such possibility of correction from the data is present for the detector construction tolerances, ΔR and ΔZ, discussed in the previous paragraph.

7.2.3 Machine and Beam-induced Backgrounds in the Luminometer

A full simulation of the impact of e^+e^- pairs from IPC processes on the luminometers has been performed for $\sqrt{s} = 91.2$ GeV, where the requirements for the precision of the luminosity measurement are the strongest. The total energy deposited by IPC pairs in each calorimeter is $\sim$250 MeV per bunch crossing. This energy is rather low and moreover, the calorimeter cells which see the largest energy deposits are at the lowest radii at the rear of the calorimeter and would not enter in the fiducial volume relevant

DRAFT FOR ADVISORY COMMITTEE - DO NOT DISTRIBUTE

for the luminosity measurement. Consequently, the IPC background is not expected to compromise the precision on the luminosity measurement. In any case, this background could be easily eliminated by placing a thin layer of tungsten shielding at the inner radius of the luminometers.

Using the forward scattered synchrotron radiation spectrum at $|z| = 2.1$ m from SYNC_BKG, the total energy released on each luminosity calorimeter per crossing was found to be $\sim$ 340 MeV and $\sim$ 7 MeV without and with the proposed beam-pipe shield respectively, at $\sqrt{s} = 365$ GeV where the effect of SR is largest. These values are very low and will have no effect on the performance of the detector.

In LEP, the primary source of background for the luminosity measurement was from so-called off-momentum particles generated by beam-gas scattering in the straight sections before the experiments and deflected by the quadrupoles into the luminometers [206]. The off-momentum particles that reached the luminometers had typically lost more than about half their energy in the beam-gas scattering process. Hence, energy requirements combined with angular requirements were able to bring the background rate of coincidences between the two arms of the luminometer system down to a negligible level. Early studies of beam-gas interactions at FCC-ee have been performed, for $\sqrt{s} = 91.2$ GeV, with a vacuum of 10^{-9} mbar. The studies demonstrate an induced rate of particles leaving the beam pipe of 140 kHz per meter per beam in the region close to the IP. Assuming, probably very conservatively, a similar rate of off-momentum particles into each luminometer results in a coincidence rate about two orders of magnitude below the Bhabha rate, before any energy and angular requirements. Thus, this background source appears to be considerably smaller than at LEP. This seems to be consistent with what one would expect: the strong focussing of the FCC-ee which boosts the physics rate should have no influence on the beam-gas scattering rate.

7.2.4 Electromagnetic Focussing of Bhabha Electrons

The final state Bhabha scattering electrons and positrons will be focussed by the strong electromagnetic field of the opposing bunch in the same way as the beam particles. The effect is being studied using events generated by BHWIDE [212] and injected into GuineaPig++ [140], which then tracks the final state particles to the outside from a randomly chosen scattering point within the collision diamond.

7.3 The CLD Detector Design

The CLD detector has been adapted to the FCC-ee specificities from the most recent CLIC detector model [213], which features a silicon pixel vertex detector and a silicon tracker, followed by highly granular calorimeters (a silicon-tungsten ECAL and a scintillator-steel HCAL). A superconducting solenoid provides a strong magnetic field and a steel yoke interleaved with RPC muon chambers closes the field.

To compensate for the lower field strength (2 T instead of 4 T), the tracker radius was enlarged from 1.5 to 2.1 m. Another change concerns the hadron calorimeter: its depth was reduced from 7.5 to 5.5 λ_I to account for the lower maximum centre-of-mass energy. A difference with respect to CLIC stems from the continuous operation of a circular collider, which hinders the use of power-pulsing. The impact on cooling and material budgets will depend on technology choices and therefore detailed engineering studies on cooling systems will be needed. Based on the developments for the ALICE ITS upgrade, the material budget per layer for the vertex detector has been increased in an "ad-hoc" manner by a factor 1.5 with respect to the CLIC vertex detector.

JPo explained

Lambda-I is not explained.

A comparison of the main parameters in the CLD concept and the CLIC detector model is presented in Table 7.2. The CLD concept is illustrated in Fig. 7.4.

7.3.1 CLD Vertex and Tracking System

The CLD vertex detector consists of a cylindrical barrel closed off in the forward directions by disks. The layout is based on double layers, i.e. two sensitive layers fixed on a common support structure (which

DRAFT FOR ADVISORY COMMITTEE - DO NOT DISTRIBUTE

Table 7.2: Comparison of key parameters of CLD and CLIC detector models.

Concept	CLICdet	CLD
Vertex inner radius [mm]	31	17
Tracker half length [m]	2.2	2.2
Tracker outer radius [m]	1.5	2.1
ECAL absorber	W	W
ECAL X_0	22	22
HCAL absorber	Fe	Fe
HCAL λ_I	7.5	5.5
Solenoid field [T]	4	2
Overall height [m]	12.9	12.0
Overall length [m]	11.4	10.6

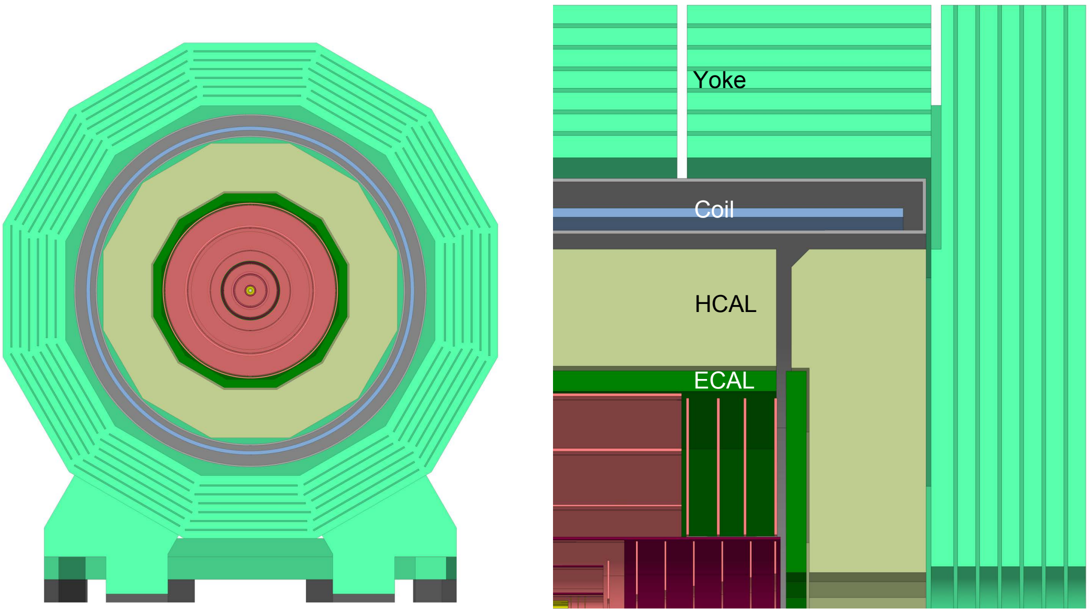

Figure 7.4: The CLD concept detector: end view cut through (left), longitudinal cross section of the top right quadrant (right).

includes cooling circuits). The barrel consists of three double layers and the forward region is covered by three sets of double-disks.

The CLD concept features an all-silicon tracker. Engineering and maintenance considerations led to a design with a main support tube for the inner tracker region including the vertex detector. The inner tracker (IT) consists of three barrel layers and seven forward disks. The outer tracker (OT) completes the system with an additional three barrel layers and four disks. The overall geometrical parameters of the tracker are given in Table 7.2. The layout (see Fig. 7.4) respects the 150 mrad cone reserved for the luminometer.

Preliminary engineering studies have been performed for the CLIC detector to define the support structures, cooling systems etc. needed for the tracker barrel layers and disks. For the outer tracker barrel support, these studies were completed by building and testing a prototype. The same concepts and material thicknesses are currently used for CLD. The additional budget needed for the 200 µm thick layer of silicon including the extra material for support structures, cables and cooling infrastructure has been estimated. The total material budget in terms of X_0 is about 11% in the barrel and at the level of 20% in the forward region.

DRAFT FOR ADVISORY COMMITTEE - DO NOT DISTRIBUTE

Full simulation studies have been carried out in order to assess the performance of the CLD tracker. The single point resolutions assumed for the sub-detector elements were: *i)* vertex detector: 3×3 μm^2, *ii)* inner-most layer of inner tracker: 5×5 μm^2, and *iii)* other layers of inner tracker and outer tracker: 7×90 μm^2. The momentum resolution obtained for muons is shown in Fig. 7.5. For high momentum muons in the central region, the goal of $\Delta p_\mathrm{T}/p_\mathrm{T}^2 < 5\times 10^{-5}$ GeV^{-1} is reached. The study showed a tracking efficiency of 100% for single muons with a transverse momentum above 1 GeV. The efficiency also remains high for softer muons, falling off gradually to reach about 96% for $p_\mathrm{T} = 0.1$ GeV. The tracking efficiency for particles in more complex environments was studied using light-quark pair events at $\sqrt{s} = 91$ and 365 GeV. A tracking efficiency of almost 100% was found whenever $p_\mathrm{T} > 1$ GeV.

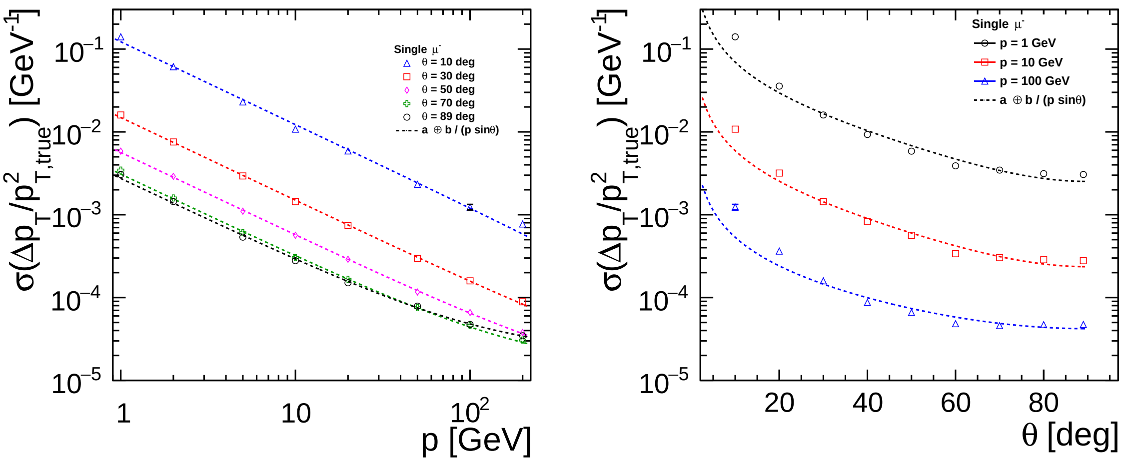

Figure 7.5: Transverse momentum resolution for single muons as a function of momentum at fixed polar angle θ = 10, 30, 50 70 and 89 degrees (left), and as a function of polar angle at fixed momentum p = 1, 10 and 100 GeV (right).

7.3.2 Backgrounds in the CLD Tracking System

The effect of IPC and SR backgrounds on the CLD tracker performance has been studied through a full GEANT4 simulation of the interaction region and the CLD detector. The simulation used `DD4hep` [214] and the `ddsim` software framework developed by the CLIC-dp collaboration. The number of hits with an energy deposit above a threshold of a few keV in the silicon sensors, provides an estimate of the number of hits that the sensors would record. When occupancies were determined, these numbers were multiplied by an average cluster size, taken as 5 (2.5) for the pixel (strip) sensors and a safety factor of three. A pitch of 25×25 μm^2 was assumed for the pixels of the vertex detector and of 1×0.05 mm^2 for the strips of the inner and outer tracker.

According to the simulation, the IPC background will cause on average about 1400 (50) hits per BX in the VXD, at $\sqrt{s} = 365$ (91.2) GeV. The occupancy is highest in the innermost barrel layer of the VXD, on average reaching $\sim 1.5\times 10^{-4}$ (7.5×10^{-6}) per BX. The peak occupancy reaches $\sim 3.8\times 10^{-4}$ (1.2×10^{-5}) at the edges of the VXD barrel ladders and about half of this for low radii of VXD endcaps. As an example, Fig. 7.6 shows the hit density in the VDX at $\sqrt{s} = 365$ GeV. The highest hit density in the tracker is observed at the inner radii of the first disk. The induced occupancy is $\sim 3\times 10^{-4}$ (1.8×10^{-5}) per BX. At the Z peak, where two consecutive bunch crossings would be separated by 20 ns, the readout electronics is likely to integrate the deposited charge over several BXs. Even with a "slow" readout electronics integrating over, say, 1 μs, hence 50 BXs, the maximum occupancy observed would remain below 10^{-3}. In summary, detector occupancies induced by IPC backgrounds are very low everywhere and are not expected to affect the tracking performance.

JPo be explained at
Acronyms should be explained at their first use, or at least have entries in the glossary. In this section one can find VXD, ECAL, HCAL, SiPM, MPGD

DRAFT FOR ADVISORY COMMITTEE - DO NOT DISTRIBUTE

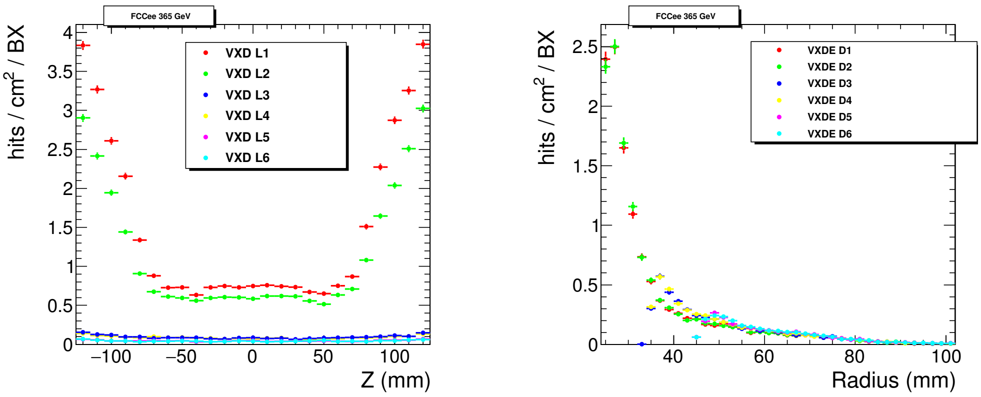

Figure 7.6: Hit density per BX in the CLD VXD induced by the IPC background at $\sqrt{s} = 365$ GeV; barrel layers (left), endcap disks (right).

As discussed in Section 7.1, synchroton radiation in the detector volume is negligible at all energies except the top energy. At this energy, the resulting large number of hits (∼60,000 per BX) in the inner and outer tracking detectors without shielding is very effectively reduced to a negligible level by the tungsten shielding of the beam pipe. The shielding does not fully protect the vertex detector, however, where a total of about 500 hits per BX would be created, mostly in the first and second double-layers. The maximum occupancy does not exceed 5×10^{-4}, and is not expected to affect the tracking performance.

7.3.3 CLD Calorimetry

Studies in the context of linear colliders have concluded that high-granularity calorimetry may be one of the most promising options to reach the required jet energy resolution of 3–4% with particle-flow reconstruction. In contrast to a purely calorimetric measurement, particle-flow reconstruction requires the reconstruction of the four-momenta of all visible particles in an event. The momenta of charged particles (about 60% of the jet energy) are measured in the tracking detectors. Photons (about 30% of the jet energy) and neutral hadrons are measured in the electromagnetic and hadron calorimeter, respectively. An overview of particle-flow reconstruction and the associated Pandora PFA software can be found in Ref. [215]. Experimental tests are described in detail in Ref. [216].

An ECAL segmentation of $5\times$ 5 mm^2 has been deemed adequate to resolve energy depositions from nearby particles in high-energy jets. The technology chosen as baseline option is a silicon-tungsten sandwich structure. In order to limit the leakage beyond the ECAL, a total depth of around 22 X_0 was chosen. A longitudinal segmentation with 40 identical Si-W layers was found to give the best photon energy resolution. A full simulation study using Pandora PFA has been performed for single photons with energies between 10 and 100 GeV. The resulting photon energy resolution is shown in Fig. 7.7.

The hadron calorimeter consists of steel absorber plates, each 19 mm thick, interleaved with scintillator tiles. The polystyrene scintillator, in a steel cassette, is 3 mm thick with a tile size of $30\times$ 30 mm^2. Analogue readout of the tiles with SiPMs is envisaged. The HCAL consists of 44 layers and is around 5.5 λ_I deep, which brings the combined thickness of ECAL and HCAL to 6.5 λ_I. A study of the CLD performance using Pandora PFA was carried out with light-quark pair events at $\sqrt{s} = 91$ and 365 GeV. Figure 7.7 shows the jet energy resolution obtained as a function of polar angle.

7.3.4 CLD Muon System

The CLD muon system comprises six detection layers with an additional seventh layer in the barrel immediately following the coil. The latter may serve as a tail catcher for hadron showers. The detection layers are proposed to be built as RPCs with cells of $30\times$ 30 mm^2 (alternatively, crossed scintillator bars

DRAFT FOR ADVISORY COMMITTEE - DO NOT DISTRIBUTE

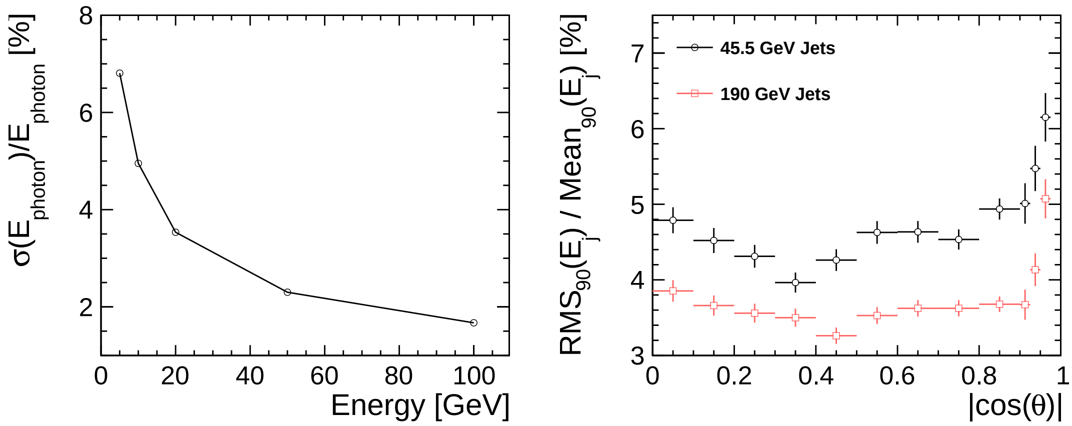

Figure 7.7: CLD calorimeter performance. Photon energy resolution as a function of energy(left). Jet energy resolution for light quark jets as a function of polar angle (right).

could be envisaged). The yoke layers and thus the muon detectors are staggered to avoid gaps.

7.4 The IDEA Concept Detector

The IDEA detector concept, developed specifically for the FCC-ee, is based on established technologies resulting from years of R&D. Additional R&D is needed to finalise and optimise the design. The structure of the IDEA detector is outlined in Fig. 7.8 and its key parameters are listed in Table 7.3. The detector comprises a silicon pixel vertex detector, a large volume extremely light drift chamber, a thin, low mass superconducting solenoid coil, a pre-shower detector, a dual-readout calorimeter and a muon system inside the magnet return yoke.

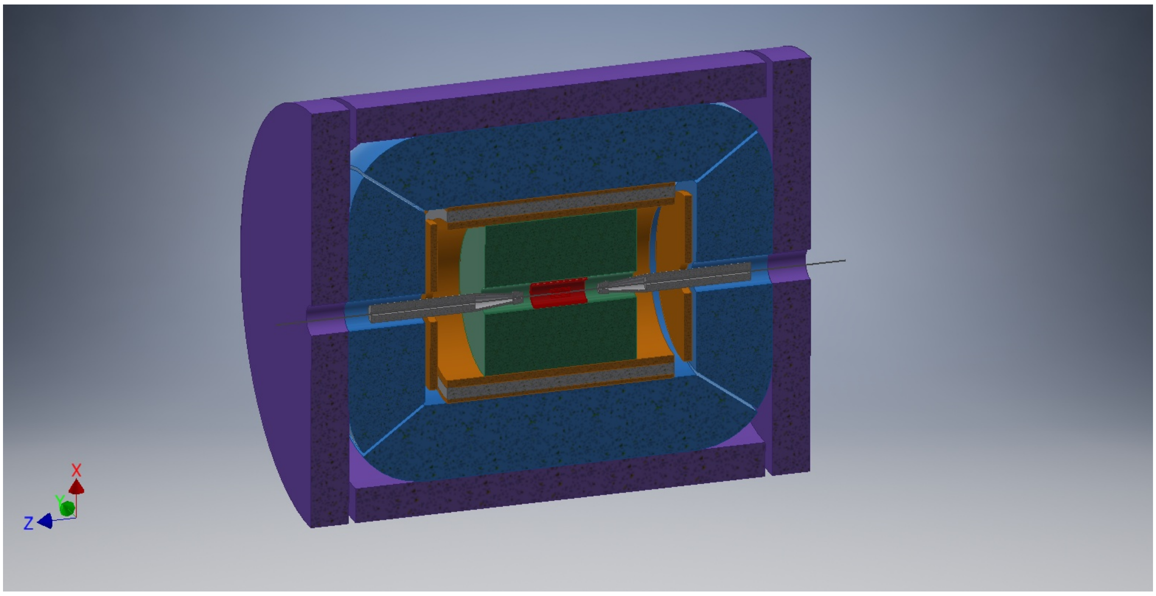

Figure 7.8: Schematic layout of the IDEA detector. Sub-detectors are outlined in different colours: vertex detector (red), drift chamber (green), pre-shower (orange), magnet (grey), calorimeter (blue), magnet yoke and muon system (violet).

DRAFT FOR ADVISORY COMMITTEE - DO NOT DISTRIBUTE

Table 7.3: Key parameters of the IDEA detector

Vertex technology	silicon
Vertex inner / outer radius	1.7 cm / 30 cm
Tracker technology	Drift Chamber + Silicon Wrapper
Tracker half length / outer radius	2.0 m / 2.0 m
Solenoid bore radius / half length	2.1 m / 3.0 m
Pre-shower / calorimeter absorber	lead / lead
Pre-shower inner / outer radius	2.4 m / 2.5 m
DR calorimeter inner / outer radius	2.5 m / 4.5 m
Overall height / length	12 m / 11 m

7.4.1 IDEA Vertex Detector

The innermost detector, surrounding the beam pipe, is a silicon pixel detector. Recent test beam results on the detectors planned for the ALICE inner tracker upgrade (ITS) [217], based on the ALPIDE readout chip [218], indicate an excellent resolution, $\sim$5 µm and high efficiency at low power and dark noise rate [219]. The very light detectors, 0.3–1.0% X_0 per layer, would be a good starting point for the IDEA vertex detector.

7.4.2 IDEA Drift Chamber

The drift chamber (DCH) is designed to provide good tracking, high precision momentum measurement and excellent particle identification by cluster counting. The main peculiarity of this chamber is its high transparency, in terms of radiation lengths, obtained as a result of the novel approach adopted for the wiring and assembly procedures. The total amount of material in the radial direction towards the barrel calorimeter is of the order of $1.6\%\ X_0$, whereas, in the forward direction, it is about $5.0\%\ X_0$, including the endplates which are instrumented with the front-end electronics. The original ancestor of the DCH design is the drift chamber of the KLOE experiment [220] which was more recently developed as the MEG2 [221] drift chamber.

The DCH is a unique volume, high granularity, all stereo, low mass cylindrical drift chamber, co-axial with the 2 T solenoid field. It extends from an inner radius R_{in} = 0.35 m to an outer radius R_{out} = 2 m, for a length L = 4 m and consists of 112 co-axial layers, at alternating sign stereo angles, arranged in 24 identical azimuthal sectors. The square cell size varies between 12.0 and 14.5 mm for a total of 56,448 drift cells. Profiting from the peculiar design of the wiring, which was successfully employed for the recent construction of the MEG2 drift chamber, the large number of wires poses no particular concern. The chamber is operated with a very light gas mixture, 90% He – $10\%\ iC_4H_{10}$, corresponding to a maximum drift time less than 400 ns. The number of ionisation clusters generated by ~~an $m.i.p.$~~ is about 12.5 cm^{-1}, allowing cluster counting/timing techniques to be employed to improve both spatial resolution ($\sigma_x < 100\,\mu m$) and particle identification ($\sigma(dN_{\text{cl}}/dx)/(dN_{\text{cl}}/dx) \approx 2\%$). The angular coverage extends down to $\sim 13^\circ$.

JPo
I am not familiar with the gas mixture - is the [illegible] significant?
JPo
What is an mip ?

A drift distance resolution of 100 µm has been obtained in a MEG2 drift chamber prototype [222] (7 mm cell size), with very similar electrostatic configuration and gas mixture. A better resolution is expected for the DCH, as ~~a result of~~ the longer drift distances and cluster timing techniques may improve it further. Analytical calculations for the expected momentum, transverse momentum and angular resolutions, conservatively assuming a 100 µm point resolution, are plotted in Fig. 7.9(left),.

The expected performance relating to particle separation is presented in Fig. 7.9 (right). Results are based on the cluster counting technique, where it is assumed that one can reach a relative resolution on the measurement of the number of primary ionisation clusters, N_{cl}, equal to $1/\sqrt{N_{\text{cl}}}$. For the whole range of momenta, particle separation with cluster counting outperforms the dE/dx technique by more

DRAFT FOR ADVISORY COMMITTEE - DO NOT DISTRIBUTE

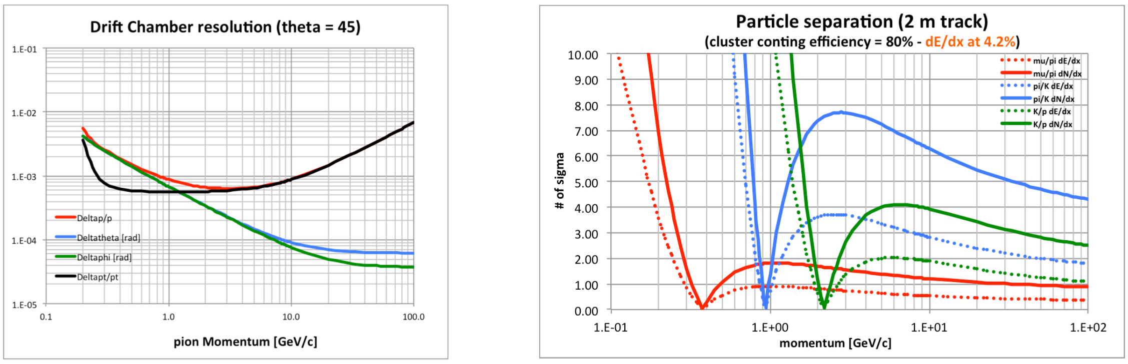

Figure 7.9: IDEA drift chamber performance. Momentum resolutions for $\theta = 45^\circ$ (left), particle type separation in units of standard deviations as a function of the particle momenta (right).

than a factor of two, estimating an expected pion/kaon separation at better than three standard deviations for all momenta except in a narrow range from 850 MeV to slightly above 1.0 GeV.

A layer of silicon micro-strip detectors surrounds the outside of the drift chamber providing an additional accurate space point as well as defining the tracker acceptance precisely.

7.4.3 IDEA Tracking System Performance

Simulations have been performed to obtain a first estimate of the performance of the IDEA tracking system, which has a seven layer cylindrical vertex detector and a two layer pre-shower counter, with 20µm pixel size, inside and outside the cylindrical drift chamber, all embedded in a 2 T magnetic field. Details of ionisation clustering for cluster counting/timing analysis were not simulated, limiting the spatial resolution to an assumed 100 µm. Results of this study, combined with those derived from a fast simulation study, point to a transverse momentum resolution of $\sigma_{p_\mathrm{T}}/p_\mathrm{T} \simeq a \cdot p_\mathrm{T} \oplus b$, with parameters $a \simeq 3 \times 10^{-5}\,\mathrm{GeV}^{-1}$ and $b \simeq 0.6 \times 10^{-3}$, for tracks at $\theta = 65^\circ$. The lightness of the drift chamber is reflected in the small multiple scattering b term. Correspondingly, an impact parameter resolution of $\sigma_{d_0} = a \oplus b/p \sin^{3/2}\theta$, with a= 3 µm and b =15 µm GeV, was found. Lastly, angular resolutions of better than 0.1 mrad in both azimuthal and polar angle were demonstrated for $p > 10\,\mathrm{GeV}$.

7.4.4 Backgrounds in the IDEA Tracking System

In order to study the effects of backgrounds from IPC and from synchrotron radiation in the IDEA drift chamber, a GEANT4 simulation of the IDEA detector has been performed using FCCSW[1], the common simulation software developed for the FCC experiment. The impact of the IPC background on the DCH is equivalent to the addition of a few hits per beam-crossing at the innermost layers with negligible effect on the tracking performance. More detailed simulations are under way.

7.4.5 IDEA Pre-shower Detector

A pre-shower detector is located between the magnet and the calorimeter in the barrel region and between the drift chamber and the end-cap calorimeter in the forward region. In the barrel region, the magnet coil works as an absorber of about 1 X_0 and is followed by a layer of MPGD chambers; a second layer of chambers follows after another 1 X_0 of lead. In the forward region, a 1 X_0 lead absorber is followed by silicon micro-strip detectors and then a second layer of lead and one MPGD chamber. About 75% of the

[1] http://fccsw.web.cern.ch/fccsw/index.html

DRAFT FOR ADVISORY COMMITTEE - DO NOT DISTRIBUTE

π^0's can be tagged by having both photons from their decay identified by the pre-shower. ~~Both silicon and MPGD~~ chamber layers provide a precise acceptance determination for both charged particles and photons, in addition to increasing the tracking resolution. The optimisation of the pre-shower system is still in progress.

7.4.6 IDEA Dual Readout Calorimeter

A lead/fibre calorimeter is located behind the ~~second~~ pre-shower layer. The calorimeter is based on the dual readout technique [223], which has been extensively studied and demonstrated over ten years of R&D by the DREAM/RD52 collaboration [224, 225]. The calorimeter is 2 m deep, corresponding to approximately 7 λ_I. A couple of possible layouts have been implemented for a realistic 4π detector. Both cover the full volume up to $|\cos(\theta)| = 0.995$, with no cracks. In one case, the calorimeter is made of wedge shaped towers with 92 different sizes, while, in the other case, it is built from rectangular towers coupled with triangular ones. The total number of fibres is of the order of 10^8 in both cases.

The dual readout calorimeter is sensitive to the signals from scintillation light (S) and Cherenkov light (C) separately resulting in a very good energy resolution for electromagnetic as well as for hadronic showers. By combining the two signals, the resolution, as estimated from ~~a~~ GEANT4 simulations of a full-containment detector, is found to be about 10.3%/$\sqrt{E}$ for electrons and 34%/$\sqrt{E}$ for isolated pions with negligible constant terms.

The dual readout calorimeter provides very good intrinsic discrimination between muons, electrons/photons and hadrons for isolated particles [226]. Figure 7.10 demonstrates a nearly perfect separation in the C/S ratio for 80 GeV electrons and protons for an ideal detector: for an electron efficiency of 98%, the rejection factor for protons is 600. In reality, the rejection will be somewhat worse. However, in addition to the C/S ratio, there are a few other variables, like the lateral shower profile, the starting time of the signal, and the charge-to-amplitude ratio, which can be used to enhance the particle identification performance. The discrimination power will be further enhanced when the information of the pre-shower and the muon chambers is added, also extending the separation power into hadronic jets and making it suitable for the application of particle-flow-like algorithms. The intrinsic high transverse granularity provides good matching of showers to tracks and pre-shower signals.

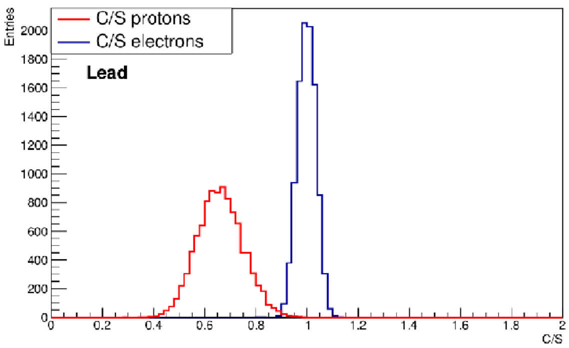

Figure 7.10: Particle identification performance of the dual readout calorimeter: C/S ratio for 80 GeV electrons and protons.

The need to disentangle signals produced by partially overlapping or very close hadronic and electromagnetic showers, is a strong requirement for several important physics channels (like final states from $\tau \to \rho\nu$ decays) and it is likely that a longitudinal segmentation would be an important asset in that respect. Several ways to implement it can be envisaged and studied: the classical division of the calorimeter in two (or more) compartments, an arrangement with fibres starting at different depths

DRAFT FOR ADVISORY COMMITTEE - DO NOT DISTRIBUTE

(e.g. half of the fibres starting after one interaction length), the reconstruction of the longitudinal energy deposition from timing information. Each of them has pros and cons and needs to be studied both with simulations and with beam tests.

7.4.7 IDEA muon system

The muon system consists of layers of muon chambers embedded in the magnet yoke. The area to be covered is substantial, requiring an inexpensive chamber technology. Recent developments in the industrialisation of μRwell-based large area chambers, as planned for the CMS upgrade, are very promising.

7.5 Magnet System

Both detector concepts, CLD and IDEA, employ a 2 T solenoidal field. In the case of CLD, the coil is situated outside the calorimeter system, as is the case for the detector designs considered in the linear collider studies. The larger tracker radius of CLD is compensated, in part, by a somewhat thinner hadron calorimeter and the coil has rather similar dimensions of 7.4 m length and 3.7 m inner radius. For the IDEA concept, a solution, similar to that of the ATLAS detector [227], is being pursued, in which a thin coil is placed inside the calorimeter system, where it functions as the first absorber layer of the pre-shower detector. Presently planned dimensions are a length of 6.0 m and an inner diameter of 4.2 m. With today's technology, a radial thickness of 30 cm including an effective Al thickness of 10 cm looks feasible. At perpendicular incidence, this corresponds to a material thickness of $0.74\,X_0$ and $0.16\,\lambda_\mathrm{I}$. Further R&D effort would be needed to pursue a more aggressive solution where the physical thickness as well as the material budget could be reduced to about 70% of these numbers.

~~7.6 Constraints on readout systems~~

~~Number of channels, event size (dominated by backgrounds), trigger considerations, etc~~

~~7.7 Infrastructure Requirements~~

~~Engineering design for the luminometer mechanical support Water cooling power Electric power Gas~~

DRAFT FOR ADVISORY COMMITTEE - DO NOT DISTRIBUTE

Chapter 8

Safety

The conceptual design of a major scientific and technical facility would not be complete without considering its safety - the protection of workers from accidents and professional illness, the protection of neighbours from nuisances and of the environment from temporary or permanent degradation. The FCC design study is no exception. The technologies and trades employed in the realization of a particle accelerator are numerous and so are the safety hazards and risks associated with them. The conceptual safety study for the FCC-ee collider aims to demonstrate that hazard and risks control is possible with standard means, as in traditional industries, or with techniques specifically elaborated for a particle accelerator facility.

The first section introduces CERN's legal context and the concept for hazard and risk management. The second section treats specific risk controls for particular areas of occupational health and safety, whereas section three deals with radiation hazards and radiation protection measures.

8.1 Safety Policy and Regulatory Framework

CERN is an intergovernmental organization straddling the border between Switzerland and France. The consequences for its safety policy are outlined. Following these principles, the safety strategy for the FCC design study follows a two-stage approach: a hazard register informs about the occurrence of safety hazards in the planned facilities and about 'Standard Best Practice' to control the associated risks. Only safety risks from hazards which not covered by this approach are subject of detailed analysis, as outlined in the next section.

8.1.1 Legal Context of CERN

By virtue of its intergovernmental status, CERN is entitled to adopt its own internal organizational rules, which prevail over national laws, to facilitate the execution of its mission.

In response to its unique geographical situation (straddling without discontinuity across the Swiss-French border) and its highly specific technical needs, the Organization stipulates its safety policy, in the frame of which it establishes and updates rules aimed to ensure uniform safety conditions across its site. CERN's safety rules apply to the Organization's activities, as well as to persons participating in its activities or present on its site.

When establishing its safety rules CERN takes into account the laws and regulations of the Host States, EU regulations and directives as well as international regulations, standards and directives.

As a general principle, CERN seeks compliance of its activities, installations and equipment with the laws and regulations of the Host States, EU regulations and directives or international regulations, standards and directives, whenever possible. Where such compliance is not possible or desirable due to technical or organizational constraints, clearance from the HSE unit based on a risk assessment and compensatory measures is normally required.

8.1.2 Hazard Register and Safety Performance Based Design

A hazard register, a systematic collection of safety hazards associated with the technologies employed for the construction and operation of the accelerator complex, is at the heart of the safety assessment of the conceptual design.

Hazard registers are an established technique for safety assessments in industry and services. Here, a process-centred approach was used. In a first step, based on the project breakdown structure of the conceptual design, a systematic description of processes present in the life-cycle of the accelerator facility is established, ordered by technology and operational phase. Each process is characterised by activities, by equipment employed and by substances used or released. Hazards are related to activities, equipment and substances.

As an example, the process of providing electrical power for accelerator magnets, associated to Powering technology, is employed during operation and commissioning of the accelerator. It employs transformers and power converters as equipment, located in surface and underground locations. This equipment is at the origin of electrical hazards, but also of noise and potential environmental pollution in the case of dispersion of insulation fluids.

Wherever appropriate, it has been assumed that the identified hazards will be mitigated by compliance with laws and regulations of the Host States, EU regulations and directives, international regulations, standards and directives and recommendations from technical or prevention organisms. These sources of hazard elimination or mitigation are summarised under 'Standard Best Practice'.

Due to the unique nature of the FCC infrastructure, Standard Best Practice may appear inappropriate. In these cases, CERN's HSE Unit has proposed to apply a performance-based design approach to the FCC study. In this approach, essential safety objectives are defined, such as preservation of human lives or prevention of environmental damage. The safety performance of design choices is evaluated for different incident scenarios, by heuristic methods or by simulation. If the objectives are met, the design can be approved, in the contrary case one has to look for alternative, more appropriate designs.

8.2 Occupational Health and Safety

Two main hazards in underground areas were identified for the FCC conceptual design: fire and oxygen deficiency. The results of these studies are summarised in the following sections. The agreed safety objectives in the two studies were:

Table 8.1: Safety objectives in the design-oriented safety study for the FCC

	A: Life Safety	B: Environmental Protection	C: Property Protection	D: Continuity of Operation
1	Safety of valid occupants	Limited release of pollutants to air	Continuity of essential services	Limit downtime
2	Safe evacuation or staging of injured occupants	Limited release of pollutants to water	Incident shall not cause further incidents	
3	Safe intervention of rescue teams		Limit property loss	

The design choices for the accelerator tunnel are an inner diameter of 5.5 metres, and smoke- and fire-resistant compartment walls every 424 metres. The compartment doors are normally open; smoke-

DRAFT FOR ADVISORY COMMITTEE - DO NOT DISTRIBUTE

or ODH detectors can trigger their closure. Each compartment is ventilated transversally, under normal circumstances the used air is evacuated along the direction of the tunnel. An extraction duct traverses all compartments and can be used to extract smoke or helium. Both ventilation and extraction can be controlled individually for each compartment.

8.2.1 Fire Hazard

The most critical phases for fire hazard were identified as operation with beam, long shutdown and technical stop. During operation, all electrical systems are powered and represent potential ignition sources, whereas in the other periods personnel is present and may cause inadvertently a fire, e.g. during hot work. Three fire scenarios were studied (cf. Table x)

Table 8.2: Fire scenarios in the design-oriented safety study for the FCC

Scenario	Description	Ignition source
Fire 1	Cable tray fire	Electrical fire
Fire 2	Cable drum fire	Hot work
Fire 3	Transport vehicle fire	Battery malfunction

Life safety and safety of occupants and rescue teams were quantified by fractional effective dose (FED), a measure for the harm from toxic fire products to the occupants, by temperature conditions, and distance of visibility through the developing smoke. These parameters were estimated with the industry-standard CFD program for fire- and smoke propagation, FDS 6.5 from the National Institute of Science and Technology. It was found that valid occupants could evacuate the affected compartment to safety in all scenarios. Injured occupants would be at risk if they had to wait for the arrival of rescue forces. Here, innovative solutions are required such as autonomous firefighting robots which control fire and smoke before arrival of the rescue forces. The use of such robots will also improve the safety levels of rescue teams. The proposed fire compartment size is sufficient to ascertain fire fighter safety during an intervention, together with secure communications and structural stability of the tunnel.

Environmental safety requires management of firefighting water and of smoke in order to avoid re-lease of chemical or radioactive contaminants to the environment. Property protection and continuity of operation depend on the damage to accelerator equipment. While damaging temperatures can be limited to the immediate vicinity of the fire seat, smoke would spread in at least one compartment and make re-use of the equipment it contains questionable. An autonomous firefighting robot with an intervention time under 15 minutes would reduce smoke-related damage significantly. Shorter fire- and smoke compartments would also limit smoke-related damage, but at higher cost and complexity.

The CFD evaluations of fire and smoke spread have shown the importance of a rapid fire / smoke detection system with a response time under 2 minutes. Development work in fibre optical detectors and algorithms for fire detection is necessary in this field. Main Conclusions:

- The life safety objective for valid occupants and the safety of rescue forces are fulfilled in all scenarios.
- Early fire detection and early intervention by autonomous agents would ascertain life safety of injured occupants and improve property protection and continuity of operation.
- Environmental safety can be achieved with standard measures.

8.2.2 Oxygen Deficiency

Oxygen deficiency hazard in accelerator facilities arises from the release of asphyxiating cryogenic liquids (He, Ar, N2) in closed environments, where they may displace oxygen upon a sudden expansion of the fluids.

DRAFT FOR ADVISORY COMMITTEE - DO NOT DISTRIBUTE

It was determined that the commissioning and maintenance phases are most critical during the projects' life-cycle due to the presence of personnel in the underground areas.

Thomas Otto: He spill from SCRF cryostats

Main Conclusions:

- The Safety objectives that are not fulfilled in this exercise can be mitigated by standard organisational measures and therefore will not affect the design of the FCC tunnel.

- Additional studies, with appropriate CFD tools, are mandatory in the frame of the technical de-sign of the FCC accelerator.

- For worst-case scenario Cryo 6, the expected damage is the loss of one compartment, one full cell of the machine and a downtime of about 1 year.

Full report available in https://edms.cern.ch/document/1818330

8.3 Radiation Protection

For the mitigation of risks associated with the presence of ionising radiation, the standard prescriptive methods have been used based on the existing CERN radiation protection rules and procedures. The result of these studies are summarised in this section.

Thomas Otto: Markus Widorski: adapt radiation risk and mitigation to ee collider

The design phase of a new project includes the evaluation of radiological risks as well as their limitation and minimization by appropriate protection and optimization measures. Design constraints will ensure that the exposure of persons working on the sites as well as the exposure of the public will re-main below dose limits under normal as well as abnormal conditions of operation and that the optimization principle is implemented. A radiation monitoring system, which represents an essential part of the risk control measures, will assess all relevant radiological parameters throughout the lifetime of the installation.

The FCC-hh will feature similar radiological hazards as the Large Hadron Collider or other high-energy accelerator installations. These existing installations present a valuable and reliable source of experience to evaluate and manage radiological risks at even much larger facility such as the FCC. The main differences influencing the radiological risks at the FCC-hh are the increased beam energy and luminosity. Both will lead to higher activation levels in some sections of the accelerator and the experiments.

Radiation protection is concerned with two aspects: the radiation protection of personnel operating and maintaining the installations and the potential radiological environmental impact of the facility. The second topic is addressed in chapter XX. The radiological hazards can be classified by their sources to exhaustively assess the potential radiological risks to the personnel working on the FCC sites: from particle beam operation and from activated solids, liquids or gases.

8.3.1 Particle Beam Operation

Radiation hazards from high energy particle beams arise through their interaction with matter or other particles. The primary radiation and the subsequently generated stray radiation must be absorbed by shielding to protect persons working near the accelerator during beam operation. An access safety and control system must prevent persons from accessing hazardous areas during beam operation. In addition, sufficient shielding must be provided to protect persons against increased radiation levels and hence undue radiation doses. Areas accessible during beam operation will be designed as non-radiation areas to avoid the need of specific restrictions for radiation protection reasons.

DRAFT FOR ADVISORY COMMITTEE - DO NOT DISTRIBUTE

Lateral shielding thickness of several meters of rock or concrete is sufficient to shield against catastrophic or continuous beam losses. Chicanes through the shielding structures will be designed to effectively reduce radiation streaming through them during beam operation, while allowing access to the accelerator tunnel and experimental caverns during periods where the particle beam is stopped.

Underground facilities accessible during beam operation will generally be located inside of the circle drawn by the accelerator to avoid exposure from penetrating forward stray radiation such as muons.

The shafts above the experiments represent large openings on top of the circulating high energy beams. Considering the self-shielding effect of the detectors around the interaction points, the distance to the surface and a concrete shielding cap, the radiation levels on top of the shafts will be low enough to avoid any relevant direct exposure to stray radiation or sky-shine effects on the surface sites or beyond.

8.3.2 Activation of Solids

Activation of solids represents a potential hazard to persons mainly through exposure to gamma radiation during interventions inside the accelerator tunnel e.g. in-situ maintenance or during the handling of radioactive parts. The radiation levels differ considerably between different sectors of the accelerator, as a function of the beam operation time and the decay time since the stop of beam operation. Locations close to the beam interaction points, the beam cleaning insertions as well as the final beam absorbers will exhibit the highest radiation levels from activation, in excess of those at analogous locations at the Large Hadron Collider.

Optimization during the design of the technical installations is the first objective. Robotic solutions for maintenance and other interventions will be envisaged to reduce the exposure of personnel. Bypass tunnels for high radiation areas will avoid passing through these radiation areas.

Activated materials is routinely removed for maintenance or for disposal from the accelerator tunnel and experimental caverns. Dedicated areas will be reserved for handling and storage of this equipment, in the underground and on the surface sites. Corrosion and machining of activated materials can produce activated dispersed solids in the accel-erator areas and workshop areas. Experience shows that this does not lead to relevant radiation risks and standard procedures apply.

8.3.3 Activated or contaminated liquids

Infiltration water or leakage water from closed demineralized water circuits, raw water or cooling circuits will be collected by the tunnel drainage system. The water will be pumped to the surface sites for collection and further treatment before being cleared and released.

The demineralized water filtering units are collecting and concentrating radioactive particles and will be treated through standard procedures. Ventilation cooling units for the tunnel and experimental areas air may concentrate air-borne radioactivity in their condensates, mainly in the form of tritiated water. This liquid waste water will be collected and treated according standard procedures. The activation of cryogenic liquid Helium which is used in the superconducting circuits, results in the production of some amounts of Tritium. Sufficient storage capacities for potentially contaminated Helium are foreseen on the different sites.

8.3.4 Activated or radioactive gases and radioactive aerosols

Air in the accelerator and experimental areas will become radioactive during beam operation. All ventilation systems will be conceived to operate in full or partial recycling mode to limit releases to the environment. In case of access, the areas will be sufficiently ventilated with fresh air beforehand to avoid undue exposure of intervening personnel. Areas with different activation potential will be separated, allowing to only vent areas where actually access is required and thus to avoid unnecessary releases of radioactive air. By experience, potential outgassing from activated concrete or Radon decay products

DRAFT FOR ADVISORY COMMITTEE - DO NOT DISTRIBUTE

will only remain present in small concentrations as they are continuously removed by the filters in the ventilation system during access periods.

Dust activation and airborne corrosion products do not represent relevant sources of exposure to intervening personnel. Aerosols are continuously removed by the air treatment systems.

DRAFT FOR ADVISORY COMMITTEE - DO NOT DISTRIBUTE

Chapter 9

Energy Efficiency

Volker Mertens: Volker Mertens, 3 pages

9.1 Requirements and Design Considerations

A power cycle of FCC can be distinguished in three stages: ramp-up, flat top and ramp-down. A particular challenge is to provide the peak power demand during the ramp-up, as the external electrical network might not be able to provide such high amplitude of power. The following solutions, or combinations of them, are proposed:

- **Supply of peak power from external network:** The peak power demand is provided by the external power network. This is the simplest solution, however partial reinforcements of the external power network (Réseau de transport d'électricité - RTE) might be necessary.
- **Optimisation of the ramp up duration:** The slope of the ramp-up is approximately proportional to the peak power required during this phase. Giving more time to the ramp up would significantly decrease the peak power demand. See Fig. 9.1a.
- **Optimisation of the ramp-up shape:** The ramp-up function of the current can be done in constant voltage mode or constant power mode. The latter should be preferred, as it would allow to reduce the peak power and aim for a more rectangular power demand. See Fig. 9.1b, comparing ramp up with constant voltage and constant power.

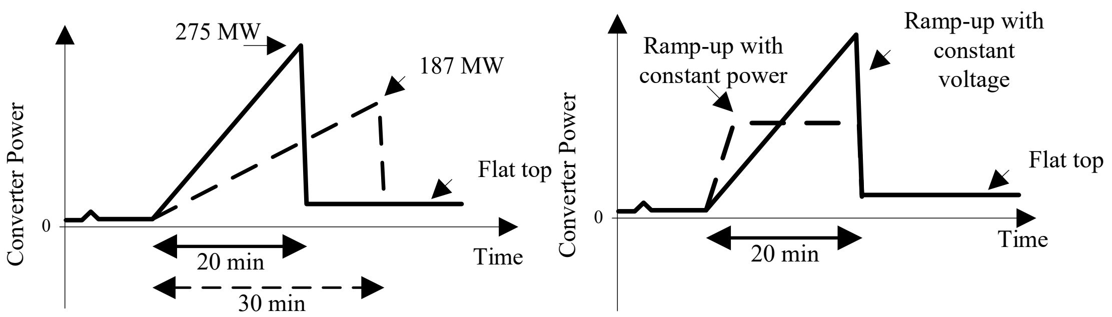

(a) adapting the ramp-up time (b) adapting the ramp-up mode

Figure 9.1: Proposed optimisation of the ramp-up process of the dipole circuits only, by means of (a) adapting the ramp-up time; (b) adapting the ramp-up mode.

– **Use of energy storage systems:** This concept uses a combination of switch-mode power converter and energy storage system for the dipole circuits. During ramp-up, the peak power is fully or partially provided by the energy storage system, which is recharged using energy recovery during ramp-down. This idea is already used for the power system of the PS Booster 2 GeV (POPS-B) as well as for the power system of PS (POPS). The energy storage system for FCC could be based on high voltage DC capacitors, batteries, or a combination of the two. This concept eliminates the positive peak power during ramp-up and also the negative peak power during ramp-down, resulting therefore in a flat power profile without any peaks. As a consequence, the RTE transmission and the CERN distribution networks can be reduced in terms of component ratings of substations, cables and transformers. Moreover, the elimination of the power peaks results in a significant reduction of transmission and distribution losses. See Fig. 9.2.

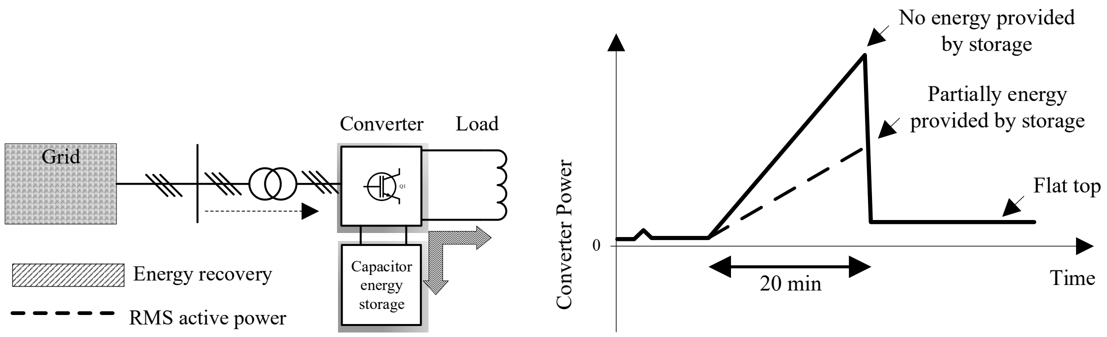

(a) Simplified diagram of the principle combining switch mode converter with energy storage

(b) Relation between storage size and peak power demand from the network

Figure 9.2

The ideal solution for the FCC powering is certainly a combination of the concepts presented above, optimising parameters such as equipment costs, civil engineering and electrical losses.

9.2 Power Consumption

9.3 Energy Management and Saving

One of the principal challenges of the 21st century will be the development of solutions for the sustainable use of energy. In this context, one of the key design aspects of FCC must be a strict focus on energy efficiency, energy storage and energy recovery. This project must be used as a technology driver, pushing towards more efficient ways to use electrical and thermal energy. The foundation for sustainable energy management is the use of real-time energy monitoring, for example using smart meters. This opens up possibilities to precisely predict and to optimise the overall CERN power consumption profile, with the objective to reduce the peak power as well as the electric losses. For the reduction of the peak power consumption of CERN during the FCC era, also cycling loads of the injector chain need to be taken into consideration. In particular, concepts to reduce the power cycles of the SPS need to be studied. By systematically applying the concept of energy storage for the powering of the magnet circuits, FCC will be able to recover a significant part of the energy stored in the magnets. When combining energy storage with complementary measures such as optimisation of the power cycles, the costs for the electrical infrastructure as well as for the electrical losses can be greatly reduced. The design of each individual element of the power system must contribute to the ongoing trend of loss reduction and energy saving.

9.4 Waste Heat Valorisation

DRAFT FOR ADVISORY COMMITTEE - DO NOT DISTRIBUTE

Chapter 10

Environment

Johannes Gutleber: Johannes Gutleber, 4 pages

10.1 Requirements and Approach Considerations

10.1.1 Legal Requirements

For the correct operation of CERN's facilities, its status as an international organisation requires that it establishes the requirements and constraints concerning the management of its environmental impact in a pro-active and consensus-based process with the host state on whose territory the installation lies (see Art. II 2 of "L'accord de statut de 1972 entre le CERN et la France"). Where there is standard infrastructure on the surface sites (e.g. office buildings, car parks, ordinary workshops), CERN implements the national laws and regulations that apply at the location where the facility is located (see also "Art. II Convention entre la France et la Suisse de 1965"). A specific process is necessary for the non-standard installations like the accelerators, the experiments and the technical infrastructure needed to operate these facilities.

Different rules apply to a project with underground infrastructure which crosses the international border and which has surface sites in both Switzerland and France:
Underground infrastructure: In Switzerland, underground volumes below a depth that is considered *useful* for the land owner is not subject to the acquisition of rights-of-way and the law applying to private property. A communication from the Département Fédéral des Affaires Étrangères (DFAE) on July 16 1982, informs CERN that it is exempt from right-of-way acquisition regulations for the LEP/LHC underground structures. In France, land ownership extends to the centre of the earth. Therefore either a process to acquire the underground volumes or to acquire the rights of way needs to take place. For both host states, CERN remains liable for any potential impact on the population and the environment resulting from the construction and operation of underground and surface installations.
Surface sites: The land needs to be acquired or leased in both host countries. In Switzerland, an environmental impact assessment needs to be performed when new car parks are constructed **[REF]** or if excavation material needs to be processed on Swiss territory **[REF]**. The "Ordonnance relative á l'étude de l'impact sur l'environnement (Oct. 1988 and 2016)" **[REF]** and "L'étude de l'impact sur l'environnement (EIE) (2009)" **[REF]** define the scope and contents of the assessment. In France, a recent law introducing a new environmental impact management process **[REF]** applies.

Both host states have regulations and laws concerning the continuous assessment and limitation of environmental impact for a variety of different topics. While the processes comprise very similar topics, the organisation of the information and the reporting templates are different for the two host states. In Switzerland the impact study may be limited to certain topics depending on the project needs, whereas in France all topics need to be discussed.

France and Switzerland require that the initial assessment process is carried out from the design phase, followed by regular reviews of the effectiveness of the mitigation measures and assessment of residual or new impacts which become apparent during the construction and operation phases.

The host countries also require an early and continuous involvement of the population in the project development and construction preparation phases. This involvement goes beyond information exchange. It calls for an active participation, giving people the possibility to contribute in well-defined and limited ways in shaping the project in particular, developing the potential for added value.

Since the project is international in character, the Espoo agreement applies **[REF]**. CERN has to ensure that both host states are informed about the effects of any new infrastructure project in their country and the effects on the neighbouring countries. This includes for instance, the use of energy, consumption of water, traffic and the management of waste across the borders.

10.1.2 Environmental Compatibility Management Concept

The international nature of the project and the similarity of the surface points suggest a uniform and streamlined framework to carry out an environmental impact assessment. This approach splits the project into locations (e.g. underground structure, individual surface points, associated infrastructures), topics relevant for the impact assessment (e.g. water, air, noise) and the life cycle phases of the project (e.g. construction, operation, maintenance and dismantling). Different requirements and constraints apply to the various locations and phases. For some it may be necessary to meet the standard national guidelines of the relevant host state or, for some particular installations, the guidelines need to be agreed between CERN and the host state on a case-by-case basis. It is planned to have a central, uniform platform to manage the analysis, the assessment of proposed mitigation measures, the follow up of the effectiveness of mitigation measures and the analysis of the residual impact. This platform will permit the extraction of information according to the specific needs of the individual host states. Specialised companies and software solutions exist and should be used whenever possible (e.g. Envigo by eon+). A market survey and competitive selection process should be performed in cooperation with the host state partners in order to ensure that a suitable set of experts and tools are selected for this process. It is considered good practice in Switzerland that the owner of a large-scale project delivers a "Notice d'Impact sur l'Environement (NIE)", which is more comprehensive than the minimum required environmental impact assessment. The uniform framework mentioned here permits this approach.

JPo: If I recall correctly, France at least, requires dismantling to be analysed as well

FIGURE to be done

The need to perform the environmental impact assessment and management process, before a decision to construct the infrastructure takes place, calls for preparation of the assessment framework with the help of experienced consultants and the authorities of the host states in the years 2018 - 2020. An operational framework consisting of infrastructure, consultants and authority partners who are informed about the project vision and goal can consequently perform the work together with the scientific and engineering team until the design has reached maturity by 2023. By this time, CERN must have reached consensus with the authorities and the population to a degree that permits formally initiating a public consultation process as required in both host states not later than 2023. The process is considered lengthy in both countries and is expected to require a few iterations. The goal is to obtain clearance to submit a request for construction permits by 2026, after a decision by the community to construct the project.

JPo: a decision by the physics community or the international community ? Would benefit from clarification.

10.1.3 Environmental Compatibility Management Concept

10.2 Environmental Impacts

10.2.1 Radiological Impact

The hadron collider will operate at seven times higher particle energy than the LHC, causing higher radiation and activation levels in some parts of the accelerator and experiments. The potential radiological environmental impact comprises (1) dose from stray radiation emitted during beam operation, (2) dose

DRAFT FOR ADVISORY COMMITTEE - DO NOT DISTRIBUTE

from radiation emitted by radioactive materials and waste, (3) operation of ion sources and X ray emitting devices and (4) the dose from release of activated water and air. Safeguards will be included in the design of the accelerator infrastructure to control the impact on the environment. Dedicated monitoring systems and procedures will ensure continuous parameter recording and auditing throughout the entire operational phase of the facility and will facilitate control of the impact. LHC operational experience shows that the radiological impact on the environment and population are well below the legal limits. Since the beginning of the operation of the LHC, levels of stray radiation measured on surface sites remain negligible. The effective dose received by the public exposed to atmospheric and effluent releases of the existing particle collider remain below 10 µSv/year. Release levels and dose values are regularly reported to the host states [REF RP5]. This experience provides confidence that the particle collider described in this report can indeed be operated in compliance with the host-state laws and regulations.

The accelerator will be located at least 50 m below the surface and experiment interaction points will be at least 100 m below ground level. There will be no publicly accessible underground infrastructure. Therefore sufficient shielding against stray radiation from beam operation exists at all times. Two scenarios need to be considered to estimate the environmental impact: continuous beam losses during the operation and the effect of a total loss of the stored, high energy particles. In both cases, 15 m of lateral shielding by rock is sufficient to ensure a negligible impact on the environment and population [REF RP1, RP2]. Muon radiation emitted from losses in the plane of the accelerator will be attenuated by hundreds of meters of rock. The shafts are the only direct connections to the surface. At the interaction points they are sufficiently deep (100 m to 500 m) to exclude radiological impact from stray radiation [REF RP4]. Additional concrete slabs could be placed on top of the shafts to exclude residual impact from scattered radiation.

Activities involving handling, transport and storage of radioactive materials and the operation of X-ray emitting equipment on the surface sites are well regulated and are no different from current operations at CERN. The standard procedures in place within the current framework of radiation protection at CERN are well developed and proven to effectively control the radiological impact.

Beam operation activates air and potentially water close to the machine. The potential environmental impact originating from these sources is addressed as follows:

- Air activation:
  Redundant, partially or fully recycling ventilation systems will limit the release of gaseous isotopes (mainly short-lived) during beam operation. This operation scheme is different from the LHC and has the potential to help achieve annual doses to members of the public lower than those with LHC [REF RP5]. Aerosol releases are expected to be insignificant due to the low activity content and efficient air filtration at the release points, similar to the LHC. Long term experience at many accelerator installations confirm this estimation [REF RP5].
- Water activation:
  Drain water, raw water and demineralised water in the accelerator tunnel can become activated during beam operation and can carry trace amounts of radioactive corrosion products. Demineralised water circuits will be operated in a filtered, closed circuit. Leakage and infiltration water will be collected in the tunnel and will be pumped to retention and treatment basins at the surface. The water will be continuously monitored so that release will only occur after clearance. Experience shows that radioactivity in water is not a relevant source of radiological impact on the environment at the LHC [REF RP5]. The production rate of radioactivity in water at the future collider is expected to be lower or equal to the LHC, given the possibility to optimise pipe routing and avoid high activation areas [REF RP1].
- Ground activation and migration of radioactivity towards the biosphere:
  A limited amount of rock around the tunnel will be activated. Along the arcs, the largest part of the collider ring, activation remains at very low levels, well within the set limits [REF RP1]. Sections with higher activation potentials (e.g. collimation regions, regions close to the high lu-

DRAFT FOR ADVISORY COMMITTEE - DO NOT DISTRIBUTE

minosity interaction points) will be located in rock with negligible water migration risk so that transfer to the biosphere can be avoided. Detailed ground investigations at an early design stage phase must be carried out to optimise the tunnel placement. Considering the low levels of concentrations produced [REF RP1] and the small residual risk, no radiological impact is expected. Effective mitigation measures to limit the rock activation, such as additional wall shielding can be implemented, if necessary.

– Solid materials:
Equipment and solid materials removed from the accelerator area can be radioactive. Their handling, transport, storage and elimination is subject to regulations and processes already in place for the operating installations at CERN. No radiological exposure is expected in the environment from these tasks.

The impact of ionising radiation on personnel during operation and maintenance phases, as well as the management of radioactive waste are described in Sections **SAFETY [REF] and WASTE MANAGEMENT [REF]** respectively.

Depending on the operating phase, the beam energy of FCC-ee is between 0.45 and 1.75 times that of LEP, but the luminosities are significantly higher [REF]. Compared to the hadron machine, the stored beam energy will be many orders of magnitudes lower. The significant difference of the processes lead to much lower activation of material [REF RP6]. In general, the radiological impact potential of the lepton collider is about two orders of magnitude lower than the hadron collider.

The potential sources for environmental radiological impact are identical to those for the hadron collider: (1) dose from stray radiation emitted during beam operation, (2) dose from radiation emitted by radioactive materials and waste, (3) operation of sources and X ray emitting devices and (4) the dose from release of activated water and air. Safeguards will be included in the design of the accelerator infrastructure to control the impact on the environment. Dedicated monitoring systems and procedures will ensure continuous parameter recording and auditing throughout the entire operational phase of the facility and will facilitate the control of the impact.

FCC-hh and FCC-ee share the same infrastructure, in particular that for the treatment of air and water, the main exposure pathways. Measures to control and limit the environmental radiological impact of the FCC-hh will therefore also be adequate for the FCC-ee. During the detailed design phase, emphasis can include adequate, but not over-engineered, measures for this particular machine.

The impact of ionising radiation on trained personnel during operation and maintenance phases as well as the management of radioactive waste are described in Sections **SAFETY [REF] and WASTE MANAGEMENT [REF]** respectively.

10.2.2 Conventional Impact

A preliminary review of underground and surface sites has been performed with expert organisations in France and Switzerland **[2 REFs existing to be cited later]**. The studies established a working framework for the subsequent optimisation of the placement of the particle collider which is compatible with the existing requirements and constraints of both host states. The first investigation revealed that a placement of the collider compatible with the legal and regulatory boundary conditions in both countries can be developed. No conflicts with geothermal boreholes, seismic activities, underground technical features such as pipelines, critical power and communication lines could be found. Also, no relevant conflicts with underground water layers or hydrocarbons could be identified and puncture of protected water reservoirs can be avoided. However, dedicated underground investigations need to be carried out soon in order to validate the preliminary findings with more accurate data. The entire Geneva basin features water-saturated ground, but the water remains locally confined. Consequently it is unlikely that water, which is for human consumption and which reaches the surface or rivers would be activated by ionising radiation.

DRAFT FOR ADVISORY COMMITTEE - DO NOT DISTRIBUTE

Compatibility with protection of flora and fauna as well as agricultural activities has been considered from the beginning by taking into account a number of national and European conservation laws and guidelines **[REFs to be done]**. In this context, preliminary surface site candidates have been identified and the collider layout and design have been developed accordingly. A few surface sites require further optimisation in the design phase in order to simplify potential landscaping or indemnity processes and to ease accessibility by road. Swiss law requires the reservation of a certain surface area for agricultural activities in order to remain self-sufficient in case of crisis [**?**]. This constraint requires attention in the subsequent design phase, but means to ensure the feasibility have already been identified. The legal framework in both countries require further detailed information in order to jointly develop an optimised placement. These data can only be obtained by dedicated ground investigations and need to occur before the relevant environmental impact analysis can take place. Confirmation that inadvertent activation of water due to infiltration can be avoided may need to be verified by targeted surveys in a limited number of locations. The environmental impact during the construction phase, which extends over many years, needs to be studied. The reuse of the excavated material (in order of priority: on-site use, processing and re-use, landscaping, storage), construction site traffic, noise and dust are all elements which also need to be considered.

Official bodies of both host countries (Secrétariat Generale de la Région Auvergne-Rhône-Alpes and Département de l'aménagement, du logement et de l'énergie de la République et canton de Genève) have stated that for emerging urban areas and where there is a region with high-value natural assets, early participation of the authorities and representatives of the population in the further development of the project plans is required. Surface sites need to blend into the landscape. Synergies with local and regional activities that profit from the infrastructure in the host countries need to be developed. Examples include cooling via the GeniLac [**?**] water project, waste-heat recuperation for residential districts and healthcare providers, possibilities for temporary energy storage and release in cooperation with neighbouring industries. For the construction phase, particular attention needs to be given to noise, dust and traffic. For the operation phase, topics include the consumption of water, electricity, the emission of noise and the increased need to provide all kinds of infrastructure for an ever growing community of scientists, engineers and visitors.

The immediate subsequent design phase of the project will focus on the further optimisation of the collider and surface site placement, based on the findings already obtained in cooperation with the host state authorities and their nominated technical advisory bodies for the concept phase. This work will, in compliance with the regulations of both host countries, involve representatives of the local population in order to ensure a seamless evolution of the project design towards a later construction decision.

References to be worked into the text for this section:

RP1 Radiological studies for the FCC-hh arc sections, 2018, EDMS XXXXXXX

RP2 Radiological studies for the FCC-hh collimation regions, 2018, EDMS XXXXXXX

RP3 Radiological studies for the FCC-hh regions adjacent to the main beam interaction points, 2018, EDMS XXXXXXX

RP4 Radiological studies for the FCC-hh experimental caverns, 2018, EDMS XXXXXXX

RP5 Quarterly Report on Environmental Monitoring at CERN 4/2016, M. Alessi et al., 2017, EDMS 1742355

RP6 Impact radiologique du projet LHC sur l'environnement, M. Höfert et al., 1997, CERN-TIS-97-006

RP7 Radioactive Waste Management at CERN, Technical Note, L. Bruno, M. Magistris, 2017, EDMS 1453489

RP8 Stored and estimated future radioactive waste at CERN (until 2100), M. Magistris, 2017, EDMS

DRAFT FOR ADVISORY COMMITTEE - DO NOT DISTRIBUTE

1911619

RP9 Potential Exposures at High-Energy Proton Storage Rings, M. Höfert et al., 1995, CERN-TIS-95-013

RP10 Radiation Protection Considerations in the Design of the LHC, CERN's Large Hadron Collider, M. HÃűfert et al., 1996, CERN-TIS-96-014

10.2.3 Radiological Impacts

10.2.4 Conventional Impacts

10.3 Waste Management

10.3.1 Radioactive Waste Management

10.3.2 Conventional Waste Management

DRAFT FOR ADVISORY COMMITTEE - DO NOT DISTRIBUTE

Chapter 11

Education, Economy and Society

Johannes Gutleber: Johannes Gutleber, 3 pages

11.1 Requirements and Approach Considerations

11.2 Host State Realization Concept

11.2.1 France

11.2.2 Switzerland

11.3 Socio-Economic Opportunities

11.3.1 Scientific Publications

11.3.2 The Value of Training

11.3.3 Opportunities for Industries

11.3.4 Cultural Effects

11.3.5 The Value of Knowledge

Chapter 12

Strategic Research and Development

Michael Benedikt: Michael Benedikt, 10 pages

12.1 Strategic Considerations

12.2 Accelerator Related R&D

12.3 Detector Related R&D

12.4 Infrastructures Related R&D

Several of the concepts presented in chapter 5.4.2 are new technologies which have not yet been used for infrastructures of particle accelerators. Two principal R& D subjects were identified:

Electrical DC distribution networks: With the increasing availability of modern power electronics technologies such as switch-mode converters with higher power ratings, DC networks are increasingly being currently used for HV transmission systems, so-called HVDC lines. In addition, DC networks are in operation for a few specific technical applications such as the supply of motors of the trains in the London Underground network. Applying this principle of DC distribution to the FCC powering system would require the conversion from AC to DC and the distribution of the electric power within a DC network in the FCC tunnel. Combined with energy storage, this concept would present major advantages compared to conventional solutions. See chapter 5.4.2. However, DC distribution still represents several technical challenges, as the electrical components for DC current and voltage switching, short-circuit current switching, fault detection and protection system selectivity are not yet available on a wide industrial basis. Research institutes and industry are currently addressing these topics to develop standardised and reliable industrial solutions.

Energy storage systems: The development of novel energy storage systems has seen an impressive progress over the recent past years, mainly driven by the automotive sector and the increasing use of renewable energies. Batteries appear to be the most promising solution for FCC, in particular due to an ongoing development towards higher storage energy densities. In particular, Lithium Titanium Oxide (LTO) batteries seems to be the best solution nowadays. The most suitable battery technology for this application are Lithium batteries, and in particular the Lithium Titanium Oxide (LTO) type. The main issue of lithium batteries is their limited life-time, which is limited typically to a maximum of 3000 charge-discharge cycles. For LTO batteries, the life-time ranges from 5000 up to 20000 cycles, which would be the suitable range for FCC. In terms of size, LTO batteries are also very interesting; the required energy for a FCC dipole circuit could fit in the equivalent volume of 10 racks of 19”, which compare to the required size for supercapacitors or standard capacitors is an impressive advancement. Nevertheless, the research on energy storage is very active today and we expect significant improvements in energy

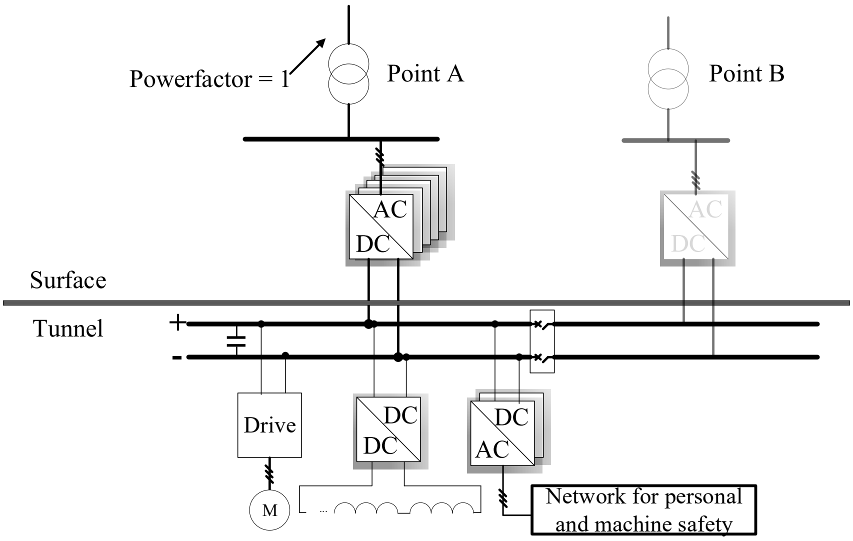

Figure 12.1: Simplified DC distribution grid to supply electrical loads of FCC.

4551 density, size and wait in the coming years.

4552 ## 12.5 Risks

4553 # Appendices

DRAFT FOR ADVISORY COMMITTEE - DO NOT DISTRIBUTE

Appendices A

Collider Parameter Tables

A Collider

B LHC as Injector

C Superconducting SPS

Appendices B

Experiment Parameter Tables

Appendices C

Infrastructures Parameter Tables

A Layout

B Civil Engineering

C Resource Use

Glossary

Arc A circular collider is composed of bent cells called arcs that are separated by straight sections (see LSS). An arc half-cell forms the periodic part of the arc lattice (see lattice).

Beam pipe Volumes of different shape (e.g. cylindrical, conical, flanges and bellows) and material (e.g. metallic, ceramic) used to transport the beam. The contained ultrahigh-vacuum reduces beam-gas interactions to a level at which the beam lifetime is acceptable.

Beam screen Perforated tube inserted into the cold bore of the superconducting magnets in order to protect the cold bore from synchrotron radiation and ion bombardment.

Beamline A series of functional elements, such as magnets and vacuum pipe, which carry the beam from one portion of the accelerator to another.

Beta function An optical function proportional to the square of the local transverse beam size. The beta function details how the beam width changes around the accelerator. There are separate Îš functions for the x and y planes.

Bunch A group of particles captured inside a longitudinal phase space bucket.

CERN European Organisation for Nuclear Research.

Collimator A device that removes beam particles at large amplitudes. They are used to keep beam-losses low and to protect critical elements of the accelerator.

Collision A close encounter of particles during which dynamic quantities such as energy, momentum, and charge may be exchanged.

Critical temperature Temperature Tc below which characteristics of superconductivity appear. The value varies from material to material and depends on the magnetic field.

Cryo magnet Complete magnet system integrated into one cryostat, including main magnet coils, collars and cryostat, correction magnets and powering circuits.

Cryogenic system A system that operates below a temperature set by convention at 150 K (-123.15°C).

Dark matter Invisible matter that makes up 26% of the universe and which can only be detected from its gravitational effects. Only 4% of the matter in the Universe are visible. The remaining 70% are accounted to dark energy.

Dipole A magnet with two poles, like the north and south poles of a horseshoe magnet. Dipoles are used in particle accelerators to keep particles moving in a circular orbit.

Dynamic aperture Maximum transverse oscillation amplitude that guarantees stable particle motion over a given number of turns. If the motion amplitude of a particle exceeds this threshold, the betatron oscillation of the particle will not have any bounds, and the motion will become unstable, leading to loss of the particle. It is expressed in multiples of the beam size together with the associated number of turns. Unlike the physical aperture, dynamic aperture separating stable and unstable trajectories is not a hard boundary.

Electron-cloud A cloud of electrons generated inside an accelerator beam pipe due to gas ionization, photoemission from synchrotron radiation, or âĂIJbeam-induced multipactingâĂİ via electron acceleration in the field of the beam and secondary emission. Electron clouds may cause single- and multi-bunch beam instabilities as well as additional heat load on the beam screen inside the cold magnets.

Electroweak symmetry breaking Although electromagnetism and the weak force have the same strength at high energies, electromagnetism is much stronger than the weak force in our everyday experience. The mechanism by which, at low energies, a single unified electroweak force appears as two separate forces is called electroweak symmetry breaking.

Emittance The area in phase space occupied by a particle beam. The units are mm-milliradians for transverse emittance and eV·sec for longitudinal emittance.

Experimental insertion region Place in the particle collider foreseen to host the interaction region in which the two beams are brought to collision and the surrounding particle physics experiments.

FCC Future Circular Collider is a feasibility study aiming at the development of conceptual designs for future energy and high-intensity frontier particle colliders based on a technically feasible and affordable circular layout permitting staged implementation.

FCC-hh Future circular energy-frontier hadron-hadron collider reaching up to 100 TeV centre-of-mass collision energies at luminosities of $5 - 10x10^{34}cm^{-2}s^{-1}$. Operation with protons and ions is envisaged.

Hadron A subatomic particle that contains quarks, antiquarks, and gluons, and so experiences the strong force. The proton is the most common hadron.

Higgs boson An elementary particle linked with a mechanism to model, how particles acquire mass.

HL-LHC High Luminosity upgrade of the LHC to a levelled constant luminosity of $5x10^{34}cm^2s^{-1}$. A dedicated FP7 design study (HiLumi LHC DS) precedes the upgrade implementation.

HTS High Temperature Superconductors have critical temperatures above 77 K.

Impedance A quantity that characterizes the self-interaction of a charged particle beam, mediated by the beam environment, such as the vacuum chamber, RF cavities, and other elements encountered along the accelerator or storage ring.

Kelvin Unit of measurement for temperature (K) using as null point the absolute zero, the temperature at which all thermal motion ceases. 0 K = -273.15°Celsius.

Lattice The arrangements of quadrupoles, dipole magnets, drift spaces and higher-order magnetic elements in the optical description of an accelerator.

LEP The Large ElectronâĂŞPositron Collider, which was operated at CERN until 2000.

Lepton A class of elementary particles that do not experience the strong force. The electron is the most common lepton.

LHC The Large Hadron Collider is a circular particle collider for protons and heavy ions with a design centre-of-mass energy of 14 TeV for proton-proton collisions at a peak luminosity of $1x10^{34}cm^2s^{-1}$ at CERN in Geneva, Switzerland.

Linac A LINear ACcelerator for charged particles in which a number of successive radiofrequency cavities that are powered and phased such that the particles passing through them receive successive increments of energy.

DRAFT FOR ADVISORY COMMITTEE - DO NOT DISTRIBUTE

LSS Long Straight Section: quasi-straight segments of a circular collider, which are available for beam interactions or utility insertions (e.g. injection, extraction, collimation, RF).

LTS Low Temperature Superconductors have critical temperatures below 77 K.

Luminosity Luminosity is the rate of collision events normalized to the cross section. It is expressed as inverse square centimetre and inverse second $(cm^{-2}s{-}1)$ or barn (1 barn = $10^{-24}cm^2$).

MDI The Machine Detector Interface refers to the topics and regions where the beamlines of the accelerator overlap with the physics experimentâĂŹs detector. Key elements include mechanical support of final beamline elements, luminosity monitoring, feedback, background suppression and radiation shielding.

Nb3Sn A metallic chemical compound of niobium (Nb) and tin (Sn). A LTS with TC = 18.3 K that can withstand magnetic field intensities up to 30 Teslas.

NEG Non-Evaporable Getter materials are mostly porous alloys or powder mixtures of Al, Zr, Ti, V and iron (Fe). They help to establish and maintain vacuums by soaking up or bonding to gas molecules that remain within a partial vacuum.

Optics An optical configuration refers to a powering scheme of the magnets. There can be several different optics for a single lattice configuration. Different optics exist for instance for injection and for luminosity operation corresponding to different $\beta*$ values in the experimental insertions.

Phase Space A six-dimensional space consisting of a particle's position (x, y, z) and divergence (x′, y′, z′). Phase space is represented in two dimensions by plotting position on the horizontal axis and the corresponding divergence on the vertical axis.

Quench The change of state in a material from superconducting to resistive. If uncontrolled, this process damages equipment due to thermal stress induced by the extremely high-currents passing through the material.

RAMS Reliability, Availability, Maintainability and Safety. Four non-functional key characteristics that determine the performance and total cost of technical systems.

RF cavity An electromagnetically resonant cavity used to convey energy (accelerate) to charged particles as they pass through by virtue of the electric field gradient across the cavity gap(s). Radio Frequency is a rate of oscillation in the range of around 3 kHz to 300 GHz.

SC coating A very thin layer of SuperConducting material on normal-conducting material (e.g. copper). Used for various purposes such as quench avoidance of a neighbouring superconductor, reduction of production costs due to use of cheaper support material and impedance reduction.

Standard Model The Standard Model explains how the basic building blocks of matter interact, governed by four fundamental forces.

Strand A superconducting strand is a composite wire containing several thousands of superconducting filaments (e.g. Nb_3Sn) dispersed in a matrix with suitably small electrical resistivity properties (e.g. copper).

Strong force One of four known fundamental forces (the others are the weak force, electromagnetism and gravity). The strong force is felt only by quarks and gluons, and is responsible for binding quarks together to make hadrons. For example, two up quarks and a down quark are bound together to make a proton. The strong interaction is also responsible for holding protons and neutrons together in atomic nuclei.

DRAFT FOR ADVISORY COMMITTEE - DO NOT DISTRIBUTE

Superconducting cable Superconducting cables are formed from several superconducting strands in parallel, geometrically arranged in the cabling process to achieve well-controlled cable geometry and dimensions, while limiting the strand deformation in the process. Cabling several strands in parallel results in an increase of the current carrying capability and a decrease of the inductance of the magnet, easing protection.

Superconductivity A property of some materials, usually at very low temperatures that allows them to carry electricity without resistance.

Synchrotron A circular machine that accelerates subatomic particles by the repeated action of electric forces generated by RF fields at each revolution. The particles move in constant circular orbits by magnetic forces that continually increase in magnitude.

Synchrotron Radiation Electromagnetic radiation generated by acceleration of relativistic charged particles in a magnetic or electric field. Synchrotron radiation is the major mechanism of energy loss in synchrotron accelerators and contributes to electron-cloud build-up.

Tesla Unit of magnetic field strength. 1 T is the field intensity generating one newton (N) of force per ampere (A) of current per meter of conductor.

TeV Tera electron Volts (10^{12} eV). Unit of energy. 1 eV is the energy given to an electron by accelerating it through 1 Volt of electric potential difference.

Tevatron A 2 TeV proton on anti-proton collider that was operated at Fermilab in Batavia, Illinois (USA) until 2011. The top quark was discovered using this collider.

Vacuum Pressures much below atmospheric pressure.

Weak force A force carried by heavy particles known as the W and Z bosons. The most common manifestation of this force is beta decay, in which a neutron in a nucleus is transformed into a proton, by emitting an electron and a neutrino. Weak neutral current is a very weak interaction mediated by the Z boson that is independent of the electric charge of a particle. Particles can exchange energy through this mechanism, but other characteristics of the particles remain unchanged.

DRAFT FOR ADVISORY COMMITTEE - DO NOT DISTRIBUTE

References

[1] *The European Strategy for Particle Physics Update, CERN-Council-S-0106*, `https://cds.cern.ch/record/1567258`, 2013.

[2] T. Behnke, J. E. Brau, B. Foster, J. Fuster, M. Harrison, J. M. Paterson, M. Peskin, M. Stanitzki, N. Walker, and H. Yamamoto, *The International Linear Collider Technical Design Report - Volume 1: Executive Summary*, `arXiv:1306.6327 [physics.acc-ph]`.

[3] K. Fujii et al., *Physics Case for the 250 GeV Stage of the International Linear Collider*, `arXiv:1710.07621 [hep-ex]`.

[4] M. Aicheler, P. Burrows, M. Draper, T. Garvey, P. Lebrun, K. Peach, N. Phinney, H. Schmickler, D. Schulte, and N. Toge, *A Multi-TeV Linear Collider Based on CLIC Technology*, .

[5] CLICdp, CLIC Collaboration, M. J. Boland et al., *Updated baseline for a staged Compact Linear Collider*, `arXiv:1608.07537 [physics.acc-ph]`.

[6] A. Blondel and F. Zimmermann, *A High Luminosity e^+e^- Collider in the LHC tunnel to study the Higgs Boson*, `arXiv:1112.2518 [hep-ex]`.

[7] A. Blondel et al., *LEP3: A High Luminosity e^+e^- Collider to Study the Higgs Boson*, `arXiv:1208.0504 [physics.acc-ph]`.

[8] C.-S. S. Group, *CEPC-SPPC Preliminary Conceptual Design Report. 1. Physics and Detector*, .

[9] C.-S. S. Group, *CEPC-SPPC Preliminary Conceptual Design Report. 2. Accelerator*, .

[10] T. T. D. S. W. Group, *First Look at the Physics Case of TLEP*, JHEP **01** (2014) 164, `arXiv:1308.6176 [hep-ex]`.

[11] W. Chou, *private communication*, February, 2018.

[12] The LEP Electroweak Working Group, the SLD Electroweak Group, the SLD Heavy Flavour Group, and the ALEPH, DELPHI, L3, OPAL and SLD Collaborations, *Precision electroweak measurements on the Z resonance*, Phys. Rept. **427** (2006) 257–454, `arXiv:hep-ex/0509008 [hep-ex]`.

[13] The LEP Electroweak Working Group and the ALEPH, DELPHI, L3, OPAL Collaborations, *Electroweak Measurements in Electron-Positron Collisions at W-Boson-Pair Energies at LEP*, Phys. Rept. **532** (2013) 119–244, `arXiv:1302.3415 [hep-ex]`.

[14] M. J. G. Veltman, *Limit on Mass Differences in the Weinberg Model*, Nucl. Phys. **B123** (1977) 89–99.

[15] Gfitter Group Collaboration, M. Baak, J. CÃžth, J. Haller, R. Hoecker, A.and Kogler, K. MÃűnig, M. Schott, and J. Stelzer, *The global electroweak fit at NNLO and prospects for the HC and ILC*, Eur. Phys. J. **C74** (2014) 3046, `arXiv:1407.3792 [hep-ph]`.

[16] F. Jegerlehner, *Electroweak effective couplings for future precision experiments*, Nuovo Cim. **C034S1** (2011) 31–40, `arXiv:1107.4683 [hep-ph]`.

[17] P. Janot, *Direct measurement of $\alpha_{QED}(m_Z^2)$ at the FCC-ee*, JHEP **02** (2016) 053, `arXiv:1512.05544 [hep-ph]`. [Erratum: JHEP11,164(2017)].

[18] C. Jarlskog, *Neutrino counting at the Z-peak and right-handed neutrinos*, Physics Letters B **241** (May, 1990) 579–583. `http://dx.doi.org/10.1016/0370-2693(90)91873-A`.

[19] G. Barbiellini, X. Berdugo, G. Bonvicini, P. Colas, L. Mirabito, and *et al.*, *Neutrino Counting*, . `http://cds.cern.ch/search?sysno=000112318CER`.

[20] OPAL Collaboration, G. Abbiendi and *et al.*, *Photonic events with missing energy in e^+e^- collisions at $\sqrt{s} = 189$ GeV*, Eur.Phys.J. **C18** (2000) 253–272, `arXiv:hep-ex/0005002 [hep-ex]`.

[21] ALEPH Collaboration, A. Heister and *et al.*, *Single photon and multiphoton production in e^+e^- collisions at $\sqrt{s}$ up to 209-GeV*, Eur.Phys.J. **C28** (2003) 1–13. `http://link.springer.com/article/10.1140%2Fepjc%2Fs2002-01129-7`.

DRAFT FOR ADVISORY COMMITTEE - DO NOT DISTRIBUTE

[22] L3 Collaboration, P. Achard and *et al.*, *Single photon and multiphoton events with missing energy in e^+e^- collisions at LEP*, Phys.Lett. **B587** (2004) 16–32, `arXiv:hep-ex/0402002 [hep-ex]`.

[23] DELPHI Collaboration, J. Abdallah and *et al.*, *Photon events with missing energy in e^+e^- collisions at $\sqrt{s} = 130$ to 209 GeV*, Eur.Phys.J. **C38** (2005) 395–411, `arXiv:hep-ex/0406019 [hep-ex]`.

[24] P. Janot, *Top-quark electroweak couplings at the FCC-ee*, JHEP **04** (2015) 182, `arXiv:1503.01325 [hep-ph]`.

[25] P. Azzi, C. Bernet, C. Botta, P. Janot, M. Klute, P. Lenzi, L. Malgeri, and M. Zanetti, *Prospective Studies for LEP3 with the CMS Detector*, `arXiv:1208.1662 [hep-ex]`.

[26] M. E. Peskin, *Comparison of LHC and ILC Capabilities for Higgs Boson Coupling Measurements*, `arXiv:1207.2516 [hep-ph]`.

[27] A. Drozd, J. Ellis, J. Quevillon, and T. You, *The Universal One-Loop Effective Action*, JHEP **03** (2016) 180, `arXiv:1512.03003 [hep-ph]`.

[28] J. Fuentes-Martin, J. Portoles, and P. Ruiz-Femenia, *Integrating out heavy particles with functional methods: a simplified framework*, JHEP **09** (2016) 156, `arXiv:1607.02142 [hep-ph]`.

[29] A. Pich, I. Rosell, J. Santos, and J. J. Sanz-Cillero, *Fingerprints of heavy scales in electroweak effective Lagrangians*, JHEP **04** (2017) 012, `arXiv:1609.06659 [hep-ph]`.

[30] J. de Blas, J. C. Criado, M. Perez-Victoria, and J. Santiago, *Effective description of general extensions of the Standard Model: the complete tree-level dictionary*, `arXiv:1711.10391 [hep-ph]`.

[31] B. Grzadkowski, M. Iskrzynski, M. Misiak, and J. Rosiek, *Dimension-Six Terms in the Standard Model Lagrangian*, JHEP **10** (2010) 085, `arXiv:1008.4884 [hep-ph]`.

[32] A. Freitas, *Numerical multi-loop integrals and applications*, Prog. Part. Nucl. Phys. **90** (2016) 201–240, `arXiv:1604.00406 [hep-ph]`.

[33] J. de Blas, M. Ciuchini, E. Franco, S. Mishima, M. Pierini, L. Reina, and L. Silvestrini, *Electroweak precision observables and Higgs-boson signal strengths in the Standard Model and beyond: present and future*, JHEP **12** (2016) 135, `arXiv:1608.01509 [hep-ph]`.

[34] J. de Blas, M. Ciuchini, E. Franco, S. Mishima, M. Pierini, L. Reina, and L. Silvestrini, *Electroweak precision constraints at present and future colliders*, PoS **ICHEP2016** (2017) 690, `arXiv:1611.05354 [hep-ph]`.

[35] J. de Blas, M. Ciuchini, E. Franco, S. Mishima, M. Pierini, L. Reina, and L. Silvestrini, *The Global Electroweak and Higgs Fits in the LHC era*, in *5th Large Hadron Collider Physics Conference (LHCP 2017) Shanghai, China, May 15-20, 2017*. 2017. `arXiv:1710.05402 [hep-ph]`.

[36] S. De Curtis, M. Redi, and A. Tesi, *The 4D Composite Higgs*, JHEP **04** (2012) 042, `arXiv:1110.1613 [hep-ph]`.

[37] D. Barducci, S. De Curtis, S. Moretti, and G. M. Pruna, *Future Electron-Positron Colliders and the 4-Dimensional Composite Higgs Model*, JHEP **02** (2014) 005, `arXiv:1311.3305 [hep-ph]`.

[38] D. Barducci, A. Belyaev, M. S. Brown, S. De Curtis, S. Moretti, and G. M. Pruna, *The 4-Dimensional Composite Higgs Model (4DCHM) and the 125 GeV Higgs-like signals at the LHC*, JHEP **09** (2013) 047, `arXiv:1302.2371 [hep-ph]`.

[39] E. Accomando, D. Barducci, S. De Curtis, J. Fiaschi, S. Moretti, and C. H. Shepherd-Themistocleous, *Drell-Yan production of multi Z'-bosons at the LHC within Non-Universal ED and 4D Composite Higgs Models*, JHEP **07** (2016) 068, `arXiv:1602.05438 [hep-ph]`.

DRAFT FOR ADVISORY COMMITTEE - DO NOT DISTRIBUTE

[40] D. Barducci, S. De Curtis, S. Moretti, and G. M. Pruna, *Top pair production at a future e^+e^- machine in a composite Higgs scenario*, JHEP **08** (2015) 127, `arXiv:1504.05407 [hep-ph]`.

[41] I. Esteban, M. C. Gonzalez-Garcia, M. Maltoni, I. Martinez-Soler, and T. Schwetz, *Updated fit to three neutrino mixing: exploring the accelerator-reactor complementarity*, JHEP **01** (2017) 087, `arXiv:1611.01514 [hep-ph]`.

[42] R. N. Mohapatra, *Mechanism for Understanding Small Neutrino Mass in Superstring Theories*, Phys. Rev. Lett. **56** (1986) 561–563.

[43] R. N. Mohapatra and J. W. F. Valle, *Neutrino Mass and Baryon Number Nonconservation in Superstring Models*, Phys. Rev. **D34** (1986) 1642.

[44] J. Bernabeu, A. Santamaria, J. Vidal, A. Mendez, and J. W. F. Valle, *Lepton Flavor Nonconservation at High-Energies in a Superstring Inspired Standard Model*, Phys. Lett. **B187** (1987) 303–308.

[45] G. C. Branco, W. Grimus, and L. Lavoura, *The Seesaw Mechanism in the Presence of a Conserved Lepton Number*, Nucl. Phys. **B312** (1989) 492–508.

[46] M. Malinsky, J. C. Romao, and J. W. F. Valle, *Novel supersymmetric SO(10) seesaw mechanism*, Phys. Rev. Lett. **95** (2005) 161801, `arXiv:hep-ph/0506296 [hep-ph]`.

[47] M. B. Gavela, T. Hambye, D. Hernandez, and P. Hernandez, *Minimal Flavour Seesaw Models*, JHEP **09** (2009) 038, `arXiv:0906.1461 [hep-ph]`.

[48] S. Iso, N. Okada, and Y. Orikasa, *Classically conformal B^{-} L extended Standard Model*, Phys. Lett. **B676** (2009) 81–87, `arXiv:0902.4050 [hep-ph]`.

[49] S. Iso and Y. Orikasa, *TeV Scale B-L model with a flat Higgs potential at the Planck scale - in view of the hierarchy problem -*, PTEP **2013** (2013) 023B08, `arXiv:1210.2848 [hep-ph]`.

[50] V. V. Khoze and G. Ro, *Leptogenesis and Neutrino Oscillations in the Classically Conformal Standard Model with the Higgs Portal*, JHEP **10** (2013) 075, `arXiv:1307.3764 [hep-ph]`.

[51] V. V. Khoze and A. D. Plascencia, *Dark Matter and Leptogenesis Linked by Classical Scale Invariance*, JHEP **11** (2016) 025, `arXiv:1605.06834 [hep-ph]`.

[52] T. Asaka, S. Blanchet, and M. Shaposhnikov, *The nuMSM, dark matter and neutrino masses*, Phys. Lett. **B631** (2005) 151–156, `arXiv:hep-ph/0503065 [hep-ph]`.

[53] T. Asaka and M. Shaposhnikov, *The nuMSM, dark matter and baryon asymmetry of the universe*, Phys. Lett. **B620** (2005) 17–26, `arXiv:hep-ph/0505013 [hep-ph]`.

[54] L. Canetti and M. Shaposhnikov, *Baryon Asymmetry of the Universe in the NuMSM*, JCAP **1009** (2010) 001, `arXiv:1006.0133 [hep-ph]`.

[55] L. Canetti, M. Drewes, and M. Shaposhnikov, *Sterile Neutrinos as the Origin of Dark and Baryonic Matter*, Phys. Rev. Lett. **110** (2013) no. 6, 061801, `arXiv:1204.3902 [hep-ph]`.

[56] M. Drewes and B. Garbrecht, *Leptogenesis from a GeV Seesaw without Mass Degeneracy*, JHEP **03** (2013) 096, `arXiv:1206.5537 [hep-ph]`.

[57] L. Canetti, M. Drewes, T. Frossard, and M. Shaposhnikov, *Dark Matter, Baryogenesis and Neutrino Oscillations from Right Handed Neutrinos*, Phys. Rev. **D87** (2013) 093006, `arXiv:1208.4607 [hep-ph]`.

[58] L. Canetti, M. Drewes, and B. Garbrecht, *Probing leptogenesis with GeV-scale sterile neutrinos at LHCb and Belle II*, Phys. Rev. **D90** (2014) no. 12, 125005, `arXiv:1404.7114 [hep-ph]`.

[59] P. Hernï£¡ndez, M. Kekic, J. Lï£¡pez-Pavï£¡n, J. Racker, and N. Rius, *Leptogenesis in GeV scale seesaw models*, JHEP **10** (2015) 067, `arXiv:1508.03676 [hep-ph]`.

[60] A. Abada, G. Arcadi, V. Domcke, and M. Lucente, *Lepton number violation as a key to low-scale leptogenesis*, JCAP **1511** (2015) no. 11, 041, `arXiv:1507.06215 [hep-ph]`.

[61] P. Hernï£¡ndez, M. Kekic, J. Lï£¡pez-Pavï£¡n, J. Racker, and J. Salvado, *Testable Baryogenesis in Seesaw Models*, JHEP **08** (2016) 157, `arXiv:1606.06719 [hep-ph]`.

DRAFT FOR ADVISORY COMMITTEE - DO NOT DISTRIBUTE

[62] M. Drewes and S. Eijima, *Neutrinoless double β decay and low scale leptogenesis*, Phys. Lett. **B763** (2016) 72–79, arXiv:1606.06221 [hep-ph].

[63] M. Drewes, B. Garbrecht, D. Gueter, and J. Klaric, *Leptogenesis from Oscillations of Heavy Neutrinos with Large Mixing Angles*, JHEP **12** (2016) 150, arXiv:1606.06690 [hep-ph].

[64] T. Asaka, S. Eijima, and H. Ishida, *On neutrinoless double beta decay in the νMSM*, Phys. Lett. **B762** (2016) 371–375, arXiv:1606.06686 [hep-ph].

[65] M. Drewes, B. Garbrecht, D. Gueter, and J. Klaric, *Testing the low scale seesaw and leptogenesis*, JHEP **08** (2017) 018, arXiv:1609.09069 [hep-ph].

[66] T. Asaka, S. Eijima, H. Ishida, K. Minogawa, and T. Yoshii, *Initial condition for baryogenesis via neutrino oscillation*, Phys. Rev. **D96** (2017) no. 8, 083010, arXiv:1704.02692 [hep-ph].

[67] A. Abada, G. Arcadi, V. Domcke, and M. Lucente, *Neutrino masses, leptogenesis and dark matter from small lepton number violation?*, JCAP **1712** (2017) no. 12, 024, arXiv:1709.00415 [hep-ph].

[68] D. Wyler and L. Wolfenstein, *Massless Neutrinos in Left-Right Symmetric Models*, Nucl. Phys. **B218** (1983) 205–214.

[69] M. C. Gonzalez-Garcia and J. W. F. Valle, *Fast Decaying Neutrinos and Observable Flavor Violation in a New Class of Majoron Models*, Phys. Lett. **B216** (1989) 360–366.

[70] E. K. Akhmedov, M. Lindner, E. Schnapka, and J. W. F. Valle, *Dynamical left-right symmetry breaking*, Phys. Rev. **D53** (1996) 2752–2780, arXiv:hep-ph/9509255 [hep-ph].

[71] E. K. Akhmedov, M. Lindner, E. Schnapka, and J. W. F. Valle, *Left-right symmetry breaking in NJL approach*, Phys. Lett. **B368** (1996) 270–280, arXiv:hep-ph/9507275 [hep-ph].

[72] S. M. Barr, *A Different seesaw formula for neutrino masses*, Phys. Rev. Lett. **92** (2004) 101601, arXiv:hep-ph/0309152 [hep-ph].

[73] A. Pilaftsis, *Radiatively induced neutrino masses and large Higgs neutrino couplings in the standard model with Majorana fields*, Z. Phys. **C55** (1992) 275–282, arXiv:hep-ph/9901206 [hep-ph].

[74] A. Abada, C. Biggio, F. Bonnet, M. B. Gavela, and T. Hambye, *Low energy effects of neutrino masses*, JHEP **12** (2007) 061, arXiv:0707.4058 [hep-ph].

[75] D. Aristizabal Sierra, A. Degee, and J. F. Kamenik, *Minimal Lepton Flavor Violating Realizations of Minimal Seesaw Models*, JHEP **07** (2012) 135, arXiv:1205.5547 [hep-ph].

[76] C. S. Fong, M. C. Gonzalez-Garcia, E. Nardi, and E. Peinado, *New ways to TeV scale leptogenesis*, JHEP **08** (2013) 104, arXiv:1305.6312 [hep-ph].

[77] V. Cirigliano, B. Grinstein, G. Isidori, and M. B. Wise, *Minimal flavor violation in the lepton sector*, Nucl. Phys. **B728** (2005) 121–134, arXiv:hep-ph/0507001 [hep-ph].

[78] Y. Cai, T. Han, T. Li, and R. Ruiz, *Lepton-Number Violation: Seesaw Models and Their Collider Tests*, arXiv:1711.02180 [hep-ph].

[79] S. Antusch, C. Biggio, E. Fernandez-Martinez, M. B. Gavela, and J. López-Pavon, *Unitarity of the Leptonic Mixing Matrix*, JHEP **10** (2006) 084, arXiv:hep-ph/0607020 [hep-ph].

[80] S. Antusch and O. Fischer, *Non-unitarity of the leptonic mixing matrix: Present bounds and future sensitivities*, JHEP **10** (2014) 094, arXiv:1407.6607 [hep-ph].

[81] C. P. Burgess, S. Godfrey, H. Konig, D. London, and I. Maksymyk, *Model independent global constraints on new physics*, Phys. Rev. **D49** (1994) 6115–6147, arXiv:hep-ph/9312291 [hep-ph].

[82] F. del Aguila, J. de Blas, and M. Perez-Victoria, *Effects of new leptons in Electroweak Precision Data*, Phys. Rev. **D78** (2008) 013010, arXiv:0803.4008 [hep-ph].

[83] E. Akhmedov, A. Kartavtsev, M. Lindner, L. Michaels, and J. Smirnov, *Improving Electro-Weak Fits with TeV-scale Sterile Neutrinos*, JHEP **05** (2013) 081, arXiv:1302.1872 [hep-ph].

DRAFT FOR ADVISORY COMMITTEE - DO NOT DISTRIBUTE

[84] L. Basso, O. Fischer, and J. J. van der Bij, *Precision tests of unitarity in leptonic mixing*, EPL **105** (2014) no. 1, 11001, `arXiv:1310.2057 [hep-ph]`.

[85] E. Fernandez-Martinez, J. Hernandez-Garcia, and J. Lopez-Pavon, *Global constraints on heavy neutrino mixing*, JHEP **08** (2016) 033, `arXiv:1605.08774 [hep-ph]`.

[86] M. Blennow, P. Coloma, E. Fernandez-Martinez, J. Hernandez-Garcia, and J. Lopez-Pavon, *Non-Unitarity, sterile neutrinos, and Non-Standard neutrino Interactions*, JHEP **04** (2017) 153, `arXiv:1609.08637 [hep-ph]`.

[87] S. Antusch, E. Cazzato, and O. Fischer, *Sterile neutrino searches at future e^-e^+, pp, and e^-p colliders*, Int. J. Mod. Phys. **A32** (2017) no. 14, 1750078, `arXiv:1612.02728 [hep-ph]`.

[88] DELPHI Collaboration, P. Abreu et al., *Search for neutral heavy leptons produced in Z decays*, Z. Phys. **C74** (1997) 57–71. [Erratum: Z. Phys.C75,580(1997)].

[89] FCC-ee study Team Collaboration, A. Blondel, E. Graverini, N. Serra, and M. Shaposhnikov, *Search for Heavy Right Handed Neutrinos at the FCC-ee*, Nucl. Part. Phys. Proc. **273-275** (2016) 1883–1890, `arXiv:1411.5230 [hep-ex]`.

[90] S. Antusch, E. Cazzato, and O. Fischer, *Displaced vertex searches for sterile neutrinos at future lepton colliders*, JHEP **12** (2016) 007, `arXiv:1604.02420 [hep-ph]`.

[91] S. B. Nielsen, *Prospects of Sterile Neutrino search at FCC-ee*, .

[92] S. Antusch, E. Cazzato, M. Drewes, O. Fischer, B. Garbrecht, D. Gueter, and J. Klaric, *Probing Leptogenesis at Future Colliders*, `arXiv:1710.03744 [hep-ph]`.

[93] S. L. Glashow, J. Iliopoulos, and L. Maiani, *Weak Interactions with Lepton-Hadron Symmetry*, Phys. Rev. **D2** (1970) 1285–1292.

[94] G. Mann and T. Riemann, *Effective Flavor Changing Neutral Current in the standard theory and Z-boson decay* , Annalen Phys. **40** (1984) 334.

[95] A. Abada, V. De Romeri, S. Monteil, J. Orloff, and A. M. Teixeira, *Indirect searches for sterile neutrinos at a high-luminosity Z-factory*, JHEP **04** (2015) 051, `arXiv:1412.6322 [hep-ph]`.

[96] COMET Collaboration, Y. Kuno, *A search for muon-to-electron conversion at J-PARC: The COMET experiment*, PTEP **2013** (2013) 022C01.

[97] L3 Collaboration, O. Adriani et al., *Search for LFV in Z decays*, Phys. Lett. **B316** (1993) 427–434.

[98] OPAL Collaboration, R. Akers et al., *A Search for LFV Z^0 decays*, Z. Phys. **C67** (1995) 555–564.

[99] DELPHI Collaboration, P. Abreu et al., *Search for LF number violating Z^0 decays*, Z. Phys. **C73** (1997) 243–251.

[100] ATLAS Collaboration, G. Aad et al., *Search for the LFV decay $Z \to e\mu$ in pp collisions at $\sqrt{s}$= 7 TeV with the ATLAS detector*, Phys. Rev. **D90** (2014) no. 7, 072010, `arXiv:1408.5774 [hep-ex]`.

[101] M. Dam. Private communication, 2016.

[102] W. Altmannshofer and D. M. Straub, *New physics in $B \to K^*\mu\mu$?*, EPJ **C73** (2013) 2646, `arXiv:1308.1501 [hep-ph]`.

[103] A. Buras, F. De Fazio, J. Girrbach, and M. V. Carlucci, *The Anatomy of Quark Flavour Observables in 331 Models in the Flavour Precision Era*, JHEP **02** (2013) 023, `arXiv:1211.1237 [hep-ph]`.

[104] R. Gauld, F. Goertz, and U. Haisch, *An explicit Z'-boson explanation of the $B \to K^*\mu^+\mu^-$ anomaly*, JHEP **01** (2014) 069, `arXiv:1310.1082 [hep-ph]`.

[105] S. Descotes-Genon, L. Hofer, J. Matias, and J. Virto, *Global analysis of $b \to s\ell\ell$ anomalies*, JHEP **06** (2016) 092, `arXiv:1510.04239 [hep-ph]`.

[106] LHCb Collaboration, R. Aaij et al., *Test of lepton universality using $B^+ \to K^+\ell^+\ell^-$ decays*, Phys. Rev. Lett. **113** (2014) 151601, `arXiv:1406.6482 [hep-ex]`.

DRAFT FOR ADVISORY COMMITTEE - DO NOT DISTRIBUTE

[107] LHCb Collaboration, R. Aaij et al., *Angular analysis of the $B^0 \to K^{*0}\mu^+\mu^-$ decay using 3 fb^{-1} of integrated luminosity*, JHEP **02** (2016) 104, `arXiv:1512.04442 [hep-ex]`.

[108] Belle Collaboration, A. Abdesselam et al., *Angular analysis of $B^0 \to K^*(892)^0\ell^+\ell^-$*, in *LHC Ski 2016*. 2016. `arXiv:1604.04042 [hep-ex]`. `https://inspirehep.net/record/1446979/files/arXiv:1604.04042.pdf`.

[109] J. F. Kamenik, S. Monteil, A. Semkiv, and L. V. Silva, *Lepton polarization asymmetries in rare semi-tauonic $b \to s$ exclusive decays at FCC-ee*, Eur. Phys. J. **C77** (2017) no. 10, 701, `arXiv:1705.11106 [hep-ph]`.

[110] S. Jadach, *The KKMC homepage*, `https://jadach.web.cern.ch/jadach/KKindex.html`.

[111] T. Riemann, *The ZFITTER homepage*, `http://sanc.jinr.ru/users/zfitter`.

[112] J. Gluza, *EW precision calculation mini-workshop at CERN, report in preparation and talk given at the second FCC physics workshop*, `https://indico.cern.ch/event/669224/` and `https://indico.cern.ch/event/618254/`.

[113] I. Dubovyk, A. Freitas, J. Gluza, T. Riemann, and J. Usovitsch, *The two-loop electroweak bosonic corrections to $\sin^2\theta^{\mathrm{b}}_{\mathrm{eff}}$*, Phys. Lett. **B762** (2016) 184–189, `arXiv:1607.08375 [hep-ph]`.

[114] D. Schulte, *FCC-hh Design Highlights*, ICFA Beam Dyn.Newslett. **72** (2017) 99–109.

[115] K. Oide, *et al.*, *Design of beam optics for the future circular collider e+eâĹŠ collider*, Phys.Rev.Accel.Beams **19** (2016) no.11, 111005.

[116] A. Bogomyagkov, E. Levichev, and D. Shatilov, *Beam-beam effects investigation and parameters optimization for a circular e+e- collider TLEP to study the Higgs boson*, Phys. Rev. ST Accel. Beams **17** (2014) 041004.

[117] Particle Data Group, *High-Energy Collider Parameters: e^+e Colliders*, `http://pdg.lbl.gov/2017/reviews/rpp2017-rev-hep-collider-params.pdf`, Jan., 2016.

[118] G. von Holtey, *et al.*, *Study of beam induced particle backgrounds at the LEP detectors*, Nucl.Instrum.Meth. **A403** (1998) 205–246.

[119] M. Aiba, *et al.*, *Top-up injection schemes for future circular lepton collider*, Nucl.Instrum.Meth. **A880** (2018) 98–106.

[120] A. Milanese, *Efficient twin aperture magnets for the future circular e+/e-collider*, Phys.Rev.Accel.Beams **19** (2016) no.11, 112401.

[121] N. Muchnoi, *Compton Polarimeter*, Fcc-ee polarization workshop, oct. 17-28, cern, geneva. switzerland, Oct., 2017.

[122] K. Oide, *at al*, *PROGRESS IN THE DESIGN OF BEAM OPTICS FOR FCC-ee COLLIDER RING*, Proc. ipac 2017, may 15-19, copenhagen, denmark, May, 2017.

[123] K. Oide, *FCC-ee Optics Design*, ICFA Beam Dyn.Newslett. **72** (2017) 19–25.

[124] R. Servranckx and K. L. Brown, *Chromatic Corrections for Large Storage Rings*, IEEE Trans.Nucl.Sci. **26** (1979) 3598.

[125] H. Koiso, A. Morita, Y. Ohnishi, K. Oide, and K. Satoh, *Lattice of the KEKB colliding rings*, Prog. Theor. Exp. Phys. **2013** (2013) no.3, 03A009.

[126] K. Oide, *KEKB B-factory, the luminosity frontier*, Prog.Theor.Phys. **122** (2009) 69–80.

[127] Y. O. at al., *Accelerator design at SuperKEKB*, PTEP **2013** (2013) 03A011.

[128] *Final focus system with odd dispersion scheme*, Int.J.Mod.Phys.Proc.Suppl. **2, Suppl. 2B** (1993) 861–863.

[129] P. Azzi, *FCC-ee Progress on physics and experiment studies*, Fcc week 2016, 11–15 april 2016, rome, italy, apr, 2016.

[130] *SAD*, `http://acc-physics.kek.jp/SAD/index.html`.

DRAFT FOR ADVISORY COMMITTEE - DO NOT DISTRIBUTE

[131] E. Forest and J. Milutinović, *"Leading Order Hard Edge Fringe Fields Effects Exact (1 + Delta) and Consistent With Maxwell's Equations for Rectilinear Magnets"*, Nucl.Instrum.Meth. **A269** (1988) 474.

[132] R. Assmann, P. Raimondi, G. Roy, and J. Wenninger, *Emittance optimization with dispersion free steering at LEP*, Phys. Rev. ST Accel. Beam **3** (2000) 121001.

[133] A. Franchi *et al.*, *Vertical emittance reduction and preservation in electron storage rings via resonance driving terms correction*, Phys. Rev. ST Accel. Beam **14** (Mar., 2015) 034002.

[134] G. von Holtey *et al.*, *Study of beam induced particle backgrounds at the LEP detectors*, Nucl. Instrum. Meth. **A403** (1998) 205.

[135] https://www.cst.com.

[136] *HFSS*, http://www.ansys.com/Products/Electronics/ANSYS-HFSS.

[137] *Unavoidable trapped mode in the interaction region of colliding beams*, Physical Review Accelerators and Beams .

[138] M. Boscolo and H. Burkhardt, *Tracking Simulation for Beam Loss Studies with Application to FCC*, Ipac'15.

[139] M. Boscolo, H. Burkhardt, and M. Sullivan, *Machine detector interface studies: Layout and synchrotron radiation estimate in the future circular collider interaction region*, Phys. Rev. Accel. Beams **20 no.1** (2017) 011008.

[140] *GUINEA-PIG*, https://twiki.cern.ch/twiki/bin/view/ABPComputing/Guinea-Pig.

[141] https://kt.cern/technologies/non-evaporable-getter-neg-thin-film-coatings.

[142] A. Rossi, *SEY and electron cloud build-up with NEG materials*, Cern, geneva, switzerland, 2005.

[143] E. Belli, *Impedance model and collective effects for FCC-ee*, Fcc week 2017, 29 may-2 jun 2017, berlin, germany, May, 2017.

[144] A. Butterworth, *Cavity design and beam-cavity interaction*, Fcc week 2017 - 30 may 2017, berlin (germany) - https://indico.cern.ch/event/556692/contributions/2484361/, May, 2017.

[145] S. G. Zadeh, *Cavity Design approaches and HOM damping for FCC-ee*, Proceedings fcc week 2017 - 30 may 2017, berlin (germany) - https://indico.cern.ch/event/556692/contributions/2484333/, May, 2017.

[146] *ABCI*, http://abci.kek.jp/.

[147] Y. Suetsugu, K. Kanazawa, K. Shibata, T. Ishibashi, and H. H. et al., *Design and construction of the SuperKEKB vacuum system*, Journal of Vacuum Science & Technology A: Vacuum, Surfaces, and Films **30.3** (2012) 031602.

[148] *The PEP-II movable collimators*, Slac-pub-11752, 2001.

[149] T. Ishibashi et al., *Low impedance movable collimators for SuperKEKB*, Proceedings of ipac'17, copenhagen, denmark, may 14-19, 2017, May, 2017.

[150] F. Marcellini et al., *DAFNE broad-band button electrodes*, Nuclear Instruments and Methods in Physics Research Section A: Accelerators, Spectrometers, Detectors and Associated Equipment **402.1** (1998) 27–35.

[151] A. Rodrigues, et al., *Sirius status report*, Ipac'16, 2016.

[152] E. Belli, G. Castorina, M. Migliorati, A. Novokhatski, S. Persichelli, B. Spataro, and M. Zobov, *Coupling Impedances and Collective Effects for FCC-ee*, In 8th int. particle accelerator conf.(ipac'17), copenhagen, denmark, 14-19 may, 2017, May, 2017.

[153] Y. Suetsugu, M. Shirai, , and K. Shibata, *Possibility of combtype rf shield structure for high-current accelerators*, Phys. Rev. ST:AB **6.10** (2003) 103201.

[154] N. Mounet, *ImpedanceWake2D*, https://twiki.cern.ch/twiki/bin/view/ABPComputing/ImpedanceWake2D, 2011.

DRAFT FOR ADVISORY COMMITTEE - DO NOT DISTRIBUTE

[155] *PyHEADTAIL*, `https://github.com/PyCOMPLETE/PyHEADTAIL`.

[156] J. Haissinski Il Nuovo Cimento **B 18** (1973) 72.

[157] A. W. Chao, *Physics of collective beam instabilities in high energy accelerators*. Wiley, 1993.

[158] *DELPHI*, `https://twiki.cern.ch/twiki/bin/view/ABPComputing/DELPHI`.

[159] E. Belli and M. M. et al., *Single beam collective effects in FCC-ee due to beam coupling impedance.*, 2016.

[160] A. Drago, *Feedback Systems for FCC-ee*, Oral presentation at fcc week 2016, 11-15 april 2016, rome, italy., apr, 2016.

[161] A. Drago, *Feedback Systems for FCC-ee*, Oral presentation at eefact2016, 58th icfa advanced beam dynamics workshop on high luminosity circular e+e-colliders, 24-27 october 2016. cockcroft institute at daresbury laboratory, uk, oct, 2016.

[162] `https://indico.cern.ch/event/556692/contributions/2590394/`.

[163] G. R. et al., *Electron cloud in the CERN accelerator complex*, No. cern-acc-2016-0099, 2016.

[164] H. Fukuma, *Electron cloud instability in KEKB and SuperKEKB*, ICFA Beam Dyn. Newslett **48** (2009) 112–118.

[165] G. Rumolo and F. Zimmermann, *Theory and Simulation of the Electron cloud instability*, Proceedings of the lhc workshop chamonix xi. 2001, 2001.

[166] K. Ohmi and F. Zimmermann, *Head-Tail Instability Caused by Electron Clouds in Positron Storage Rings*, PRL **85(18)** (2000) 3821–3824.

[167] K. Ohmi, F. Zimmermann, and E. Perevedentsev, *Study of the fast head-tail instability caused by the electron cloud*, Cern-sl-2001-011 ap, 2001.

[168] M. Bicer, *First look at the physics case of TLEP*, Journal of High Energy Physics **2014** (2014) 164.

[169] P. Janot, *Perspectives for Future Circular Colliders (1/3)*, Cern academic training, oct 11, cern, geneva. switzerland, Oct., 2017.

[170] A. Renieri, *Possibility of Achieving Very High Energy Resolution in e^+e^--Storage Rings*, Frascati Preprint **INF/75/6 (R)** (1975) .

[171] D. d'Enterria, *Higgs Physics at the Future Circular Collider*, PoS ICHEP'16 Chicago (2016) 434.

[172] M. V. Garcia and F. Zimmermann, *Optimized Monochromatization for Direct Higgs Production in Future Circular e^+e^- Colliders*, In 8th Int. Particle Accelerator Conf. (IPAC'17), Copenhagen, Denmark, 14-19 May, 2017 (2017) 2950–2953.

[173] S. Jadach and R.A. Kycia, *Lineshape of the Higgs boson in future lepton colliders*, Phys. Lett. B **755** (2016) 58.

[174] P. Janot, *Direct measurement of $\alpha_{\rm QED}(m_Z^2)$ at the FCC-ee*, JHEP **202** (2016) 053.

[175] M. Boscolo, H. Burkhardt, and M. Sullivan, *Machine detector interface studies: Layout and synchrotron radiation estimate in the future circular collider interaction region*, Phys. Rev. Accel. Beams **20** (Jan, 2017) 011008. `https://link.aps.org/doi/10.1103/PhysRevAccelBeams.20.011008`.

[176] A. Milanese and M. Bohdanowicz, *Twin Aperture Bending Magnets and Quadrupoles for FCC-ee*, IEEE Transactions on Applied Superconductivity **28** (April, 2018) 1–4.

[177] *magnetic measurements reports for dipoles PXMBHAACAC and quadrupole PXMQNDI8WC*, To be published, 2018.

[178] A. B. P. J. K. O. D. S. F. Zimmermann, *FCC-ee parameter update*, private communication (2017) .

[179] R. C. S. Gorgi Zadeh and U. van Rienen, *Preliminary Cavity design for FCC-ee*,

DRAFT FOR ADVISORY COMMITTEE - DO NOT DISTRIBUTE

fcc-acc-rpt-0005, Rostock University, 2016. EDMS NO. 1612380.

[180] O. Etisken, Y. Papaphilippou, and A. K. Ciftci, *Conceptual design of a pre-booster ring for FCC e+e- injector*, Journal of Physics: Conference Series, Volume 874 (2017) .

[181] S. A. O. B. A. B. N. Schwerg, *Material Options for the Superconducting RF System of the Future Circular Collider*, FCC-DRAFT-TECH-2017-002, https://cds.cern.ch/record/2289506 (2017) .

[182] W. Delsolaro, *Thin film research: CERN experience and possible future applications*, TESLA Technology Collaboration (TTC) Meeting, Milano, Italy, 2018, 2018.

[183] D. L. H. S Posen, *Nb3Sn superconducting radiofrequency cavities: fabrication, results, properties, and prospects*, Superconductor Science and Technology (2017) .

[184] K. Ilyina-Brunner, *Magnetron Sputtering of Nb3Sn thin films on copper for SRF application*, fourth Annual Meeting of the Future Circular Collider study, Amsterdam, The Netherlands, 2018, 2018.

[185] C. A. Clemente, *Surface quality and improvements on the SRF cavity manufacturing by electrohydraulic forming*, fourth Annual Meeting of the Future Circular Collider study, Amsterdam, The Netherlands, 2018, 2018.

[186] C. P. E.Palmieri, *Coating studies on 6 GHz seamless cavities*, fourth Annual Meeting of the Future Circular Collider study, Amsterdam, The Netherlands, 2018, 2018.

[187] E. Montesinos, *FPC challenges and perspectives for FCC*, third Annual Meeting of the Future Circular Collider study, Berlin, Germany, 2017, 2017.

[188] I. Syratchev, *Introduction to HEIKA. Tentative structure and objectives*, tbd, CERN, 2015. CLIC Workshop 2015, CERN, Geneva, Switzerland.

[189] A. Yu., Baikov, C. Marrelli, and I. Syratchev, *Toward High-Power Klystrons With RF Power Conversion Efficiency on the Order of 90%*, IEEE Trans. on Electron devices **62** (October, 2015) 3406. tbd.

[190] I. Guzilov, *BAC method of increasing the efficiency in Klystrons*, in *IEEE Vacuum Electron Sources Conference 2014, St. Petersburg, Russia*. 2014.

[191] G. Burt, D. Constable, C. Lingwood, V. Hill, C. Marrelli, and I. Syratchev, *Particle-in-cell Simulation of a Core Stabilization Method Klystron*, in *IEEE International Vacuum Electronics Conference, IVEC 2017, London, UK*. 2017.

[192] I. Syratchev, *High efficiency klystron technology*, third Annual Meeting of the Future Circular Collider study, Berlin, Germany, 2017, 2017.

[193] I. S. J.Cai, *KlyC: Large Signal Simulation Code for Klystrons*, submitted to IEEE TED, January 2016, 2017.

[194] P. Baudrenghien, *LLRF Lessons Learned LHC and PEP-II Relevance to FCC hh/ee*, second Annual Meeting of the Future Circular Collider study, Rome, Italy, 2016, 2016.

[195] J. F. et al., *Lessons learned from positron-electron project low level rf and longitudinal feedback*, PRST AB, 052802 (2010) .

[196] I. Karpov, R. Calaga, and E. Shaposhnikova, *HOM power in FCC-ee cavities*, fcc-draft-acc-2018, CERN, 2018. http://cds.cern.ch/record/2302276/files/CERN-ACC-2018-0005.pdf.

[197] S. G. Zadeh, *Cavity Design approaches and HOM damping for FCC-ee*, third Annual Meeting of the Future Circular Collider study, Berlin, Germany, 2017, 2017.

[198] http://blond.web.cern.ch.

[199] J. F. E. Müller, *Modification of the simulation code BLonD for lepton rings*, fcc-draft-tech-2017-001, CERN, 2017. https://cds.cern.ch/record/2284587.

[200] J. F. E. Müller, *FCC-ee broadband impedance and longitudinal single bunch stability*, fcc-draft-acc-2017-035, CERN, 2017. http://cds.cern.ch/record/2289514.

[201] R. Calaga, *Beam dynamics issues for FCC-ee*, first FCC-ee RF mini review, 2016.

DRAFT FOR ADVISORY COMMITTEE - DO NOT DISTRIBUTE

[202] A. Butterworth, *Cavity design and beam-cavity interaction*, third Annual Meeting of the Future Circular Collider study, Berlin, Germany, 2017, 2017.

[203] M. Migliorati, *FCC-ee Single-beam collective effects*, second Annual Meeting of the Future Circular Collider study, Rome, Italy, 2016, 2016.

[204] D. Schulte, *Beam-Beam Simulations with GUINEA-PIG*, . `https://cds.cern.ch/record/382453`.

[205] T. Sjöstrand, S. Mrenna, and P. Skands, *PYTHIA 6.4 physics and manual*, Journal of High Energy Physics **5** (May, 2006) 026, `hep-ph/0603175`.

[206] OPAL Collaboration, G. Abbiendi, et al., *Precision luminosity for* Z^0 *lineshape measurements with a silicon-tungsten calorimeter*, Eur. Phys. J. **C14** (2000) 373–425, `hep-ex/9910066`.

[207] D. Bédérède et al., *SICAL – a high precision silicon-tungsten luminosity calorimeter for ALEPH*, Nucl. Inst. Meth. **A365** (1995) no. 1, 117–134. `http://www.sciencedirect.com/science/article/pii/0168900295004092`.

[208] H. Abramowicz et al., *The International Linear Collider Technical Design Report - Volume 4: Detectors*, `arXiv:1306.6329 [physics.ins-det]`.

[209] M. Aicheler et al., *A Multi-TeV Linear Collider Based on CLIC Technology: CLIC Conceptual Design Report*, CERN-2012-007. SLAC-R-985. KEK-Report-2012-1. PSI-12-01. JAI-2012-001, Geneva, 2012. `https://cds.cern.ch/record/1500095`.

[210] J. Crawford, E. Hughes, L. O'Neill, and R. Rand, *A precision luminosity monitor for use at electron-positron storage rings*, Nuclear Instruments and Methods **127** (1975) no. 2, 173 – 182. `http://www.sciencedirect.com/science/article/pii/0029554X75904851`.

[211] S. Jadach, W. Placzek, E. Richter-Waas, B. Ward, and Z. Was, *Upgrade of the Monte Carlo program BHLUMI for Bhabha scattering at low angles to version 4.04*, Computer Physics Communications **102** (1997) no. 1, 229 – 251. `http://www.sciencedirect.com/science/article/pii/S0010465596001567`.

[212] S. Jadach, W. Placzek, and B. Ward, *"BHWIDE 1.00:* $O(\alpha)$ *YFS exponentiated Monte Carlo for Bhabha scattering at wide angles for LEP1/SLC and LEP2"*, Physics Letters B **390** (1997) no. 1, 298 – 308. `http://www.sciencedirect.com/science/article/pii/S0370269396013822`.

[213] N. Alipour Tehrani et al., *CLICdet: The post-CDR CLIC detector model*, . CLICdp-Note-2017-001.

[214] M. Frank, F. Gaede, C. Grefe, and P. Mato, *DD4hep: A Detector Description Toolkit for High Energy Physics Experiments*, Journal of Physics: Conference Series **513** (2014) no. 2, 022010. `http://stacks.iop.org/1742-6596/513/i=2/a=022010`.

[215] J. S. Marshall and M. Thomson, *The Pandora software development kit for pattern recognition*, Eur. Phys. J. **C75** (2015) 439.

[216] F. Sefkow et al., *Experimental tests of particle flow calorimetry*, Rev. Med. Phys. **88** (2016) 1 – 53.

[217] ALICE Collaboration, *Technical Design Report for the Upgrade of the ALICE Inner Tracking System*, J. Phys. G **41** (2014) 087002. ALICE-TDR-017.

[218] ALICE Collaboration, M. Mager, *ALPIDE, the Monolithic Active Pixel Sensor for the ALICE ITS upgrade*, Nucl. Instrum. Meth. **A824** (2016) 434–438.

[219] ALICE Collaboration, G. Aglieri Rinella, *The ALPIDE pixel sensor chip for the upgrade of the ALICE Inner Tracking System*, Nucl. Instrum. Meth. **A845** (2017) 583–587.

[220] M. Adinolfi et al., *The tracking detector of the KLOE Experiment*, Nucl. Instrum. Meth. **A488** (2002) 51.

[221] A. M. Baldini et al., *MEG Upgrade Proposal*, ArXiv e-prints (Jan., 2013) , `arXiv:1301.7225 [physics.ins-det]`.

DRAFT FOR ADVISORY COMMITTEE - DO NOT DISTRIBUTE

[222] A. M. Baldini et al., *Single-hit resolution measurement with MEG II drift chamber prototypes*, Journal of Instrumentation **11** (July, 2016) P07011, `arXiv:1605.07970 [physics.ins-det]`.

[223] DREAM Collaboration, R. Wigmans, *The DREAM project: Towards the ultimate in calorimetry*, Nucl. Instrum. Meth. **A617** (2010) 129–133.

[224] N. Akchurin et al., *The electromagnetic performance of the RD52 fiber calorimeter*, Nucl. Instrum. Meth. **A735** (2014) 130–144.

[225] RD52 (DREAM) Collaboration, R. Wigmans, *New results from the RD52 project*, Nucl. Instrum. Meth. **A824** (2016) 721–725.

[226] N. Akchurin et al., *Particle identification in the longitudinally unsegmented RD52 calorimeter*, Nucl. Instrum. Meth. **A735** (2014) 120–129.

[227] A. Collaboration, *"The ATLAS Experiment at the CERN Large Hadron Collider"*, Journal of Instrumentation **3** (2008) no. 08, S08003. `http://stacks.iop.org/1748-0221/3/i=08/a=S08003`.

[228] L. A. Aamport, *The Gnats and Gnus Document Preparation System*, G-Animal's Journal (1986) .

DRAFT FOR ADVISORY COMMITTEE - DO NOT DISTRIBUTE